

THÈSE DE DOCTORAT

de l'Université de recherche Paris Sciences et Lettres
PSL Research University

Préparée à MINES ParisTech

Analysis and modelling of the failure behavior of carbonitrided parts

Ecole doctorale n°364

Sciences Fondamentales et Appliquées

Spécialité Mécanique Numérique et Matériaux

COMPOSITION DU JURY :

Mme. Sandrine THUILLIER
Université de Bretagne Sud,
Rapporteur et Président

M. Jose CESAR DE SA
Université de Porto,
Rapporteur

M. David Moore PARKS
Massachusetts Institute of Technology,
Examineur

M. Pierre-Olivier BOUCHARD
Mines ParisTech,
Examineur

M. Pierre MONTMITONNET
Mines ParisTech,
Examineur

M. Guillaume DELATTRE
FAURECIA,
Invité

**Soutenue par Cyprien KAROLAK
le 28 septembre 2016**

Dirigée par **Pierre-Olivier BOUCHARD**
et **Pierre MONTMITONNET**



Acknowledgment

I would like to thank M. Romain Soubeyran and Ms. Elisabeth Massoni, respectively Director of Mines Paristech and Director of the Center for Material Forming, for giving me the opportunity to carry out my PhD thesis at CEMEF.

I also wish to express my gratitude to the members of my PhD thesis committee, Mrs. Sandrine Thuillier and M. José César De Sa, for taking the time during summer vacations to assess my work.

I would like to thank my industrial advisor, Guillaume Delattre, for all the time he spent giving me the industrial context of the project and guidelines regarding the simulations. Thanks as well to M. Laurent Guérin and M. Christophe Lemaitre, who launched this PhD topic at Faurecia. I would like to thank these persons at Faurecia who helped me: M. Bruno Desert for the heat treatment support, Ms. Aurelie Achille for the material characterization information, and Jerome Chottin, Valérie Woimbee, David Even, Tudor Balan.

I want to express my sincere gratitude to my thesis supervisors, Pierre-Olivier Bouchard and Pierre Montmitonnet, for sharing their extensive knowledge during these four years. They guided me and encouraged me always with patience, especially during the last year, which was difficult at times. Pierre-Olivier, thank you for imparting me with a part of your numerical knowledge regarding fracture modeling, for our friendly discussions and your wife's lemon pie. Pierre, thank you for your patience in imparting of your numerical and experimental skills and for challenging me to think outside the box. Your style of problem-solving influenced my thinking and encouraged me to consider my own ideas from a different perspective.

I offer my deep thanks to all the members of this project who created the opportunity for me to go to MIT and live for half a year in Boston; it was a life-changing experience. I would especially like to thank M. David Parks for his scientific advices, both in our face to face meetings and transmitted ones over the Atlantic. I express my kindest gratitude as well for his warm welcome in Boston, and for inviting me to the lobster party with his friends and family. My thanks also to M. Tomasz Wierzbicki for allowing me to work in the Crashworthiness Laboratory at MIT.

And I would also like to offer some kind words for other persons who helped me during these four years: M. Patrick Coels for his help regarding all the administrative processes, and for our endless discussions regarding life, sport and politics; Ms. Marie-Francoise Guénégan and Ms. Geneviève Anseeuw for their administrative support and travel bookings; M. Gilbert Fiorucci for all the tests done together: hundreds of teeth broken for the benefit of science; and M. Francis Fournier, M. Erick Brotons, and M. Marc Boyssou for the specimen machining.

And now I wish to thank some persons for their help and support from a personal point of view. I will start with Jose Alves, with whom I shared my office. There were so many things we lived through together; look at our life the first day of our PhD - and now. Wasn't this the best years of our life? I would like to thank all the international crew at CEMEF - keep on trucking, guys! We learned so much stuff together; isn't it awesome to be surrounded by foreigners! Special thanks to Miren for the work outs, food and many advices. Your healthy cakes are so tasty, and I am starving! ☺ Special thanks to Luis, Carlos, Danai, Ghalia, Victor and Juliana for your good mood every day; and Spaciba to Dima for the Russian initiation at CEMEF, and all the discussions about life we had together. I

want to say thanks to Francoise Trucas for the discussions and support when I needed it. Thanks as well to the French team at MIT for all the scientific talks we had on Friday and Saturday nights, especially the ones in NYC during Labor Day weekend, Stéphane ☺.

During my PhD, working out helped me to cool down my mind and to find new ideas for my research. I would also like to thank the redline team, especially Leo and Yuan, for the sporting moments we shared together and everything you did for me in Boston; it was the beginning of a great friendship.

I would like to thank my parents for their support and encouragement during these 4 years, and even more because I am where I am thanks to you. Thank you as well Yaya and Mini-Portion for the numerous reminders that I should be working on my manuscript. Sorry that I extended the pleasure one year more, but it was worth it, don't you think? ☺

I would like to thank Ray, or Super Ray, X-Ray for the closest, for his support, about everything lunch discussions and life advice over the sea. It is unbelievable we are texting almost every day, I am so glad than I met you.

And finally, I want to thank the person who stayed with me during the last year of this project. It was difficult, but you were strong and very close to me and gave me motivation to work on the weekends. Thank you for this, and I look forward to doing the same with your PhD Lenchka.

Contents

Introduction	9
Chapter I : Analysis and subject set-up	13
I. 1 Post mortem analysis	15
I. 1. 1 Static strength test	15
I. 1. 1. a Test bench description.....	15
I. 1. 1. b Recliners observations.....	16
I. 1. 2 First assumptions on teeth failure mechanism	19
I. 1. 3 Toward the material characterization – Hardness tests	21
I. 2 Literature review	22
I. 2. 1 Carbonitriding treatment	22
I. 2. 2 Influence of carbonitriding on the microstructure	25
I. 2. 3 Influence of carbonitriding on the mechanical behavior	26
I. 2. 4 Influence of carbonitriding on the fracture behavior	28
I. 3 Work methodology	30
Chapter II : Failure of carbonitrided steel components: a literature review	31
II. 1 Damage mechanisms	33
II. 1. 1 Ductile damage.....	33
II. 1. 1. a Stress states characterization.....	33
II. 1. 1. b Ductile damage mechanisms.....	34
II. 1. 2 Brittle damage	38
II. 1. 3 Functionally Graded Materials	39
II. 2 Damage models	42
II. 2. 1 Ductile failure	42
II. 2. 1. a Porous solid plasticity	42
II. 2. 1. b Coupled damage models	42
II. 2. 1. c Uncoupled failure criteria	43
II. 2. 2 Brittle failure.....	48
II. 3 Numerical modeling of failure in a finite element framework	49
II. 3. 1 Crack propagation numerical techniques.....	50
II. 3. 2 Element deletion technique	53
II. 4 Strategy adopted for the modeling of carbonitrided components failure	54
Chapter III : Semi-industrial test.....	57
III. 1 Test bench design	59

III. 1. 1	Technical specifications.....	59
III. 1. 2	Description	60
III. 2	Semi-industrial test results and analysis.....	61
III. 2. 1	Test bench set up and first trials	62
III. 2. 2	Engagement depth study	67
III. 2. 2. a	Tooth strength	68
III. 2. 2. b	Tooth failure process.....	69
III. 2. 2. c	Discussion.....	74
III. 2. 3	Influence of the CN layer on the tooth failure	75
III. 2. 3. a	Influence on the strength	76
III. 2. 3. b	Influence on the tooth failure process	77
III. 3	Conclusion.....	82
Chapter IV	: Mechanical characterization.....	85
IV. 1	Fracture tests.....	87
IV. 1. 1	Triaxiality and Lode angle analysis	87
IV. 1. 2	Shear tests	89
IV. 2	Core material	92
IV. 2. 1	Low stress triaxiality characterization	92
IV. 2. 1. a	Experimental methodology	93
IV. 2. 1. b	Experimental results.....	95
IV. 2. 1. c	Fracture surfaces study.....	97
IV. 2. 1. d	Discussion	99
IV. 2. 2	High triaxiality characterization.....	100
IV. 2. 2. a	Experimental method.....	101
IV. 2. 2. b	Experimental results.....	103
IV. 2. 2. c	Fracture surface Analysis	105
IV. 2. 2. d	Discussion	107
IV. 2. 3	Conclusion	107
IV. 3	Characterization of the CN layer	107
IV. 3. 1	4PBT.....	108
IV. 3. 1. a	Experimental method.....	108
IV. 3. 1. b	Results	109
IV. 3. 1. c	Discussion	110
IV. 3. 2	Tensile tests.....	111

IV. 3. 2. a	Experimental methodology	111
IV. 3. 2. b	Results	112
IV. 3. 2. c	Discussion	114
IV. 3. 3	Conclusion	115
IV. 4	Influence of the external layer on the behavior and failure mechanism in tension	116
IV. 4. 1	Influence on the strength and ductility	116
IV. 4. 2	Influence of the CN layer on the failure process	117
IV. 4. 3	Discussion	119
IV. 5	Conclusion of chapter IV	120
Chapter V	: Parameters identification	123
V. 1	Plastic behavior for the core material	126
V. 2	Fracture criteria for the core material	129
V. 2. 1	Analysis of strain, stress triaxiality and Lode parameter at fracture	129
V. 2. 2	Test of criteria from the literature	137
V. 2. 2. a	Identification based on strain sensors	137
V. 2. 2. b	Improved estimation of the loading paths	139
V. 2. 2. c	Improved identification of damage model parameters	141
V. 2. 3	Proposition of a new exponential criterion	144
V. 2. 4	Fracture criterion reduction	148
V. 2. 5	Discussion	149
V. 3	Fracture criterion for the CN layer	152
V. 3. 1	4PBT	153
V. 3. 2	Tensile tests	154
V. 3. 3	Discussion	156
V. 4	Summary	157
Chapter VI	: Models validation: tooth failure	159
VI. 1	Failure implementation in LS-DYNA	161
VI. 1. 1	Core Material: power-law damage function defined through GISSMO	161
VI. 1. 2	Carbonitrided layer: critical stress implementation	163
VI. 2	Semi-industrial tests simulation - methodology	163
VI. 3	Experiment – simulation comparison with the core material only (CMO)	165
VI. 3. 1	Force-displacement curves	165
VI. 3. 2	Fracture process	167
VI. 3. 2. a	Overall observation	167
VI. 3. 2. a	Shear crack analysis	170

VI. 3. 3	Comparison with Faurecia's previous method	175
VI. 3. 4	Discussion	176
VI. 4	Experiment – simulation comparison with the complete CNed component	179
VI. 4. 1	Force displacement curves	179
VI. 4. 2	Fracture process	180
VI. 4. 2. a	Overall facture process.....	180
VI. 4. 2. b	Shear crack propagation – comparison with the CMO	182
VI. 4. 3	Comparison with Faurecia's previous method	190
VI. 4. 4	Discussion	191
VI. 4. 4. a	Impact of variations of the CN behavior	191
VI. 4. 4. b	Influence of mesh size	195
VI. 4. 4. c	Simplified ductile fracture criterion – Lou & Huh criterion	197
VI. 5	Conclusion.....	199
Chapter VII	: Conclusion.....	201
	Bibliography.....	208
	Appendix.III.1: obtaining CMO with CarboStop paint	214
	Appendix IV.1: Butterfly measurements and experimental force displacement curves.....	216
	Appendix V.1: comparaison experimental numerical forces displacements curves	219

Introduction

The automotive supplier *Faurecia Automotive Seating* develops and manufactures automotive seating. In the present economic situation, especially for the automotive industry, competitiveness is the main key for profitability. Thus, companies must continuously offer efficient and innovative products to face the fierce competition on this market.

Automotive seats are composed of frames, mechanisms, motors, seat covers and many other subsystems. In any car, seats play an essential role in terms of comfort, safety and modularity for drivers and passengers. Seats account for 5% of a vehicle's total cost and 6% of its weight. They represent the second largest expense for automakers. The latter are trying to produce lighter cars to be environment friendly but keep still offering more and more equipment. Thus lighter seats are one of the main motivations of Faurecia. This leads to decrease the amount of raw material used and limit at the same time manufacturing costs without decreasing components mechanical strength and fatigue properties.

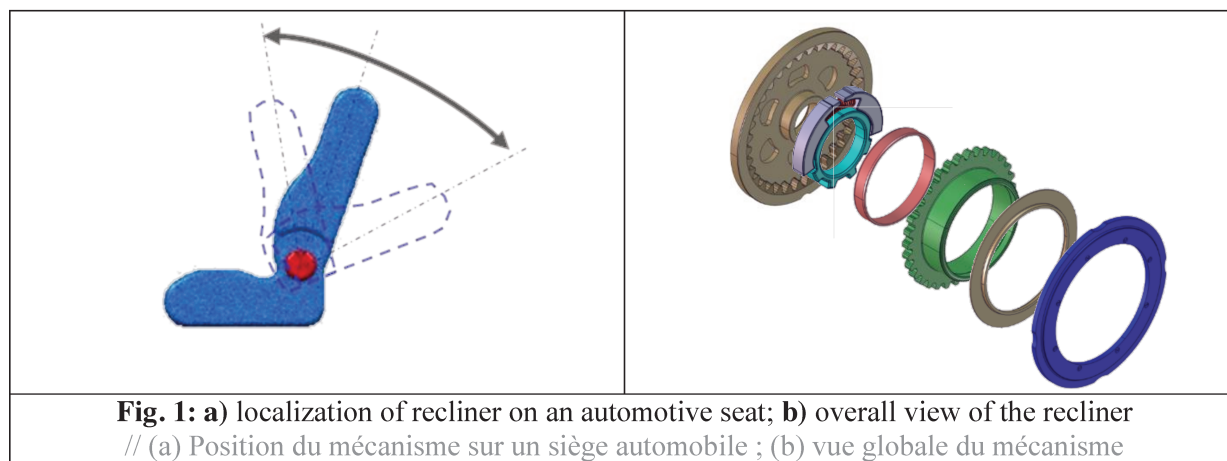
The subdivision of *Faurecia Automotive Seating* based in Caligny (France) designs and manufactures seat mechanisms. It is ranked at the first position worldwide in terms of frames and seat mechanisms (recliners, tracks...) sales. Recliners enable to adjust the back seats angle (see **Fig. 1.a** localization of the recliner on seats). They have a comfort but also a safety role. Indeed, for a rear crash, passengers are thrown on the seat back. During impact, recliners are submitted to high mechanical stresses and must preserve the connectivity between the two parts of the seat for safety reasons. These mechanisms are composed of several parts made out of steel and composites. Obviously, the parts sustaining high stresses under dynamic loading conditions are made of steel.

The weight reduction of these mechanisms requires to optimize components shape and to use high strength steel. Computer-Aided Design (CAD) and Finite Element Analysis (FEA) are the main tools used for designs validation and optimization. Their accuracy is directly related to the material characterization and modeling. Using high strength steels enables to decrease parts volume, and consequently the mass of the subsystem. However, buying and manufacturing raw high strength steel is costly. This often requires slower machining processes and expensive tools. The choice made by *Faurecia* to have a compromise on these specifications is to enhance steel components mechanical properties by performing a carbonitriding treatment at the end of the manufacturing process. In this way, the steel purchasing and manufacturing process is still at a reasonable cost like the ones of low carbon steel. But the in-use mechanical properties are much better.

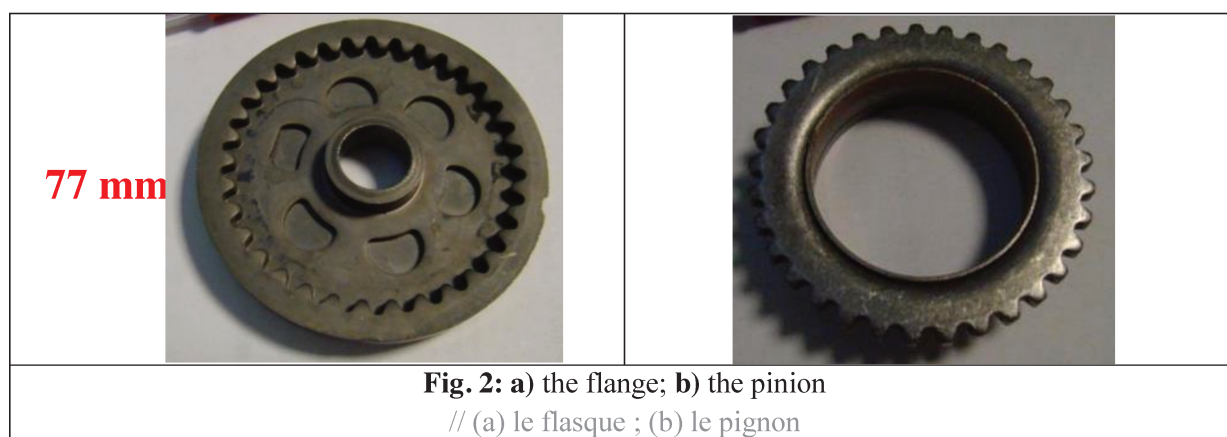
In terms of material behavior, the knowledge of this carbonitrided steel is presently limited to plastic behavior laws assessed by hardness tests [C. Moussa, 2012]. However, to be on the market, every product in the automotive industry must satisfy European and American regulations (for the European Union it is the regulation ECE R 17). Satisfying these regulations provides approval certificates allowing to sale these products in other European and American countries. Seats, as many other automotive products, are tested through crash tests. Regarding seats, a rear crash (considered as the most damaging accident for recliners) is simulated. As experimental tests are very costly, Faurecia needs to simulate accurately this test to design new mechanisms. This can be done by understanding

and modeling damage and failure behavior of carbonitrided steel components. This topic has been quickly studied during a Master Project [Denitui, 2007] but no numerical model has been assessed yet. **The present work aims at analyzing and better understanding the failure of such carbonitrided steels in order to model its behavior and predict failure in simulations involving the whole mechanism.**

A newly designed recliner (**Fig. 1.b**) was chosen as a starting point for experimental observations. It is composed of numerous parts, and the two main ones are the flange and the pinion. These two parts are shown in **Fig. 2**.



This recliner belongs to the family of Continuous Recliners (CR); this means that these two parts are always in contact, either to maintain the position of the seat back in regard of the seating or to adjust it. The flange is welded to the seating and is the fixed part. The pinion is the mobile part and welded to the backrest. The pinion is engaged to the flange. This gear, and thus the teeth, must sustain the load of the back seat itself with the passenger during a rear crash. This is the reason why this work will focus on teeth failure.



The main objective of the PhD is to develop numerical tools capable of predicting failure for such carbonitrided steel components. The identified laws will be integrated to the calculation methodology at Faurecia using the commercial Finite Element (FE) code **LS-DYNA**. For this PhD, simulations will be done with finer meshes than the ones used at Faurecia. This is necessary if one wants to account for the carbonitrided layer, which is only hundreds of microns from the surface. However, using such fine

meshes on the whole mechanism is extremely costly from an industrial point of view. This is why coarser meshes will be tested at the end of this work to check the resulting loss of accuracy.

Rear crashes are the most damaging situations for seat recliners. Faurecia recreates the stress state met by the recliner during the crash on a subsystem test called: static strength test. It is used to characterize all the recliners at Faurecia. However, this test is not compatible when one wants to focus only on teeth failure. In addition, it is not possible with this test to get accurate information of load versus displacement. A semi-industrial test was thus designed during the PhD to get accurate observations of teeth failure mechanisms and experimental data for validation purpose.

At the end, predicting failure of such carbonitrided gears requires to:

- study the failure mechanisms on post mortem full recliners,
- study the plastic and failure behavior of the carbonitrided material which exhibits graded mechanical properties,
- predict and model this failure by using adapted numerical techniques for the carbonitrided layer and the core material,
- validate these numerical models with teeth failure using a controlled semi-industrial test.

The present PhD manuscript consists of **six** chapters.

In the **first** chapter, the industrial issue is detailed and the failure process of recliners teeth is studied; this establishes the starting point of the carbonitrided (CN) steel failure observations. Based on these observations, first assumptions are made regarding the failure mechanism of one tooth. Firstly the brittle external layer fails with the increasing load but the tooth still resists due to a ductile core material. This core material finally fails for a given critical strain. The need for more precise experimental observations is emphasized. Hardness tests justify that the treated steel be regarded as a Functionally Graded Material (FGM). This chapter presents a literature review of the carbonitriding thermo-chemical treatment and its influence on steels mechanical behavior.

Chapter **two** is a bibliographic survey of the fracture behavior of Functionally Graded Materials. Focus is put on FGM having a transition area between brittle and ductile fracture. A review on numerical tools for failure modeling of the external brittle layer is also provided. Finally, numerical techniques used to predict ductile failure are introduced.

Chapter **three** presents the test bench designed during this PhD for quantitative observations of teeth fracture. This device enables to study the influence of the tooth depth of engagement on the failure process. Thus, it recreates as well as possible the multiple stress states met by recliners teeth during a crash test. Such a complex test bench requires 3D Digital Image Correlation to get rigorous quantitative observations. The influence of the external layer on the tooth failure is studied as well with this test bench. It points out that the core material fails mainly in shear and emphasizes the need to identify precisely the mechanical behavior of the material at a stress triaxiality ratio close to zero but slightly positive.

Chapter **four** presents different mechanical tests carried out to measure the mechanical properties of the carbonitrided steel. Focus has been set on the ductile core material which sustains most of the load. A first set of tests was done with only this ductile material. Multiple stress states were tested by varying shapes and loading conditions on these specimens. A second set of experiments, with the whole carbonitrided material, is used to characterize the external brittle layer. It is composed of four point bending tests and tensile tests, which enable to submit the external layer to homogeneous stress state.

Chapter **five** describes the numerical methodology used to calibrate the models. The FE code **Forge** is used to run inverse analysis and identify the plastic behavior law parameters of the ductile material. It has been decided to use fracture criteria to predict failure. The Kill-Element (or Element Erosion technique) is the only numerical method available in **LS-DYNA** 3D to propagate failure through the mesh. Parameters of failure criteria have been identified by inverse analysis. The choice of the accurate failure criteria for the core material is done by focusing on stress states at stress triaxiality close to 0.

Chapter **six** is the final chapter of the dissertation. Material laws and failure criteria assessed with laboratory tests are here validated with the semi-industrial test. Results are analyzed in terms of load and displacement to failure. Comparisons with results obtained with the former Faurecia's failure methodology are provided. Great attention is paid to local stress analysis all along the tooth failure process. This can be done thanks to FE simulations with sensors placed in critical areas. Final prediction is improved compared to Faurecia's initial methodology, but some differences are observed compared to experimental data. These differences are discussed through all experimental and numerical hypotheses made in this work. Finally, a coarser mesh (corresponding to the one used by Faurecia in their FE analyses of full recliners) is used and results are compared to the ones obtained with the finer mesh used in this PhD.

Finally, conclusions and perspectives of the present work are addressed in Chapter **seven**.

Chapter I : Analysis and subject set-up

Content

I. 1	Post mortem analysis.....	15
I. 1. 1	Static strength test.....	15
I. 1. 1. a	Test bench description.....	15
I. 1. 1. b	Recliners observations.....	16
I. 1. 2	First assumptions on teeth failure mechanism.....	19
I. 1. 3	Toward the material characterization – Hardness tests	21
I. 2	Literature review	22
I. 2. 1	Carbonitriding treatment	22
I. 2. 2	Influence of carbonitriding on the microstructure.....	25
I. 2. 3	Influence of carbonitriding on the mechanical behavior	26
I. 2. 4	Influence of carbonitriding on the fracture behavior.....	28
I. 3	Work methodology.....	30

Résumé en Français

Le but de ce chapitre est d'analyser et de comprendre la problématique industrielle de la rupture des pièces carbonitrurées. Pour cela, des mécanismes complets testés à rupture chez Faurecia sur le banc d'essai de tir statique sont observés. Ces mécanismes sont composés de 2 pièces carbonitrurées : le pignon et le flasque. Des observations à l'œil nu ont permis de voir que le pignon est plus endommagé que le flasque lors des essais ; les observations vont ainsi se concentrer sur les pignons et plus particulièrement sur les dents qui soutiennent le chargement.

Des observations au Microscope Electronique à Balayage (MEB) ont permis de justifier deux comportements à rupture dans les dents : fragile en surface et ductile à cœur (**Fig.I.7**). **Fig.I.8** (a et b) montrent un faciès de rupture intergranulaire avec une bonne vision des grains prouvant une rupture aux joints de grains. **Fig.I.9** (a et b) montrent un faciès de rupture ductile avec des cupules. Un hypothétique processus de rupture d'une dent est montré **Fig.I.10**. Une fissure dans la couche CN apparaît sous la surface de contact avec le flasque. Elle se propage dans la dent à mesure que l'effort appliqué augmente. Puis, une fissure sur le côté opposé au contact s'amorce et se propage vers l'intérieur de la dent. La rupture finale d'une dent correspond à la coalescence des deux fissures. Cet essai en revanche ne permet pas de faire des observations quantitatives : il est impossible de connaître l'historique de chargement subi par une dent. De plus, une dizaine de dents sont plus ou moins endommagées à chaque essai sur un pignon. Ces observations révèlent le besoin de développer un nouveau banc d'essais qui permettra d'effectuer des observations quantitatives. L'essai se fera sur une dent uniquement, avec possibilité d'adapter la profondeur de contact entre la dent et un outil qui viendrait en contact avec cette dernière. L'effort ainsi que les déplacements devront être enregistrés ; l'observation in situ de la rupture des dents devrait être possible et corrélée avec les efforts et déplacements.

Des essais complémentaires de micro-dureté sont réalisés et confirment que c'est un matériau à gradient de propriété (**Fig.I.12**). Une étude bibliographique du traitement de carbonituration et de son influence sur les propriétés et la microstructure est faite. Ce traitement induit une microstructure martensitique avec de l'austénite résiduelle en surface, alors que à cœur la microstructure est ferritique avec essentiellement de la bainite. La présence de martensite en surface induit la présence de fortes contraintes résiduelles grimant jusqu'à -800 MPa près de la surface. Le comportement dual à rupture de l'acier CN est aussi observé dans la littérature.

Le chapitre se conclut sur la présentation de la méthode de travail qui va suivre pour répondre à la problématique. La démarche est à la fois expérimentale et numérique. Les essais vont permettre de mieux comprendre et quantifier la rupture du matériau CN ce qui est essentiel pour pouvoir la modéliser. La partie numérique va être dédiée au choix des critères mécaniques pour indiquer la rupture du matériau. Les critères seront doubles car nous sommes en présence d'un matériau avec deux comportements à rupture. La méthode numérique de propagation de la rupture sera aussi choisie en adéquation avec le contexte industriel de ce projet de thèse.

Introduction

This first chapter is dedicated to the analysis of the industrial issue and the understanding of carbonitrided (CN) recliner teeth failure mechanisms. Faurecia characterizes all its recliners by testing them on a so called “static strength test”. A part of this chapter describes this test bench. Observations of the CN components begin with the tested RC 70 recliner. During in-use loading conditions, one can see that the entire load is sustained by the recliner teeth; teeth strength is thus the key point of this study. First assumptions regarding their failure mechanism are done. Firstly, the brittle external layer (called as well CN layer in this manuscript) fails with multiple cracks with the increasing load. But the loaded tooth still resists due to a ductile core material. This core material finally fails with one critical crack propagating through the whole tooth. However, the need of more precise experimental observations is quickly emphasized. Indeed, variability in the failed recliners makes impossible any quantitative analysis. Technical specifications of the test bench designed to get quantitative data are introduced here.

In addition, hardness tests justify that the treated steel be regarded as a Functionally Graded Material (FGM). It points out that the material can be divided in 3 layers through its thickness. This chapter presents a literature review of the carbonitriding treatment and its influence on the mechanical behavior of the treated material.

I. 1 Post mortem analysis

I. 1. 1 Static strength test

I. 1. 1. a Test bench description

Recliners are tested at the end of their design set up on a frame seat in dynamic conditions. This enables to ensure the complete seat respects security specifications and that it can receive the agreement to be sold according to the regulation. In the meantime, it is mandatory for Faurecia to test the recliners on a subsystem test where they are the only part failing. This makes the interpretation of the test easier and more accurate; such tests on one recliner are also cheaper. The recliners subsystem test is called “Static strength test”. This is a quasi-static test, which makes easier results analysis. It reproduces on the recliner the loading conditions occurring during a rear crash or a luggage crash. Indeed, during a front crash, a piece of luggage can be thrown on the back seat inducing a high stress level in the recliner. These are the two most damaging situations for recliners, thus they must be studied carefully.

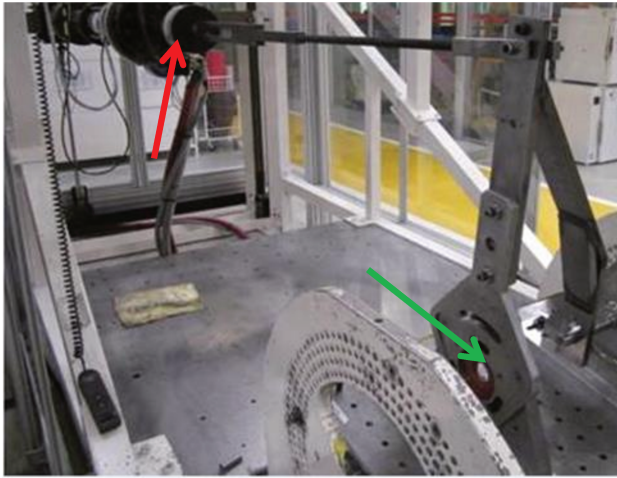
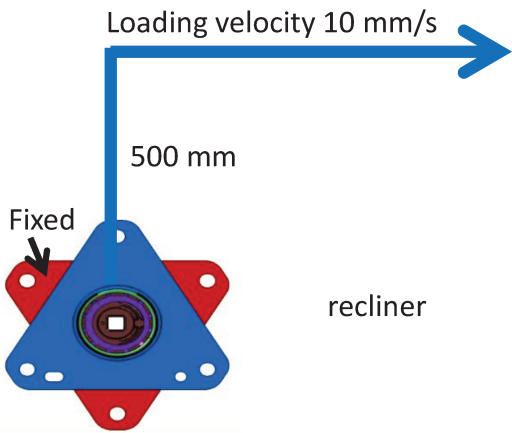
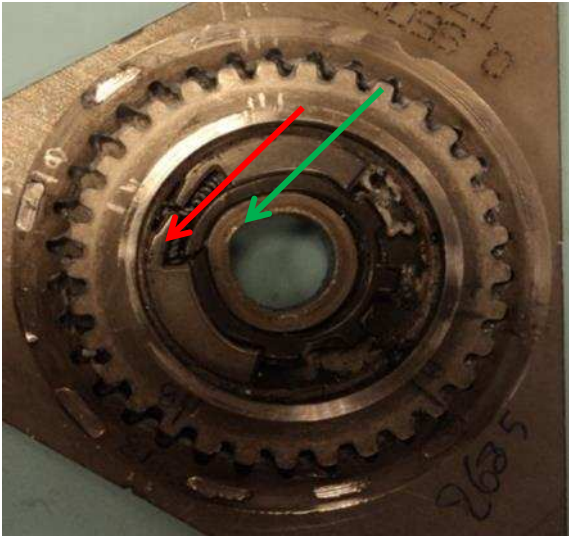

	
<p>Fig.I.1: the static strength test bench // le banc d'essai du tir statique</p>	<p>Fig.I.2: a representative schematic of the test // schéma de l'essai</p>

Fig.I.1 is a picture of the test bench. One can see the massive hydraulic jack (red arrow on **Fig.I.2**) used to impose the velocity. The green arrow shows the location of the recliner set up on the test bench. **Fig.I.2** is a representative schematic of the test bench. A triangular plate (red on **Fig.I.2**) is welded on the flange; another one (blue on **Fig.I.2**) is welded on the pinion. Thus it is the same condition as on a seat. The flange is welded to the seat part, thus fixed, and the pinion is welded to the back seat, the mobile part. The displacement is applied on the mobile blue plate with a powerful hydraulic jack at a velocity of 10 mm/s. The applied load is recorded as a function of jack displacement. The fracture load is used to determine the fracture torque; the latter is compared with numerical simulation.

I. 1. 1. b Recliners observations

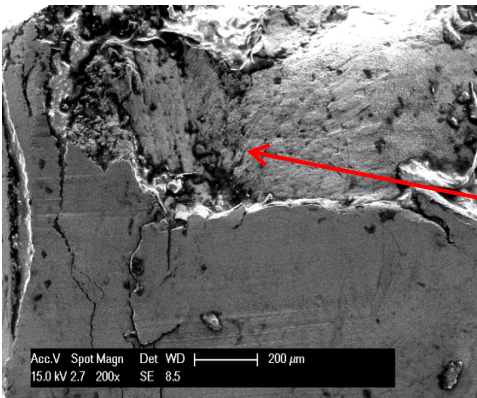
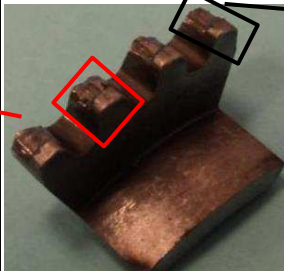
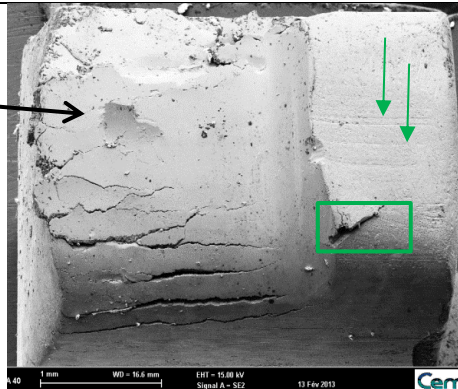
After the test, the triangles are machined away, leaving the recliner as shown in **Fig.I.3**. The aim of this section is not to quantify fracture properties, but to start with a study of the whole mechanism failure modes.

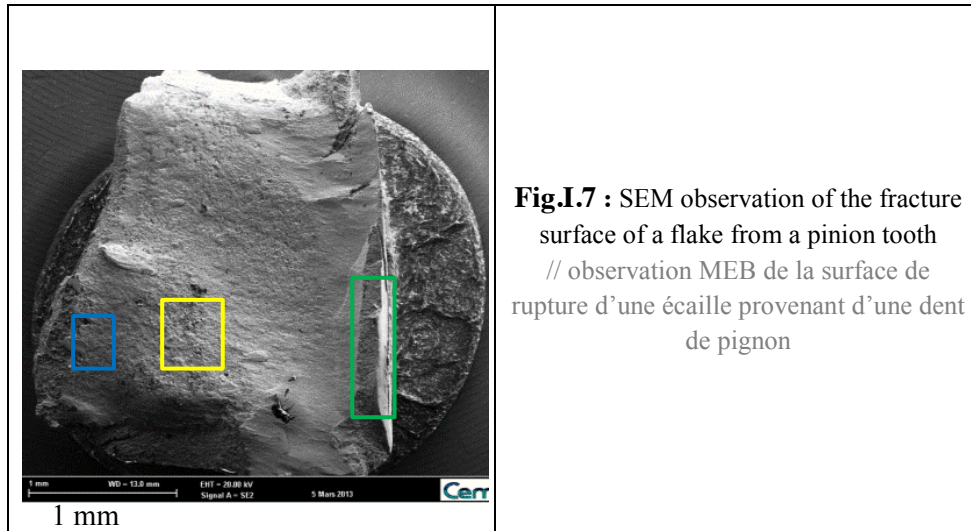
First, the contact between the pinion and the flange is not made on all teeth, just like undamaged recliners where, indeed, only eleven teeth are engaged in contact. Moreover, the central mechanism is broken (red arrow in **Fig.I.3**), and the central annulus is not circular anymore (green arrow), it has been deformed plastically. After cleaning to remove the lubricant, some damaged teeth are observed, especially on the pinion (**Fig.I.4**). The flange is bulkier than the pinion, and thus has higher strength.

	
<p>Fig.I.3: tested recliner // mécanisme testé</p>	<p>Fig.I.4: damaged teeth pinion // pignon endommagé</p>

The teeth are not damaged on their whole surface, but only on a part of it. This is due to an undesired axial out of plane displacement of the pinion in the mechanism under the load applied in the test (**Fig.I.5**). This may be explained by the failure of the central part, made of sintered steel materials, whose strength is lower than the CN steel.

	<p>Fig.I.5: Lateral view of a tested recliner; the pinion has moved 2.8 mm normal to the flange plane // Vue latérale d'un mécanisme testé, le pignon est sorti de 2.8 mm par rapport au flasque</p>
---	---

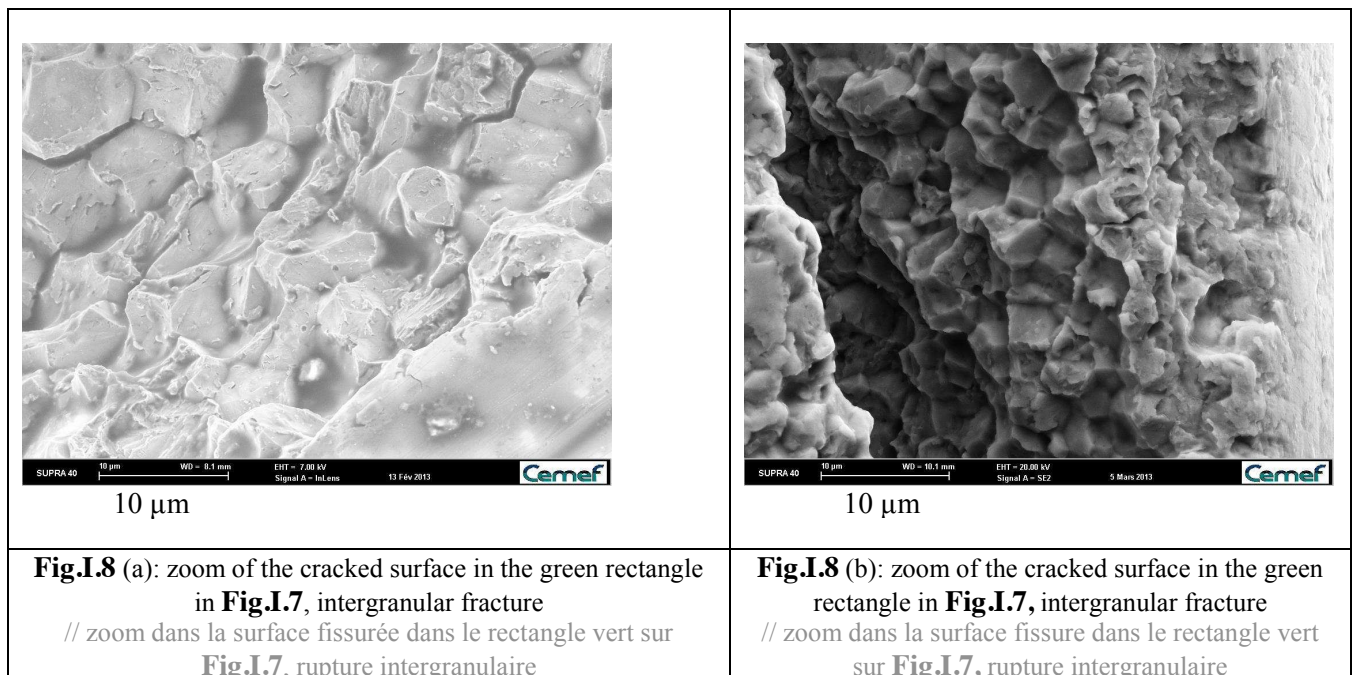
		
<p>Fig.I.6 (a): SEM picture of a tooth surface showing trace of flaking off // image MEB de la surface d'une dent montrant des traces d'écaillage</p>	<p>Fig.I.6 (b): cut pinion specimen // échantillon extrait d'un pignon</p>	<p>Fig.I.6 (c): SEM picture of a tooth surface with horizontal cracks // image MEB de la surface d'une dent avec des fissures horizontales</p>



As seen in **Fig.I.4**, the teeth are more or less damaged but the magnifications of the binocular or of the optical microscope are not high enough; Scanning-Electron-Microscope (SEM) is a much better tool for investigating fracture surfaces. In **Fig.I.6 (a)** and **Fig.I.6 (c)**, two kinds of tooth damage mechanisms are visible. **Fig.I.6 (b)** shows the location of these two SEM pictures. On the first one, it seems a flake has been emitted, probably from the CN layer, whereas on **Fig.I.6 (c)** only a few horizontal cracks are seen. Indeed, by screening the lubricant, several fragments of metal, 2x2.5x0.3 mm, were found. They seem to come from the external, CN surface of teeth (**Fig.I.7**). Also in **Fig.I.6 (c)**, the right part of the surface is intact, with straight lines from the forming process (green arrows) proving the absence of contact with the flange during the whole test.

❖ CN layer: brittle failure

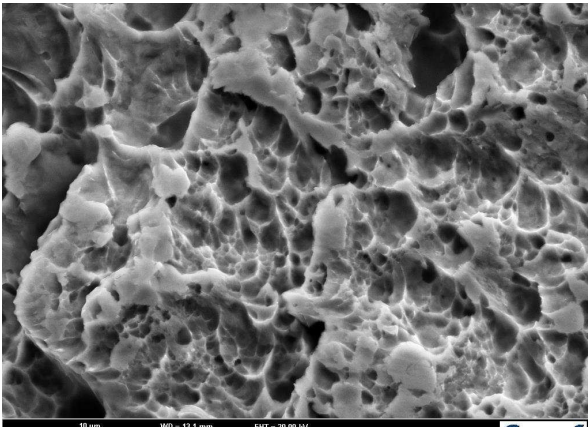
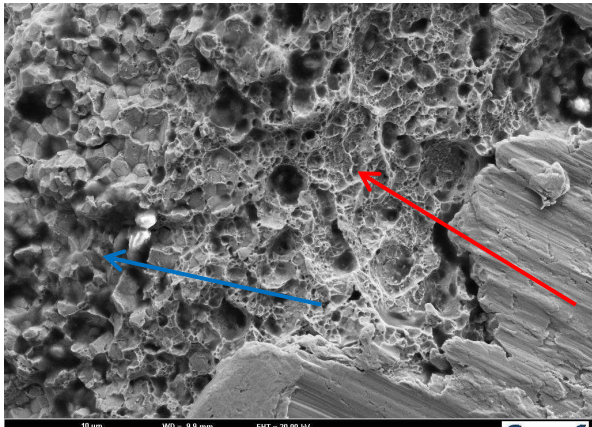
In **Fig.I.8**, larger magnification allows investigating the fracture surface inside a crack on a tooth (**Fig.I.8 (a)**) or on the flake fracture surface (**Fig.I.8 (b)**), at the locations of green rectangles on **Fig.I.6 (c)** and **Fig.I.7**. Intergranular fracture mode seems to indicate a brittle failure mechanism. The same kind of failure can be observed in external cracks on tested flanges.



❖ Core material: ductile failure

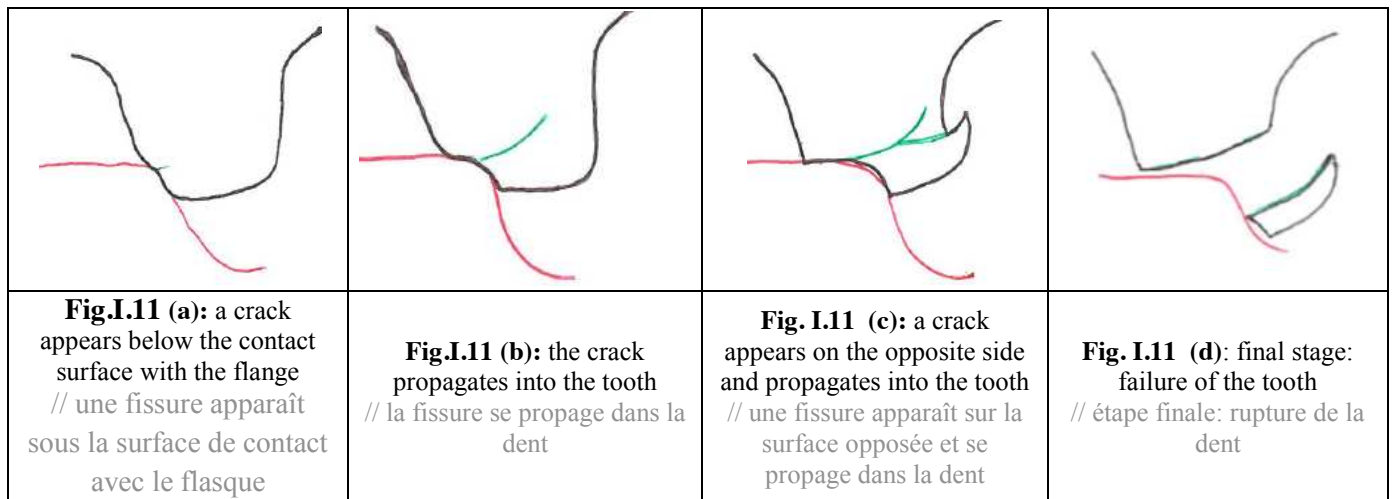
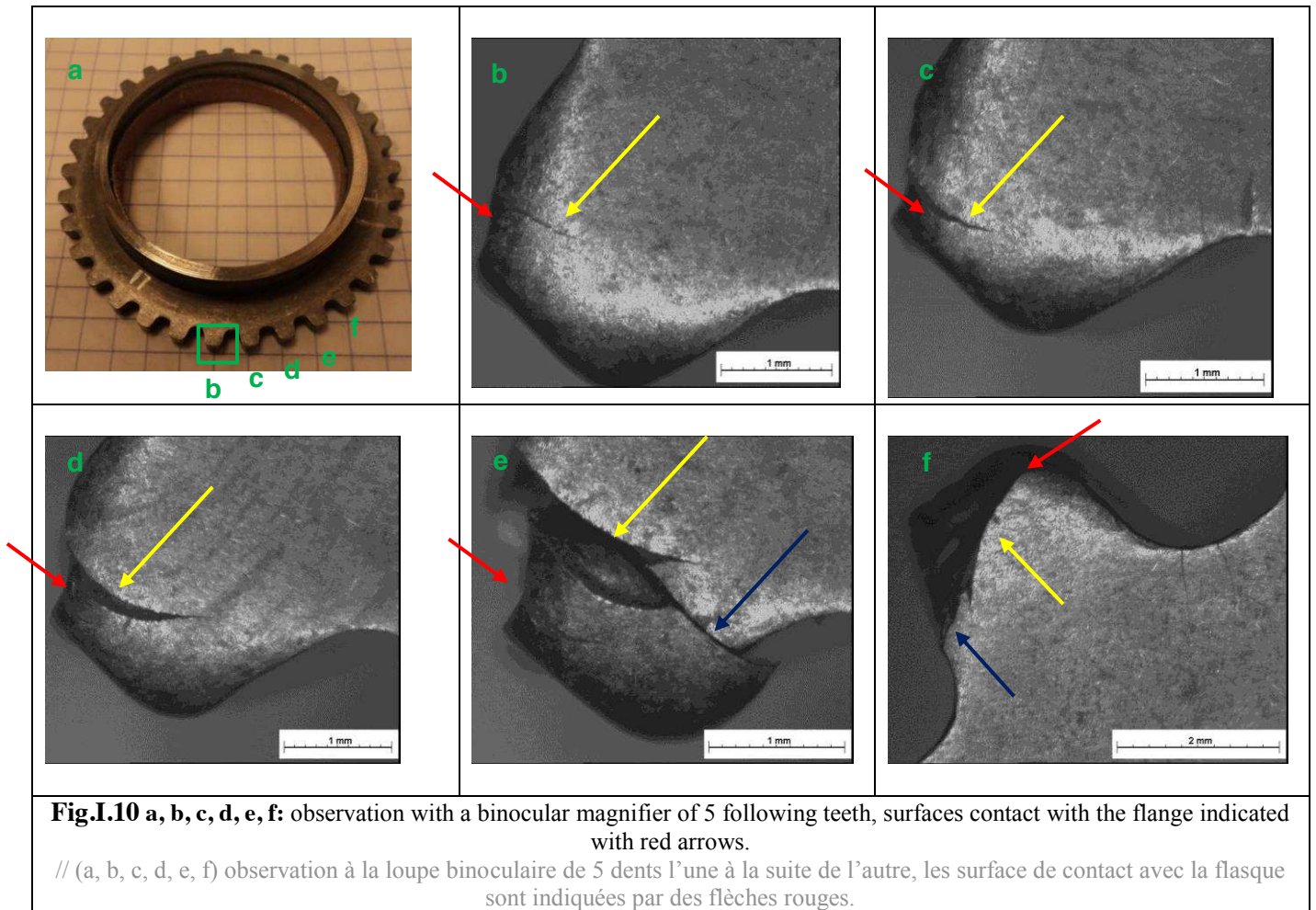
The SEM observations of the flake fracture surface center, (**Fig.I.7**, yellow rectangle) shows a different fracture morphology (**Fig.I.9** (a)). Indeed, the grain boundaries are not visible anymore; the surface is covered with dimples, characteristic of a ductile failure mode with micro-void growth.

Furthermore, **Fig.I.9** (b) shows dimples deep in the material (red arrow) neighboring grain boundaries closer to the surface (blue arrow). This picture shows a transition layer between brittle and ductile fracture. On both **Fig.I.9** (a) and **Fig.I.9** (b), the specimen surface is on the left side of the pictures.

 <p>10 µm</p>	 <p>10 µm</p>
<p>Fig.I.9 (a): zoom into the yellow rectangle of Fig.I.7, fracture with dimples // zoom dans le rectangle jaune de la Fig.I.7, rupture avec cupules</p>	<p>Fig.I.9 (b): zoom into the blue rectangle of Fig.I.7, transition area with dimples (red arrow) and intergranular fracture (blue arrow) // zoom dans le rectangle bleu de la Fig.I.7, surface de transition avec cupules (flèche rouge) et fissure intergranulaire (flèche bleue)</p>

I. 1. 2 First assumptions on teeth failure mechanism

These two behaviors suggest that fracture of a tooth is not a single mechanism, but is divided in several stages. Coming back to low magnification pictures helps understanding how fracture occurs. **Fig.I.10** (a) shows a global view of the recliner where teeth b, c, d, e and f will be analyzed to understand the global failure mechanisms. **Fig.I.10** (b) shows a crack (indicated with a yellow arrow) just below the contact surface with the flange (shown on all the pictures with the red arrow). One can see on the **Fig.I.10** (b) and (c) the strain induced by the contact with the flange. To see such a crack propagating further into the tooth, it is necessary to refer to the next teeth, **Fig.I.10** (c) and (d), which have probably been submitted to a larger contact force. Then on **Fig.I.10** (e), a crack appears on the opposite side of the tooth (blue arrow) and seems to propagate until it meets the other side crack. Obviously, in the final stage, a flake can be formed. These observations strongly support a hypothetical fracture mechanism of a tooth described in **Fig.I.11** (a) to (d).

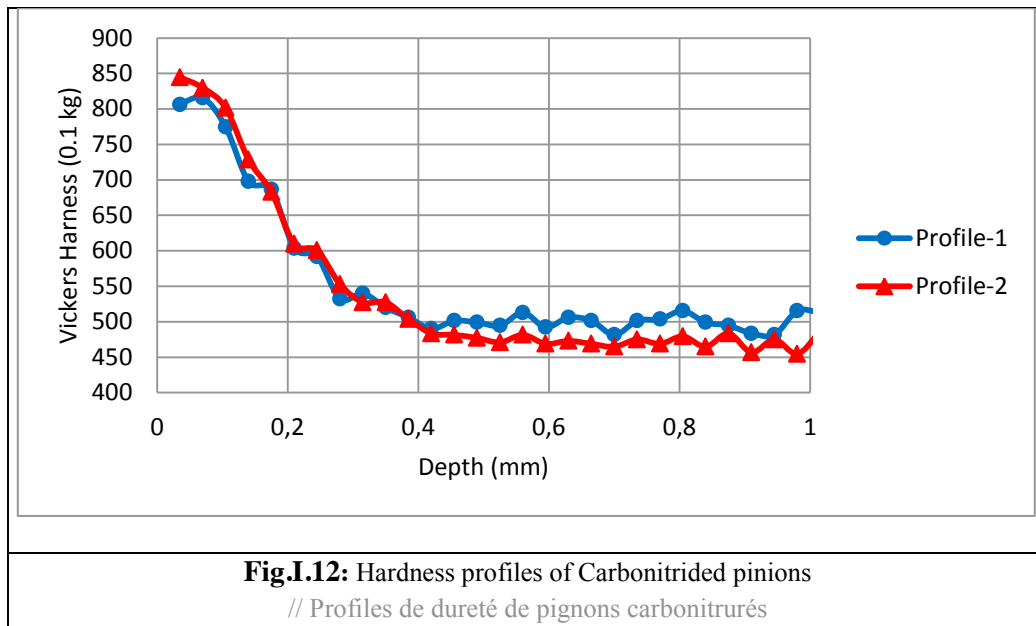


This fracture mechanism will have to be confirmed by future experiments, but it seems to correspond well with observations. However, it does not account for the reduced contact surface between the pinion and the flange, which may be the consequence of the axial displacement due to the failure of the recliner central mechanism (**Fig.I.3** & **Fig.I.5**).

Such heterogeneity in terms of fracture behavior justifies the material is not homogeneous anymore. But, observations of tested pinions cannot bring more information about the behavior or even the thickness of this brittle external layer. Hardness tests profiles can shed light on this particular point.

I. 1. 3 Toward the material characterization – Hardness tests

Several hardness profiles have been measured on pinions. Cross sections were polished until $1\mu\text{m}$ grains and then with diamond solution to remove all the residual stresses due to the cutting process. Polishing with diamond solution was done to ensure an accurate measurement of the diagonals of the indentations. **Fig.I.12** is a graph with 2 hardness profiles coming from two pinions. Before the treatment, hardness was constant through the thickness and equal to 250 HV 0.1.



Three layers can be distinguished on these hardness profiles:

- the first one, up to $100\mu\text{m}$, where the hardness is higher than 770 HV 0.1. This is the **subsurface** layer,
- the second one, from 100 until $400\mu\text{m}$, where the hardness decreases from 770 to 500. This is the **transition** layer,
- the last one, with constant hardness values (around 475 HV 0.1), deeper than $400\mu\text{m}$. This is the **core** material.

So this material has heterogeneous properties as a function of the depth. This is seen with fracture behavior and hardness tests. This is a Functionally Graded Material. By linking these results with the previous observations of the tested recliners, it can be concluded that the transition between the brittle failure and the ductile one is located inside the transition layer. No more information can be extracted from the post mortem recliners or from the hardness profiles. Further observations on teeth failure are presented in Chapter three.

I. 2 Literature review

The first observations showed the material properties are not homogeneous due to the carbonitriding (CNing) treatment. This section is a literature review of this thermochemical treatment. Carbonitriding will be introduced in the first part, with its principle and typical conditions. Then its influence on the material behavior will be studied to show its benefits. Finally, its influence on the fracture behavior will be studied. Due to the lack of information regarding CNing, other thermo-chemical treatment will be addressed as well in this last part.

I. 2. 1 Carbonitriding treatment

Carbonitriding is a thermo-chemical treatment that can be divided in two steps: first, heating to change the phase and promote diffusion of carbon and nitrogen atoms, then martensitic quenching [Leroux, 2012]. The parts are heated in an environment with high carbon and nitrogen atoms content. This will change the chemical composition of the part and thus its mechanical properties. Carbonitriding enables to substantially increase the strength of a component in an external layer while keeping a ductile behaviour in the core to avoid brittle failure through the whole part. Steels used for carbonitriding treatment have low to medium carbon contents (C10, C12, 20MnB5...). In this project, the carbonitrided 20MnB5 steel grade is studied; hereunder (**Table 1.1**) is the composition of the non-treated 20MnB5 steel grade.

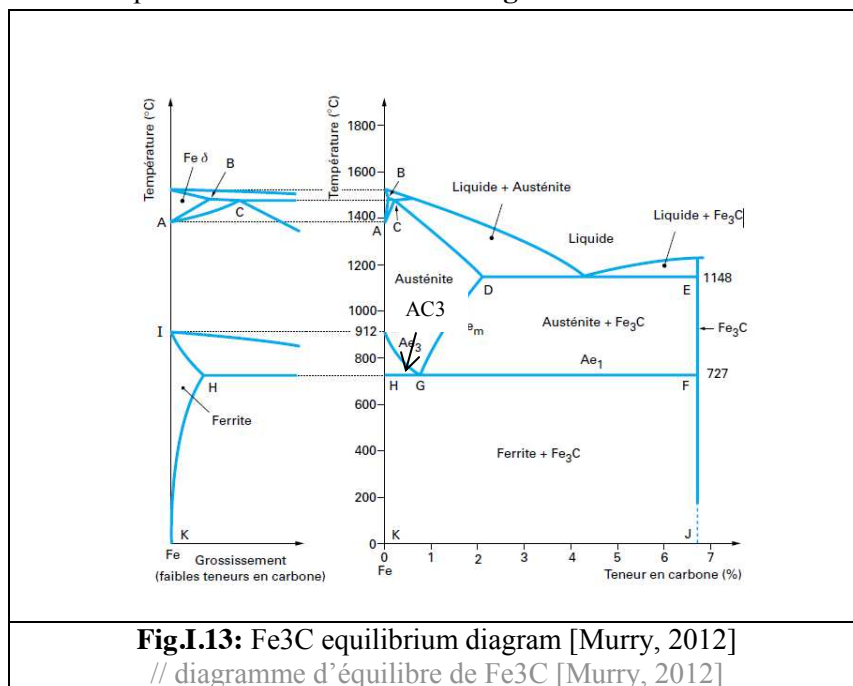
C	Si max	Mn	P max	S max	Cr	B
0.17 to 0.23	0.4	1.1 to 1.4	0.035	0.040	-	0.0008 to 0.005

Table 1.1: chemical composition in weight % of 20MnB5 steel, [NF EN 10083-3]

// Composition chimique en % massique de l'acier 20MnB5, [NF EN 10083-3]

❖ Heating stage and Carbon and Nitrogen diffusion

The first step is to heat the material in the austenitic, γ phase, above the AC_3 line (see **Fig.I.13**). Of course the AC_3 temperature depends on alloying elements present in the material: manganese tends to decrease it, stabilizing the austenitic phase. In austenite, iron is in the face-centred cubic crystal (FCC) structure with a greater solubility of carbon than in the body-centred cubic ferrite phase (BCC), α phase of iron at room temperature. This can be seen in **Fig.I.14**.



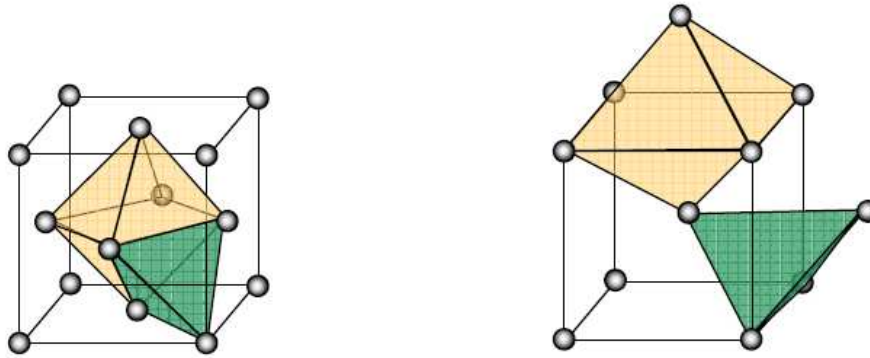


Fig.I.14: octahedral sites (orange) and tetrahedral sites (green) of the FCC and BCC structures
 // sites octaédriques (orange) et sites tétraédriques (vert) des mailles CFC et CC

The main goal of this treatment is carbon and nitrogen diffusion. Methanol (CH_3OH) is used to bring Carbon atoms. Nitrogen atoms are brought by N_2 and ammonia (NH_3). Carbon content as well as temperature are monitored in the oven to minimize treatment variability between multiple batches. Carbon hardens the material and, above 0.05%, allows martensite formation at the end of quenching. The role of nitrogen is still debated. Like carbon, nitrogen diffuses in the octahedral sites of the FCC structure. However, being a γ -forming element, it does not promote carbon oversaturation leading to martensite; it is said to expand the elementary mesh of ferrite and make the diffusion of carbon faster. However, according to [Yahia, 1995] nitrogen influence on carbon diffusion is negligible and both elements seem to repel each other.

❖ Quenching stage and residual stresses

Once the carbon and nitrogen diffusion is over, components are quenched, in order to obtain martensite with a high hardness ($> 700 \text{ HV}$, 850 HV for the 20MnB5). At Faurecia, once chemical treatment is done, parts are thrown in quenching oil, the temperature of which is controlled around 60°C . The quench prevents the carbon atoms from moving by a fast cooling; this is the only way to obtain martensite, a metastable phase. **Fig.I.15** illustrates the origin of the martensite structure.

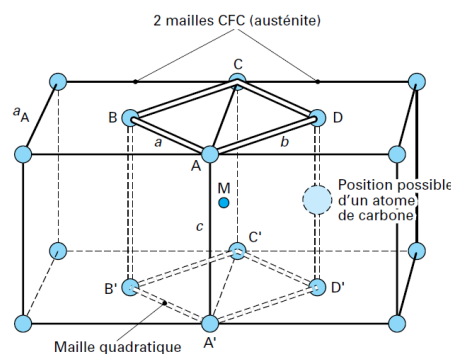


Fig.I.15: origin of the quadratic structure according to Bain [Murry, 2012]
 // origine de la maille quadratique selon Bain [Murry, 2012]

The Ms point for Martensitic transformation Start depends mostly on the carbon content, and secondly on alloying elements such as manganese, **Eq.I.1**. Because the carbon content decreases as depth increases, the martensitic transformation does not begin at the surface where the cooling is faster, but deeper because the Ms point temperature increases as the carbon content decreases. **Fig.I.16** pictures the variation of the Ms point with the depth.

$$Ms(^{\circ}C) = 539 - 423(C\%) - 30.4(Mn\%) - 17.7(Ni\%) - 12.1(Cr\%) - 7.5(Mo\%) \quad \text{Eq.I.1}$$

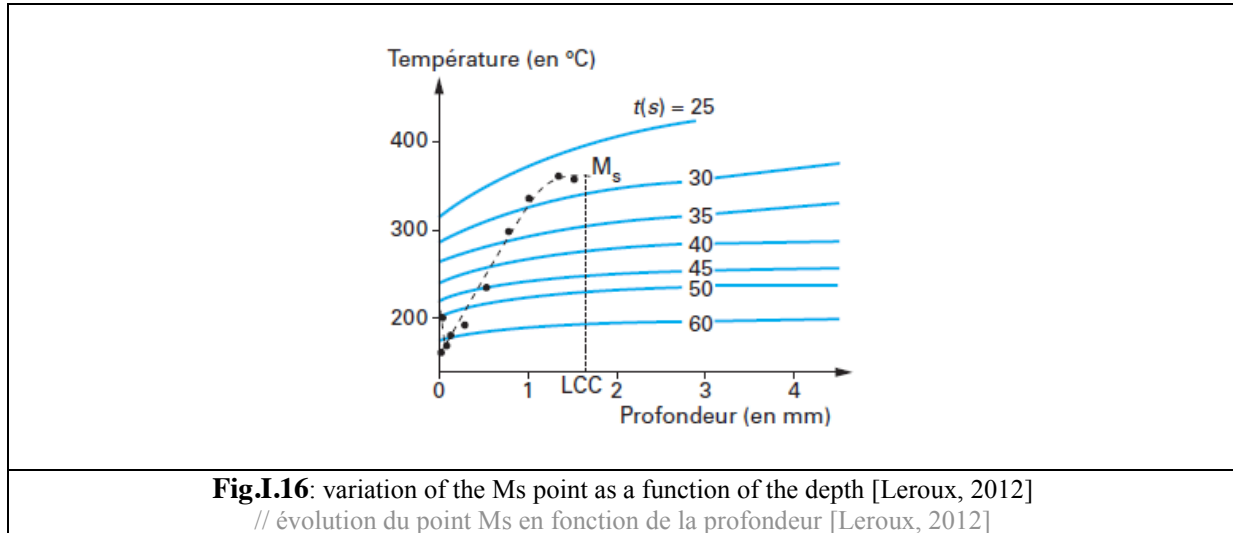
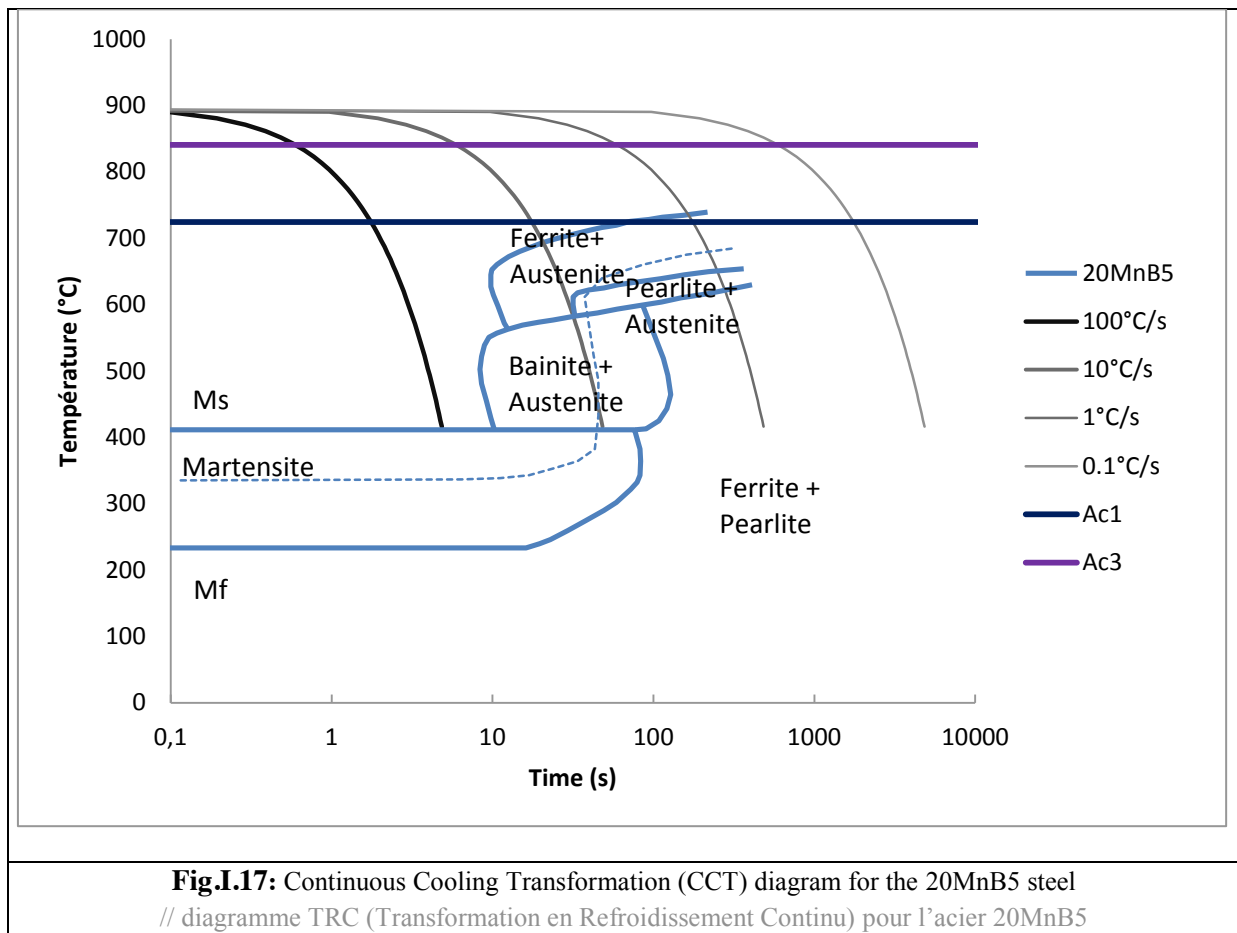


Fig.I.17 is a CCT diagram for the 20MnB5 steel grade. It shows that the microstructure, and thus the mechanical properties, is directly linked to the cooling velocity. The Ms point and Mf for Martensitic finish can be seen. A martensitic microstructure requires a cooling faster than 1°C/s. This cooling rate can be obtained at the surface of the part, but not deeper. This is why there are no martensite grains in the core; the structure is more bainitic with austenite and pearlite. For the untreated 20MnB5 (so without the carbon content depending on the depth), the Ms point is equal to 410°C. It will be lower once carbon diffusion is finished.



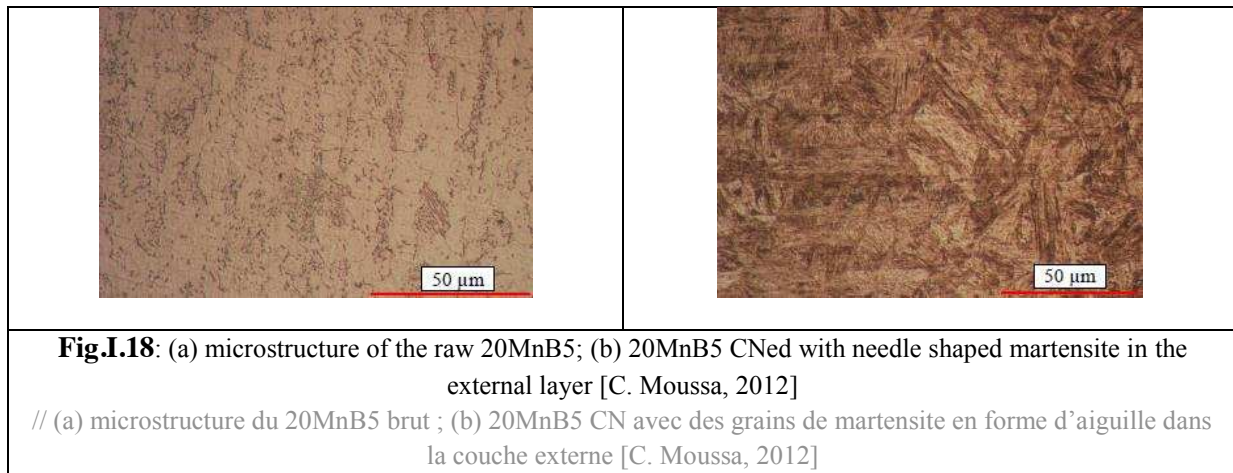
❖ **Tempering**

Tempering consists in heating the parts at a temperature lower than AC1 (see **Fig.I.17**), maintaining the temperature for a while and then slowly cooling them. Parts can be tempered at the end of the quenching stage. It decreases the residual stresses due to the quench and enables to increase the toughness and the ductility of the external layer. This decreases in the same way the superficial hardness.

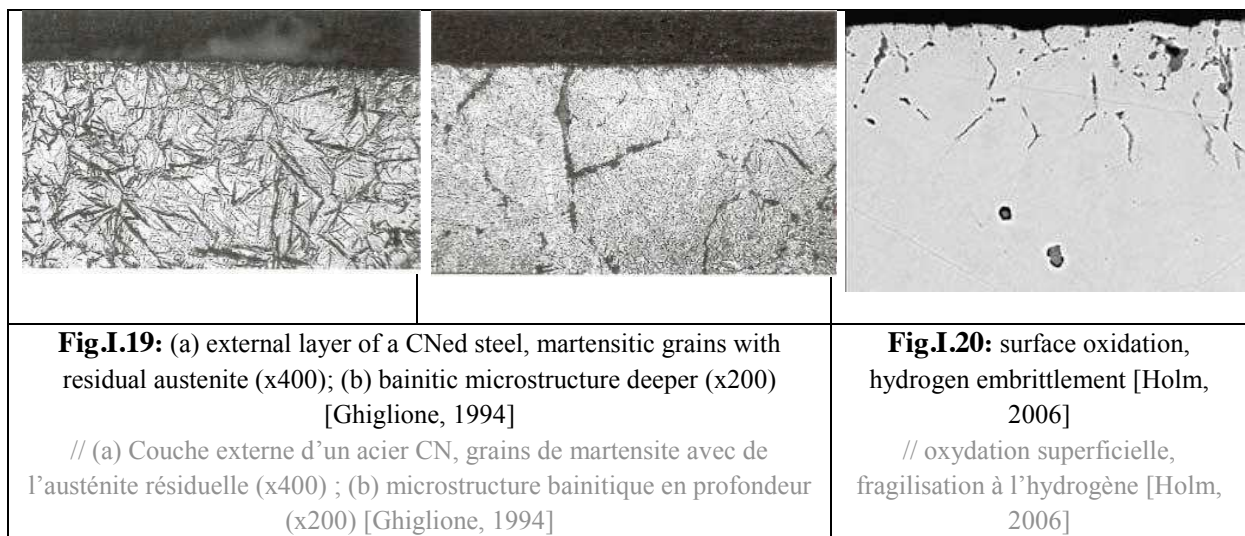
Faurecia chooses not to perform any tempering on the pinion due to the hardness decrease. This can affect the pinions fatigue resistance.

I. 2. 2 Influence of carbonitriding on the microstructure

Carbonitriding, especially the quenching stage, changes significantly the steel microstructure. **Fig.I.18** pictures this evolution with (a) the microstructure before and (b) after the treatment. Before the treatment, there is a ferritic matrix with some carbides. The other micrograph is mainly composed of needle shaped martensitic grains (the dark needles) with residual austenite (the white matrix).



The heterogeneity of this external layer can be easily seen on **Fig.I.19** (a). It is composed of needle shaped martensitic grains with a high hardness (which depends on the carbon content but can reach 1000 HV [Ghiglione, 1994]) and softer residual austenite. The microstructure deeper **Fig.I.19** (b) is mainly composed of bainite and ferrite. **Fig.I.20** introduces a possible issue met by carbonitrided steel: subsurface oxidation. The way these voids appear is not well understood yet [Galerie, 2002], but they are related to the nitrogen content. If nitrogen content reaches in the steel a critical value, it will split up unstable carbides in the subsurface layer. Of course, this critical value depends on the alloy elements present in the steel. The thickness of this subsurface layer is inferior to 30 μm .



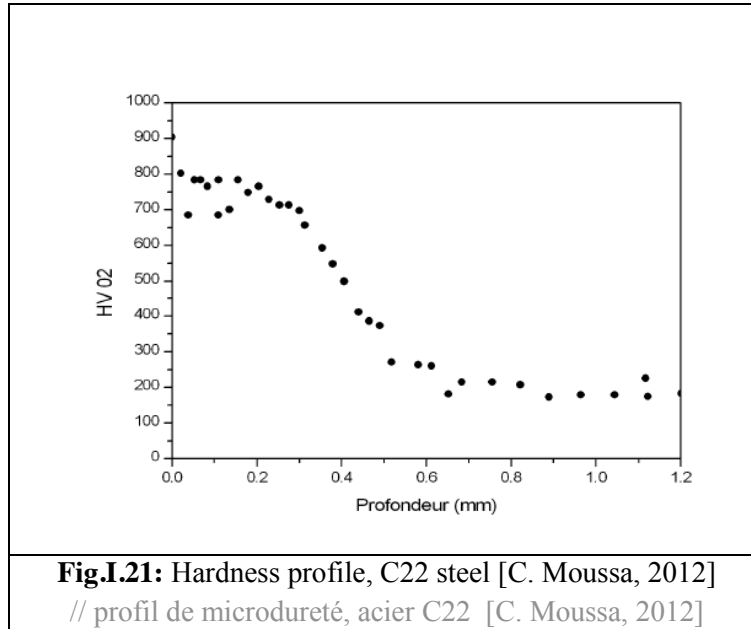
I. 2. 3 Influence of carbonitriding on the mechanical behavior

Because of the microstructure change, the mechanical behavior of the carbonitrided steel is affected. This paragraph deals with hardness and residual stresses.

❖ Hardness

Hardness profiles with the same evolution than the ones introduced in I. 1. 3 are found in the literature. For instance, **Fig.I.21** shows the hardness profile of a C22 steel. One can see a high and constant hardness value in the first 0.2 mm depth, followed by a transition area where the hardness decreases from 750 until 200 HV at 0.5 mm depth. Then, the core material where the carbon and nitrogen atoms did not diffuse, shows a constant hardness value. One can remark three dots in the subsurface layer

showing hardness slightly lower than 700 HV. These points with lower hardness are due to residual austenite [Murry, 2012], [Ghiglione, 1994]. Indeed, all the austenite does not transform into martensite. There are residual austenitic grains in the martensitic microstructure. They lower the hardness level, but increase at the same time the ductility of the material. It is still debated whether this is a benefit or a drawback, but in terms of failure, increasing the ductility is a benefit.



❖ Residual stresses

The multiple phases transformations during the carbonitriding treatment induce residual stresses in the whole material. They are compressive in the external layer [Barralis & Castex, 1999] due to the martensitic transformation which is expansive. The ratio $\frac{\Delta V}{V}$ depends on the carbon content, but can reach 1.35 % with a carbon content of 0.8%.

In the meantime, residual stresses are rather tensile in the core material to guarantee the stress equilibrium on the part. **Fig.I.22** pictures the variation of the residual stress as a function of depth for an AISI 1015 steel. At the surface, the level of the residual stress is around -900 MPa. It decreases very quickly to reach the constant value of +30 MPa at 0.4 mm depth. This is very close to the depth where hardness profiles reach the constant value. One sees the residual stress level is slightly positive deeper than 0.4 mm, this is to guarantee the stress equilibrium.

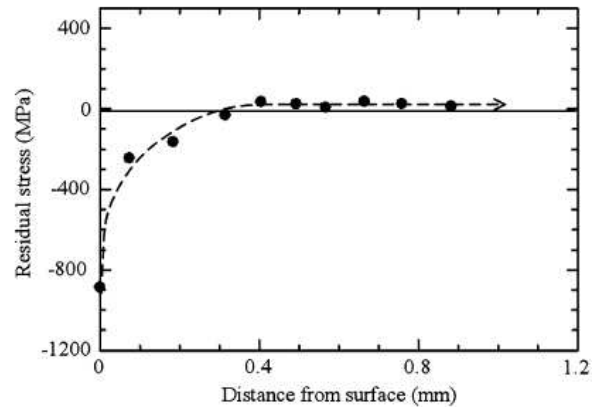


Fig.I.22: residual stress profile for a carbonitrided AISI 1015 steel [Kanchanomai & Limtrakarn, 2008]

// profil de contraintes résiduelles pour un acier CN AISI 1015 [Kanchanomai & Limtrakarn, 2008]

The values and the profile of residual stresses depend on steel grade and treatment parameters, but they all have the same variation: quite compressive in the external layer, they increase quickly to reach the value of the core material. These compressive residual stresses are interesting for fatigue strength because they will stop the propagation of small cracks. This is why carbonitriding treatment is widely used for parts that are submitted to continuous stress, for instance gears which transmit power in car and plane industries.

I. 2. 4 Influence of carbonitriding on the fracture behavior

The treatment changes the fracture behavior of the steel grade. Indeed, the failure mode for untreated low carbon steel is macroscopically homogeneous and ductile. Material fails after a level of plastic strain. Readers can refer to [Gachet, 2013] for ductile failure of a low carbon steel.

After treatment, failure mode is different. [Kanchanomai & Limtrakarn, 2008] and [Denitui, 2007] show the failure is brittle in an external layer and then ductile deeper. **Fig.I.23** illustrates well this heterogeneous behavior by SEM observations of a tensile specimen. The area A, in the external layer, shows cracks propagated through this area around the grain boundaries inducing an intergranular fracture (**Fig.I.23 (b)**). The picture of **Fig.I.23 (d)** illustrates the failure mode in the core material, Area C. This is where the final fracture occurred. The surface is composed of multiple dimples of various sizes, which is a characteristic of ductile fracture mode. Between these 2 areas, there is the intermediate area B shown in **Fig.I.23 (c)**. Here, dimples are elongated and less numerous than in the core material. So material has a ductile mode of failure. Just one crack propagated through this area.

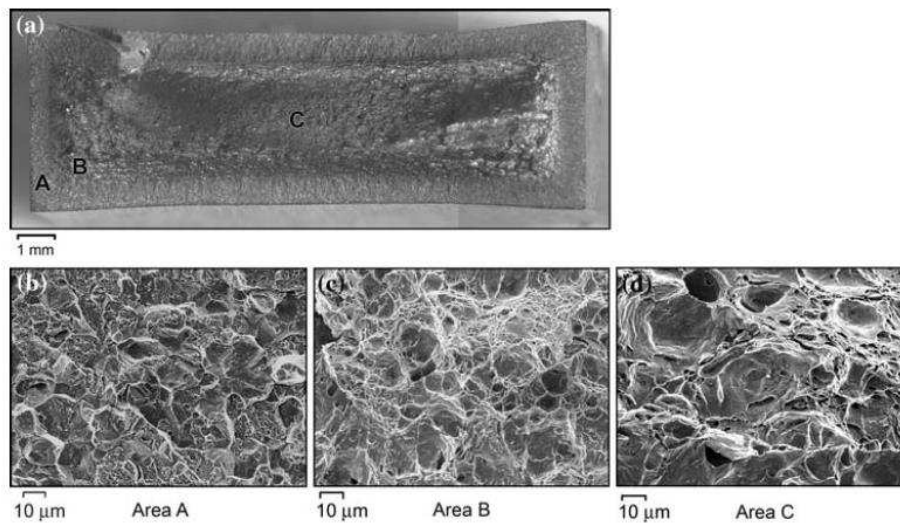


Fig.I.23: SEM micrographs of fracture surface of C-Nitrided AISI 1015 steel [Kanchanomai & Limtrakarn, 2008]
 // images MEB de la surface de rupture d'un acier CN AISI 1015 [Kanchanomai & Limtrakarn, 2008]

Unfortunately, fracture of carbonitrided steel has not been widely studied in the literature. Thus, the literature review was extended to other thermochemical treatments such as nitriding of steels [Firrao & Ugues, 2005]. Nitriding is a thermochemical treatment that consists in diffusing nitrogen atoms while heating the part in ferritic phase. This is the difference with the carbonitrided treatment in which parts are heated to be in the austenitic phase, above AC3 line. Typically the temperature for the nitriding treatment is around 500-600°C, whereas for carbonitriding it is higher than 860°C. **Fig.I.24 (a)** represents the hardness profiles of two nitrided steels. It is the same evolution as for the carbonitrided steel. **Fig.I.24 (b)** shows the fracture surface of a nitrided steel, broken with a Charpy test. One can see the change of direction of the main crack around 120 μm depth. This corresponds to the layer with the highest hardness. This change of direction is an indication that failure mode is not the same in the external layer and deeper in the bulk material.

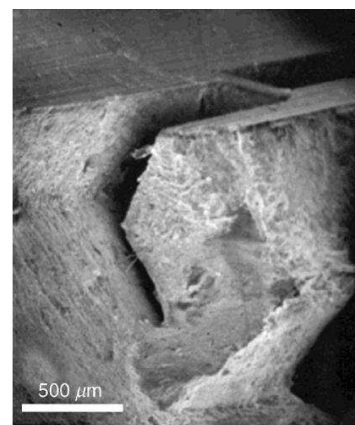
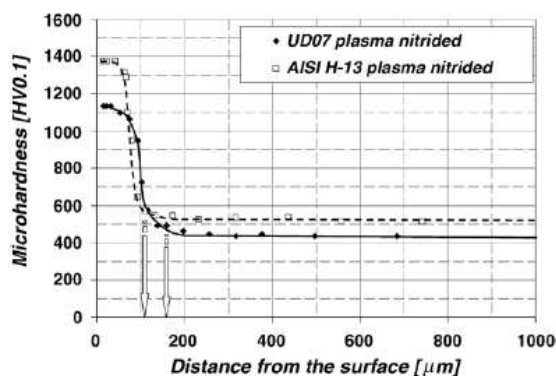


Fig.I.24: (a) Microhardness profile, nitrided steel ; (b) fracture surface of a nitrided low alloy steel [Firrao & Ugues, 2005]
 // (a) profil de microdureté, acier nituré ; (b) surface de rupture d'un acier nituré faiblement allié [Firrao & Ugues, 2005]

I. 3 Work methodology

The first observations and the literature review justify the material is heterogeneous and is a so-called Functionally Graded Material (FGM). Failure should be modeled in a different way in the ductile core material and in the brittle external layer. Modeling failure of such components requires combining experimental and numerical approaches.

❖ Experimental approach

Observations of post-mortem recliners enable to make a first assumption on the tooth failure mechanism. Literature review about carbonitrided steel failure corroborates this failure mechanism. A crack appears early in the loading process and propagates through the external brittle layer with an intergranular failure mode. It stops in the more ductile area, the intermediate layer in which microstructure starts to be bainitic. Then, a final crack propagates into the core material for the complete failure.

Modeling this process requires more rigorous and quantitative observations. A test bench is designed for the purpose of this PhD. It aims at testing only one tooth of the pinion. Displacements and forces will be controlled and monitored. Observations of the cracks propagation will be possible during loading.

Distinct failure mechanisms were observed on the tested recliners. This can be due to the variation of the contact surface between two opposed teeth. Thus, contact depth will be adjustable, allowing studying its influence on the tooth failure mechanism. The design and analysis carried out using this test bench is described in chapter three.

❖ Numerical approach

The numerical approach will start with a literature review of the methods used to model failure. Special focus will be placed on the mechanical criteria used to predict failure and the techniques used to model failure in a finite element mesh.

Because of the heterogeneity of the material, the mechanical model will not be the same to predict the brittle failure of the external layer and the ductile one of the core material. Literature review will be extended to Functionally Graded Materials.

Finally, numerical methods will have to be compatible with the industrial requirements. Indeed, the method will be applied to model failure of the full recliner. Consequently, meshes will be quite coarse, and simulation will have to be done in a limited computation time. The second chapter of this manuscript will deal with the literature review related to these particular topics. State of the art methods will be introduced as well as the ones adapted to an industrial project.

Chapter II : Failure of carbonitrided steel components: a literature review

Contents

II. 1	Damage mechanisms	33
II. 1. 1	Ductile damage	33
II. 1. 1. a	Stress states characterization	33
II. 1. 1. b	Ductile damage mechanisms	34
II. 1. 2	Brittle damage	38
II. 1. 3	Functionally Graded Materials	39
II. 2	Damage models	42
II. 2. 1	Ductile failure	42
II. 2. 1. a	Porous solid plasticity	42
II. 2. 1. b	Coupled damage models	42
II. 2. 1. c	Uncoupled failure criteria	43
II. 2. 2	Brittle failure	48
II. 3	Numerical modeling of failure in a finite element framework	49
II. 3. 1	Crack propagation numerical techniques	50
II. 3. 2	Element deletion technique	53
II. 4	Strategy adopted for the modeling of carbonitrided components failure	54

Résumé en Français

Ce deuxième chapitre est une étude de la bibliographie sur les méthodes de modélisation de la rupture. Afin d'utiliser les modèles, il est nécessaire de définir de façon précise et unique l'état des contraintes. Cela est possible avec l'utilisation de la triaxialité des contraintes (η) et du paramètre de Lode ($\bar{\theta}$) qui sont définis dans le second chapitre à partir du tenseur des contraintes.

Puis les mécanismes de l'endommagement ductile puis fragile sont introduits. Pour le ductile, il y a 2 cas : les fortes triaxialités ($1/3 \leq \eta$) et les faibles ($0 \leq \eta \leq 1/3$). Pour le premier, le processus d'endommagement est divisé en 3 étapes : la germination, la croissance et la coalescence des vides. Pour les faibles triaxialités, c'est la localisation en cisaillement qui induit l'endommagement du matériau. Pour l'endommagement fragile, il y a 2 cas aussi : rupture intra-granulaire et inter-granulaire. Pour le premier cas, les grains se fissurent suite à la propagation d'une microfissure à l'intérieur ; la surface de rupture macro est reconnaissable avec sa brillance. Pour le second cas, la microfissure se propage au niveau des joints de grains. La surface de rupture est en relief ; on aperçoit la structure des grains.

Puis les méthodes de modélisation de la rupture sont étudiées en commençant par la rupture ductile. Il y a différents types de modèles de rupture. Certains tiennent compte de la dégradation des propriétés mécaniques du fait de l'endommagement, ils sont dits « modèles d'endommagement couplés ». Ils ne seront pas utilisés dans ce projet du fait de leur dépendance à la taille de maille ; au profit des critères de rupture, c'est-à-dire des modèles non couplés. Ces critères définissent une surface de rupture, c'est-à-dire une déformation plastique à rupture en fonction de l'état de contrainte. C'est ici qu'interviennent la triaxialité et le paramètre de Lode. Il existe de nombreux critères de rupture prenant en compte l'état de contrainte via des fonctions trigonométriques ou des polynômes.

La modélisation de la rupture fragile a été moins largement étudiée que la rupture ductile, la bibliographie est moins abondante. Les critères se basent sur la contrainte (contraintes principales notamment) et non plus sur la déformation plastique, qui est infime pour un matériau fragile. Il existe aussi des critères statistiques, mais ils ne seront pas utilisés pour ce projet car ils demandent un très grand nombre d'essais pour être pertinents.

Pour finir, les outils de propagation numérique de la rupture dans le maillage sont présentés. Les méthodes de propagation discrètes, nécessitent des étapes de remaillage lorsque la fissure se propage, tandis que la méthode XFEM privilégie l'enrichissement des éléments. La méthode CZM (Cohesive Zone Model) propage les fissures aux interfaces des éléments, simulant une tenue mécanique résiduelle entre leurs lèvres à l'aide d'éléments de contact. Ces méthodes sont encore trop récentes pour traiter des problèmes complexes, de grande taille, en 3D. Ainsi, la technique du « kill element » (élimination d'éléments) sera utilisée. Cette technique consiste à supprimer les éléments déclarés en rupture d'après le critère mécanique associé.

Introduction

As seen before, failure of carbonitrided components relies on a combination of brittle failure of the external carbonitrided layer and of ductile failure of the core part. It is thus important to study both failure mechanisms as well as the existing models that would enable to model the complete failure process of carbonitrided components. Literature review offered in this Chapter 2 accounts for the industrial context of the PhD. The numerical techniques available to model failure will be studied considering the possibilities of the software LS-DYNA used by Faurecia.

This chapter is a literature review of damage mechanisms and models. In the first part the difference between ductile and brittle failure mechanisms is detailed. As opposed to brittle failure, where fracture can appear without (or with very low) plastic strain, a ductile material can undergo a significant amount of plastic strain before fracture. Carbonitrided steel components can be seen as functionally graded materials (FGM). Failure of FGM is thus reviewed as well by focusing on the transition area.

The second part is devoted to damage models. Modeling ductile failure can be done using micromechanical approaches, coupled phenomenological damage models or uncoupled failure criteria. The first two approaches may be considered as more accurate since damage growth is coupled with the material behavior law. However, these approaches also require higher efforts in terms of model calibration.

The last topic of this chapter deals with the numerical modeling of failure and crack propagation through a quick review of the most well-known techniques: discrete crack propagation, cohesive zone models, delete element technique.

II. 1 Damage mechanisms

II. 1. 1 Ductile damage

A ductile material has the capability to undergo a certain amount of plastic strain before fracture. Depending on the stress state, damage mechanisms are different. At low stress triaxiality (see Eq.II.4), failure is essentially due to shear localization in the matrix. At higher stress triaxiality level, failure is usually divided into the classical following 3 steps: voids nucleation, growth and coalescence.

II. 1. 1. a Stress states characterization

Stress state can be defined by the symmetric Cauchy stress tensor (σ) or its eigenvalues, the so-called 3 principal stresses: σ_1 , σ_2 , σ_3 . Those enable to define the 3 invariants of the stress tensor for the isotropic material:

$$p = -\sigma_h = -\frac{1}{3}tr(\sigma) = -\frac{1}{3}(\sigma_1 + \sigma_2 + \sigma_3) = -\frac{I_1}{3} \quad \text{Eq.II.1}$$

$$q = \sigma_{eq} = \sqrt{\frac{3}{2}\mathbf{S}:\mathbf{S}} = \sqrt{\frac{1}{2}[(\sigma_1 - \sigma_2)^2 + (\sigma_2 - \sigma_3)^2 + (\sigma_3 - \sigma_1)^2]} = \sqrt{3J_2} \quad \text{Eq.II.2}$$

$$r = \left(\frac{27}{2}det(\mathbf{S})\right)^{1/3} = \left(\frac{27}{2}(\sigma_1 - \sigma_h)(\sigma_2 - \sigma_h)(\sigma_3 - \sigma_h)\right)^{1/3} = \left(\frac{27}{2}J_3\right)^{1/3} \quad \text{Eq.II.3}$$

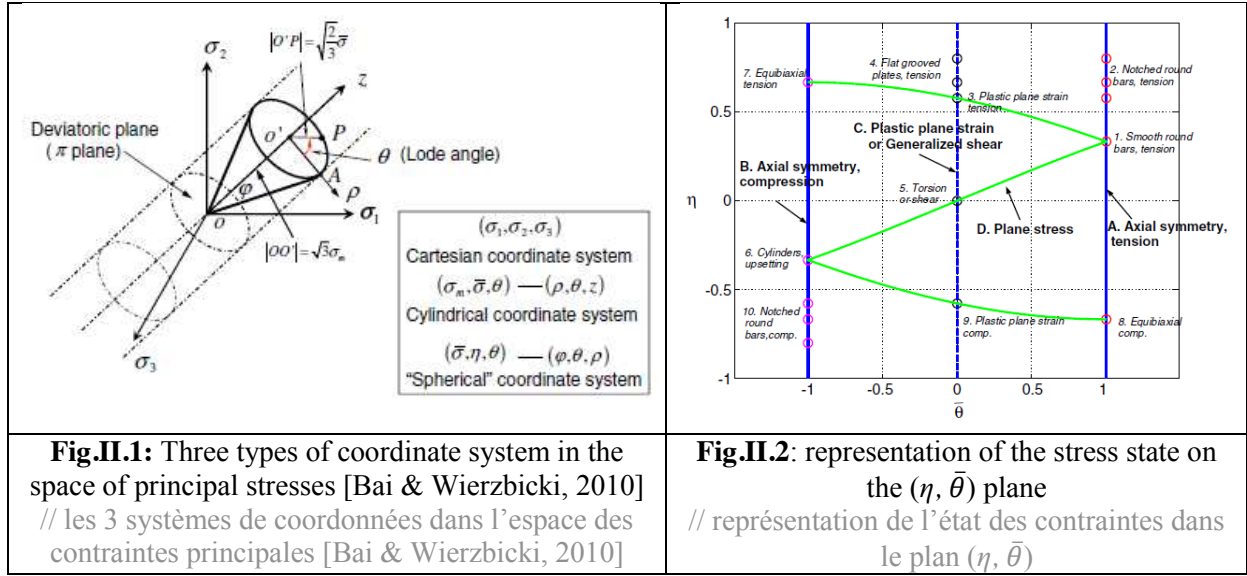
Where σ_h is the mean stress, I_1 is the first invariant of the stress tensor; J_2 and J_3 are respectively the second and the third invariants of the deviatoric stress tensor \mathbf{S} .

Characterizing the stress state in a unique way is mandatory to predict accurately failure. The stress triaxiality ratio η and the Lode angle θ are two parameters used to characterize the stress state in a unique way. The former can be expressed as a function of the hydrostatic pressure p and the equivalent von Mises stress σ_{eq} , see Eq.II.4. The latter is related to the normalized third invariant ξ , see Eq.II.5.

$$\eta = \frac{\sigma_h}{\sigma_{eq}} \quad \text{Eq.II.4}$$

$$\xi = \left(\frac{r}{\sigma_{eq}} \right)^3 = \cos(3\theta) \quad \text{Eq.II.5}$$

Fig.II.1 illustrates three ways of characterizing the stress state. If one looks at the spherical coordinate system, $(\sigma_{eq}, \eta, \theta)$ are used to define the coordinates of the material point P in the space of the principal stresses. The angle φ can be related to the stress triaxiality η through equation Eq.II.6.



$$\eta = \frac{\sqrt{2}}{3} \tan^{-1} \varphi \quad \text{Eq.II.6}$$

In this coordinate system, the range of θ is $0 \leq \theta \leq \pi/3$. It can be normalized to evolve from -1 until +1, see Eq.II.7. It is thus called the normalized Lode angle, or the Lode angle parameter $\bar{\theta}$. This definition is used in the whole manuscript hereinafter.

$$\bar{\theta} = 1 - \frac{6\theta}{\pi} = 1 - \frac{2}{\pi} \cos^{-1} \xi \quad \text{Eq.II.7}$$

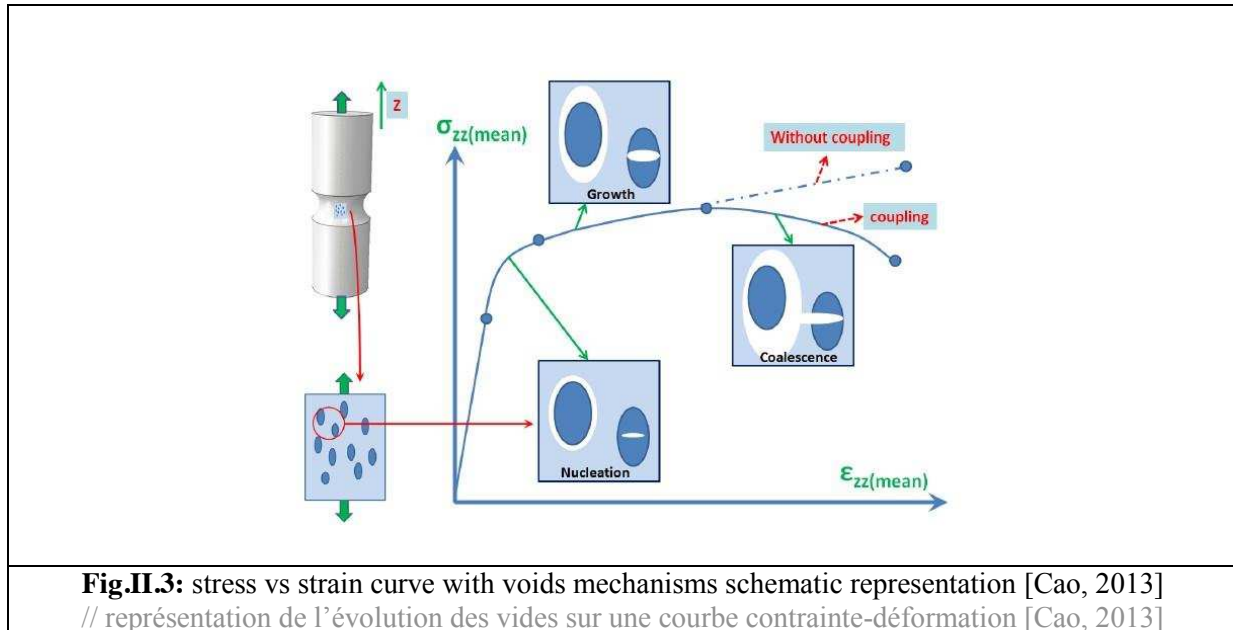
As shown in **Fig.II.2** the stress state condition can thus be defined in a unique way by using the stress triaxiality η and the Lode angle parameter $\bar{\theta}$. $\bar{\theta} = -1$ and $\eta < 0$ corresponds to axisymmetric compression configurations, $\bar{\theta} = 0$ to plastic plane strain or generalized shear, whereas $\bar{\theta} = +1$ and $\eta > 0$ represents axisymmetric tension configurations.

II. 1. 1. b Ductile damage mechanisms

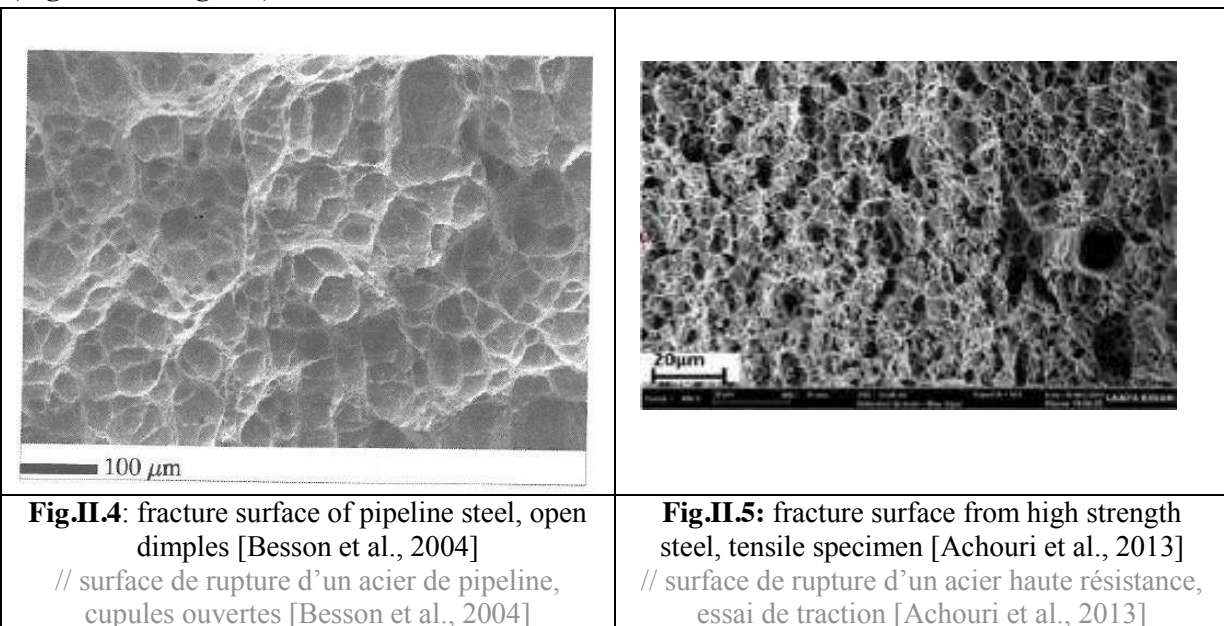
❖ Damage at high stress triaxiality level

High triaxiality ($\eta > 1/3$) corresponds to tension-dominated stress states. At this stress state, damage process in ductile materials is usually divided into 3 steps: voids nucleation, then growth and at the end coalescence. The last process leads to the formation of a macroscopic crack, and thus complete

fracture. **Fig.II.3** illustrates the succession of these mechanisms in the case of axisymmetric tension. Voids nucleation will firstly appear around particles inside the matrix or by failure of particles. These voids will grow until plastic strain is high enough for the coalescence stage, characterized by microcracks propagating between multiple voids and leading to final macroscopic failure.



This ductile failure mode in tension is characterized by fracture surfaces containing wide-open dimples (**Fig.II.4** and **Fig.II.5**).



❖ Damage at low stress triaxiality level

Low triaxiality corresponds to shear and compression stress states ($\eta \leq 0$). Bridgman was the first to carry out fracture tests including the influence of hydrostatic pressure ([Bridgman, 1952]). He carried out axisymmetric tensile tests under external hydraulic pressure to decrease the stress triaxiality. This study was performed with 20 distinct types of steel. On **Fig.II.6** (a) (respectively **Fig.II.6** (b)) is reported the average stress triaxiality (respectively final stress triaxiality) as a function of the test. Eq.II.8 and Eq.II.10 show the expression for the average and final triaxiality:

$$\left(\frac{\sigma_h}{\sigma_{eq}}\right)_{average} = \frac{1}{2} \left[\left(\frac{\sigma_h}{\sigma_{eq}}\right)_{initial} + \left(\frac{\sigma_h}{\sigma_{eq}}\right)_{final} \right] \quad \text{Eq.II.8}$$

$$\left(\frac{\sigma_h}{\sigma_{eq}}\right)_{initial} = \frac{-p_{ext}}{\sigma_{eq}} + \frac{1}{3} \quad \text{Eq.II.9}$$

$$\left(\frac{\sigma_h}{\sigma_{eq}}\right)_{final} = \frac{-p_{ext}}{\sigma_{eq}} + \frac{1}{3} + \ln\left(1 + \frac{a}{2R}\right) \quad \text{Eq.II.10}$$

Where, p_{ext} is the magnitude of the superimposed hydrostatic pressure, a and R are respectively the radius of the minimum cross-section and the radius of the circumferential notch. The $1/3$ added in Eq.II.9 accounts for the tensile stress state added to the superimposed hydrostatic pressure p_{ext} . Firstly, one can see that there is a difference between the final and the average value. Indeed, the triaxiality evolves a lot during the tests due to necking. Secondly, on **Fig.II.6** (a) one can see a limit of the stress triaxiality below which there was no fracture observed; this limit is about $-1/3$.

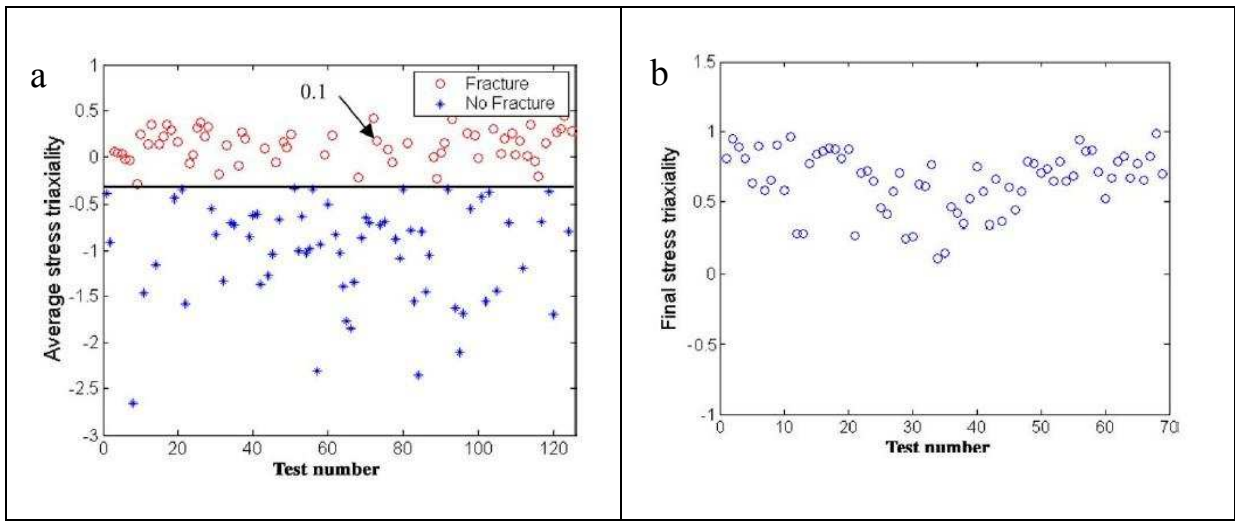
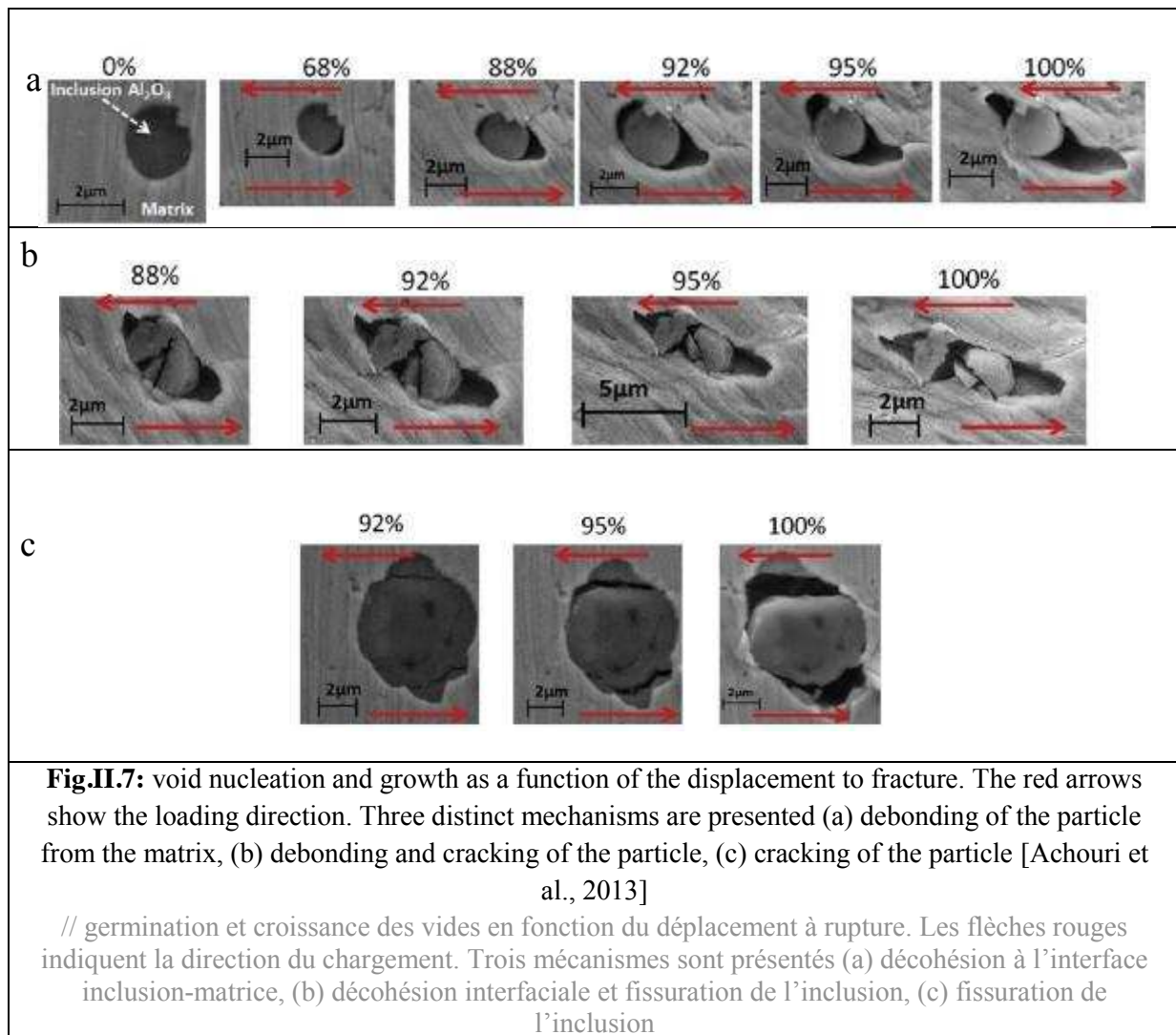


Fig.II.6: tensile tests with superimposed hydrostatic pressure, (a) average stress triaxiality; (b) final stress triaxiality at failure, [Bridgman, 1952]

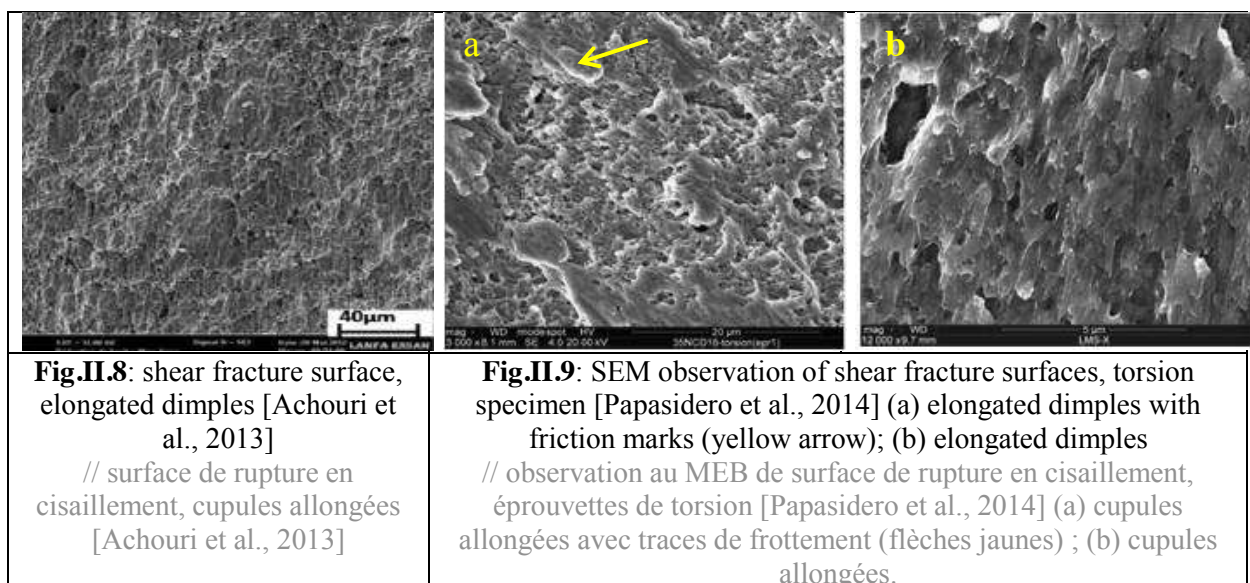
// essais de traction avec pression hydrostatique superposée (a) triaxialité moyenne ; (b) triaxialité finale à rupture [Bridgman, 1952]

This cut-off value of the stress triaxiality has been studied by [Bao & Wierzbicki, 2005] as well. They suggested that no failure can occur if the stress triaxiality ratio is lower than $-1/3$. Upsetting tests were used to test the material under negative stress triaxiality. But more recent studies [Cao et al., 2013] showed that depending on the material, failure in upsetting tests can initiate at the surface, where η is positive locally. Explanation of failure mechanisms at negative triaxiality is still an open subject.

Regarding shear dominated stress state (values of η closer to 0), [Achouri et al., 2013] carried out SEM observations (**Fig.II.7**) of voids nucleation and growth under shear loading conditions for a High-Strength-Low-Alloy steel (HSLA). Three mechanisms were identified. The first one, **Fig.II.7** (a), in which debonding between the inclusion and the ferritic matrix can be observed, without failure of the inclusion. The red arrows show the loading direction. The second one, **Fig.II.7** (b), shows mixed debonding and inclusion cracking. And the last one, **Fig.II.7** (c), illustrates particle failure only.



Like fracture surfaces obtained for high triaxiality ratios, shear dominated ones show dimples. But, in that case, dimples are elongated towards the shear direction (see **Fig.II.8** and **Fig.II.9**). Friction marks can be seen on these surfaces (yellow arrow, **Fig.II.9** (a)).



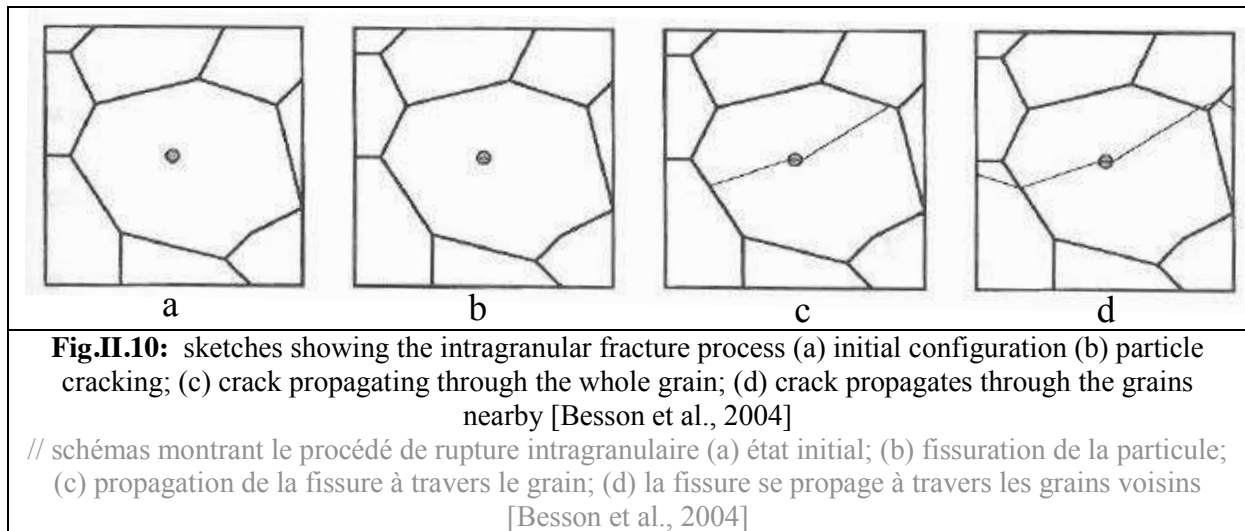
Damage mechanism for failure at medium stress triaxiality ($0 \leq \eta \leq 1/3$) is a mixed between the two mechanisms occurring at low and high triaxiality.

II. 1. 2 Brittle damage

Unlike ductile materials, brittle ones can withstand very low plastic strain before failure. Failure process is thus quite abrupt. They are different from quasi-brittle materials since quasi-brittle materials can dissipate energy prior to cracking with no or negligible permanent strains (e.g. concrete and some ceramics) [Lemaitre & Desmorat, 2005]. Focus will be here on steel grades exhibiting brittle failure. Two types of brittle fracture can be observed in steels: transgranular cleavage, and intergranular fracture.

❖ Transgranular failure

Fig.II.10 shows the four steps defining transgranular cleavage. Brittle materials with cleavage fracture can undergo a low amount of plastic strain before failure [Hahn et al., 1959]. It starts by the cracking of an inclusion or a second phase particle in the grain (**Fig.II.10** (a and b)). This crack propagates through the whole grain and firstly stops at the boundaries (**Fig.II.10** (c)). Then, when the stress level is high enough, the crack propagates in the neighboring grains (**Fig.II.10** (d)).



The fracture surface obtained is recognizable by its facets, see **Fig.II.11** and **Fig.II.12**. The black arrow on the first picture shows where fracture was initiated. One can see facets separated by grain boundaries. **Fig.II.12** shows a surface with cleavage at higher magnification. Fracture patterns inside grains are drawn by multiple parallel lines.

In crystalline materials, fracture by cleavage occurs on well-defined atomic planes (cleavage planes), for instance $\{100\}$ in BCC (Body Centred Cubic) metals and $\{0001\}$ in HCP structure (Hexagonal Close Packed) ([Besson et al, 2004]). Thus, failure is not just motivated by the first principal stress, the microstructure plays a significant role as well.

❖ Intergranular failure

The mechanism for intergranular fracture is different because final crack does not propagate through the grains but at grain boundaries. Even though this process is often observed in ceramics, it may be observed in steels when impurities such as Phosphorous (P), Tin (Sn) or Antimony (Sb) are present at grain boundaries [Besson et al., 2004]. [Tsuchiyama et al., 2008] enriched stainless steel in nitrogen

with a nitriding treatment. This caused intergranular fracture while initially the failure of this steel is rather ductile. Authors noticed it has been promoted by segregation of impurities such as phosphorus and sulfur. These particles decrease the intergranular cohesion, and cause the embrittlement.

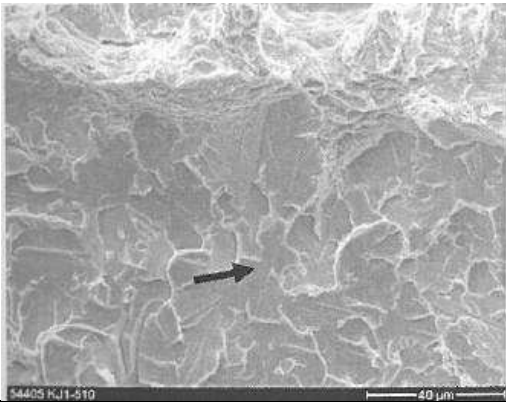


Fig.II.11: brittle fracture surface of a 22NiMoCr 37(A 508 2), specimen tested at -67°C [Siegele et al., 2006]
 // surface de rupture fragile d'un acier 22NiMoCr 37 testé à -67 °C [Siegele et al., 2006]

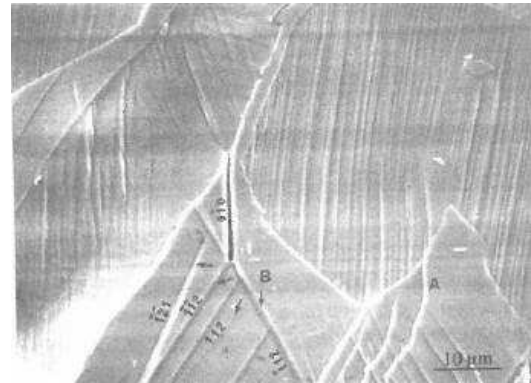


Fig.II.12: brittle fracture surface of a duplex stainless steel, [Besson et al., 2004]
 // surface de rupture fragile d'un acier inoxydable [Besson et al., 2004]

Fig.II.13 illustrates the fracture surface of an intergranular fracture. The crack propagates through the grain boundaries and leaves the grains unfail. [Krauss, 2001] analyzed the deformation and fracture in Martensitic Carbon steels. He showed that martensitic structure with carbon content higher than 0.5 were likely to have intergranular failure. Tempering the steel enables to prevent intergranular fracture. For CN steel, carbon content in the external layer is about 0.8 - 0.9 %. It confirmed what was seen in Chapter 1, external layer fails in intergranular mode.

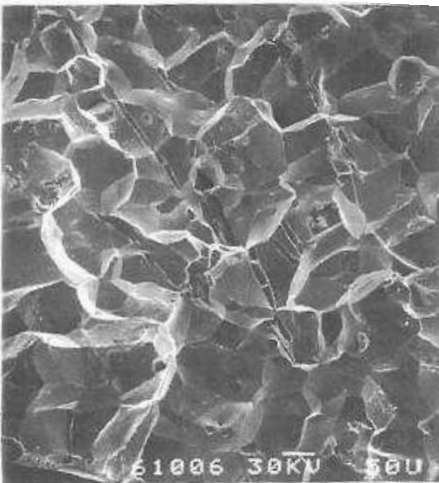
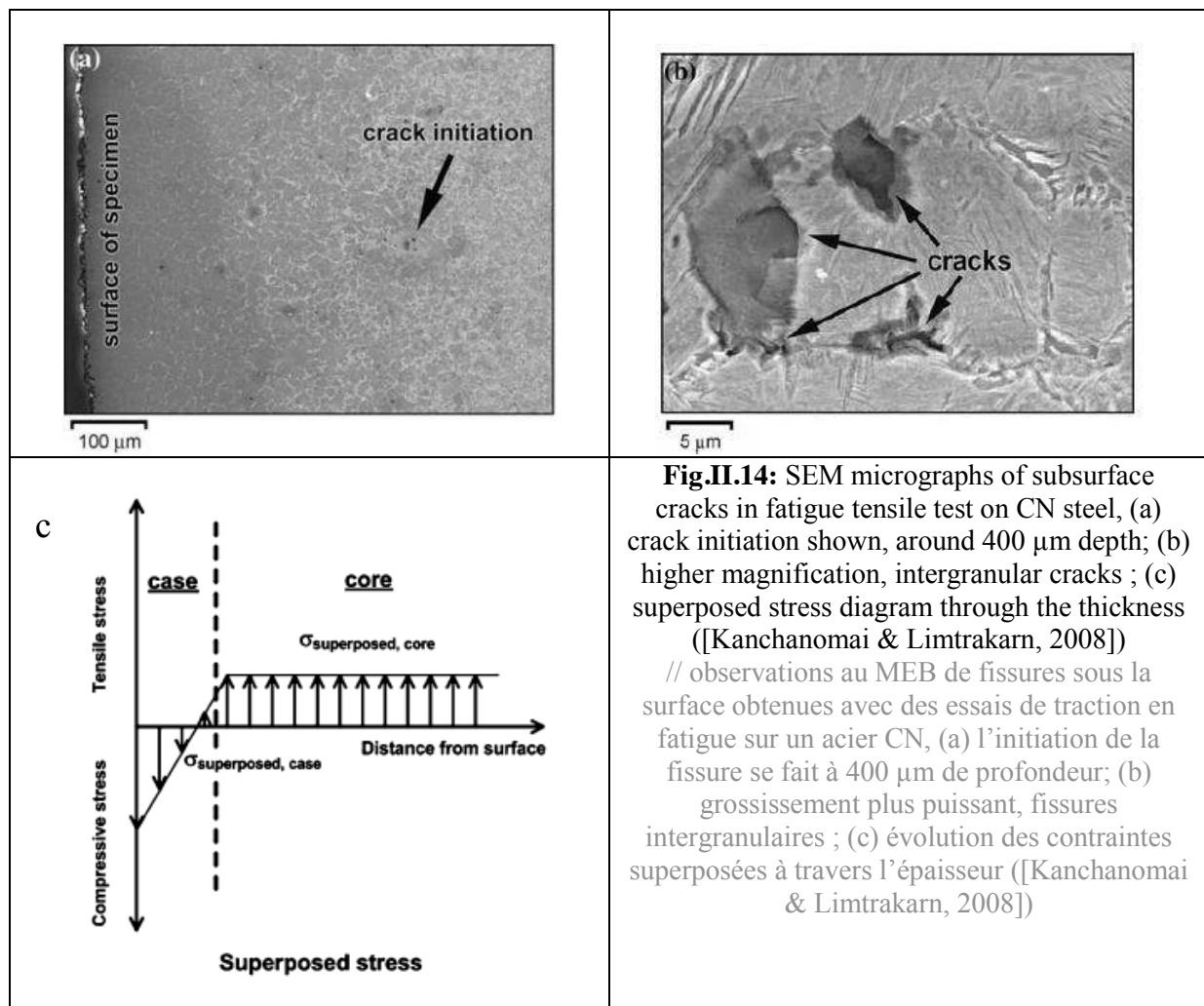


Fig.II.13: intergranular fracture observed in a low alloy steel submitted to temper embrittlement [Besson et al., 2004]
 // rupture intergranulaire observée dans un acier faiblement allié soumis à un traitement de fragilisation [Besson et al., 2004]

II. 1. 3 Functionally Graded Materials

The literature presented here deals with materials having a brittle–ductile fracture transition area. Those are different from coated materials where properties variation is roughly binary without any gradient type properties (usually a very thin layer is applied on the bulk material to improve coating adherence). This literature review had to be extended because, as noticed in Chapter 1, literature of quasi-static failure of carbonitrided steel alloys is extremely limited.

Indeed, fatigue failure has been more studied since this treatment is usually done to improve the contact fatigue resistance. As seen in Chapter 1, carbonitriding treatment induces strong residual compressive stresses in an external layer. This delays crack initiation and propagation; increasing the fatigue life [Nakonieczny, 2006]. [Kanchanomai & Limtrakarn, 2008] performed fatigue tensile test on carbonitrided steel (stress range 420 MPa, low cycle fatigue, fatigue life 10^5 cycles). On specimen tested until 80% of their fatigue life, cracks initiation did not occur at the surface, but deeper in the transition layer – 400 μm depth (see **Fig.II.14** (a-b)). These initiations were observed at grain boundaries, thus meaning intergranular fracture. Initiation occurs at the interface between the CN layer (case material) and the core material because of the residual stresses. They are indeed compressive in the external layer (-900 MPa in the subsurface) and lightly tensile in the core material (20 MPa). **Fig.II.14** (c) plots the variation of the superimposed stresses (residual stress + applied stress) for tensile loading conditions. Resulting stresses are still compressive in most of the case layer, thus failure could not initiate here. On the other hand, deeper in the material, applied stresses are added to the residual tensile stresses, the superimposed stress is higher than the applied stress. Thus, initiation occurs where the stresses are highest. Multiple cracks propagate from the transition area up to the surface. Then, only one propagates from the initiation area to the core material to break the specimen in two parts.



The authors performed quasi-static tensile tests on the same material and checked fracture surfaces. **Fig.II.15** is a SEM micrograph of the fracture surface. Further observations showed brittle intergranular fracture in an external layer and open dimples in the core material (see **Fig.1.22** Chapter 1). By looking at the fracture surface carefully, one can see the crack in the external layer is straight (red arrows), whereas deeper in the material it is not. Thus, likely in the transition layer, crack direction changes to become curved. This occurs in other areas (B in **Fig.II.15**) where fracture becomes more ductile. In that case, crack initiation was at the surface and not in the transition layer as observed on fatigue specimen.

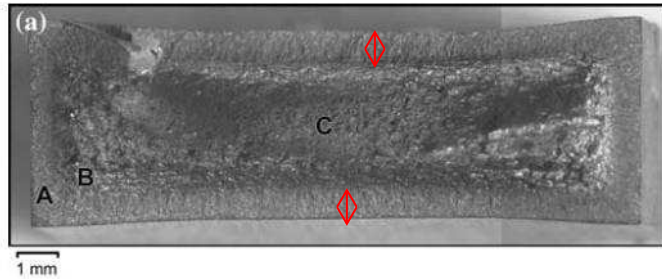


Fig.II.15: fracture surface, CN AISI 1015 steel [Kanchanomai & Limtrakarn, 2008]
 // surface de rupture, acier AISI 1015 CN [Kanchanomai & Limtrakarn, 2008]



Fig.II.16: curved crack path, 16MND5 steel [Bousquet et al., 2012]
 // chemin de fissuration courbé, acier 16MND5 [Bousquet et al., 2012]

This behavior was observed by [Bousquet et al., 2012] on heat treated 16MND5 steel alloys (equivalent to the ASTM A508 steel). Fracture mechanism was studied with Compact Tension (CT) specimen. **Fig.II.16** shows the curved fracture observed. One can notice that three cracks start to propagate until the main one propagates through the whole specimen. On untreated steel alloys, fracture surfaces do not exhibit such change of direction, fracture is at 45° (slip lines) with respect to the loading direction.

During heat treatment, materials microstructure is changed. In the case of carbonitrided steel, microstructure is mostly martensitic in the surface to become ferritic (with bainite depending on the base material) deeper in the base material. The evolution is not binary; there is a gradient where, in the transition layer, both microstructures coexist. Martensitic grains are very hard (up to 900HV depending on the carbon content), undergo very low level of plastic strain and the failure is intergranular. On the other hand, ferrite is very soft (150 HV) and can withstand a certain amount of deformation before ductile failure with voids. This heterogeneity changes the crack propagation direction. It is firstly driven by the first principal stress in the intergranular failure, and then driven by the direction of maximum plastic strain. This justifies the change of cracks propagation direction for heat treated steel (see **Fig.II.17** [Firrao & Ugues, 2005]). The crack changes direction after reaching the more ductile area than the nitrided layer.

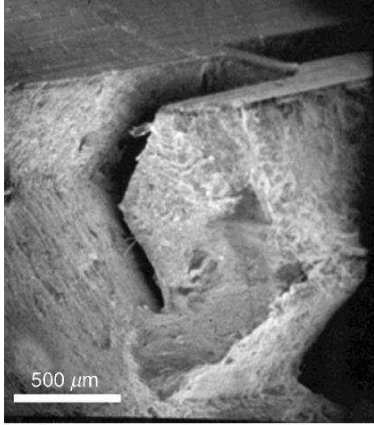


Fig.II.17: crack in a nitrided steel, crack direction change when reaching the more ductile area, ([Firrao & Ugues, 2005])
 // fissure dans un acier nitruré, la direction de propagation de la fissure change lorsqu'elle atteint la zone plus ductile.

II. 2 Damage models

This second part introduces how damage, and more generally failure, can be modeled. Since ductile materials are widely used in industry, ductile failure has been extensively studied. Models predicting such failure can be classified into three main categories: uncoupled failure criteria, coupled damage models and micromechanical damage models based on porous plasticity. However, numerical brittle failure models are less numerous.

II. 2. 1 Ductile failure

II. 2. 1. a Porous solid plasticity

Gurson based models were initially introduced by [Gurson, 1977], considering yield surface shrinkage due to voids nucleation and growth. It was modified by [Tvergaard, 1981], [Tvergaard & Needleman, 1984], [Needleman & Tvergaard, 1984] to account for void coalescence and more recently by [Nahshon & Hutchinson, 2008] to improve the fracture prediction at low triaxiality. Such models are closer to real physical ductile failure mechanisms since damage is accounted for through the use of a void volume fraction parameter in the definition of the yield surface function. The implementation of such models in FE software is however more difficult. In addition, this method requests the identification of multiple parameters (some of them requiring microstructural characterization), which makes it difficult to use in an industrial environment. See [Cao, 2013] for an example of parameters identification.

II. 2. 1. b Coupled damage models

Phenomenological coupled damage approaches rely on the definition of a damage parameter, D , calculated as a function of the stress state in a phenomenological way. Unlike uncoupled criteria, the damage parameter affects the material behavior law. This method was developed by [Chaboche, 1984] and [Lemaitre, 1986], [Lemaitre & Desmorat, 2005]. Regarding the Lemaitre model, considering that the damaged area (D) of any cross section cannot bear any load, which is thus reported on the intact area fraction ($1-D$), the effective stress is defined using the damage variable D through equation, Eq.II.11:

$$\sigma'_{ij} = \frac{\sigma_{ij}}{1 - D} \quad \text{Eq.II.11}$$

where $D=0$ for an undamaged material, and D tends to 1 for a failed material. Damage growth is expressed by Eq.II.12:

$$\dot{D} = \frac{\dot{\lambda}}{1-D} \left(\frac{Y}{S} \right)^b = \dot{\varepsilon}^p \left(\frac{Y}{S} \right)^b \quad \text{Eq.II.12}$$

with:

$$Y = \frac{\sigma_{eq}^2}{2E(1-D)^2} \left(\frac{2}{3}(1+\vartheta) + 3(1-2\vartheta)\eta^2 \right) \quad \text{Eq.II.13}$$

where S (MPa) and b are Lemaitre damage material parameters; $\dot{\lambda} = \dot{\varepsilon}^p(1-D)$ is the plastic factor and $\dot{\varepsilon}^p = \sqrt{\frac{2}{3} \dot{\varepsilon}^p : \dot{\varepsilon}^p}$.

Coupling to the plastic behavior is achieved by using the effective stress, which depends on the damage variable as defined in Eq.II.11. The elastic modulus is affected as well by the damage through Eq.II.14:

$$E' = E_0(1-D) \quad \text{Eq.II.14}$$

where E' and E_0 are respectively the affected and the initial elastic modulus. Extensions of this Lemaitre model were proposed in [Bouchard et al., 2010] and [Cao et al., 2014] to improve the failure prediction in shear stress state and negative triaxiality.

It must be noted that coupled damage model suffers from damage localization issues that induces strong mesh sensitivity as soon as material softening occurs. This pathology can be treated using non-local damage approaches and the use of a characteristic length used for regularizing damage.

II. 2. 1. c **Uncoupled failure criteria**

This method consists in predicting failure through an external variable uncoupled with respect to other internal variables such as plastic strain. This variable, D , is introduced as the damage parameter. Failure occurs when this variable reaches a critical value, D_c ; usually, D is defined such that $D_c=1$. Because this is an uncoupled method, D does not affect elastic-plastic properties. It is defined through an integrated function along the strain path (see Eq.II.15):

$$D = \int_0^{\bar{\varepsilon}_f} f(\text{stress state}) d\bar{\varepsilon}_p \quad \text{Eq.II.15}$$

where $f(\text{stress state})$ is a function depending on the stress state. By performing experimental tests, parameters of the function f can be assessed. Thanks to its simplicity, this method has been widely studied and is extensively used in industry.

However, the two following points matter a lot for the accuracy of the prediction:

- 1) Experimental tests performed for parameters identification must cover the stress state corresponding to the one undergone by the material for the industrial application (e.g.: if the material is submitted to shear stress state, experimental tests must be as close as possible to this stress state).
- 2) Loading paths must be as proportional as possible to submit the material to only one stress state [Cao et al., 2013]. Otherwise, prediction would be less efficient.

First functions accounting for the stress state are issued from the works of Rice & Tracey [Rice & Tracey, 1969] and McClintock [McClintock, 1968]. The former was dependent on the stress triaxiality, and the later on the first and second principal stresses.

Fig.II.18 shows the fracture criterion of Al2024-T351 accounting for the stress triaxiality ([Bao & Wierzbicki, 2005]). More recently, new criteria accounting for the stress triaxiality as well as the Lode angle were developed. On **Fig.II.19** is plotted the fracture surface for Al2024-T351. The purple curve shows the plane stress condition, which enable to get closer to the fracture curve observed in **Fig.II.18**: following this curve starting from large negative triaxiality, the strain to fracture first decreases, then increases and finally decreases again.

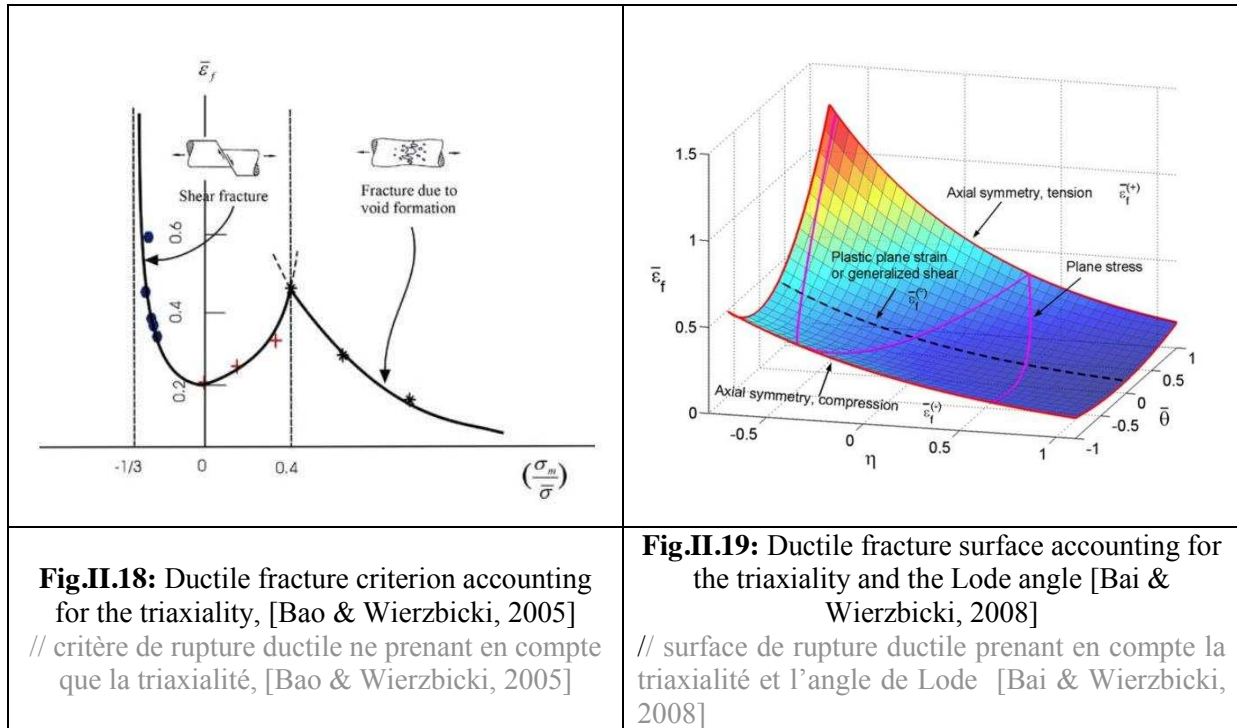


Table II.1 gathers some of the functions used to account for the stress state. One must notice in **Table II.1**, that functions of the stress state are expressed as $1/\bar{\epsilon}_f$. $C, C_1, C_2, C_3, C_4, D_1, D_2, D_3, D_4, D_5, D_6$ are material parameters and need to be assessed with experimental data. The Lode angle was firstly introduced in these criteria by Xue and Wierzbicki in 2007 through the third stress invariant [Xue, 2007].

These criteria are phenomenological; let us focus on the Bai & Wierzbicki and Lou & Huh criteria to see how they were constructed.

Models	f (stress state)
[McClintock, 1968]	$\frac{\sqrt{3}}{2(1-n)} \sinh\left(\frac{\sqrt{3}}{2(1-n)} \frac{\sigma_1 + \sigma_2}{\bar{\sigma}}\right) + \frac{3}{4} \frac{\sigma_1 - \sigma_2}{\bar{\sigma}}$ n : strain hardening exponent
[Rice & Tracey, 1969]	$\exp\left(\frac{3}{2}\eta\right)$
[Johnson & Cook, 1985]	$\frac{1}{\bar{\varepsilon}_f}, \text{ with } \bar{\varepsilon}_f = C_1 + C_2 \exp(-C_3\eta)$
Xue & Wierzbicki [Xue, 2007]	$\frac{1}{\bar{\varepsilon}_f}, \text{ with } \bar{\varepsilon}_f = C_1 \exp(-C_2\eta) - (C_1 \exp(-C_2\eta) - C_3 \exp(-C_4\eta))(1 - \xi^{1/n})^n$
[Bai & Wierzbicki, 2008]	$\frac{1}{\bar{\varepsilon}_f}, \text{ with } \bar{\varepsilon}_f = \left[\frac{1}{2}(\bar{\varepsilon}_f^{(+)} + \bar{\varepsilon}_f^{(-)}) - \bar{\varepsilon}_f^{(0)}\right] \bar{\theta}^2 + \frac{1}{2}(\bar{\varepsilon}_f^{(+)} - \bar{\varepsilon}_f^{(-)}) \bar{\theta} + \bar{\varepsilon}_f^{(0)}$ $\bar{\varepsilon}_f^{(+)} = D_1 e^{-D_2\eta}; \bar{\varepsilon}_f^{(0)} = D_3 e^{-D_4\eta}; \bar{\varepsilon}_f^{(-)} = D_5 e^{-D_6\eta}$
MMC [Bai & Wierzbicki, 2010]	$\frac{1}{\bar{\varepsilon}_f}, \text{ with } \bar{\varepsilon}_f = \left(\frac{\sqrt{3}K}{c_2} \left[\sqrt{\frac{1+c_1^2}{3}} \cos\left(\frac{\bar{\theta}\pi}{6}\right) + C_1 \left(\eta + \frac{1}{3} \sin\left(\frac{\bar{\theta}\pi}{6}\right)\right)\right]\right)^{-1/n} - \varepsilon_0$
Lou & Huh [Yin et al., 2015]	$\frac{1}{\bar{c}} \left(\frac{2}{\sqrt{3}} \cos\left(\frac{\bar{\theta}\pi}{6}\right)\right)^a \left(\frac{\langle 1 + 3\eta \rangle}{2}\right)^b$

Table II.1: examples of failure functions used in Eq.II.15

// exemples de fonctions de rupture utilisées dans Eq.II.15

❖ **Bai and Wierzbicki criterion**

This criterion ([Bai & Wierzbicki, 2008]) was constructed in the 3D space $(\bar{\varepsilon}_f, \eta, \bar{\theta})$. This space is commonly used in the fracture locus study and defines the critical strain to fracture as a function of the stress triaxiality η and the Lode angle parameter $\bar{\theta}$. These two last parameters define the stress state in a unique way.

The early study of [Rice & Tracey, 1969] assumed the influence of the stress triaxiality on the strain to fracture was exponential ($\bar{\varepsilon}_f = D_1 e^{-D_2\eta}$). This function is based on three boundary limits: $\bar{\varepsilon}_f^-$ corresponds to generalized compression ($\bar{\theta} = -1$); $\bar{\varepsilon}_f^0$ corresponds to generalized shear ($\bar{\theta} = 0$) and finally $\bar{\varepsilon}_f^+$ corresponds to generalized tension ($\bar{\theta} = 1$). Hence $\bar{\varepsilon}_f^+ = D_1 e^{-D_2\eta}$, $\bar{\varepsilon}_f^0 = D_3 e^{-D_4\eta}$, and $\bar{\varepsilon}_f^- = D_5 e^{-D_6\eta}$.

The Lode angle influence is accounted for through a degree two polynomial function:

$$\bar{\varepsilon}_f(\eta, \bar{\theta}) = \left[\frac{1}{2}(\bar{\varepsilon}_f^+ + \bar{\varepsilon}_f^-) - \bar{\varepsilon}_f^0\right] \bar{\theta}^2 + \frac{1}{2}(\bar{\varepsilon}_f^+ - \bar{\varepsilon}_f^-) \bar{\theta} + \bar{\varepsilon}_f^0 \quad \text{Eq.II.16}$$

By expressing the boundary terms, Eq.II.16 gives:

$$\begin{aligned} \bar{\varepsilon}_f(\eta, \bar{\theta}) = & \left[\frac{1}{2}(D_1 e^{-D_2\eta} + D_5 e^{-D_6\eta}) - D_3 e^{-D_4\eta}\right] \bar{\theta}^2 \\ & + \frac{1}{2}(D_1 e^{-D_2\eta} - D_5 e^{-D_6\eta}) \bar{\theta} + D_3 e^{-D_4\eta} \end{aligned} \quad \text{Eq.II.17}$$

with $D_1, D_2, D_3, D_4, D_5, D_6$ material parameters which need to be identified with experimental results. The evolution of the damage variable D is assumed to grow linearly with the equivalent plastic strain in the proportional loading case. Failure occurs when $D=1$. Its evolution is defined through Eq.II.18:

$$D(\bar{\varepsilon}_p) = \int_0^{\bar{\varepsilon}_p} \frac{d\bar{\varepsilon}_p}{\bar{\varepsilon}_f(\eta, \bar{\theta})} \quad \text{Eq.II.18}$$

where $\eta = \eta(\bar{\varepsilon}_p)$ and $\bar{\theta} = \bar{\theta}(\bar{\varepsilon}_p)$ are functions depending on the equivalent plastic strain. Proportional loading means these two parameters do not evolve during loading. Otherwise, average values are defined through:

$$\eta_{av} = \frac{1}{\bar{\varepsilon}_f} \int_0^{\bar{\varepsilon}_f} \eta(\bar{\varepsilon}_p) d\bar{\varepsilon}_p \quad ; \quad \bar{\theta}_{av} = \frac{1}{\bar{\varepsilon}_f} \int_0^{\bar{\varepsilon}_f} \bar{\theta}(\bar{\varepsilon}_p) d\bar{\varepsilon}_p \quad \text{Eq.II.19}$$

In the present study, current values of the stress triaxiality and the Lode angle parameter are used to assess the criterion parameters. It is more accurate than using the average value, but requires inverse analysis. The extraction of the loading paths and identification of the parameters are detailed in Chapter 5.

❖ **Lou & Huh criterion**

The construction of this criterion is different from the previous one. [Lou et al., 2012] are assuming that damage evolution is caused by void nucleation, growth and coalescence.

Nucleation of voids starts at the interface between inclusions and matrices with plastic strain. Initially, it was modeled by a critical positive debonding stress between inclusions and the matrix ([Argon & Safoglu, 1975]). But this model showed limits in upsetting test. Indeed, it cannot explain ductile fracture with a negative stress triaxiality ([Bao & Wierzbicki, 2004]). In the meantime, another model was proposed by [Gurson, 1977] based on plastic strain. Thus, in this Lou & Huh criterion, voids nucleation is accounted for through the plastic strain.

$$D_n = D_n(\bar{\varepsilon}) \quad \text{Eq.II.20}$$

Formulas accounting for voids growth are numerous [McClintock, 1968] [Rice & Tracey, 1969] and all related to the mean stress. It is now introduced by the stress triaxiality ratio η . [Bao & Wierzbicki, 2005] showed fracture cannot occur for a triaxiality lower than $-1/3$. Thus, the influence of the voids growth can be expressed through Eq.II.21:

$$D_g = D_g(\langle 1 + 3\eta \rangle) \quad \text{Eq.II.21}$$

where $\langle x \rangle = x$ when $x \geq 0$ and $\langle x \rangle = 0$ when $x < 0$.

Void coalescence is the final stage of ductile failure. [Weck & Wilkinson, 2008] observed coalescence processes in steel: necking of the ligaments between voids (caused by the highest principal stress) and shear linking of voids along the direction of maximal shear stress. However, the former has not been observed in sheet metal fracture ([Ghosh, 1976]). Therefore, shear linking is assumed as the void coalescence mechanism in this criterion. To our point of view, accounting for the necking coalescence mechanism would be a good way of improving this criterion. Shear fracture is caused by the maximum shear stress; thus voids coalescence is modeled with (Eq.II.22):

$$D_c = D_c\left(\frac{\tau_{max}}{\bar{\sigma}}\right) \quad \text{Eq.II.22}$$

where $\bar{\sigma}$ is the equivalent stress. Thus, by gathering all the 3 expressions, and weighting them using powers, the failure criterion can be written as Eq.II.23:

$$\left(\frac{2\tau_{max}}{\bar{\sigma}}\right)^{C_1} \left(\frac{\langle 1+3\eta \rangle}{2}\right)^{C_2} \bar{\epsilon}_f = C_3 \quad \text{Eq.II.23}$$

where $\langle x \rangle = x$ when $x \geq 0$ and $\langle x \rangle = 0$ when $x < 0$. Damage evolution is assumed to increase linearly with the equivalent plastic strain, as for the Bai & Wierzbicki criterion. Hence,

$$\frac{1}{C_3} \int_0^{\bar{\epsilon}} \left(\frac{2\tau_{max}}{\bar{\sigma}}\right)^{C_1} \left(\frac{\langle 1+3\eta \rangle}{2}\right)^{C_2} d\bar{\epsilon} = D(\bar{\epsilon}) \quad \text{Eq.II.24}$$

where C_1 , C_2 , C_3 are material parameters. Fracture initiates when D reaches 1. The normalized maximum shear stress can be expressed as a function of the principal stresses through the following relation:

$$\frac{2\tau_{max}}{\bar{\sigma}} = \frac{\sigma_1 - \sigma_3}{\bar{\sigma}} \quad \text{Eq.II.25}$$

The principal stresses can be expressed as a function of $(\bar{\sigma}, \eta, \bar{\theta})$. Readers can refer to [Bai & Wierzbicki, 2010] for the detail of the calculation. Thus, Eq.II.25 can be rewritten as:

$$\frac{2\tau_{max}}{\bar{\sigma}} = \frac{2}{3} \left(\cos \theta - \cos \left(\frac{4}{3}\pi - \theta \right) \right) \quad \text{Eq.II.26}$$

By using the Lode angle parameter instead of the Lode angle ($\bar{\theta} = 1 - \frac{6\theta}{\pi}$), Eq.II.24 can be rewritten as:

$$\frac{1}{C_3} \int_0^{\bar{\epsilon}_f} \left(\frac{2}{\sqrt{3}} \cos \left(\frac{\bar{\theta}\pi}{6} \right) \right)^{C_1} \left(\frac{\langle 1+3\eta \rangle}{2} \right)^{C_2} d\bar{\epsilon} = D(\bar{\epsilon}) \quad \text{Eq.II.27}$$

This is the expression of the Lou & Huh criterion used hereinafter.

One can see the Lode angle parameter $\bar{\theta}$ is accounted for through different ways in those criteria. Either its exponent is a degree two polynomial function in [Bai & Wierzbicki, 2008] (see Eq.II.18), or it is introduced through geometrical functions in [Bai & Wierzbicki, 2010] and [Yin et al., 2015] (see Eq.II.27).

The same remark can be done for the stress triaxiality ratio (η), mainly accounted for through exponential functions. This is the historical model for the voids growth mechanism [Rice & Tracey, 1969]. However, some authors ([Bai & Wierzbicki, 2010], [Yin et al., 2015]) used a power function. This shows that those criteria are phenomenological and have no real physical explanation.

The Bai & Wierzbicki criterion is based on the exponential of the stress triaxiality ratio, which is the model of voids growth developed by Rice & Tracey. It is supposed to be accurate to predict failure at high level of triaxiality. The Lou & Huh criterion was developed based on void nucleation, growth and coalescence mechanisms. The presence of the term related to the maximum shear stress makes it accurate to predict failure in shear stress state. But there is no rule indicating which criterion must be chosen to model failure for a given material. Thus, only experimental data covering a wide range of stress state can help choosing one criterion rather than the others.

However, these criteria present a couple of drawbacks. Their accuracy depends on the quality of the tests campaign used to assess the parameters. The set of mechanical tests must cover a wide range of stress states to yield accurate predictions. Furthermore, loading paths must be proportional in the mechanical testing. Finally, these criteria require a correct and accurate identification of strain to fracture, which is not as simple as it seems to be.

This type of failure criteria will be used to model the ductile core fracture behavior. Experimental tests used to identify the parameters are described in **Chapter 4**, and **Chapter 5** introduces the numerical method set up for parameters identification.

II. 2. 2 Brittle failure

Unlike ductile materials, brittle ones with intergranular fracture undergo very low plastic strain before failure. Thus, criteria usually depend on stress state. The conventional criterion is related to the first principal stress (Eq.II.28) [Ritchie, Knott, & Rice, 1973] and to the yield strength [Hahn et. al, 1959]. This assumes material fails in tensile stress state with the following conditions.

$$\sigma_I \geq \sigma_{Ic} \quad \text{Eq.II.28}$$

$$\sigma_{eq} \geq \sigma_Y \quad \text{Eq.II.29}$$

where σ_{Ic} is the critical maximal principal stress and σ_Y the yield strength. Eq.II.29 indicates plastic strain is required to trigger brittle fracture in **cleavage** mode. Eq.II.28 is the condition for the micro crack propagation.

However critical stress to failure of brittle materials (e.g.: ceramics) decreases when the specimen is bigger. This is due to the presence of bigger defaults; probability to find large defaults is higher when specimen is bigger. These defaults decrease the critical stress to fracture initiation.

[Griffith, 1921] introduced the energy of cohesion, required amount of energy to propagate a preexisting crack in an elastic material. It is a purely elastic method and can be expressed as Eq.II.30 to become a critical stress criterion.

$$\sigma = \left(\frac{2E\gamma_s}{\pi c} \right)^{1/2} \quad \text{Eq.II.30}$$

with c the initial crack length, E the Young modulus, and γ_s the surface energy of the material.

Later, a new model was developed by [Beremin, 1983] to account for the stochastic behavior of brittle failure (see Eq.II.31) using the Weibull stress distribution (Eq.II.32).

$$p_r = 1 - \exp \left[- \left(\frac{\sigma_w}{\sigma_u} \right)^m \right] \quad \text{Eq.II.31}$$

$$\sigma_w = \sqrt[m]{\sum_j (\sigma_I^j)^m \frac{V_j}{V_0}} \quad \text{Eq.II.32}$$

where σ_u is a critical (ultimate) stress depending on the material, m and V_0 are material parameters, V_j is the volume of the j^{th} element submitted to the first principal stress σ_I^j . p_r is the probability of failure.

This model has been widely used and modified and shows some good results ([Henry et al., 2006], [Moinereau et al., 2006], [Malaplate et al., 2008]). [Malaplate et al., 2008] used this criterion to predict the failure of a 9Cr-1Mo-V-Nb steel (T 91). They assessed the Beremin model parameters with 3 point bending specimen. **Fig.II.20** (a) plots the evolution of the failure probability assessed experimentally and calculated with the Beremin model. Experimental failure probability equals $\frac{i-0.5}{N}$, with N the number of experiments, i the number of a given result, knowing the experiments were ranked from 1 to N based on increasing tool displacement of the three point bending test. The agreement between experimental and numerical results is good. Then, based on a compact tension specimen (CT), they

evaluated the stress intensity factor for the He-loaded and and He-free materials. There is a little discrepancy between the experimental and the numerical results.

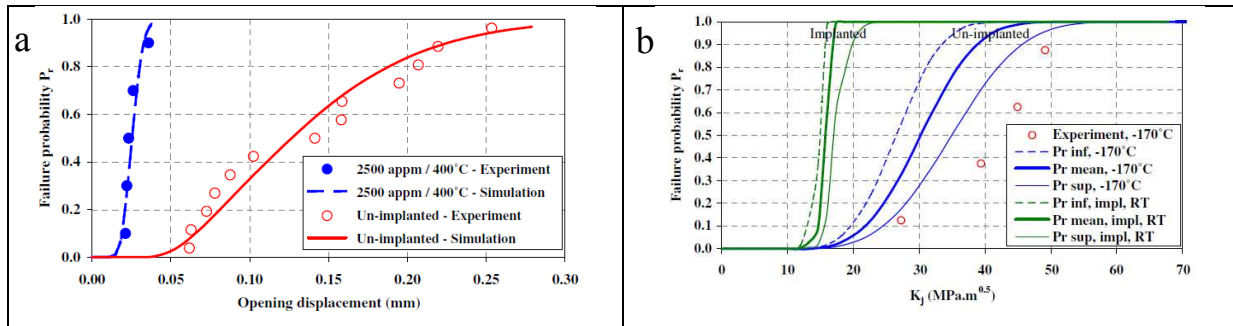


Fig.II.20: (a) comparison of experimental and calculated failure probability with the Beremin model, (b) failure probability as a function of the stress intensity factor [Malaplate et al., 2008]
 // (a) comparaison de probabilité de rupture expérimentale et calculée avec le modèle de Beremin, (b) probabilité de rupture en fonction du facteur d'intensité des contraintes [Malaplate et al., 2008]

It was seen the failure of the external CN layer is intergranular. This failure mode occurs without, or with very limited amount of plasticity undergone by the material. Thus, brittle criteria using plastic strain are not used in this work, and stress-based criteria are preferred.

As seen in the literature, brittle failure often exhibits a stochastic behavior because of the role of micro-defects and microstructure flaws on cracks initiation. The Beremin model is an efficient way of dealing with this stochastic effect. However, it is being used on compact tensile specimen, or notch bending specimen: the crack initiation and propagation is known on those specimens. Stress level is high in the volume close to the notch and decreases very quickly further from the tip. In the case of the tooth fracture study, several cracks are expected without knowing exactly where they will be opening. This makes the use of this stochastic behavior tricky to be used in this project. Indeed, numerous tests would be necessary however to identify all parameters. This approach was not developed further in this work, but could be an interesting way of improving brittle failure modeling.

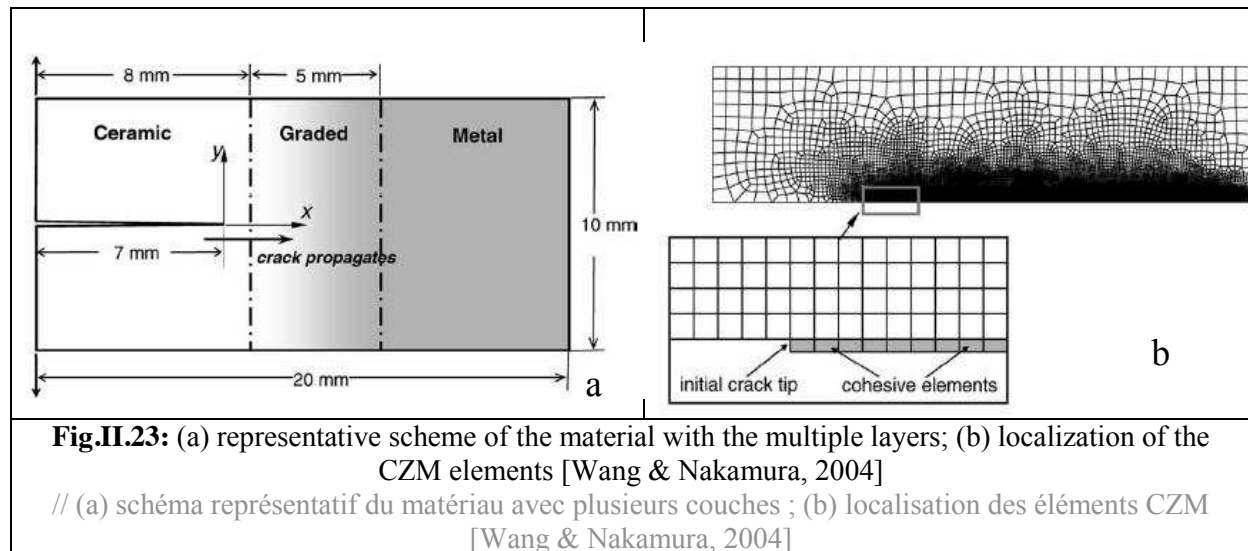
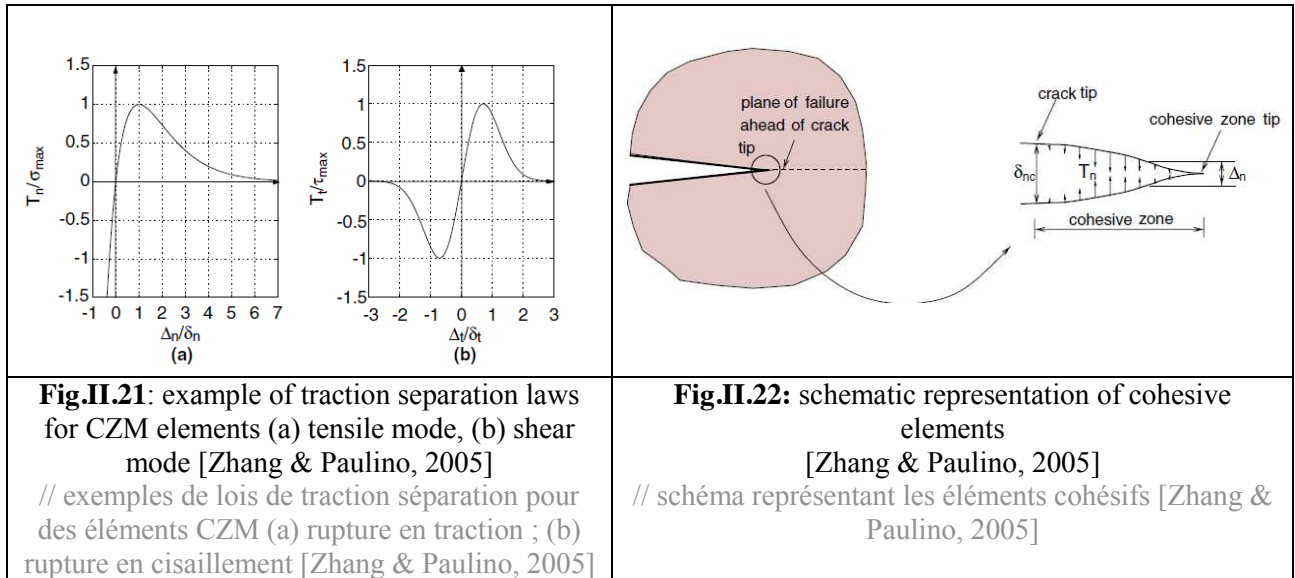
II.3 Numerical modeling of failure in a finite element framework

The previous part reviewed the mechanical criteria to predict failure initiation. Another key point in failure modeling is how to propagate a crack through the mesh. Recent techniques such as Cohesive Zone Models (CZM) or eXtended Finite Element Methods (XFEM) are briefly introduced to inform the reader about finite element crack propagation techniques. Advantages and drawbacks of these techniques are detailed as well. Unfortunately, the use of these techniques still faces robustness issues when the crack path is not known a priori or for large plastic strain ductile fracture problems. The element deletion technique is therefore considered because of its robustness (essential in an industrial context) and because it is the only technique available in LS-Dyna for 3D configurations. This technique is presented in the last section of this chapter and its advantages and drawbacks are discussed.

II. 3. 1 Crack propagation numerical techniques

- Cohesive zone models

Cohesive Zone Model (CZM) consists in defining a traction separation law (see **Fig.II.21**) describing the behavior of zero-thickness elements (cohesive elements) placed on the crack path (which has to be known a priori). Thus, a real crack is formed in-between the elements (see **Fig.II.22**), insuring a good control of fracture energy. It has been widely used to model fracture of FGM. For instance, [Wang & Nakamura, 2004] used CZM elements with evolving traction-separation laws to account for the increase of ductility deeper in the metal. **Fig.II.23** (a) illustrates the variation of the material properties simulated as a function of the depth. **Fig.II.23** (b) illustrates the mesh refinement close to the crack path. Cohesive elements are implemented where the crack is supposed to propagate. This introduces one of the main drawbacks of this technique. Because it requires the use of specific elements that need to be placed in the mesh, the crack path must be known prior to the simulation. This limits a lot its use to small parts where the crack path is known and explains why this approach is very popular for interfacial failure. For example, [Bahr et al., 2003] used it to simulate the debonding of brittle coatings applied on a more ductile bulk material.



[Tohgo & Hadano, 2006] model the fracture process of a three point bending ceramic-metal FGM. **Fig.II.24 (a)** is a schematic of the 2D mesh used. One notices the mesh refinement on the lower side, where crack will initiate. Plastic properties were assigned as a function of the percentage of the PSZ (Partially Stabilized Zirconia). **Fig.II.24 (b)** shows the experimental force displacement curve. Cracks propagation process observed are represented. This process is simulated with 4 separated simulations. **Fig.II.25 (a-b-c-d)** show the representative schematic of the 4 meshes used (Symmetric meshes were used to decrease the number of elements).

The three cracked specimen (**Fig.II.25 (b-c-d)**) are used to evaluate the toughness of the different cracks paths: crack arrest at the interface with the tougher part, continued propagation along the interface, penetration in the tough material. Cracks paths are known, this FEM analysis enables to determine the stress intensity factors for the three crack steps propagation and determines which modes will prevail. Toughness is characterized through this parameter. It is the ability of a material to resist crack propagation.

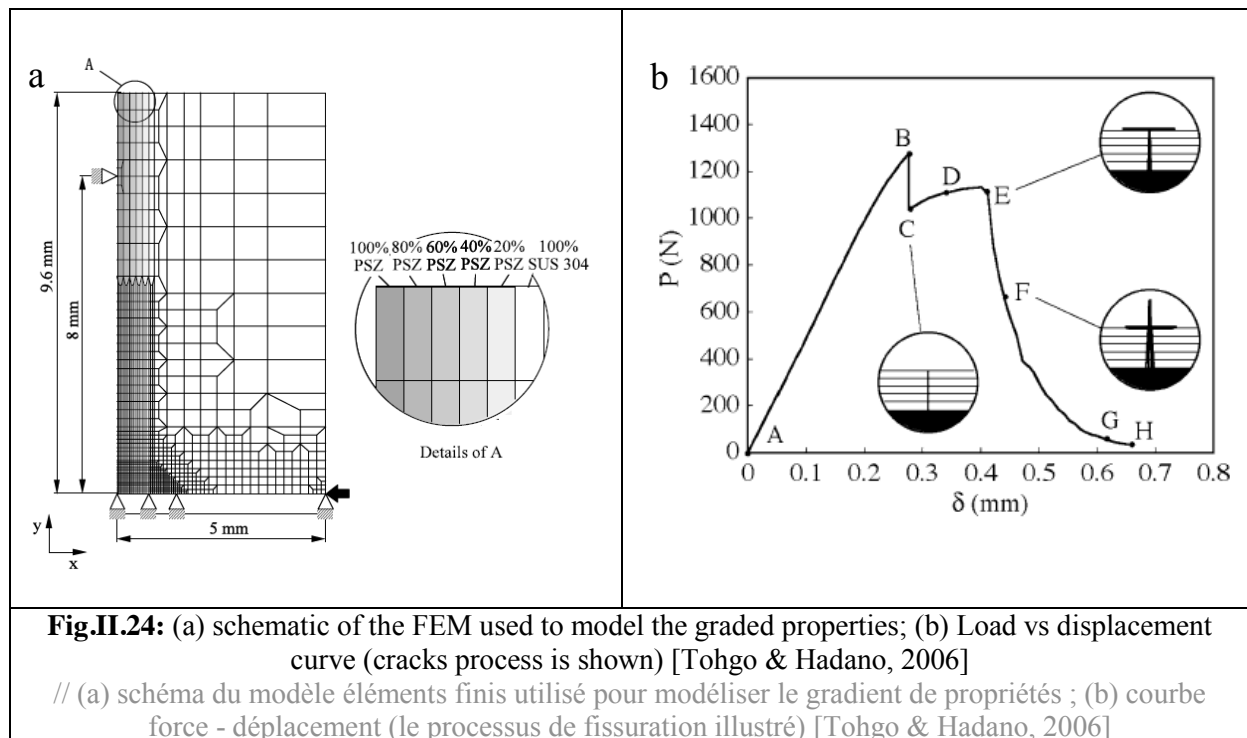
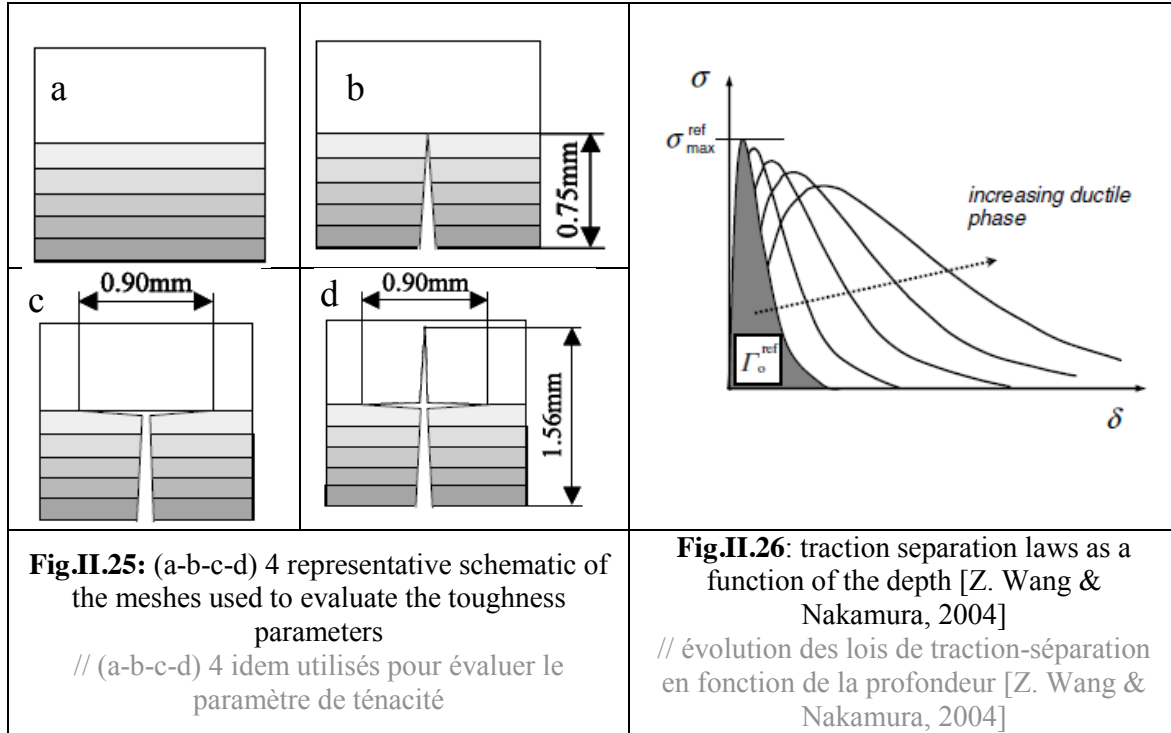


Fig.II.26 shows the evolution of the traction separation law. The more brittle behavior model the ceramic and the more ductile one the metal. One can see the failure is not abrupt; there is a progressive softening of the sustained stress. This enables to control the fracture energy G_c , which is equal to the integral of the traction separation law.

Toughness is an interesting parameter to study on a graded material since it evolves to reach the limit value of the ductile material. But its measurement is very difficult. Indeed, its measurement can be done on pre-cracked specimen: 3 or 4 points bending specimen, compact tension specimen... But it would have required too much time to be done during this project, considering the numerous tasks to be performed.

[Bahr et al., 2003] used the critical energy release rate G_c as a failure criterion for interfacial debonding between graded coating and substrate. The model was used only on a four point bending test.

[Wang & Nakamura, 2004] used evolving CZM traction separation law (see Fig.II.26) to account for the increase of the ductility in the graded material. Separation energy ($\Gamma = \int \sigma d\delta$) evolves linearly between the one of the external layer and the ductile core. This shows good results for the simulation of the double cantilever beam as well as impacting rod simulation. Both simulations were done in 2D.



In our final applications, crack path is not known a priori and this technique cannot be used. The solution of implementing CZM elements at all elements interfaces can be done on meshes with limited number of elements and nodes. But, it cannot be done in this work due to the size of the mechanism. Furthermore, in all the studied case previously, the cracks were perfectly perpendicular to the surfaces (bending specimens). Situation is different in the tooth failure, cracks are not perpendicular to the surface. In addition, 3D CZM elements are not available in LS-Dyna.

Modeling failure in a finite element mesh without knowing the crack path a priori is also possible. The two main techniques are based respectively on automatic remeshing and on elements enrichment.

- Discrete crack propagation with remeshing

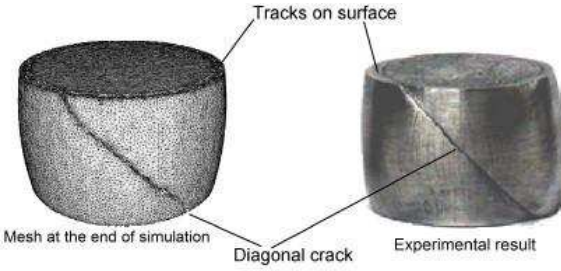
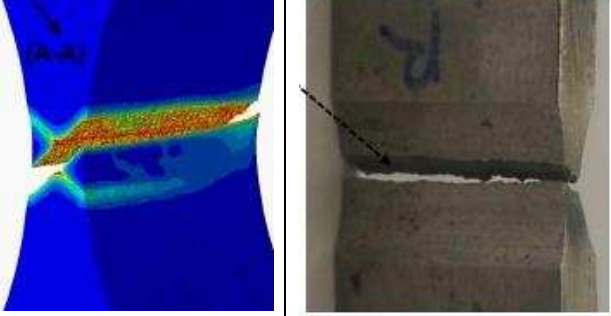
Based on crack propagation criteria [Bouchard et al., 2003], the direction of cracks can be defined at each computation increment. A new crack increment is then given to the mesher which modifies the whole mesh topology and change elements connectivity to get a new mesh including the new propagated crack. Crack propagation criteria are usually based on stress field at the crack tip or on energetic-based criteria for brittle failure. More recently, some authors proposed to use ductile damage models to define the direction of the crack propagation [Mediavilla et al., 2006] [Feld-Payet et al., 2013]. This approach has however some drawbacks in terms of robustness for 3D fracture of industrial components. In addition, several remeshing steps are needed and transport of mechanical variables may induce diffusion of mechanical fields.

- X-FEM

In 1999, [Moes et al., 1999] proposed to model crack propagation without remeshing using the eXtended Finite Element Method. X-FEM consists in enriching locally the shape functions of the elements crossed by the crack and of the elements containing the crack tip. This is an interesting technique, which does not require remeshing and which is thus less sensitive to diffusion of mechanical fields due to the transport of mechanical variables. This method is however more adapted to brittle failure than ductile failure and also suffers from robustness issues for such complex 3D industrial applications with large plastic strain. It will not be possible to use any of these two methods for our industrial applications due to the fact that they are not available in LS-Dyna. In addition, CZM technique cannot be used as well because the crack path is not known prior to the simulation. Thus, the kill-element method (or element deletion or element erosion) will be used.

II. 3. 2 Element deletion technique

This technique is implemented in multiple FEM software including LS-DYNA (called element erosion) and ABAQUS or FORGE (called kill element). It is the only technique implemented in the 3D case in the FEM software LS-DYNA to propagate failure. It consists in deleting elements when failure is reached (at one or several integration points) according to the associated mechanical failure criterion. **Fig.II.27** and **Fig.II.28** show two examples of failure modeled using a kill element technique in Forge software, based on the Xue & Wierzbicki [Xue, 2007] failure criterion. Numerical failure patterns are in good agreement with experimental ones.

 <p>Mesh at the end of simulation</p> <p>Tracks on surface</p> <p>Diagonal crack</p> <p>Experimental result</p>	
<p>Fig.II.27: comparison of numerical and experimental failure pattern, upsetting test [Cao, 2014]</p> <p>// comparaison des fissures expérimentales et numériques, essai de compression</p>	<p>Fig.II.28: comparison numerical and experimental crack path, tensile test [Cao, 2014]</p> <p>// comparaison des fissures numériques et expérimentales, essai de traction</p>

❖ Advantages

Simplicity and robustness are the main advantages of this method, which makes it very popular in the industry for 3D fracture modeling. In addition, it is a relatively fast numerical technique which does not require any specific type of element and which does not require to know the crack path prior to the calculations.

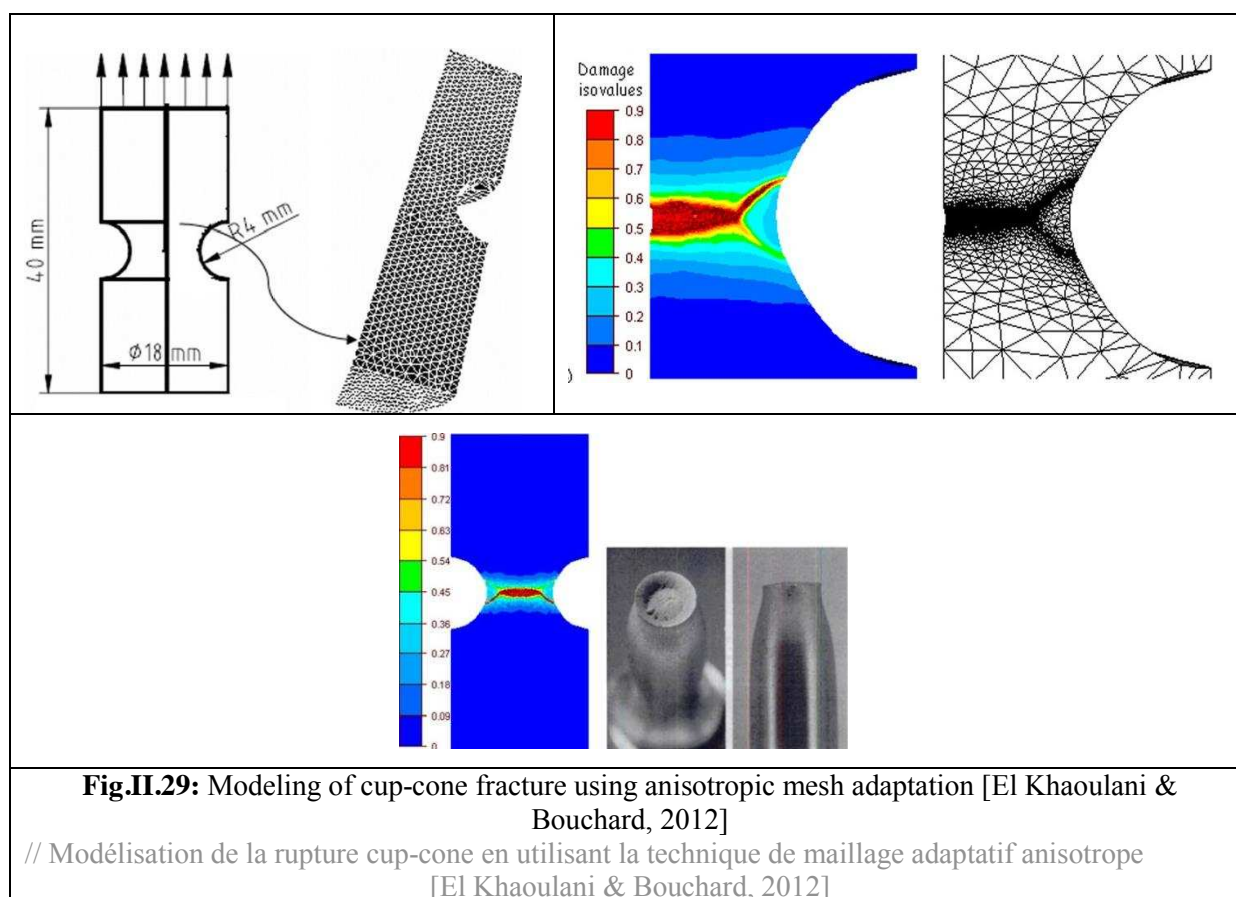
❖ Disadvantages

This technique is very dependent on the mesh size and elements shape. Indeed, deleting one element induces an abrupt artificial volume change, creates uncontrolled stress concentrating geometries and influences the stress state on the neighboring elements. Local refinement and automatic remeshing improves failure modeling with this technique [Cao, 2014]. Anisotropic remeshing based on a

posteriori error estimator reduces the elements size in the damaged area in a reasonable computation time. **Fig.II.29** shows how anisotropic mesh adaptation is used to model the well-known “cup-cone” fracture of a notched round specimen in tension [El khaoulani & Bouchard, 2012]. Starting from an isotropic mesh, the anisotropic error estimator based on the damage variable and its gradient gives an anisotropic metrics to the mesher which, in turn, refines the elements in the damaged area. Elements are particularly refined perpendicularly to the failure path so that volume loss is reduced when elements are deleted.

However, anisotropic remeshing is not available in all FEM software (e.g. LS-DYNA). Cracks formed by elements deletion have a tip size of one element width. This can alter the efficiency of brittle criteria which are based on principal stresses at the crack tip. This is why more efficient but time-consuming methods exist, (e.g. Cohesive Zone Model).

The last disadvantage of this technique is the poor control of the energy released during failure.



II.4 Strategy adopted for the modeling of carbonitrided components failure

Literature review showed how ductile failure can be modeled. Failure criteria will be used in this PhD for several reasons. Unlike coupled models, they do not present any damage localization issue and are therefore less sensitive to mesh size. Because of the industrial context of this PhD, rather coarse meshes will be used to model the tooth failure (see Chapter 6). The use of coupled models with coarse meshes can be done only by using non-local approaches, which are not available in LS-DYNA. Micro-

mechanics models require the determination of too many parameters, including microstructure-based observations, to be used in this industrial context.

Furthermore, it was seen in the literature that failure criteria based on a critical plastic strain at failure are efficient to predict failure when loading path is proportional. It will be seen in chapters 3 and 6 that tooth failure appears by a final dominant shear crack. Thus, the elements that are going to undergo the final crack will have most of their loading path in a quasi-proportional shear stress state. Calibration tests should therefore reproduce such shear dominant stress state.

Observations of post mortem recliners show external CN layer fails by intergranular failure. So, it undergoes almost no plastic strain. Stress-based criteria (principal stresses) should therefore be used. The use of toughness properties within the CN layer would also have been interesting. It would have been a good way to account for the toughness increase in the intermediate layer. However, identifying toughness for such small and brittle carbonitrided layer is extremely challenging. Furthermore, as it will be seen later, cracks tend to propagate through the whole CN layer immediately, so the measurement of the toughness variation of this layer would be very difficult.

The kill element technique will be chosen to model failure through the elements. The literature review shows more accurate techniques at first sight but none of them is robust enough to address 3D failure with significant plastic strain in an industrial context. Furthermore, even though the core material tends to fail with a single dominant crack, the external layer fails with multiple cracks, as seen in Chapter 1. Due to its simplicity, the kill-element technique can be robust and efficient on such 3D configurations with a high number of elements. The fact the cracks paths do not have to be known prior to the simulation will be helpful here. Indeed, a recliner is a complex system and it is impossible to know where failure will initiate and propagate on all the teeth in contact. It is however important to bear in mind that this “basic” technique will induce inaccuracies locally. For example, deletion of elements (with associated volume loss) may induce higher stiffness decrease than real experimental sharp cracks. Stress state at the crack tip may also be modified depending on the shape of the deleted elements. The solution would thus be to use very fine mesh to have an accurate stress state assessment ([Wang & Wierzbicki, 2015], [Wang et al., 2015], [El Khaoulani & Bouchard, 2012]), but such fine meshes are difficult to use in an industrial context.

Chapter III : Semi-industrial test

Contents

III. 1	Test bench design	59
III. 1. 1	Technical specifications	59
III. 1. 2	Description	60
III. 2	Semi-industrial test results and analysis.....	61
III. 2. 1	Test bench set up and first trials	62
III. 2. 2	Engagement depth study.....	67
III. 2. 2. a	Tooth strength.....	68
III. 2. 2. b	Tooth failure process	69
III. 2. 2. c	Discussion	74
III. 2. 3	Influence of the CN layer on the tooth failure.....	75
III. 2. 3. a	Influence on the strength	76
III. 2. 3. b	Influence on the tooth failure process.....	77
III. 3	Conclusion.....	82

Résumé en Français

Ce chapitre présente le banc d'essai semi-industriel conçu spécialement pour la thèse. Son cahier des charges est le suivant : l'essai doit être réalisé sur une seule dent en mesurant force et déplacement. Il doit être possible d'observer in situ le processus d'endommagement de la dent ; le banc doit être rigide et en même temps permettre un réglage de la surface de contact dent-outil. Le banc construit répond à tous les items du cahier des charges ; les essais réalisés pendant sa mise au point ont permis de montrer que la mesure du vrai déplacement relatif dent-outil se fera via post-traitement d'images corrélation 3D. Il permet d'observer en fonction du vrai déplacement et de l'effort appliqué l'évolution du processus d'endommagement d'une dent.

Les premiers essais ont validé en partie l'hypothèse du processus d'endommagement établie lors de l'étude des mécanismes testés. Une fissure apparaît dans la dent sous la surface de contact avec l'outil, cette zone est soumise à de fortes contraintes de traction. Cette fissure se propage dans la couche externe mais est arrêtée dans la zone de transition. La ductilité supérieure dans cette zone stoppe la propagation de la fissure. Cependant, lorsque l'effort devient trop important, une fissure se propage rectilignement dans toute l'épaisseur de la dent pour la couper en deux dans le sens tangentiel au pignon. Les fissures finales sont ici rectilignes car l'essai se fait sur une machine de traction. Les fissures étaient courbées dans les mécanismes car le mouvement relatif était celui d'un planétaire à l'intérieur d'une couronne.

Puis nous avons pu mesurer l'influence de la profondeur d'engagement sur la rupture des dents. Plus l'engagement est élevé, plus la force soutenue par la dent est élevée, ce résultat était attendu. Par contre, plus l'engagement est grand, plus la rupture de la dent est brutale. En effet, un engagement plus faible permet une flexion globale de la dent, avec une ouverture de plus de fissures, ce qui allonge le processus. Mais, quel que soit l'engagement, le processus de rupture a le même schéma : une première fissure s'ouvre sous la surface de contact avec l'outil, se propage dans la couche externe et est stoppée dans la zone de transition plus ductile. Puis une ou plusieurs fissures superficielles s'ouvrent, leur emplacement varie en fonction de la profondeur d'engagement. Finalement, la rupture finale est due à la propagation d'une fissure de cisaillement qui traverse toute la dent depuis la surface de contact avec l'outil jusqu'à la surface opposée.

Enfin, l'influence de la couche externe de carbonituration a pu être mesurée. Pour ce faire, des essais sur des dents ne contenant que le matériau de cœur ont été réalisés. Cette couche CN augmente d'au maximum 16 % l'effort axial soutenu par une dent (valeur pour le faible engagement). Sinon, pour les deux autres cas, la couche externe n'apporte que très peu à l'effort supporté par les dents. Elle ne modifie pas non plus le déplacement à rupture. En effet, de par sa fragilité, elle se fissure très rapidement. De plus, le processus de rupture n'est que partiellement modifié. En effet, les dents constituées du seul matériau de cœur n'ont pas de diminution de la ductilité en surface : il n'y a donc pas d'ouverture de fissures superficielles. Ces essais confirment que c'est le matériau de cœur qui soutient le chargement, alors que la couche externe augmente la durée de vie en contact des roues dentées, pignon et flasque.

Introduction

Observations performed in the first chapter showed pinion teeth are the most damaged areas in the post mortem recliners. Tooth failure process occurs in two steps. First multiple cracks appear in the external brittle layer at the beginning of the loading stage. Then a final major crack propagates through the whole tooth when the strain reaches a critical value. Observations emphasize the need for a more rigorous and controlled tooth failure test due to the open questions remaining after observation of post-mortem failed recliners.

The semi-industrial test presented in this chapter aims at identifying quantitatively the relation between fracture process and stress state. Technical specifications and the solution designed are introduced. Then, it is shown why 3D Digital Image Correlation (DIC) is mandatory to measure real displacements. Then, two distinct studies are carried out:

- Post-mortem observations on recliners showed multiple damage steps on tooth, possibly related to the variation of the contact surface. Thus, the influence of the contact surface is studied by varying the contact depth on the tooth.
- Then, the influence of the hard and brittle layer on the tooth failure is studied. This external hard layer is usually formed to resist fatigue and avoid any surface peening due to contact. However, in terms of quasi-static failure, since it fails immediately it may induce high stress concentration at the crack tip. Consequently its influence on the tooth failure must be quantified.

III. 1 Test bench design

III. 1. 1 Technical specifications

Simplifications from the industrial static strength test were required together with a better control of the test. Testing only one tooth is the best solution to manage precisely the contact surface and the loading conditions.

The choice of studying fracture based on the contact of only one pinion tooth required the design of a flange-like tool. It is essential that the active part of this tool, the one in contact with the pinion, has exactly the same geometry as a flange tooth. It was decided to use a material harder and thicker than the CN layer, namely cemented 100C6, 910 HV, to make the test interpretation easier. In order to simplify the test, the relative displacement will be a straight translation, and not a circular one like in a real recliner, which would be too complicated to reproduce with conventional tension/compression testing machines.

Several tests would have to be performed on one pinion, in order to get comparable results with exactly the same material. For this reason, 2 teeth out of 3 are cut on the pinion to leave enough free-space for the tool movement (see **Fig.III.1**).

Displacements will have to be managed precisely in the 3 directions, i.e:

- the applied stroke measured as precisely as possible in the vertical direction;
- test bench as stiff as possible to have minimal spurious displacements in the two other directions.

The axial force (A in **Fig.III.2**) will be measured and compared to the numerical simulation.

33 mm

Fig.III.1: pinion used for tests, 2 teeth out of 3 are cut

// Pignon utilisé pour les tests, 2 dents sur 3 ont été usinées

Pignon

TOOL

\vec{m}

\vec{R}

θ

y

z

x

Fig.III.2: representative outline of the forces applied on the tooth

// bilan des forces sur une dent

Drawing and pictures of the test bench are presented in **Fig.III.3** (a, b, c, d). It is set up on a tensile test machine. Part 5 in **Fig.III.3** (c) is fixed to the (upward moving) lower jaws of the tensile test device. The shaft 4, on the same figure, is linked to the (fixed) upper jaws. A vertical displacement is applied to part 5 while part 4 is fixed. **Fig.III.3** (d) shows a zoom of the pinion (6) and the flange-like tool (7). The pinion is fixed to the bench with a hub (black arrow in **Fig.III.3** (b)). A key (black arrow 3 in **Fig.III.3** (b)) prevents pinion rotation, and finally a screw (2 in **Fig.III.3** (d)) enables to tighten up. The part 1 on **Fig.III.3** (a) with the screw tightened up maintains the pinion. Furthermore, the bottom of this part is in contact with part 5 to prevent the hub and the pinion from bending around the X axis due to the load. The position of the tooth with respect to the tool is adjustable in the (x, z) plane with 8 screws (4 are shown with bright blue arrows in **Fig.III.3** (c), the other four are hidden in this picture but are in symmetrical positions). These 8 horizontal screws are not blocked during tests; the assembly is fixed by 4 vertical screws (2 are shown with yellow arrows in **Fig.III.3** (c)) the other two are hidden by the bench). Three micrometric screws (2 are shown on **Fig.III.3** (c) with red arrows, the third one is behind the test bench) enable to determinate precisely the position of the tested tooth with respect to the tool.

60

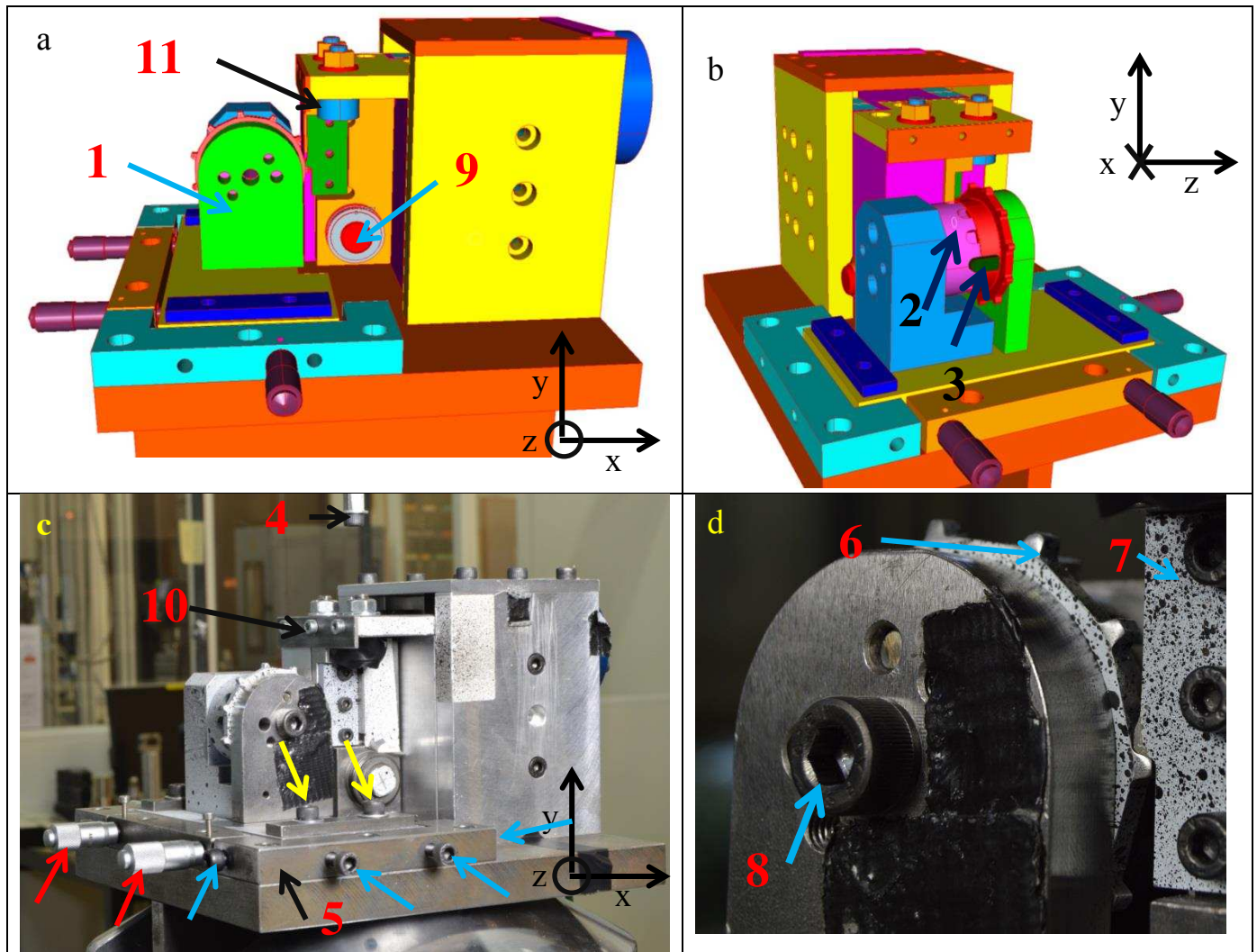


Fig.III.3: drawings of the test bench (a) front view, (b) side view; pictures of the test bench (c) set up on a tensile test machine and (d) focus on the active part

// schémas du banc d'essai (a) vue de face ; (b) vue de côté ; (c) photo du banc d'essai installé sur une machine de traction ; (d) zoom sur la partie active du montage

Finally, cameras can be set up in front of the test bench and focused on the tested tooth to monitor crack propagation.

III. 2 Semi-industrial test results and analysis

This second part introduces the results of the test campaign done with this specific bench. First trials were performed to check it was operational. Despite all the precautions taken to increase the bench stiffness, these first trials showed a non-negligible compliance in the test bench. This is why, real relative displacements of the tool in regard of the tooth have to be measured by a 3 Dimensions Digital Image Correlation system (3D DIC). VIC® system from Correlated Solutions will be used in the experimental work of this PhD. These real displacements will be used to apply exact boundary conditions into the numerical simulations of this test (Chapter 6).

Once the test methodology set up, a first test campaign was carried out to study the influence of the depth of contact on the failure process. It has been emphasized that in the post mortem recliners, the contact surface on the flange and pinion teeth varies, inducing distinct damage states.

III. 2. 1 Test bench set up and first trials

The test bench is set up on a MTS Landmark 250 tensile test machine. The 3D DIC VIC system is used with 2 AVT Pike F504B 4MP resolution cameras (see **Fig.III.4**). 50 mm lenses are used to focus on the active area. 3D DIC requires a painted spot pattern to enable displacements correlation. However, this speckle pattern prevents from observing the little cracks propagating through the external layer. The following compromise has been chosen: speckle pattern is painted on the pinion surface, but not on the tooth. This enables to correlate the displacements of the root tooth, without hiding the cracks initiation and propagation (see **Fig.III.5**). On the other hand, this does not allow any strain field analysis around cracks.



Fig.III.4: DIC system VIC® set up
in front of the test bench
// système de corrélation d'images 3D VIC® installé
devant le banc d'essai

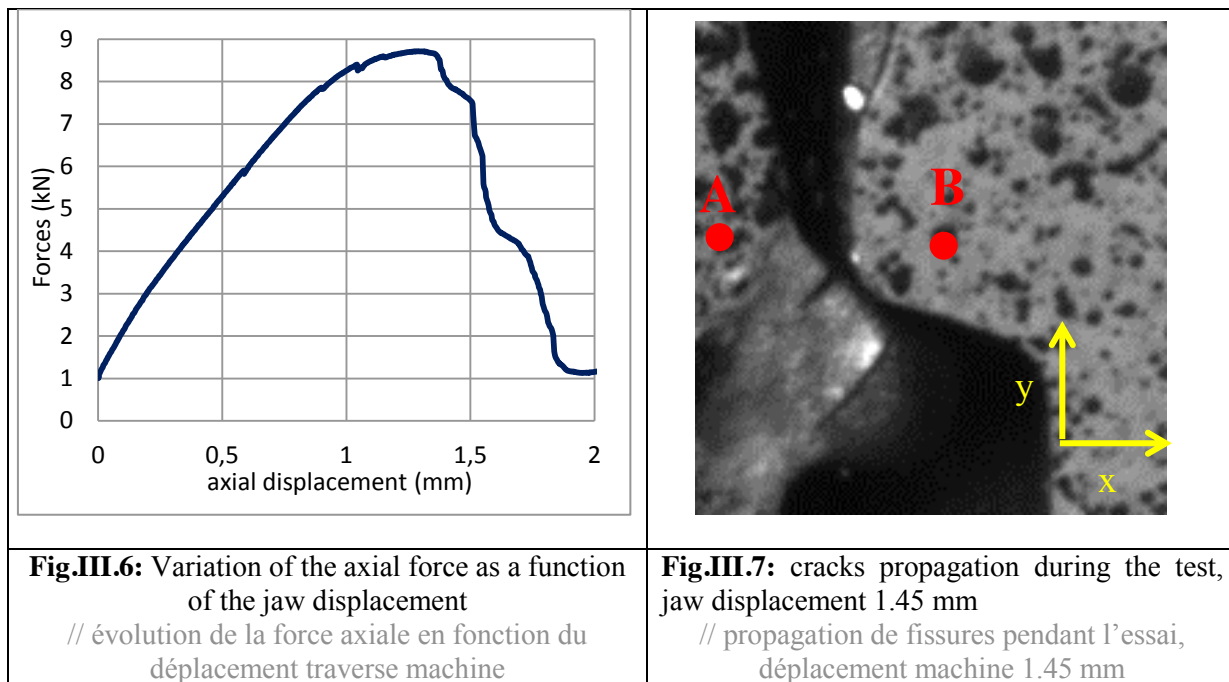


Fig.III.5: pinion painted before testing
// peinture appliquée sur le pignon avant
essais

Fig.III.6 plots the variation of the axial force as a function of the jaw axial displacement (along Y, **Fig.III.7**). **Fig.III.7** is a picture of the tested tooth at a displacement of 1.45 mm, just after the max load. One can see 2 cracks, one just under the contact with the tool (the short one), and the other, longer one, above the contact surface. Cracks propagation will be studied more precisely in the next 2 sections.

The curve in **Fig.III.6** is plotted as a function of the jaw displacement, so no correction is applied yet on the displacement. This value takes into account the relative tooth / tool displacement, as well as the tensile test machine and test bench compliances. Assessing displacements with DIC enables to account for the relative displacement only.

In **Fig.III.8** are plotted the displacements along X and Y of the 2 points A and B as a function of time (see in **Fig.III.7**). The relative displacements plotted in **Fig.III.9** are equal to the displacements of the pinion (point A) minus the tool displacements (point B).



A 3 mm ramp of displacement during 100 s is applied to break the tooth. This displacement is applied on the jaw. It is slow enough to be considered as a quasi-static loading. One can see on **Fig.III.9** that the relative displacement is not linear. Its slope is low within the first 30 s then increases exponentially until 65 s and finally becomes linear afterwards.

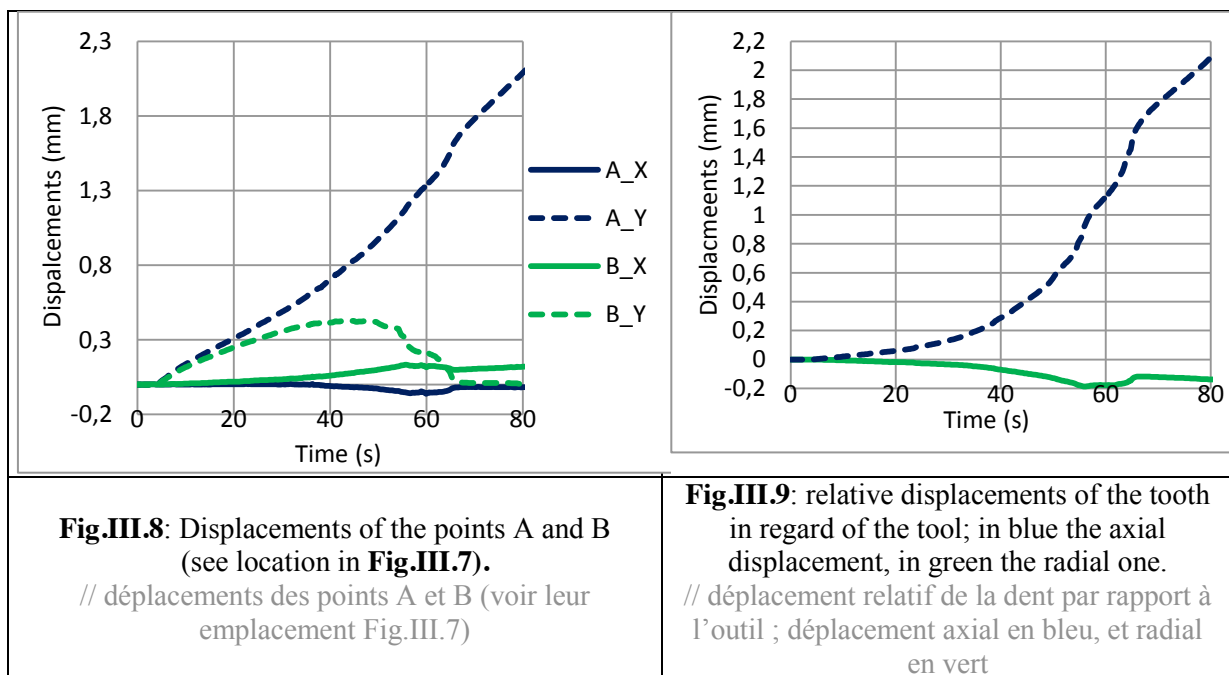
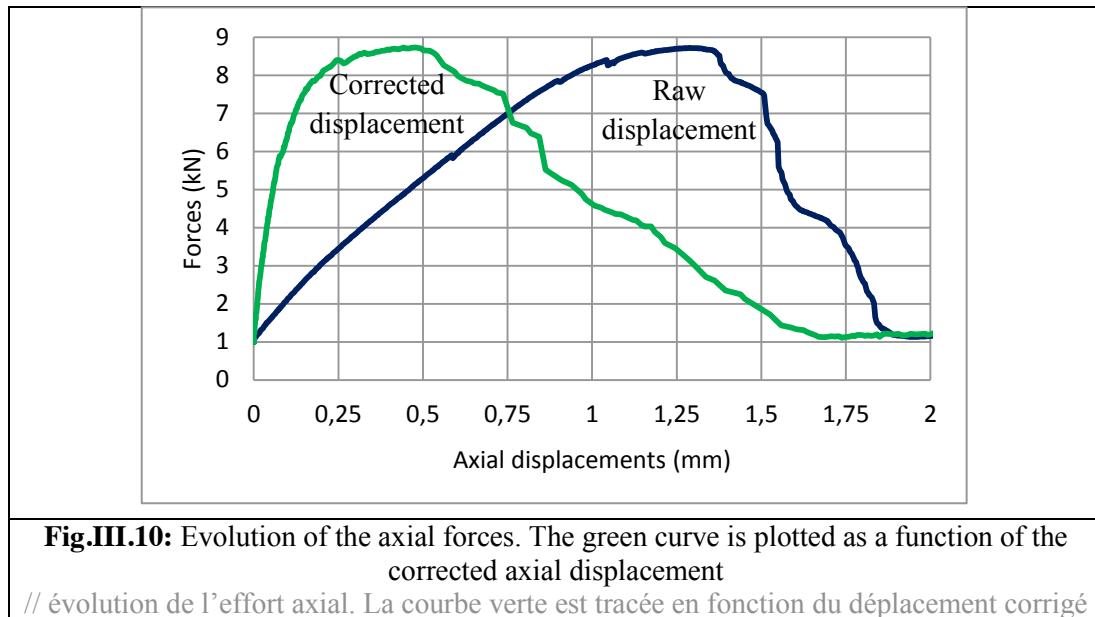


Fig.III.10 plots the variation of the forces as a function of the corrected relative displacements and the raw ones. The displacement at peak load decreases from 1.25 mm to 0.5 mm thanks to the DIC correction.



This correction will be mandatory to compare the experimental curves to the numerical simulations in which tool is assumed rigid. On the other hand, comparing the experimental data obtained from these tests does not require correcting the displacements. This process can be time consuming.

Because of the spurious displacements due to the bench compliances, real displacement will be assessed with VIC. However, the VIC-based correction procedure is too time-consuming to be performed systematically. It is of course indispensable, and has been used, when comparing with numerical simulation since tool and mounting compliance are not taken into account numerically. For the other purposes, reproducibility, influence of engagement depth, which are basically comparative, raw measurements are sufficient to conclude. **Fig.III.11** confirms that the same conclusions (here the good axial force reproducibility) can be drawn from the raw and the corrected curves (oscillations came from the filter used to link the tensile test machine to the computer running DIC software).

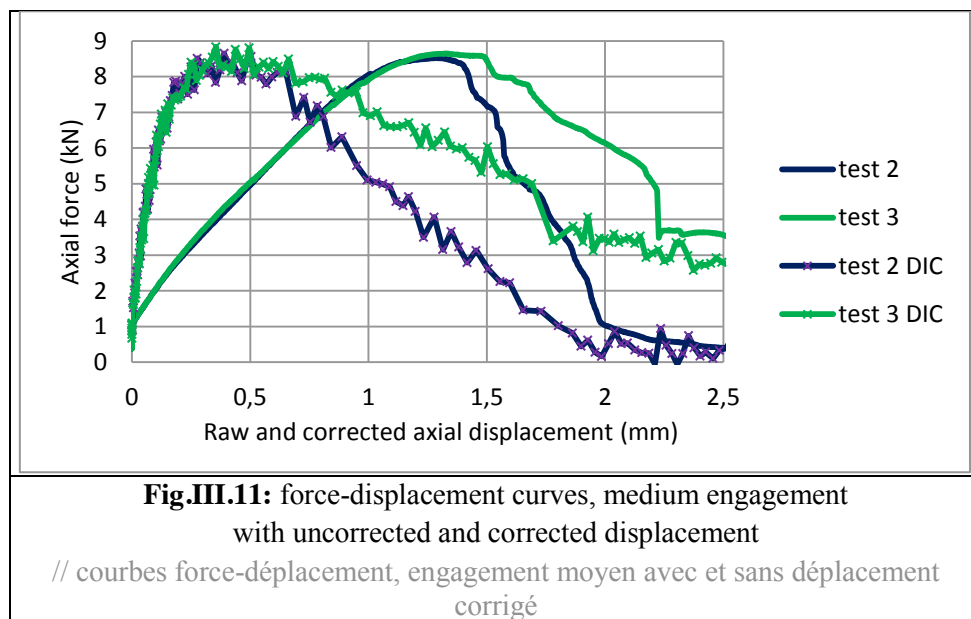


Fig.III.12 gathers the force displacement curves for the three engagement depths (tests were done on 3 pinions - see **Fig.III.15** for the definition of the engagement depth). It can be seen that scatter in terms

of maximum load is very low with almost no variation for each engagement. While load is increasing, the curves are superimposed: repeatability is good. The worst case is the medium engagement, where peak load ranges from 8.4 and 8.6 kN, so a scatter of 3%. Then, once the peak load is reached there is a slight scatter of the curves. The decrease is more progressive on some curves. It is explained by the fracture process slightly different, which induces different level of friction between the tool and the lower part of the tooth. However, for the high engagement cases, fracture is sudden on both tests.

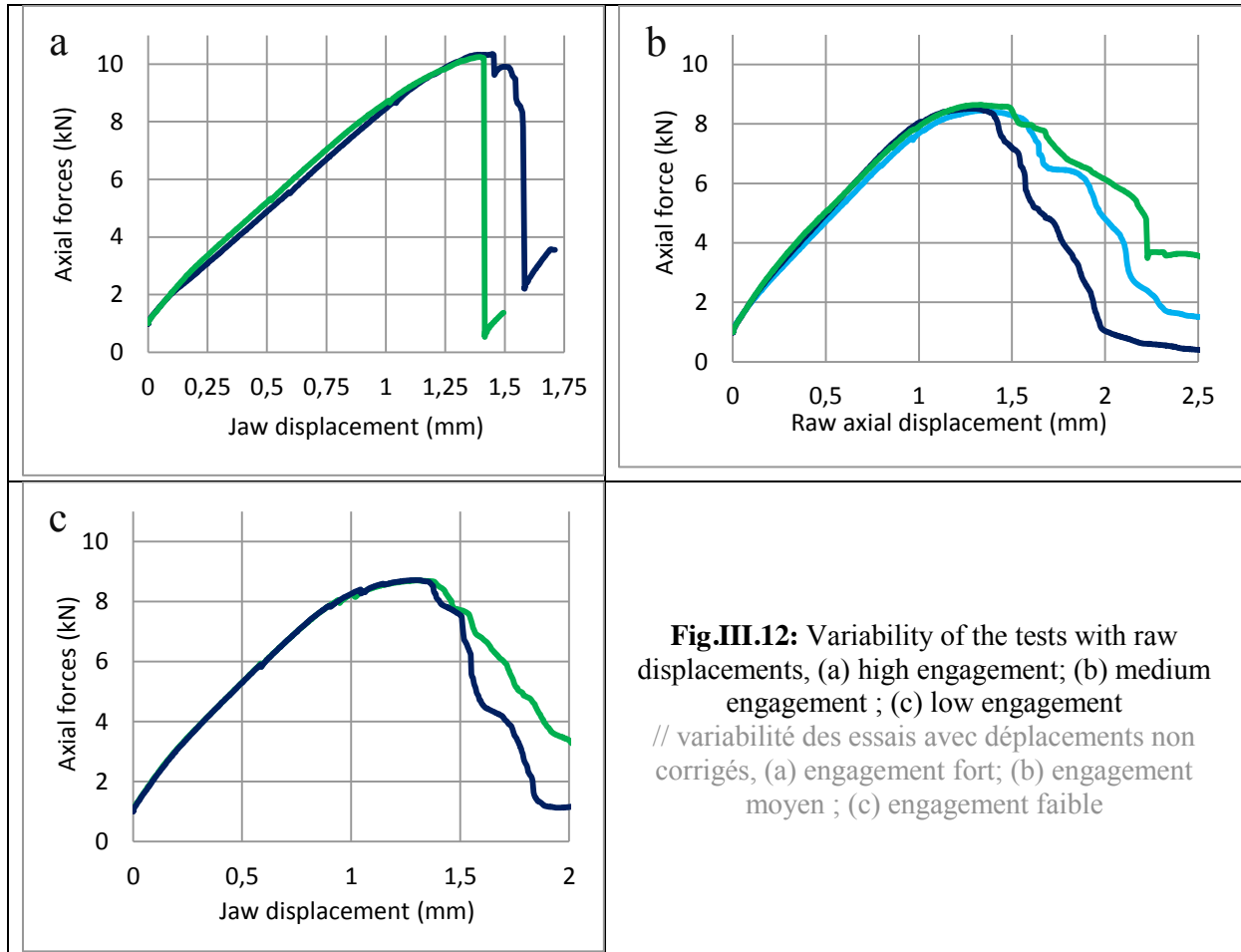


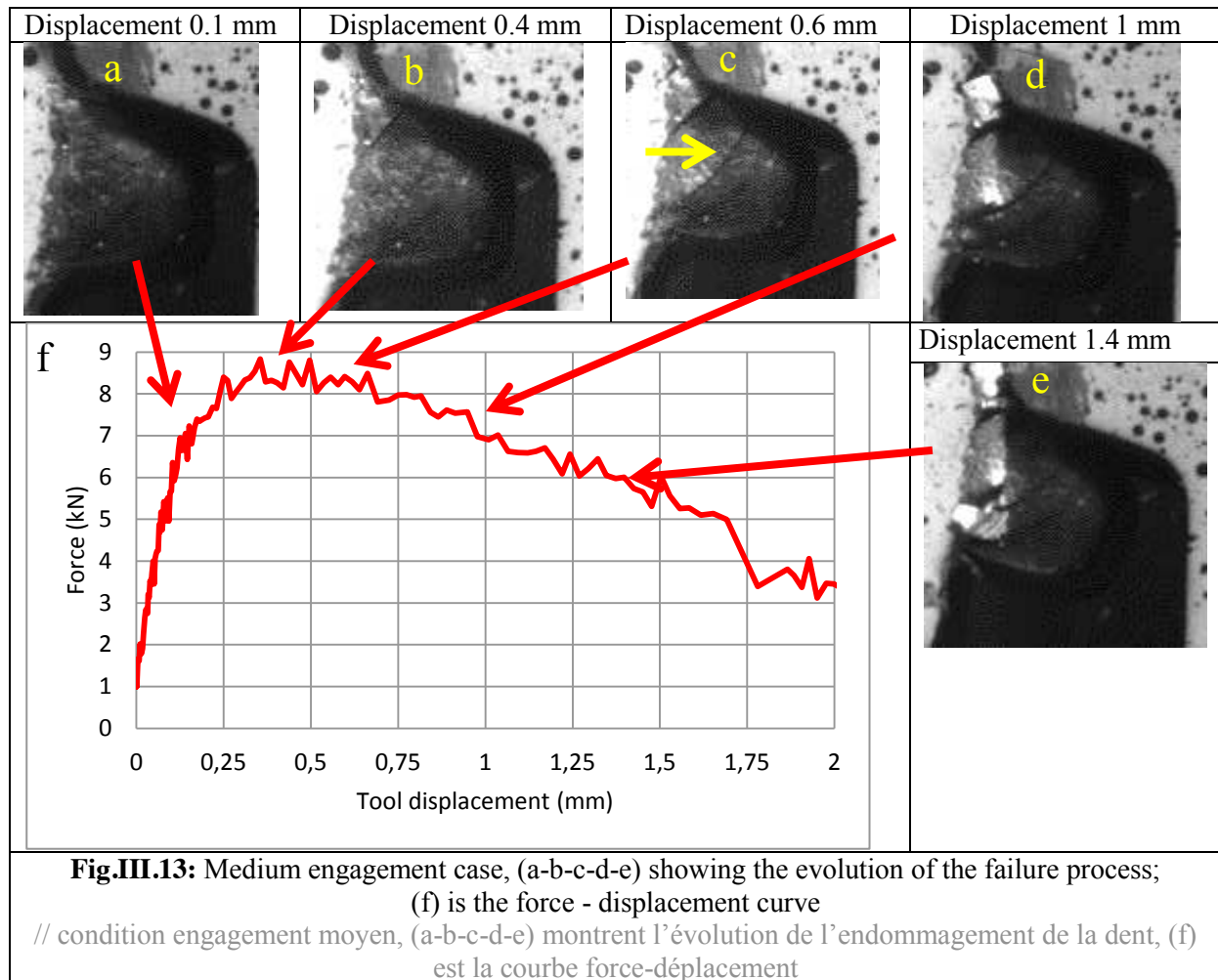
Fig.III.13 correlates the failure process and the force-displacement curve. The failure process analysis is discussed in III. 2. 2. This was one of the main technical specifications for the test bench: in situ observations while teeth are being tested.

Furthermore, since DIC is used only to correlate the displacements, the quality of the paint pattern does not matter. Calculating the strain would require a much better resolution; for instance, [K. Wang & Wierzbicki, 2015] use an air brush to get a much finer pattern.

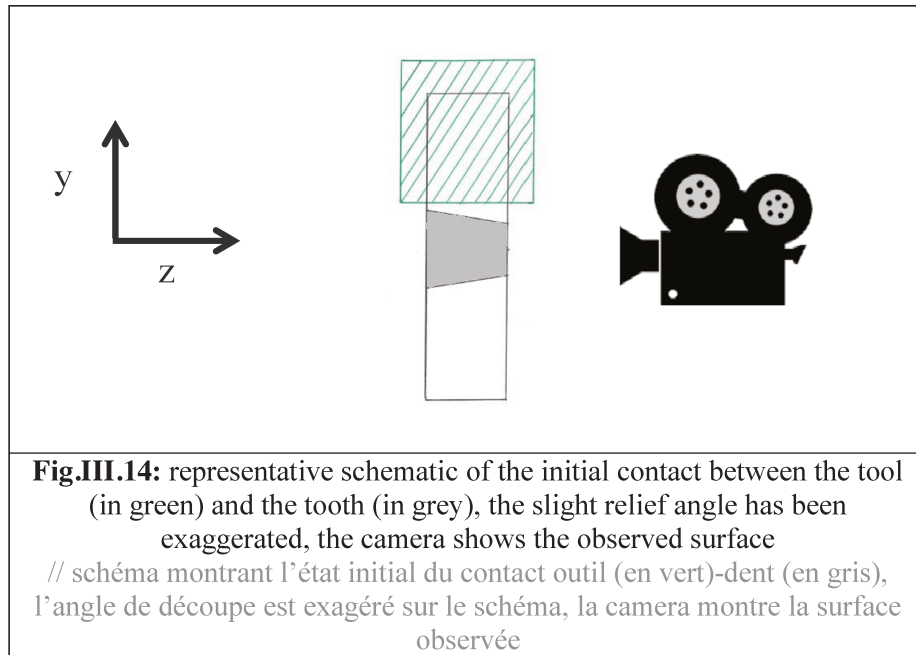
Two other points require attention:

- Because of the design of the test bench, cameras are not perpendicular to the tooth plane.
- Furthermore, tool thickness is 5 mm by design, instead of 3.5 mm for the pinion. This was decided to ensure contact on the whole tooth surface in the Z direction. A tool having the same thickness as the tooth would have brought some side effects, with deformation and failure modes such as **Fig.I.5** (c), which we are trying to avoid here. Adjusting the position of the tooth in regard of the tool would have been more difficult.

These two features may distort the vision of the engagement. Moreover, the contact between the tool and the tooth is not yet on the whole section in the Z direction at the beginning of the test, because of a slight relief angle on the pinion due to the blanking process (which is the last manufacturing step before CN treatment). Thus, first contact occurs on the side opposite to the one visible in the pictures, and then extends to the whole tooth width as the tool loads the contact. **Fig.III.14** is a representative scheme of the initial tooth - tool contact (in green). The relief angle has been exaggerated on the figure to be easier to see. The left side, where contact occurs first, is the side hidden by the bench. Thus the observed side is the one where contact occurs later. Obviously, because the angle is very low, contact is done on the whole section very quickly.



The tool is made out of cemented 100C6. Hardness has been checked and it is harder than the carbonitrided components. The shape of the active area was checked after the tests with a profile projector. It was the same geometry as the initial one, meaning it did not undergo any noticeable plastic deformation during testing. It undergoes only elastic deformation.

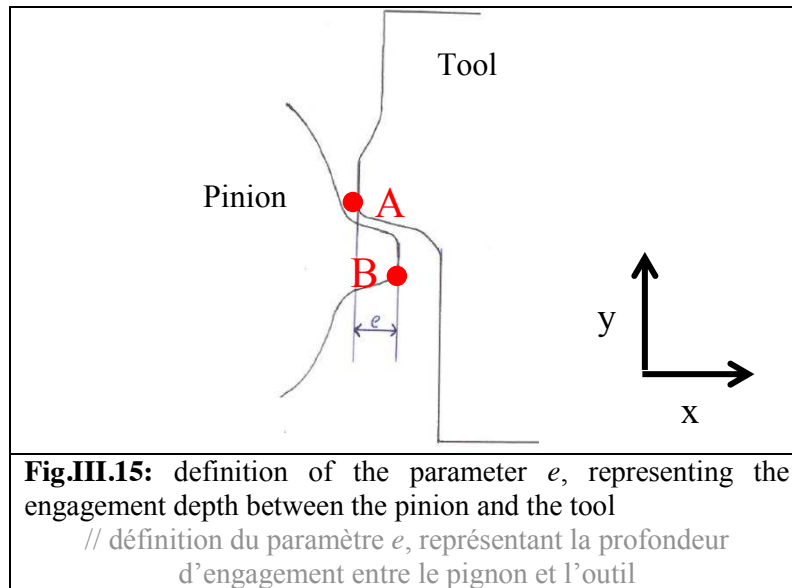


III. 2. 2 Engagement depth study

The influence of the engagement depth (distance e in **Fig.III.15**) is a key point in the recliners fracture study. Indeed, there is never contact on the whole tooth surface between the pinion and the flange. Depending on the depth of engagement, the fracture kinematics and stress state will vary so that the fracture criterion must be general enough to cope with all situations encountered.

A pinion tooth is 2.6 mm deep; varying e from 2.0 mm until 2.4 mm is a range wide enough to observe distinct behaviors. A lower engagement would induce more bending on the device and this behavior was not observed in the failed recliners study. This bending would introduce more friction between the pinion and the tool and add another unknown. These tests are carried out without any lubricant due to the necessary observation of the surface paint. Indeed, lubricant can leak on the painted surfaces preventing from accurate DIC correlation. One must keep in mind there is lubricant in the real recliner and it can change the lateral friction and thus it may influence on the fracture process.

Particular attention must be paid to the method used to measure this engagement: it must be precise and easily reproducible. Zero value on the micrometric screws (see **Fig.III.3** (c)) was set by putting dots A and B (see **Fig.III.15**) in contact. The former belongs to the tool, the latter to the pinion. In that situation, there is no engagement. Then, pinions were moved toward the tool; the distance was checked by the micrometric screws. This ensures good precision. Three tests with the same engagement were done before setting up another condition.

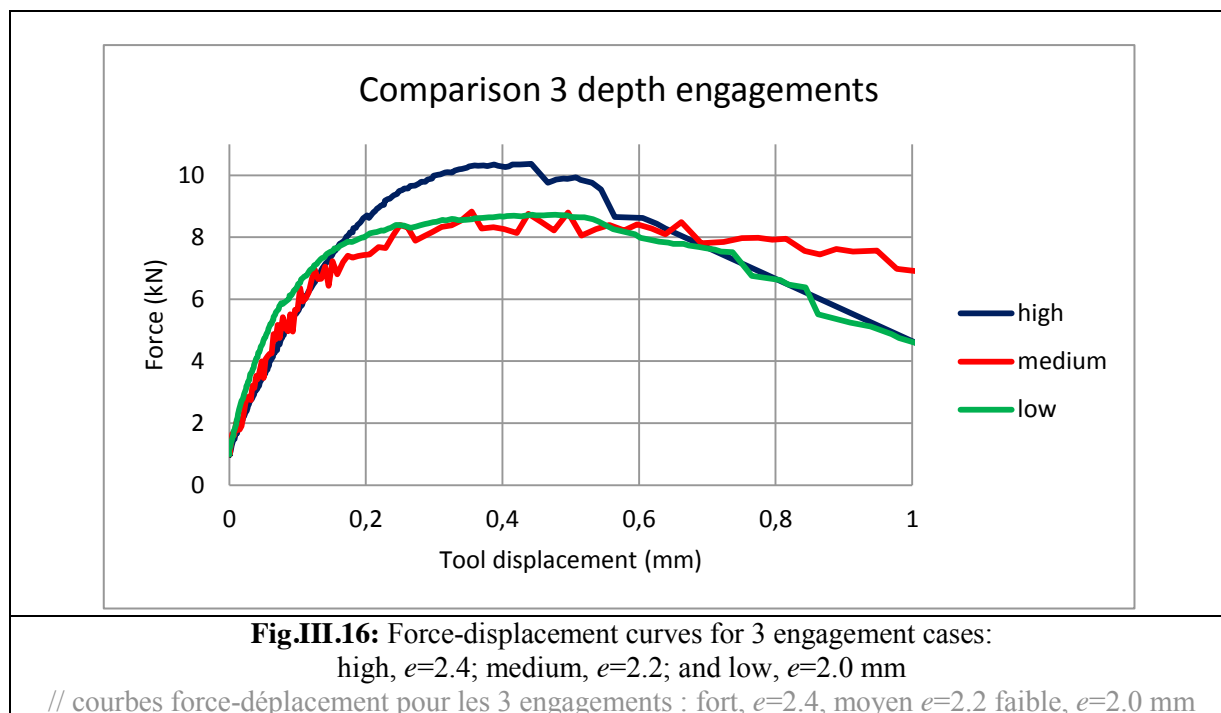


III. 2. 2. a Tooth strength

Recliners are designed to sustain a peak torque; this is directly linked to the maximum load a tooth can undergo before failure. Studying the influence of the engagement on this maximum load can help the designers to modify the geometry and the carbonitriding treatment to improve the peak torque. Three engagement conditions were studied: high, medium and low. Respectively, the depth of contact was 2.4, 2.2 and 2.0 mm. The choice has been made not to study lower engagements because it would induce more friction issues between the tooth and the tool. Tests are done three times on three pinions. The aim is to have the key (part 3 on **Fig.III.3** (b)) located at the same place regarding the tested tooth for one depth engagement tested.

Fig.III.16 plots the evolution of the force-displacement curves for the three engagements; a representative curve is picked for each engagement. The load sustained by the tooth with the highest engagement is higher than the other two. The difference is about 20 % whereas there is no noticeable discrepancy between the lowest two engagements. This is unexpected, but the engagement was checked and accurate for both configurations. In terms of displacement, the drop is more abrupt in the case with the highest engagement. It appears sooner as well, around a displacement of 0.45 mm. The decrease is slower for the other two cases; the load barely decreases for the medium case. This curve is actually that of test 3 on **Fig.III.11**. One notices also that the low engagement curve is stiffer in the elastic part than the other curves (from 1kN until 7kN). This is unexpected and difficult to explain. Exactly the same method was used to assess the real displacement. The medium curve has some instability due to the acquisition box. This instability issue was resolved on the other engagements by changing the filter enabling to smooth the data.

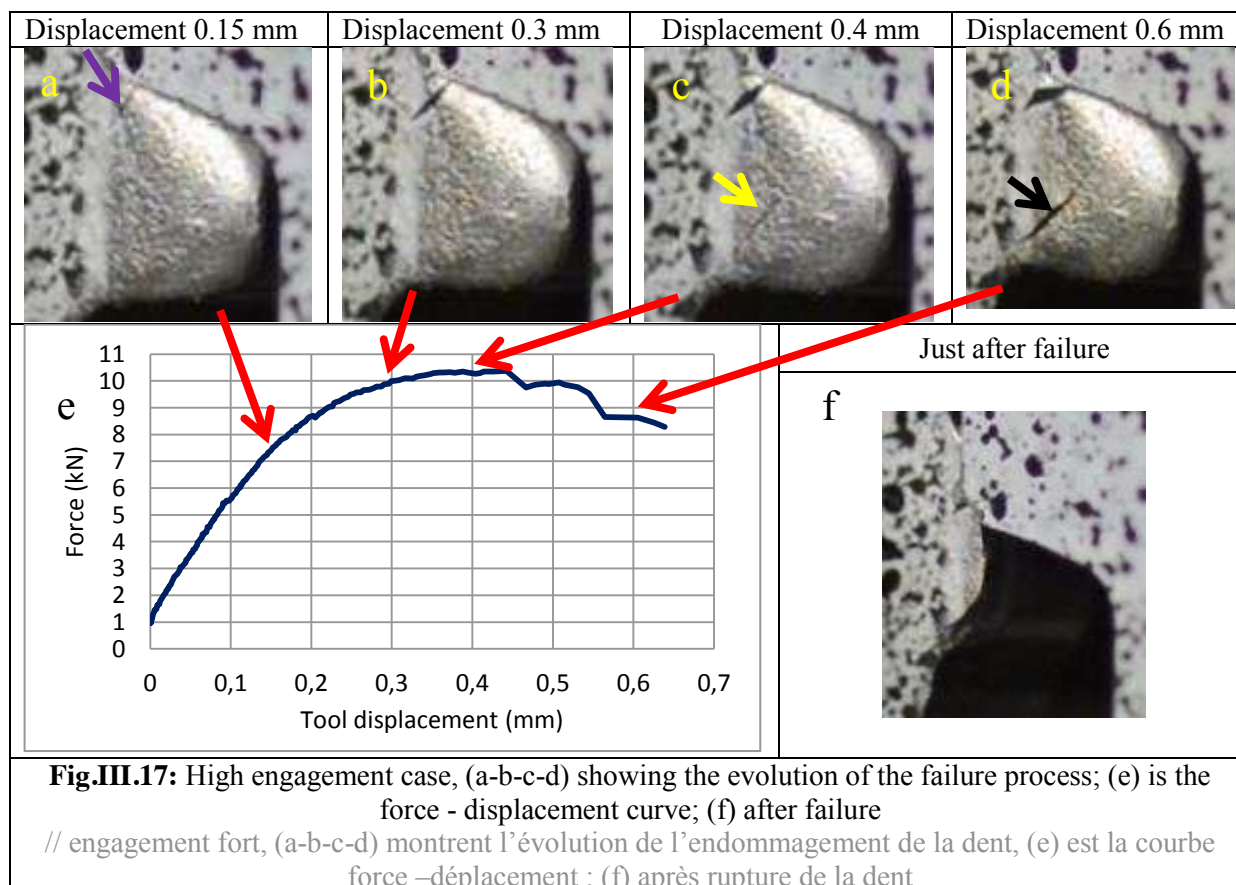
In order to get a better understanding of the influence of the engagement depth, the failure process will now be analyzed.



III. 2. 2. b Tooth failure process

Fig.III.17, Fig.III.18 and Fig.III.19 illustrate the fracture process at different steps for the three engagements.

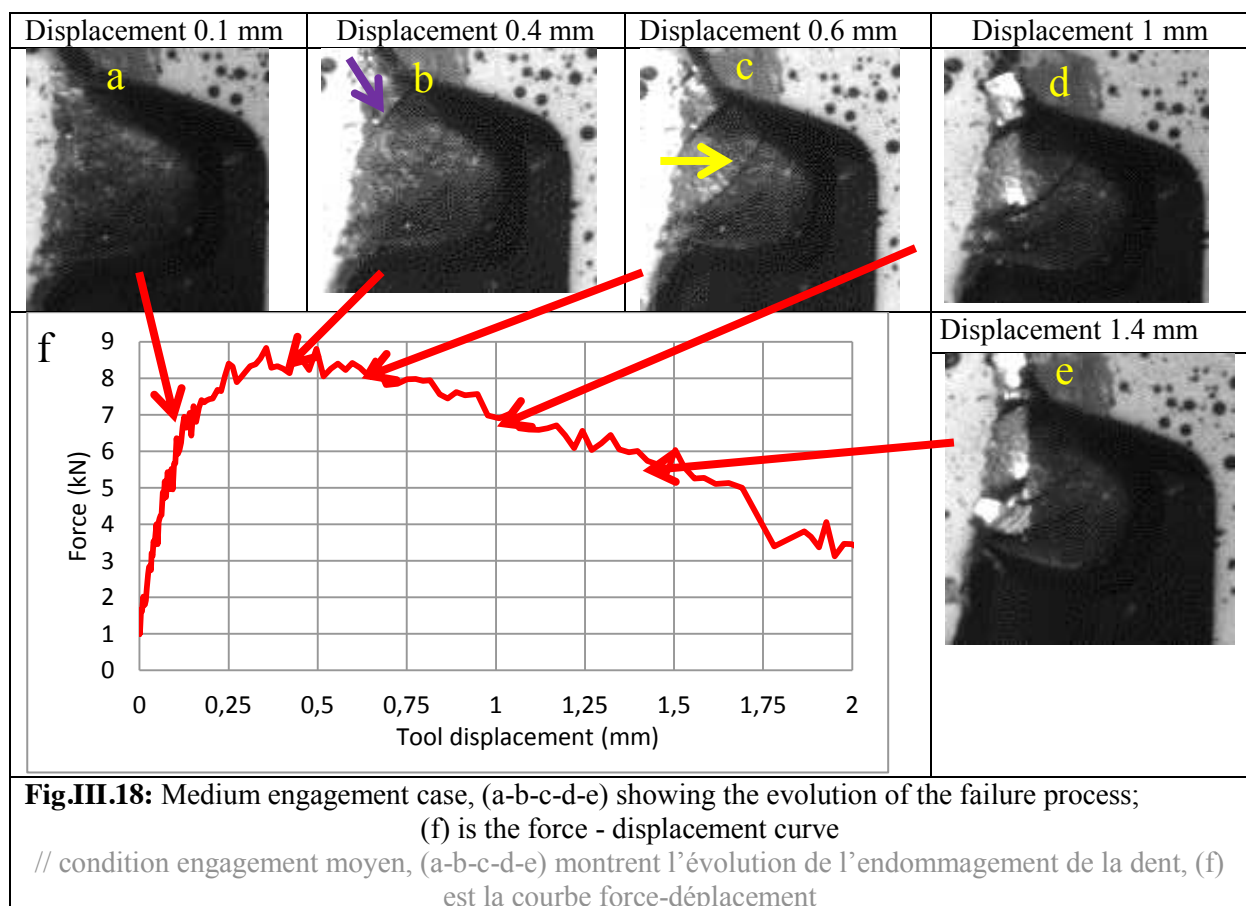
❖ High engagement



First, there is a crack just below the contact surface with the tool (see purple arrow on **Fig.III.17 (a)**). Indeed, when contact is occurring on the tooth, the area just below is submitted to a strong tensile stress state. Interrupted tests were performed to better illustrate the crack propagation steps and results are shown below. As the load is increasing and the tooth bends more and more, the core material is being plastically deformed. Its ductility is higher than the external layer, which fails with several cracks at the surface. Some of these cracks are shown by a yellow arrow (**Fig.III.17 (c)**). One notices the crack shown by the yellow arrow does not initiate at the contact surface with the tool. This crack is likely to be due to the difference of behavior between the core material and the external layer. Indeed, the former can undergo a certain amount of plastic deformation, but not the latter. Then final failure occurs with a shear crack as shown by a blue arrow on **Fig.III.19 (e)**.

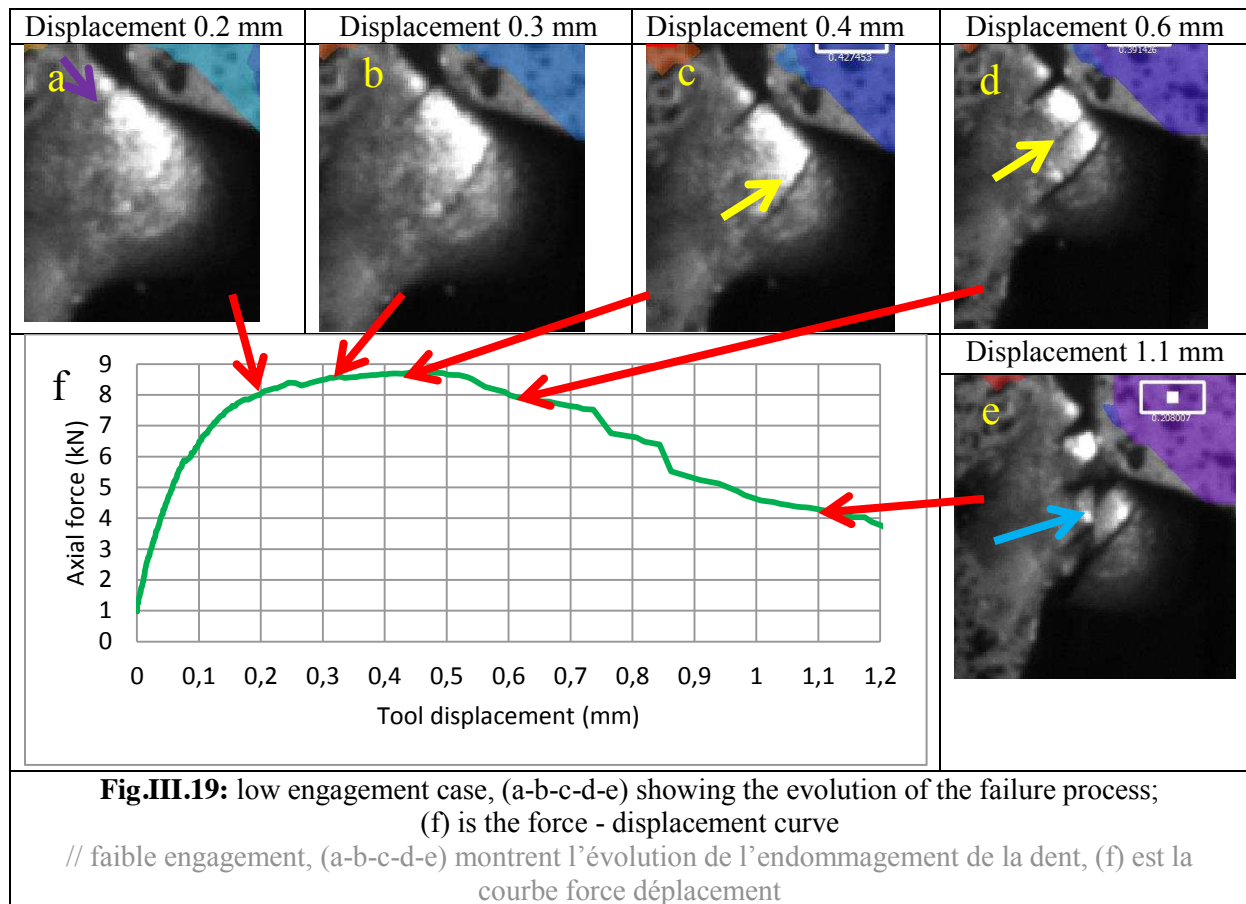
Fracture processes for the medium and low engagement are now being detailed. They are some common points with the high engagement.

❖ Medium engagement



As seen previously, there is a crack just below the contact surface with the tool (see purple arrow on **Fig.III.18 (b)**) because of strong tensile stress state. As the load is increasing and the tooth bends more and more, the core material is being plastically deformed and the external layer fails in several areas (see yellow arrow (**Fig.III.18 (c)**)). Then final failure occurs with the shear crack.

❖ Low engagement case



The crack just below the contact surface with the tool is being open (see purple arrow on **Fig.III.19** (a)) like on the others cases. Then external layer is failing (see yellow arrow on **Fig.III.19** (c-d)) as the tooth is being pushed by the tooth. Then final failure occurs with a shear crack as shown by a blue arrow on **Fig.III.19** (e).

❖ Comparison between the three engagements

Fig.III.20 (a) is a microscopic observation of a tooth after a loading of about 8 kN, depth of engagement is "medium". A purple arrow shows the first crack initiating well below the contact surface with the tool and propagating along the normal to the surface. The green one indicates the direction of loading. On **Fig.III.20** (b) a slight jump in the force curve around 6 kN (blue circle) can be seen. This same pop-in can be observed on **Fig.III.17** (f) and **Fig.III.19** (f) respectively at 5.5 and 6 kN. This pop-in corresponds to the first crack initiation. As the load increases, the tooth bends and opens the crack. It propagates at the surface of the tooth, through the whole thickness of the external brittle layer and is likely stopped in the transition layer.

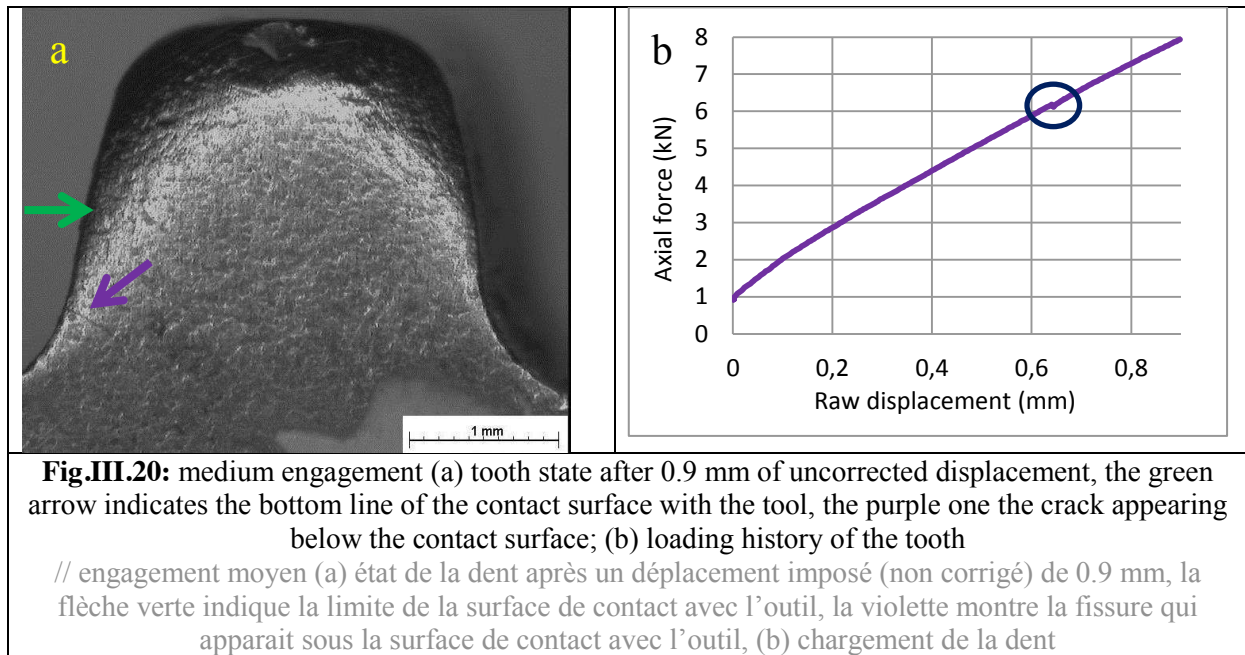


Fig.III.21 (a) illustrates a tooth at a more advanced state of damage, it has been submitted to a load of 9 kN, engagement is again "medium". The purple arrow shows the crack that propagates and stops after growing until 1.2 mm. **Fig.III.21** (c) is a cut section of the tooth (in the XY plane) to see the depth of this first crack. The tooth was cut in its middle along a plane parallel to the observed surface. Thus the depth observed corresponds to the crack propagating toward the core material. The depth is about 0.32 mm, the width about 0.18 mm. The crack propagated through the whole CN layer, and stopped in the transition area. On **Fig.III.21** (a), the yellow arrow shows the crack initiated at the contact surface and propagated along a curved path. On the contrary, the crack shown by the yellow arrow on **Fig.III.17** (c) does not initiate at the contact surface with the tool. This crack is likely to be due to the difference of behavior between the core material and the external layer. Indeed, the former can undergo a certain amount of plastic deformation, but not the latter. **Fig.III.21** (b) is a cut section of the tooth (in the YZ plane) along the yellow line on **Fig.III.21** (a). It enables to see the depth of the external crack: it is about 0.24 mm. Thus the crack propagates through the external CN layer and is quickly stopped in the transition area, where ductility is higher. The tooth is progressively sheared as the load is increasing.

Fig.III.22 illustrates the stress state that could induce the formation of this crack. The green arrows indicate the shearing of the core material due to the tool displacement. This shearing induces a tensile stress state with an angle of 45° between the 2 directions. Finally, this induces a crack opening perpendicular to the 1st principal stress. Thus, in black is shown the direction of the crack propagation. The curved path of the crack (see **Fig.III.21** (a)) is perpendicular to the tensile stress state created by the shearing during loading.

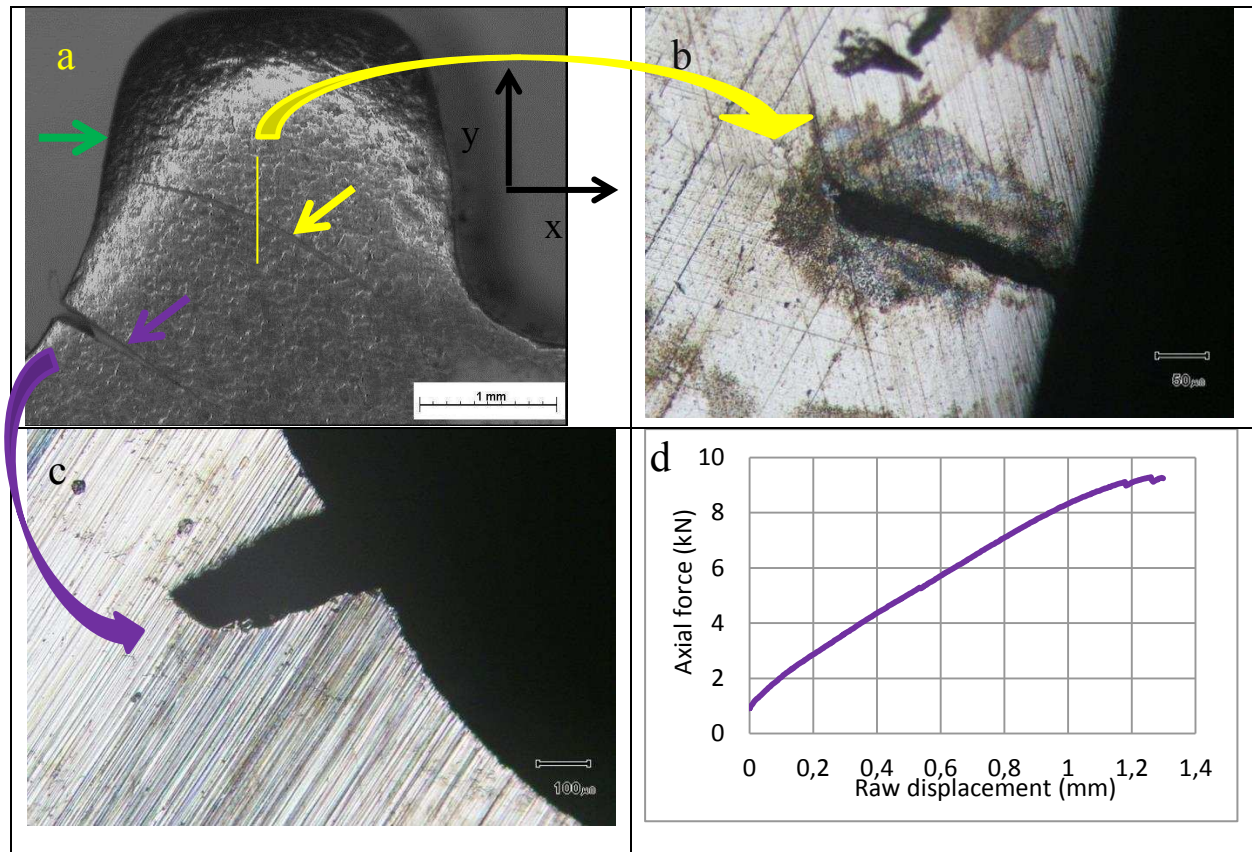


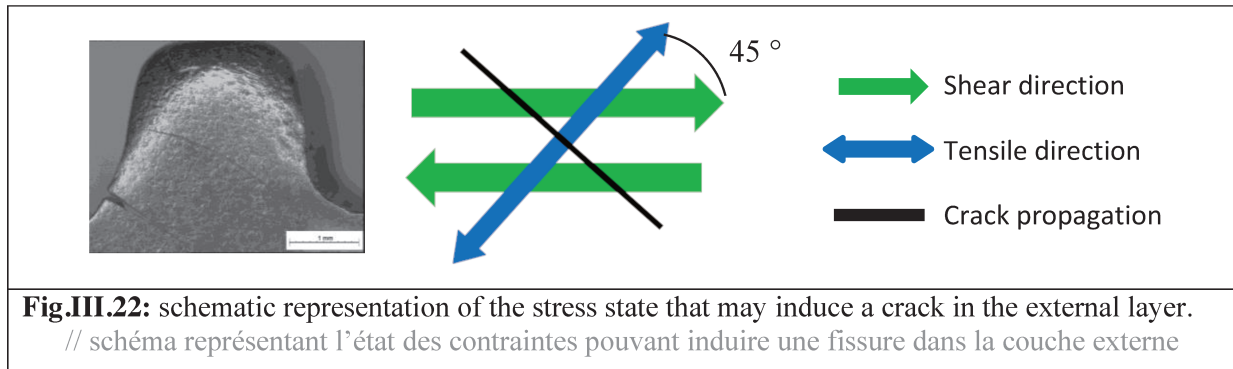
Fig.III.21: medium engagement (a) tooth state after 1.3 mm of uncorrected displacement, the green arrow indicates the bottom line of the contact surface with the tool, the purple one the crack appearing below the contact surface; (b) cut and polished section to see the crack in the root (shown by the purple arrow); (c) loading history of the tooth; (d) cut (along the yellow line) and polished section of the tooth to zoom on the crack shown by the yellow area

// engagement moyen (a) état de la dent après un déplacement imposé de 1.3 mm, la flèche verte indique la limite inférieure de la surface de contact avec l'outil, la violette montre la fissure qui apparaît sous la surface de contact avec l'outil ; (b) section coupée et polie de la dent au niveau de la fissure en fond de dent (montrée par la flèche violette) (c) chargement de la dent ; (d) section de la dent coupée (selon la ligne jaune) pour voir la profondeur de la fissure

Fig.III.23 (a) illustrates the tooth after a loading history described in **Fig.III.23** (e). Damage is very advanced, the tooth is sustaining just 4 kN, the massive load drop has already occurred. The CN layer failed completely along the shear crack. **Fig.III.23** (b) is a cut section of the tooth. A layer about 1 mm thick has been removed by polishing the tooth. Thus, the core material is observed. This picture has to be observed with the pictures **Fig.III.23** (c and d), which are zoomed views of respectively the red and yellow circles. The first micrograph illustrates the propagation of the shear crack inside the material. It propagates in a straight line, parallel to the movement of the tool. The second picture shows the core material on the opposite side where the crack did not propagate yet; there is a section of 0.6 mm width sustaining the load. One can wonder if the polishing process may have covered part of the crack. This is possible, however the upper part of the tooth is still strongly attached to the lower part (one can manipulate by hands the tooth without breaking it). So maybe a part of the crack, where the opening is thin, was covered by the polishing, but the tooth is not broken in two parts. It is however difficult to say that the tooth still sustains the whole 4 kN because a part of the axial loading is due to the friction between the tool and the second lip of the shear crack. These 4 pictures illustrate well the displacement of the upper part of the tooth. Deformations are localized around the main shear crack, the CN layer has failed on its whole section.

One can easily guess that before the test the 2 yellow dots (**Fig.III.23 (b)**) were on the same vertical line; the upper part moved about 0.7 mm toward the right side. However, two other cracks are seen on the tooth, shown by the green arrows on **Fig.III.23 (b)**. Those may be due to tensile stress, which will be confirmed by the numerical simulations.

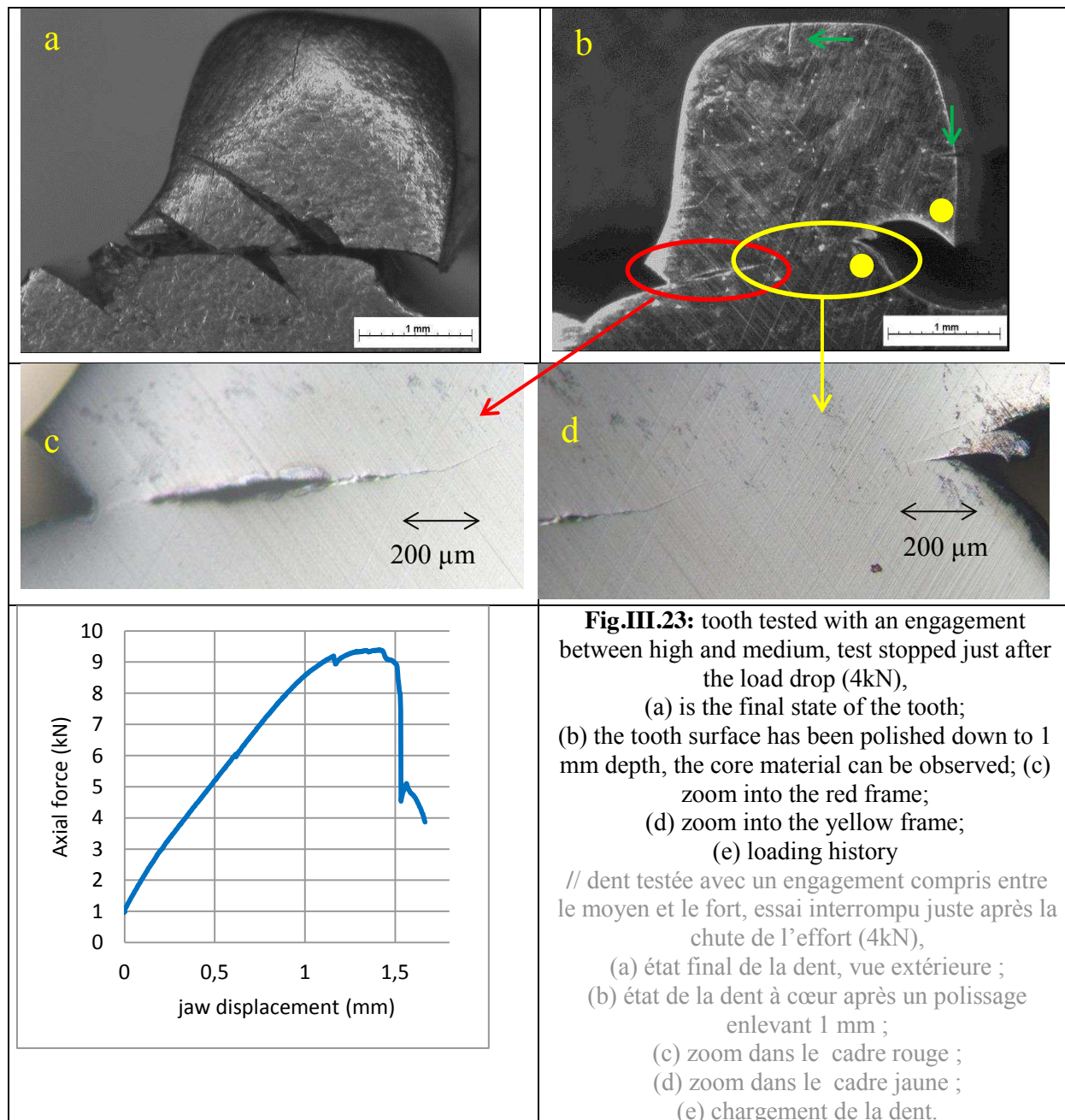
For the high engagement case, this “killer” crack initiates where the first crack initiated. For the other cases, the shear crack is well above the first crack. If one looks at the fracture process of the three cases, there are two cracks for the highest engagement (**Fig.III.17**), three for the others (**Fig.III.18** and **Fig.III.19**). The tooth bending is more important in the lower engagement case, which can explain the additional crack.



III. 2. 2. c Discussion

As expected, the case with the highest engagement has the highest peak load. However, its fracture process is more sudden. Even though the peak load appears at the same displacement as the other case, complete failure occurs at 0.6 mm displacement. **Fig.III.17 (d)** is actually the last picture taken with the VIC ® cameras. The damaged area is localized close to the tooth root. A first crack opens just below the contact surface with the tool. Another superficial crack opens on the observed surface due to strong tensile stresses. Those are induced by the shearing of the core material. Indeed, the final crack finally initiates where the first crack opened, and propagates through the tooth in a straight line. It is cutting the second superficial crack in its middle. With this engagement, no bending of the tooth is allowed. Indeed, the fact that contact is close to the root makes the pinion more robust.

The cases with lower engagements have a higher displacement to fracture. Furthermore, the process is less abrupt, more progressive; the tool with a medium engagement still sustains 7 kN after a displacement of 1 mm. However, it is difficult to know if the force is due to the tooth itself, which still resists the load, or to the friction between the two lips of the shear crack. In any case, the external layer is much more damaged with these two cases. Because the contact with the tool is farther from the root, the tooth can bend a little. The core material can undergo this deformation, but not the external layer, which fails immediately.



As expected, the peak load is lower for these 2 engagements. The tooth section available to carry the load is lower when the engagement is decreasing. On the other hand the maximum load of the medium and lower cases are similar. Since the depth of engagement has been checked by 3D DIC, it should be accurate. Numerical simulations of the semi-industrial tests carried out in chapter 6 will refute this behavior. Question about the variability between two pinions can be raised and could explain this result. Depending on the position of the tooth inside the carbonitriding treatment oven, carbon and nitrogen content could be different and induce different material properties afterwards.

III. 2. 3 Influence of the CN layer on the tooth failure

As seen in the last section, the CN layer fails in multiple areas due to its brittle behavior. Thus the load is mainly sustained by the core material. The cracks initiating in the external layer create locally areas with a high stress concentration (thus high stress intensity factors), which could be the initiation locations of major cracks in the core material. Indeed, for the higher engagement case, the final crack in the core is initiating where the first one opened in the CN layer. It is thus interesting to check the

influence of the CN layer on the tooth resistance, comparing pinions with and without CN layer. As far as possible, they should be identical in all other aspects. The pinions tested here received only the heat treatment; diffusion of Carbon and Nitrogen atoms has been prevented by the application of a specific protecting paint. With this process, all the specimens tested and presented in this manuscript were treated at the same time, reducing drastically variability. More details on the process are given in Appendix. III.1. The obtained material properties are very similar to the core material ones, except for a thin external layer of 0.1 mm, which presents a lower hardness, probably due to partial decarburization.

III. 2. 3. a Influence on the strength

Teeth were tested with exactly the same depth of engagement as in the previous part. From now on, the force - displacement curves for tooth with only the core material (CMO, Core Material Only) will be represented with cross markers while CNed components (FCN, Fully Carbo-Nitrided) will have no marker. On **Fig.III.24** are plotted the evolution of the axial forces for CMO teeth. Three representative curves are chosen, and plotted as a function of the corrected displacement. The higher the engagement, the higher the max load. It is more logical than the FCN cases. One can see a load drop on the 3 curves in the 0.15 – 0.2 mm displacement range, respectively at 8.5, 8 and 6.9 kN for the high, medium and low engagement. This corresponds to the opening of a superficial crack in the tooth root.

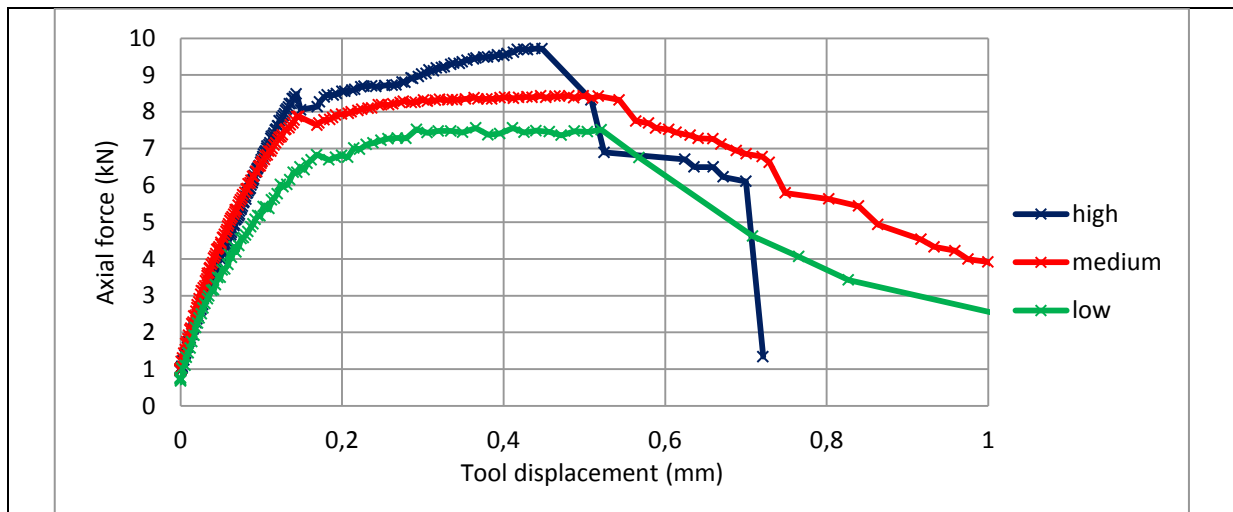


Fig.III.24: Force-displacement curves for 3 engagement cases, core material only (CMO):
high, $e=2.4$; medium, $e=2.2$; and low, $e=2.0$ mm

// courbes force-déplacement pour 3 engagements, matériau de cœur seulement : fort, $e=2.4$; moyen, $e=2.2$; et faible, $e=2.0$ mm

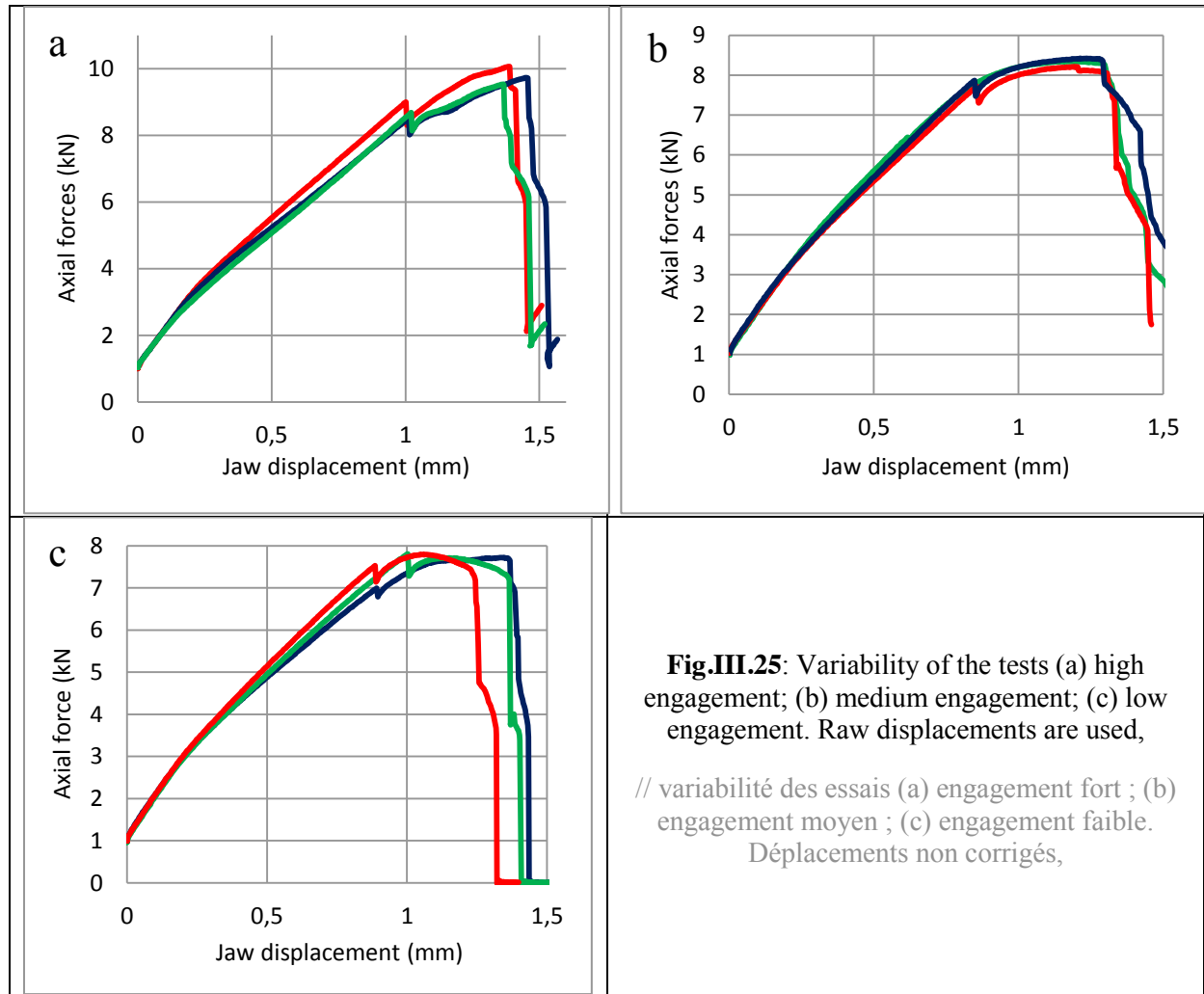
Table.III.1 gathers the peak loads for the three cases of each engagement. Repeatability is good with a maximum of 5% scatter for the high engagement. There is a slight variability on the displacement where load starts to decrease. However, it is quite abrupt on the three tests for the high engagement, and more progressive for the others. So there is no apparent change of fracture mechanism.

max load (kN)	High	Medium	Low
test 1	10	8.4	7.78
test 2	9.7	8.35	7.77
test 3	9.5	8.2	7.7
average	9.75	8.32	7.75

Table.III.1: max loads for the three engagements, and average value

// Efforts max pour les 3 engagements et valeurs moyennes

Fig.III.25 is the repeatability study for the three engagements. There is no cross markers on these curves to make reading easier. For each case, the dark blue curve is the one chosen as representative for the engagement. One can see the difference between the three curves is low until to the first little load drop (respectively at 1, 0.85 and 0.9 mm for the high, medium and low engagement) , except for the low engagement – green curve where the load drop occurs at somewhat larger uncorrected displacement.



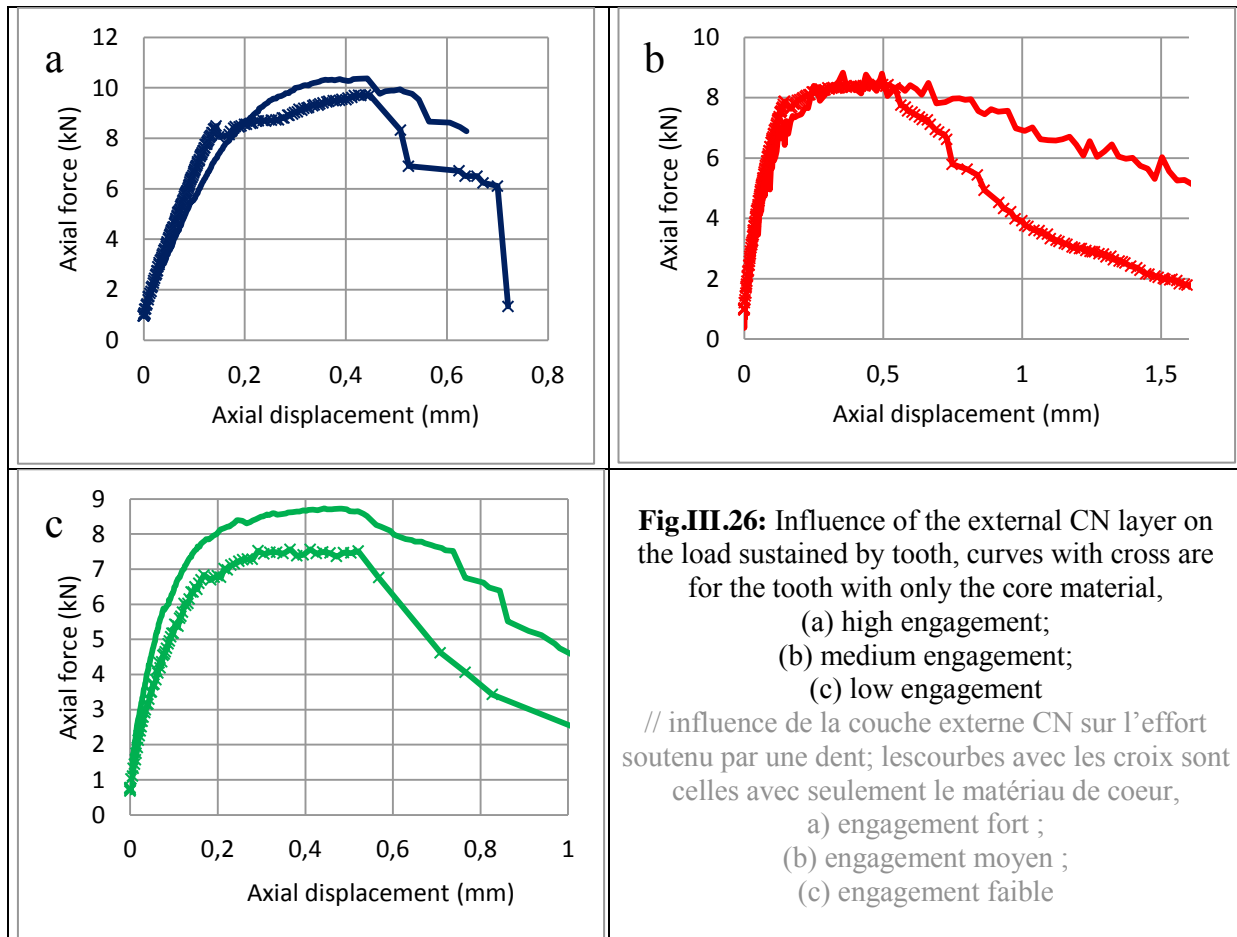
III. 2. 3. b Influence on the tooth failure process

❖ Failure process study

Fig.III.26 plots separately the force - displacement curves for the three engagements, superimposing curves with and without the external CN layer. Only the lower engagement really shows a higher load (by 16 %) for the CN pinion. In the other cases, the difference is not obvious, even negligible for the medium engagement case. It is in the range of the experimental scatter. The same remark can be done for the displacement at peak load: the external layer does not have an obvious influence on it. One can even notice that FCN samples are less stiff than CMO for the high and medium engagement cases. This is unexpected, but can be explained by the crack occurring below the contact surface with the tool. It occurs very soon for the cases with the complete CN component, (before 0.1 mm

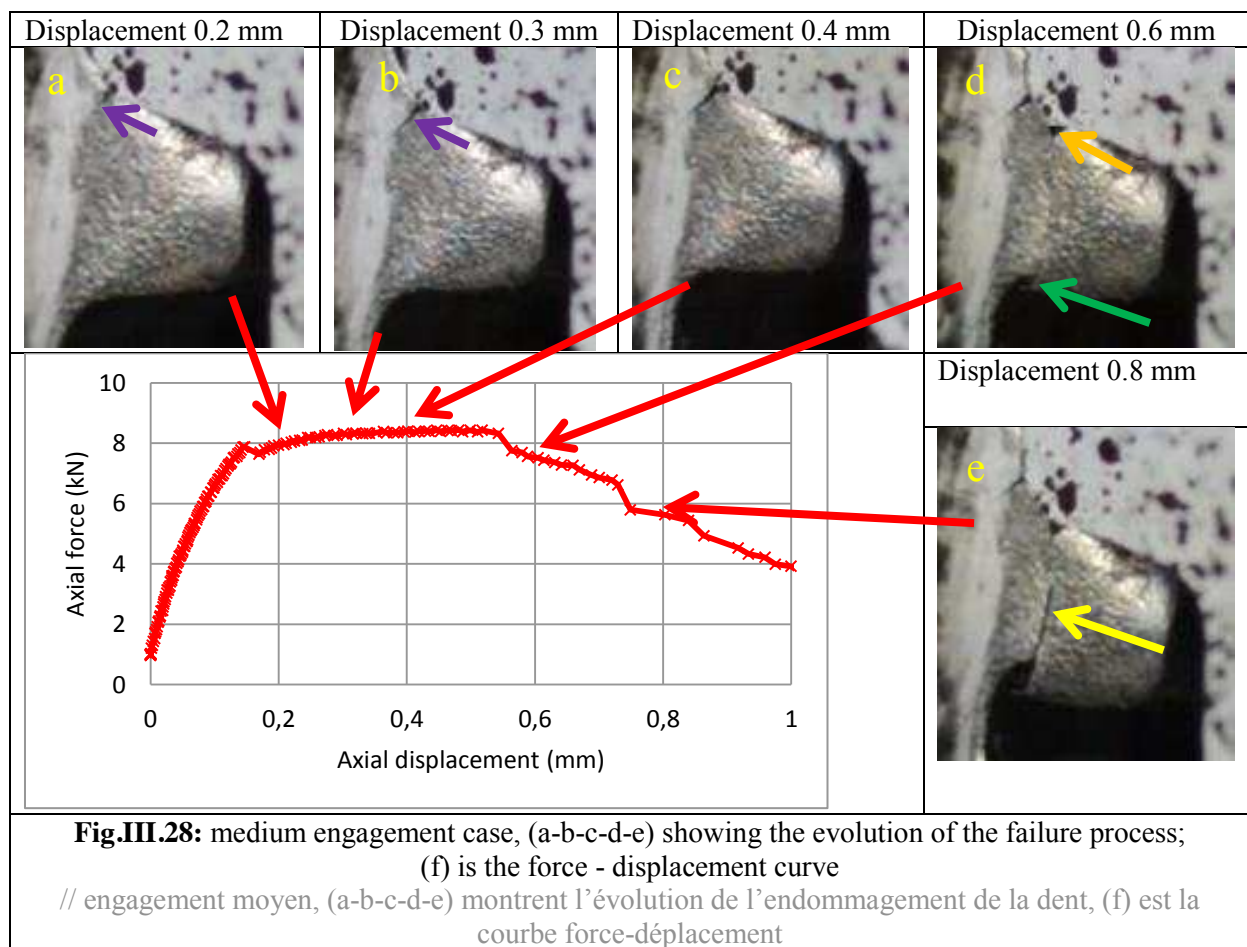
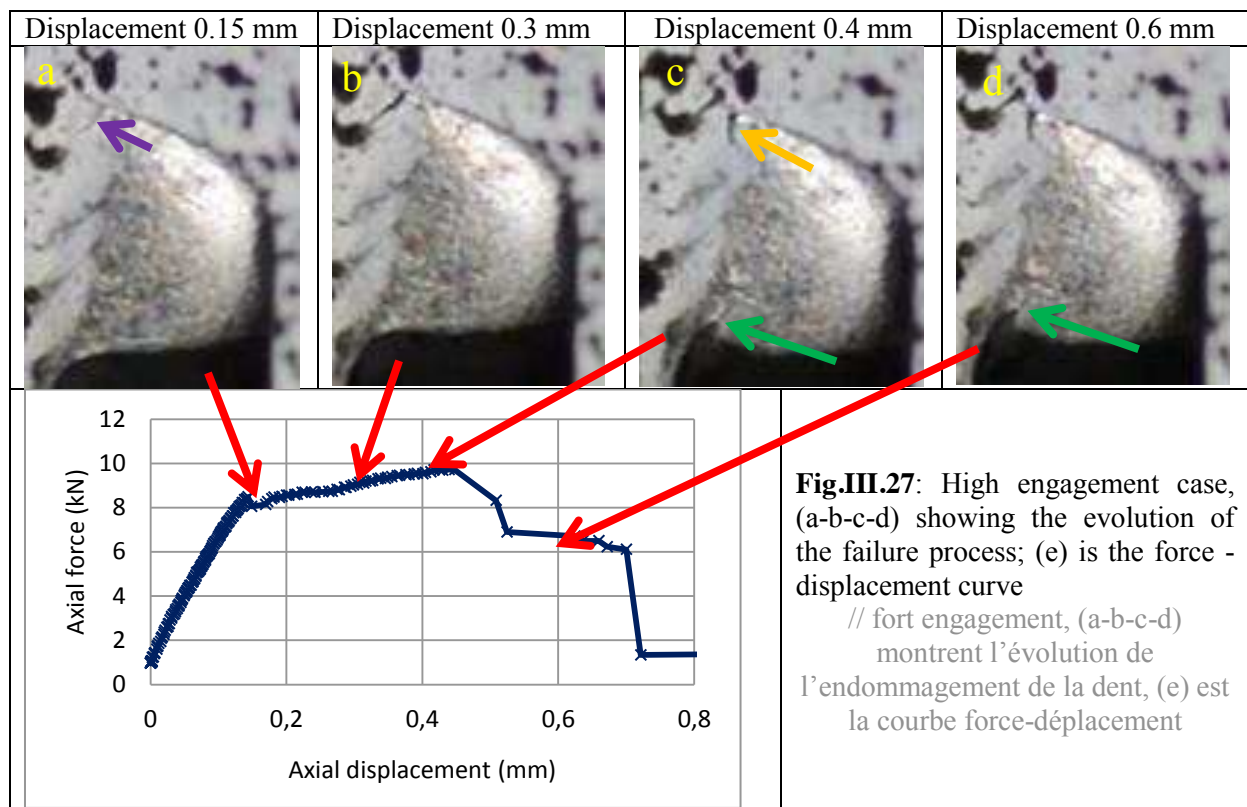
displacement). It is shown in the next section that these cracks initiate later and for a higher load for the case with the core material only.

Fig.III.27 (a – d), **Fig.III.28** (a – e) and **Fig.III.29** (a – e) show the evolution of the tooth failure process for the three engagements. They all have in common the opening of a crack at the bottom of the surface of contact with the tool (crack shown by purple arrows). This corresponds to the load drops occurring respectively at 8.5, 8 and 6.9 kN in decreasing order of engagement. The opening of this crack changes the behavior of the tooth. The load is not increasing as stiffly as before; instead deformation is localizing. The crack is opening.



As the tool displacement is increasing, a shear band builds in the tooth. It results in the formation of another crack on the opposite side of the tooth (shown by green arrows in **Fig.III.27** (c-d) and **Fig.III.28** (d)). The darkness of **Fig.III.29** does not allow seeing whether the aforementioned crack is present in the low engagement case. **Fig.III.28** (e) illustrates the last step of this shear band; the final crack is propagating through the whole tooth (yellow arrow). In the high and medium engagement case, the final crack is not initiating from the first crack but a bit higher on the tooth (orange arrows in **Fig.III.27** (c) and **Fig.III.28** (d)).

For all configurations final failure is due to shear driven ductile fracture.



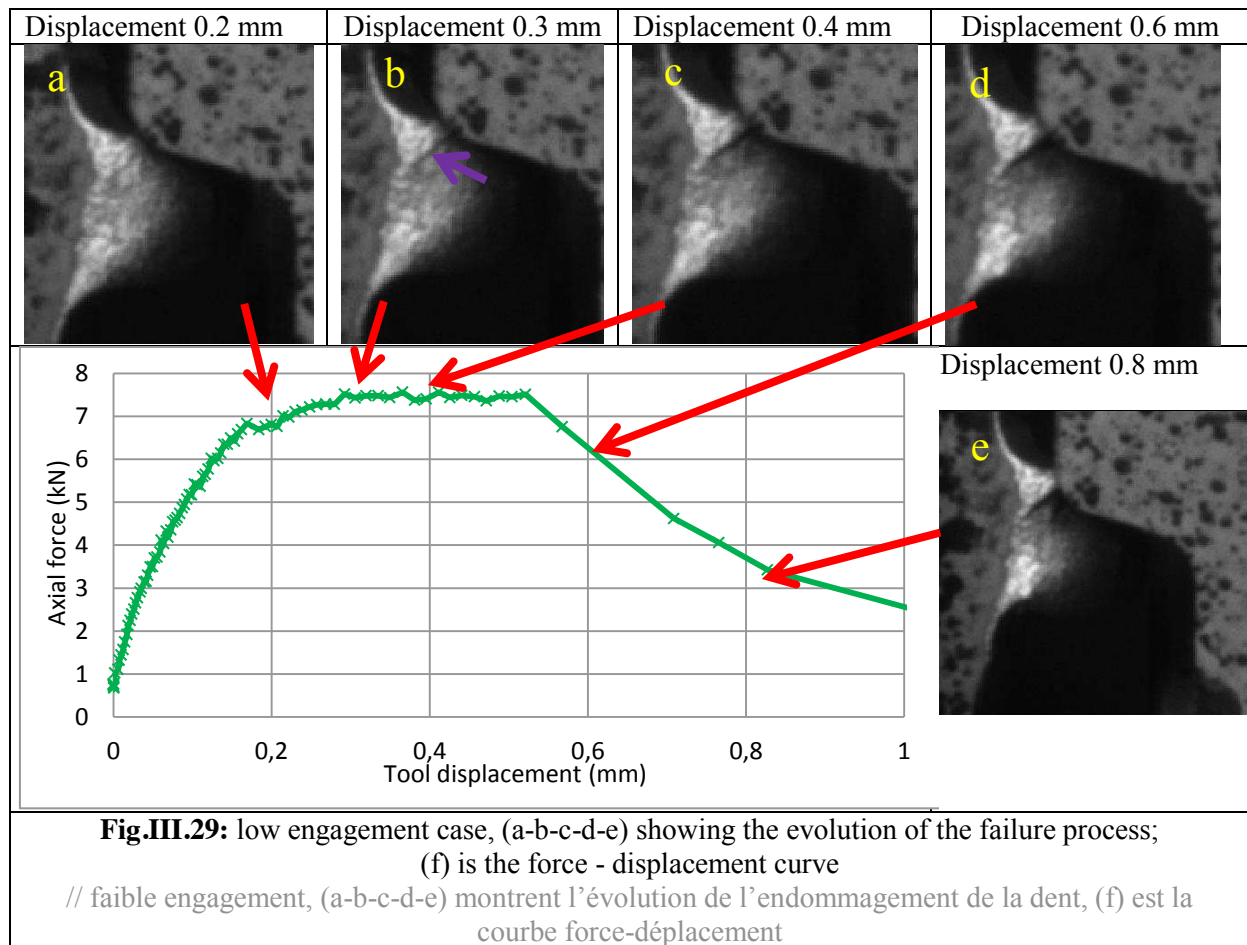
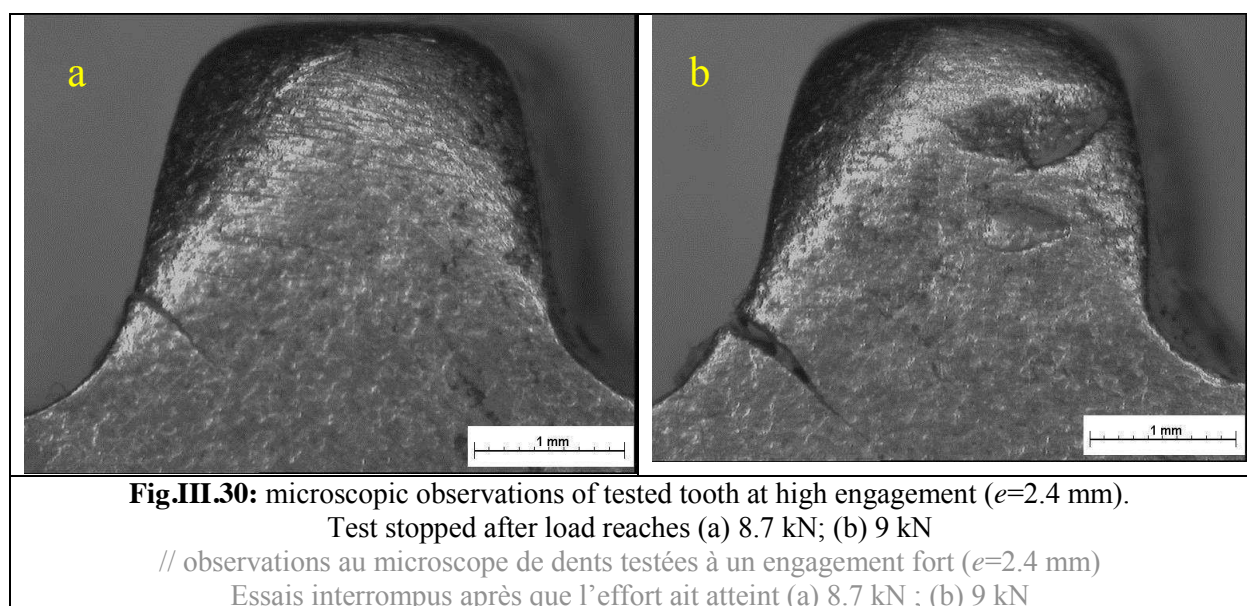


Fig.III.30 (a and b) are micrographs of teeth tested before complete failure (interrupted tests). The first tooth has been submitted to a load of 8.7 kN, and the second one to 9 kN. The crack is normal to the surface and propagates in a straight line. As the tool displacement is increasing, the crack is opening about 0.2 mm on **Fig.III.30** (b). This crack does not propagate further; on **Fig.III.30** (b) it is wide open on its first 0.8 mm, then it is narrower. The total depth is about 1.2 mm.



❖ Comparison : CMO vs FCN component - discussion

The comparison of the force-displacement curves shows the teeth with the external CN layer are a bit more resistant than without. The highest difference is for the lower engagement case where the CN layer adds 16 % on the peak load. Otherwise, the difference is less significant.

Failure processes have two common points. The first one is the opening of a crack at the bottom of the contact surface with the tool. Whatever the depth of engagement is, the area below the contact surface is submitted to strong tensile stresses. The brittle behavior of the CN layer makes it fail early, namely when the axial force reaches 6 kN, independently from the engagement. For the CMO teeth, these cracks appear later: 8.5, 8 and 6.9 kN respectively for the high, medium and low engagement. However, one can wonder if this is due to the thin (0.1 mm) decarburized layer at the extreme surface. Indeed, material behavior and thus fracture properties are different there from the base material, it is softer. Anyway, this crack does not propagate deeply; it is stopped by the ductile core material.

The second common point is that final failure is caused by a straight shear crack propagating through the whole tooth. Observations on the FCN teeth showed that it initiates on the side in contact with the tool and propagates up to the other side. However, 2 CMO cases out of 3 have shown, at the surface, another crack initiating on the opposite side of the tooth (**Fig.III.28 (e)** and **Fig.III.28 (e)**), shown by a yellow arrow in the last picture. The tool displacement is 0.8 mm, the upper part of the tooth slips on the lower part. Simulations presented in Chapter 6 will confirm that shear crack appears on the side in contact with the tool as with the complete CN component. Crack on the opposite side of the contact tooth tool in the CN layer will be discussed in Chapter 6. It reminds the fracture process shown in **Fig.I.11**.

The differences are in the superficial brittle layer. Indeed, it cannot sustain large plastic strain as the ductile material does. Thus it fails whenever the core material is deformed, either in tension, or in shear. There are 3 cracks for the medium and lower engagements, and 2 for the high engagement. Whatever the engagement, these cracks remain superficial; they propagate through the whole CN layer and are stopped in the transition area where ductility is higher as seen in **Fig.III.21 (d)**, **Fig.III.13 (d)** and **Fig.III.17 (d)** seem to indicate debonding between the CN layer and the core material. Indeed, there are brighter areas close to the second cracks caused by the reflection of the light. Because it is a graded variation of the properties, decohesion of the brittle layer was not expected as if it was a coated material. This hypothesis is related with the question raised earlier, whether the external crack initiates at the free surface or at the interface between the transition area and the external layer.

The tooth strength is related to the energy absorbed while loading. It could be assessed by calculating the area below the experimental curves. However, at which displacement the energy calculation should be stopped is questionable, since failure is generally progressive. Indeed, fracture is sudden in the high engagement cases, so displacement to fracture is easy to assess. In the other two cases, displacements to complete fracture are higher. However, one can wonder what the axial force really represents when it starts decreasing. A part of it must be due to the friction between the tool and the lip of the shear crack. This should not be counted in the energy calculation, since it is not part of the energy absorbed by the material. But for the lower engagement, the absorbed energy increases in fact since the displacement to fracture is higher. This is due to the tooth bending process, not observed in the high engagement cases. This is why the energy calculation has not been performed.

Another point is the residual stress present in the CN material. They are strongly compressive in the CN layer (up to -800 MPa) and slightly tensile in the core material.

III. 3 Conclusion

The aim of the semi-industrial test was to test only one tooth at a time with displacements controlled and forces recorded. The device had to be open enough to allow in situ observations and special attention had to be paid to the engagement depth control. The designed test-bench fulfills these technical initial specifications. Fracture process is observed in situ and can be correlated with the tool displacement. Even though its design was intended to make it as stiff as possible, there are still significant spurious displacements and compliance issues; which could be expected for such a complex test bench. Real relative displacements between the tested tooth and the tool are therefore assessed thanks to a 3D DIC system, called VIC®. Engagement depth was measured thanks to the micrometric screws. Furthermore, it is checked thanks to the DIC measurements. However, inaccuracies may come from the fact that analyzed surfaces are curved. This may explain why the maximum load obtained for medium and low engagement is equal for the full CN component.

Hypotheses made after the post mortem observations have been checked and the observations have brought a few modifications to the picture of the fracture process. Failure starts still with a crack opening at the bottom of the contact surface with the tool. This area is submitted to tensile stresses, which induces brittle failure of the CN layer. This crack is perpendicular to the surface and propagates in a straight line. However, this first crack is stopped in the transition area, where the ductility is higher. It thus remains a superficial crack. As the load is increasing, there is a shear localization of the deformation slightly above the first crack. The external layer cannot withstand the high strain supported by the core material; it thus fails in several areas. Each time, failure propagation in the CN layer is perpendicular to the maximum principal stresses. These cracks were not seen on the post mortem industrial recliners. But loading paths are not the same. Indeed, on the recliners, the relative movement between the pinion and the flange is circular; whereas on the semi-industrial test it is a linear translation. Because the test bench was set up on a universal tension/compression machine it would have been difficult to reproduce and control the same circular movement. That would have brought more compliance issues.

Then, in the end, a final crack propagates in the tooth from the side in contact with the tool to the opposite side. Crack path is linear and is due to shear localization within the tooth core material that the tool pushes parallel to the tooth root. These are two other differences with respect to the initial assumptions. First, because of the circular relative movement on the recliner, the final crack was curved. This difference was expected. With the semi-industrial test, observations showed that the final crack is propagating from the side in contact with the tool to the opposite side (see **Fig.III.23** (d)). However, observations of the post mortem recliners showed teeth with an apparent crack on the opposite side before final failure. This same crack was observed on **Fig.III.23** (a); the CN layer around the shear crack has completely failed.

The influence of the engagement depth on tooth failure mechanism has been investigated. On the one hand, a tooth with a high engagement sustains a higher load than a tooth with a lower engagement. On the other hand, a lower engagement leads to a smoother failure with possibly higher energy consumption. Whatever the engagement, failure process starts by the initiation of a crack below the contact surface with the tool. Then, couple of superficial cracks opens in the CN layer. A lower engagement leads to the opening of more cracks. This may be due to a higher bending motion component of the tooth for this configuration. Then, in the end, the final failure is occurring with a shear crack propagating through the whole tooth. A determination of the absorbed energy could have been interesting to do. But, unfortunately, the observations do not enable to study it rigorously since it is difficult to see the displacement to complete fracture. Furthermore, the axial force while it is

decreasing must be misrepresented due to friction between the tooth and the tool failed surface. This friction must not be accounted for in the absorbed energy. During real recliners failure, it has to be pointed out that the engagement depth may vary along the failure process.

The influence of the external CN layer on the tooth failure has been analyzed thanks to the use of a protecting paint. This study brings useful information. First, at equal engagement, the CN layer adds up to 16 % on the maximum load sustained by one tooth. The highest difference is for the low engagement; otherwise, difference is surprisingly low. Even though the CN layer is harder than the core material, it fails as soon as the tensile stresses reach a critical value, because of its brittleness. In both cases, final fracture occurs by a main shear crack going through the whole tooth. The CN layer does not change significantly the displacement to fracture. Thus, it can be stated that the tooth strength is supported by the core material only. This confirms remarks done in the literature review about the failure of carbonitrided steels. The external layer is used to resist contact fatigue thanks to its high hardness and strong residual compressive stress. This is also why this treatment is performed on the recliner: pinion and flange are always in contact. A hard layer is mandatory for the durability of the mechanism. The core material has to remain as ductile as possible for high toughness and energy absorption properties.

Tests on all types of teeth repeatedly proved that failure is due to a shear crack in the core material. On the other hand, no further observations were done regarding the critical amount of plastic strain undergone by the core material at the onset of fracture. These observations are required to identify the parameters of the failure criteria. This is the topic of the following chapter where the materials are studied under homogeneous, proportional loading conditions.

Chapter IV : Mechanical characterization

Contents

IV. 1	Fracture tests.....	87
IV. 1. 1	Triaxiality and Lode angle analysis	87
IV. 1. 2	Shear tests	89
IV. 2	Core material	92
IV. 2. 1	Low stress triaxiality characterization	92
IV. 2. 1. a	Experimental methodology	93
IV. 2. 1. b	Experimental results.....	95
IV. 2. 1. c	Fracture surfaces study.....	97
IV. 2. 1. d	Discussion	99
IV. 2. 2	High triaxiality characterization.....	100
IV. 2. 2. a	Experimental method.....	101
IV. 2. 2. b	Experimental results.....	103
IV. 2. 2. c	Fracture surface Analysis	105
IV. 2. 2. d	Discussion	107
IV. 2. 3	Conclusion	107
IV. 3	Characterization of the CN layer	107
IV. 3. 1	4PBT.....	108
IV. 3. 1. a	Experimental method.....	108
IV. 3. 1. b	Results	109
IV. 3. 1. c	Discussion	110
IV. 3. 2	Tensile tests	111
IV. 3. 2. a	Experimental methodology	111
IV. 3. 2. b	Results	112
IV. 3. 2. c	Discussion	114
IV. 3. 3	Conclusion	115
IV. 4	Influence of the external layer on the behavior and failure mechanism in tension	116
IV. 4. 1	Influence on the strength and ductility	116
IV. 4. 2	Influence of the CN layer on the failure process.....	117
IV. 4. 3	Discussion	119
IV. 5	Conclusion of chapter IV.....	120

Résumé en Français

Ce chapitre présente les essais de caractérisation sur éprouvettes CN ; celles-ci sont constituées de deux matériaux : le matériau de cœur et celui de la couche externe. Grâce à une peinture spécifique stoppant la pénétration des atomes de carbone et d'azote, il est possible d'obtenir un échantillon sans couche CN. Cela va permettre de tester uniquement le matériau de cœur. Il est en revanche impossible d'obtenir uniquement le matériau de la couche externe, sa caractérisation se fera avec des échantillons CN.

Ce chapitre commence par une bibliographie sur les géométries d'échantillons utilisés pour soumettre le matériau à une contrainte de cisaillement. Il est crucial de bien caractériser le matériau de cœur pour cet état de contrainte car il correspond à celui de la fissure principale. Différentes géométries sont comparées ; l'éprouvette papillon dite « butterfly » est retenue pour son efficacité à maintenir l'état de contrainte de cisaillement jusqu'à la rupture. Ce point précis fait défaut à une majorité de géométries où finalement la rupture s'amorce sur les bords des échantillons et donc en état de contrainte proche de la traction. De plus, en choisissant les déplacements appliqués, il est possible de soumettre le matériau à n'importe quel état de contrainte souhaité. Ainsi, cette éprouvette va nous permettre de tester le matériau en cisaillement pur, cisaillement avec compression, cisaillement avec traction et traction pure. Le cisaillement pur et avec un peu de traction correspond à l'état de contrainte lors de la propagation de la fissure principale. Les véritables déplacements sont déterminés avec un système de corrélation d'image en 2D. L'étude des déplacements à rupture permet de justifier une très grande différence de ductilité entre le cisaillement avec compression et le cisaillement avec traction. Des essais de traction sur éprouvettes entaillées, avec différents rayons d'entailles, complètent la gamme des caractérisations. Ils permettent de caractériser le matériau dans un état de contrainte proche de celui en tête de fissure.

Puis des essais sont effectués sur le matériau complet afin de caractériser la couche externe. Vu que c'est un matériau fragile, il va fissurer lorsqu'il est soumis à des contraintes de traction. Ainsi, des essais de flexion 4 points et des essais de traction sont réalisés. Les premiers permettent de soumettre le matériau à des contraintes de traction homogènes en fonction de la profondeur. Les essais de traction soumettent le matériau aux mêmes états de contraintes ; mais il nous est possible de qualifier l'influence de la couche CN par comparaison avec des essais sans cette dernière. On confirme ce qui a été vu précédemment avec la rupture de dent : la couche externe ne joue pas sur l'effort maximum soutenu par le matériau. En revanche, il influe énormément sur la ductilité globale : le déplacement à rupture est divisé par 3 avec la couche CN. En effet, les fissures ouvertes dans la couche fragile et arrêtées dans la zone de transition sont des zones de très fortes concentrations de contraintes. Elles facilitent ainsi l'ouverture et la propagation d'une fissure à travers le matériau de cœur. Ce résultat était inattendu car pas observé lors de la rupture des dents. Le chapitre suivant va utiliser les essais réalisés ici afin de calibrer les paramètres des modèles de rupture.

Introduction

Observations performed with the semi-industrial test showed the toughness of the tooth was mainly due to the core material. It is very ductile for a heat treated steel and can undergo a certain amount of plastic strain before failure. Tooth failure occurs by a main shear crack propagating through the whole section of the tooth. It is thus mandatory to analyze in details the failure behavior of this core material. This is done here by performing several mechanical tests with various stress states and under proportional loading conditions. Even though tooth failure occurs for a triaxiality close to zero, a rigorous assessment requires to cover a wide range of stress states. A first part of this chapter introduces the analysis based on the variation of the Lode angle and the stress triaxiality ratio. A literature review on tests inducing shear stress states is done as well. Then the experimental work description first focuses on the low stress triaxiality with the so-called “butterfly” type specimen. Then more conventional grooved and notched tensile tests are presented, thus giving more information about failure at high stress triaxiality.

These tests were performed on specimens with only the core material (CMO). The semi-industrial tests also pointed out the external CN layer fails in a combined tension - shear stress mode. This was confirmed by the literature review about the failure of brittle materials. 4-point bending and tensile tests were therefore carried out on FCN components to apply homogeneous tensile stresses on the CN layer.

In the end, influence of the CN layer cracks on the failure of the complete CN component is studied thanks to tensile tests.

IV. 1 Fracture tests

The experimental tests presented in this part will be used to calibrate the fracture criteria and the plastic behavior of the CN material. Thanks to the experimental displacement to fracture measured, numerical simulation can provide strain to failure; meaning the maximum strain sustained by the elements where fracture is initiating at the measured experimental displacement to fracture. This strain to failure will be used to calibrate the fracture criteria as well as the stress state on the loading path. This methodology requires:

- accurate measurement of the displacement to fracture;
- appropriate material behavior law to get an accurate value of strain to fracture when the experimental failure displacement is reached.

IV. 1. 1 Triaxiality and Lode angle analysis

The accuracy of phenomenological failure prediction of ductile fracture criteria relies on the diversity of the tests and accuracy of the measurements done to identify their parameters. In his book ([Bridgman, 1952]), Bridgman varied the stress state on axisymmetric tensile specimen by adding hydrostatic pressure. More recently, [Bao & Wierzbicki, 2004] carried out eleven different kinds of tests, listed in Table IV.1, to identify the parameters of a failure criterion depending only on the stress triaxiality. With all these specimens, stress triaxiality varies from -0.4 for compression test until +1 for tension. Regarding tensile specimen, stress triaxiality ratio was varied by machining notches of different radii. A notch with a lower radius induces higher stress triaxiality. Note the variations of triaxiality during each test, shown by the range mentioned in the last column.

Fig.IV.1 (a) lists the mechanical tests used to identify the parameters of the Bai & Wierzbicki criterion, which depends on the stress triaxiality and the Lode angle parameter. **Fig.IV.1** (b) pictures some of the conventional tests carried out to study failure properties. The stress state range covered with these specimens is quite wide. Designing an adequate set of specimens is important in view of the identification of a complex failure criterion. First, specimens must cover a wide range of stress state at failure. For instance, on **Fig.IV.1** (a), the Lode parameter (Lode angle parameter on **Fig.IV.1** (a)) varies from -1 to +1, and the triaxiality from -2/3 to 2/3.

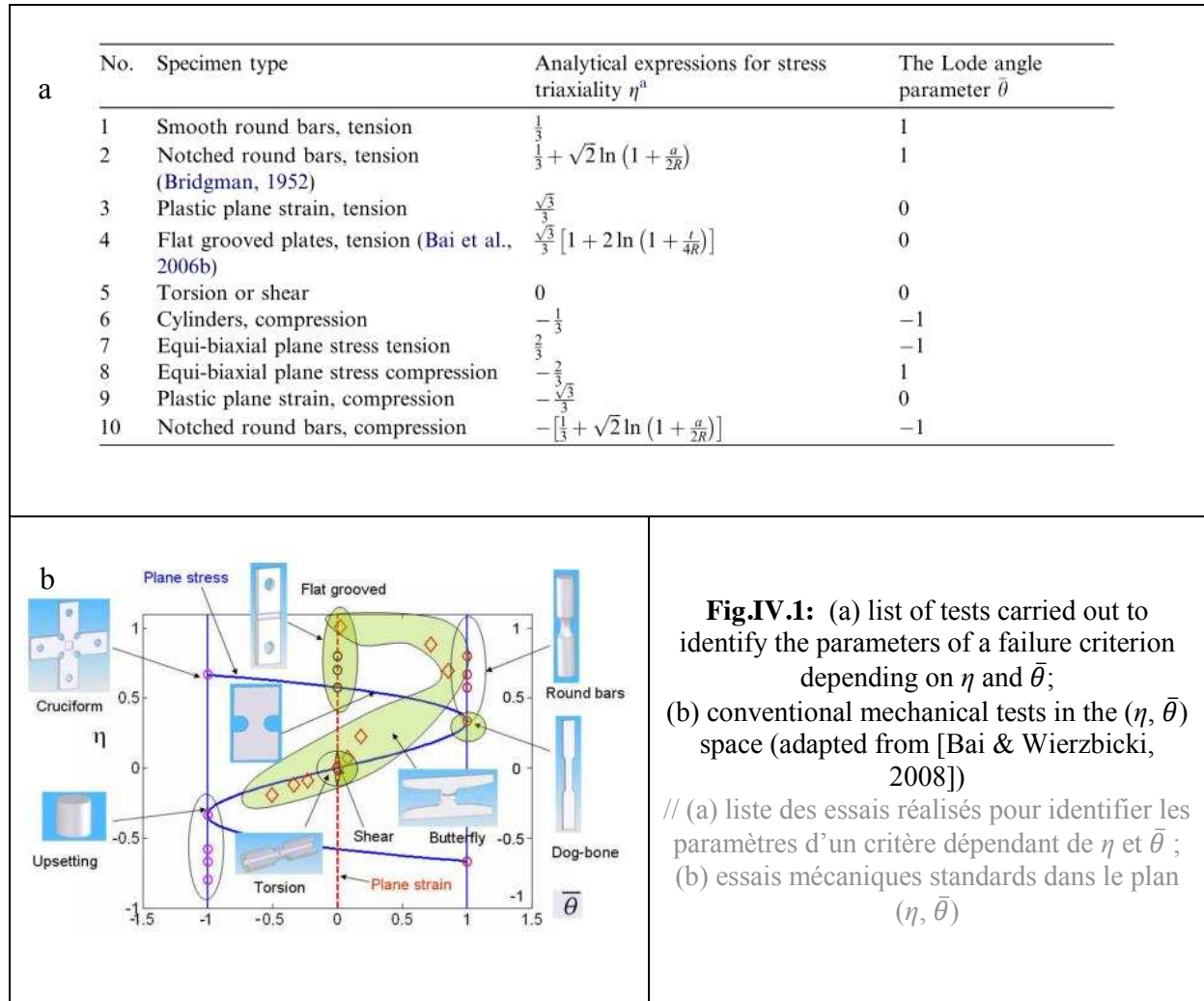
Regarding the material studied in this work, there is another test design constraint. Indeed, Faurecia uses rolled sheets for recliners manufacturing; thus specimen must be obtained from the same raw material to avoid any additional variability issue. This is why the samples used in this study are obtained from 20MnB5 3.5 mm thick sheets. Consequently, round bar specimens will not be used here.

In addition, the stress state must be as constant as possible during the test (proportional loading path), as discussed in **II.2.1**, Chapter 2.

Test number	Loading	Specimen description	stress triaxiality
1	Compression	Cylinder (D/H=0.5)	-0.33 to -0.12
2	Compression	Cylinder (D/H=0.8)	-0.32 to -0.05
3	Compression	Cylinder (D/H=1.0)	-0.32 to -0.05
4	Compression	Cylinder (D/H=1.5)	-0.32 to -0.05
5	Compression	Asymmetric	-0.4 to -0.09
6	Shear	Flat	0 to 0.02
7	Combined shear and tension	Flat	0.04 to 0.15
8	Tension	Plate with a circular hole	0.33
9	Tension	Round, smooth	0.33 to 0.5
10	Tension	Round, large notch	0.6 to 0.7
11	Tension	Round, small notch	0.9 to 1

Table.IV.1: list of the tests carried out to vary the stress triaxiality ([Bao & Wierzbicki, 2004])

// liste des essais réalisés en faisant varier la triaxialité des contraintes ([Bao & Wierzbicki, 2004])



IV. 1. 2 Shear tests

Induced shear specimens were widely studied this last decade. Thus multiple geometries were designed, from disk-shape geometries to specimens tested on tensile test machine or also combined torsion-tension specimen. **Fig.IV.2** illustrates some of these specimens found in the literature. Specimens a, b and e can be used on a universal tensile testing machine. Specimen c and f require a biaxial testing machine. The issue with these specimens is that despite the useful part of the specimen made thinner by design, failure may occur on the edges of the useful part and not in its center. On these edges, stress triaxiality ratio is not zero anymore but may increase and end up with a tensile failure mechanism. For instance, stress triaxiality is plotted on **Fig.IV.2** (d) for one of the tests. Although this is a shear test, triaxiality is close to zero (green) only in the center, and increases until the orange color on the edges ($0.33 < \eta < 0.495$). For this specimen, crack will in fact initiate on the sides, thus at higher stress triaxiality than pure shear. It is difficult to use these tests to assess failure prediction accurately in shear. This is a big issue for many shear specimens.

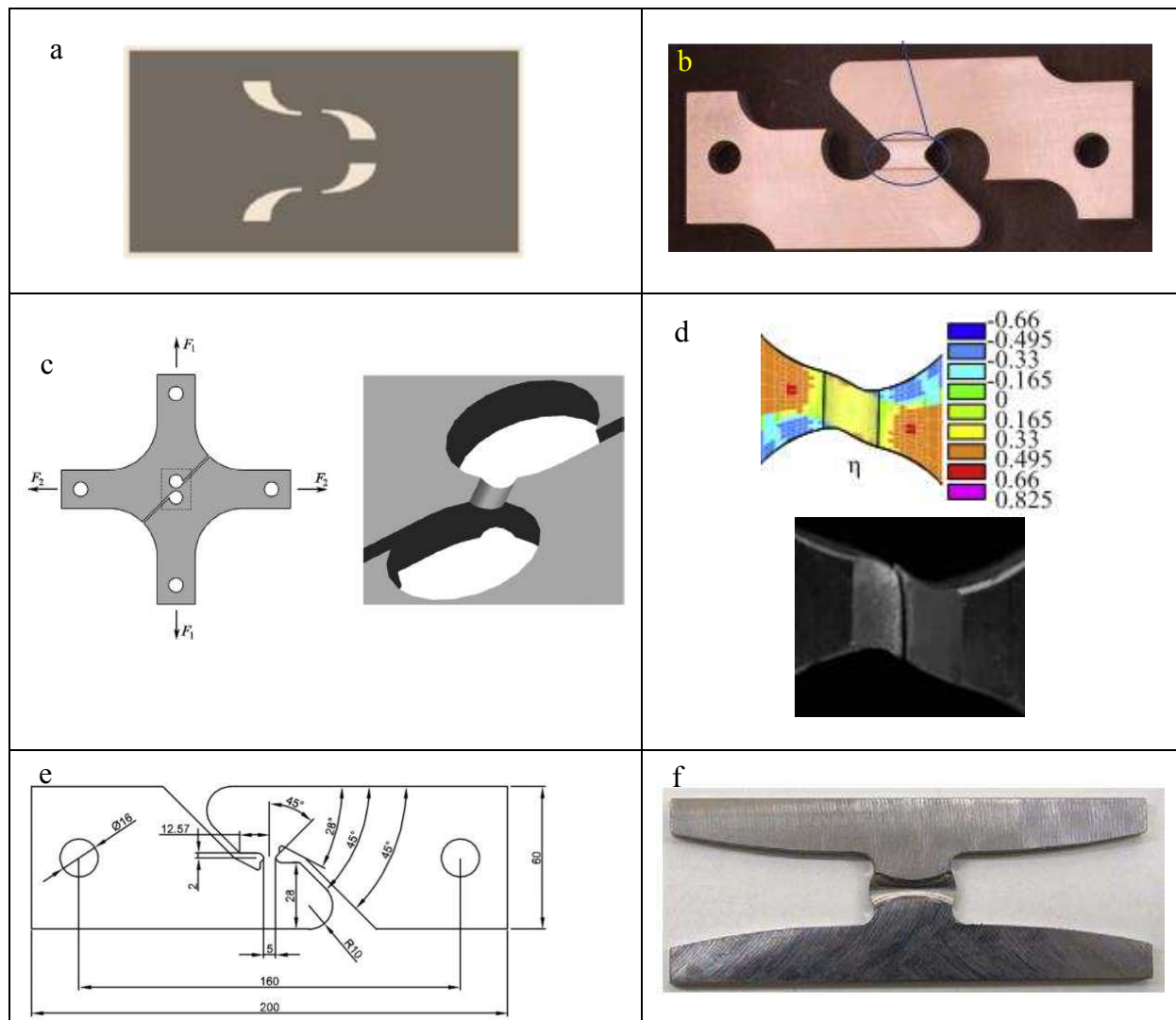


Fig.IV.2: examples of induced shear specimen found in the literature:

- (a) [Shouler & Allwood, 2010]; (b) [Bao & Wierzbicki, 2004]; (c) [Brünig et al., 2015];
 (d) triaxiality at the moment of failure and experimental crack for the Brünig specimen;
 (e) [Gruben et al., 2012]; (f) butterfly specimen [Bai & Wierzbicki, 2008]

// exemples d'éprouvettes à cisaillement induit trouvées dans la littérature :

- (a) [Shouler & Allwood, 2010]; (b) [Bao & Wierzbicki, 2004]; (c) [Brünig et al., 2015];
 (d) triaxialité à l'instant de la rupture et fissuration pour l'éprouvette de Brünig;
 (e) [Gruben et al., 2012]; (f) éprouvette Papillon [Bai & Wierzbicki, 2008]

The butterfly specimen (**Fig.IV.2** (f)) with its double curvature geometry ensures failure initiates in the middle of the gage section. This is true within a certain range of deformation. If the deformation is too high (i.e. with very ductile materials), failure may appear on the side as well. This should not be the case for heat treated steel. However, this geometry has a couple of drawbacks. First, it cannot be tested on a simple tensile test machine. It requires a biaxial machine where the two axes can be controlled independently. Then, specimen machining is tricky, because of the two curvatures. Furthermore, it must be very precise to guarantee the targeted stress distribution and failure at the center of the gage area. Lately, three new specimens were designed: **Fig.IV.3** (a) [Gachet, 2013] and (b) [Roth, 2015] are induced shear specimens. They are both set up on a tensile test machine (loading direction is given by the black arrows). The first one enables to vary the stress triaxiality thanks to the angle α_2 . But failure may initiate as well on the extremity of the reduced section. For the second specimen **Fig.IV.3** (b), the

geometry of the active part is optimized as a function of the material law in order to guarantee failure initiates in the middle of the gage section, and not on the side. Thus, loading path is pure shear until failure. The second specimen (**Fig.IV.3 (c)**) is an in-plane torsion specimen ([Yin et al., 2015]). It comes from the idea that the issue with induced shear specimens is they are likely to fail on the sides of the active area, where stress state is not pure shear but more a tensile one. In a disk-shape specimen, with a groove to concentrate the stress, there is no side. Note that other interesting torsion tests were proposed on tubular grooved specimen (see [Barsoum & Faleskog, 2007], [Jessica Papasidero, 2014]). These specimens are also interesting to maintain a shear stress state up to failure, but they are not possible for sheet-based materials.

It was seen that the core material in recliners fails in stress state close to shear, so it is essential to have a well-designed shear test. The butterfly specimen was chosen for this PhD. It requires to be tested on a biaxial machine with independent controlled axes. Thanks to these two axes, various loading paths possibilities are available.

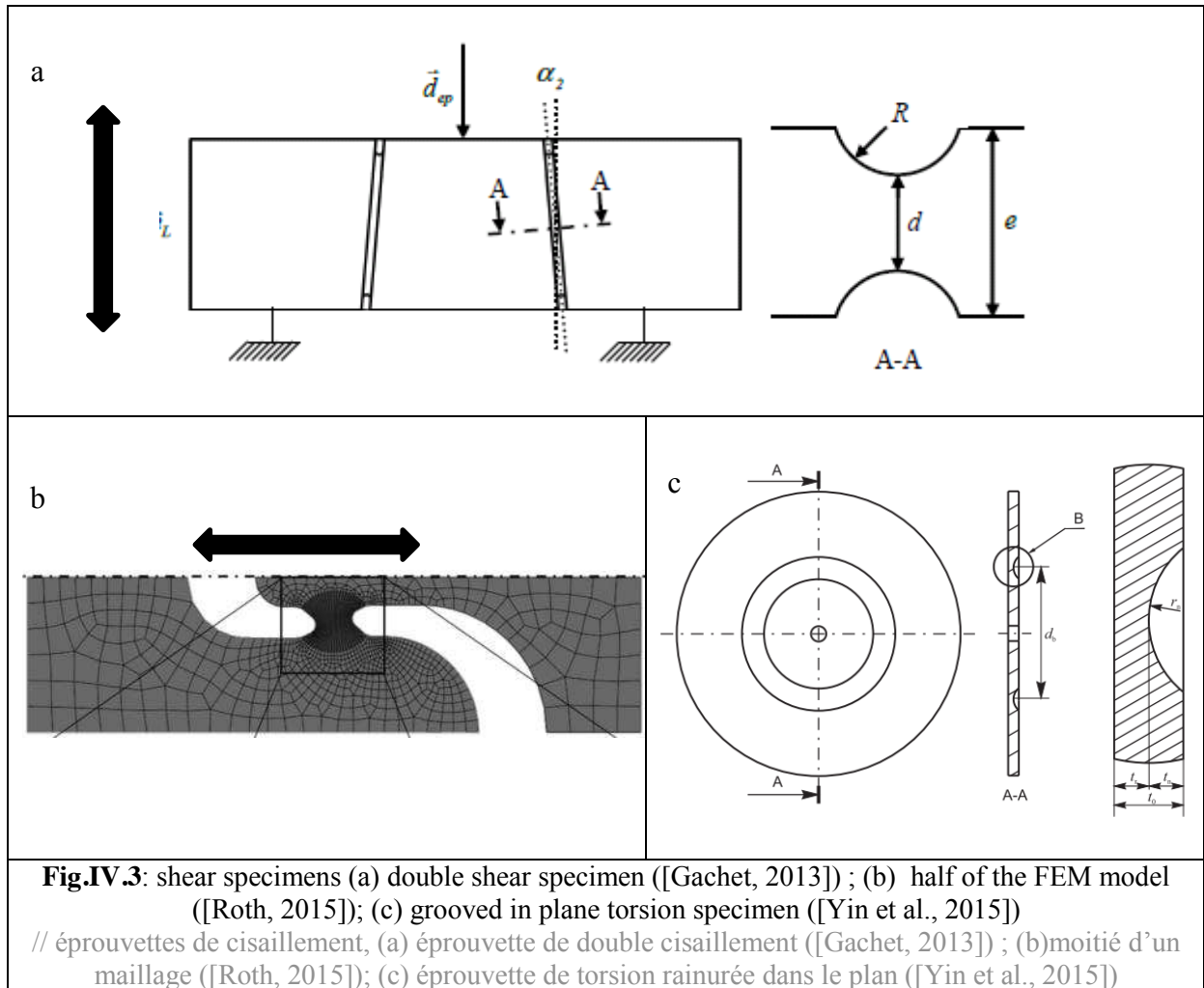
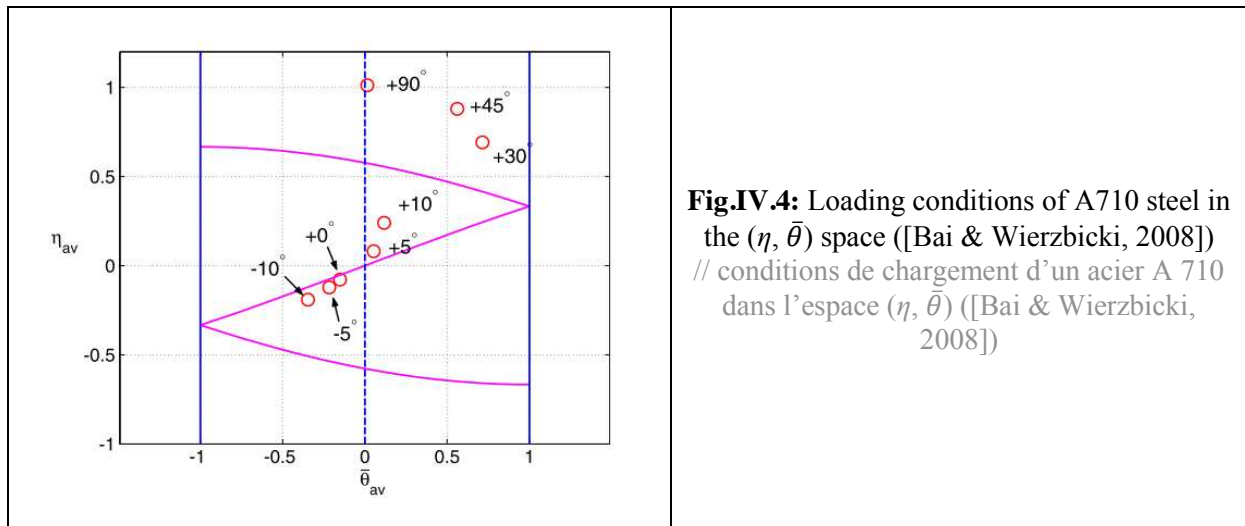


Fig.IV.4 illustrates some of the possible loading conditions. Material can be tested in pure shear state or with a bit of compression, or a bit of tension. (+0°, -10°, +5°). These conditions can reproduce the closing and opening of a shear crack. Thus, stress triaxiality can be close to zero for pure shear, and respectively negative or positive by adding compression or tension.

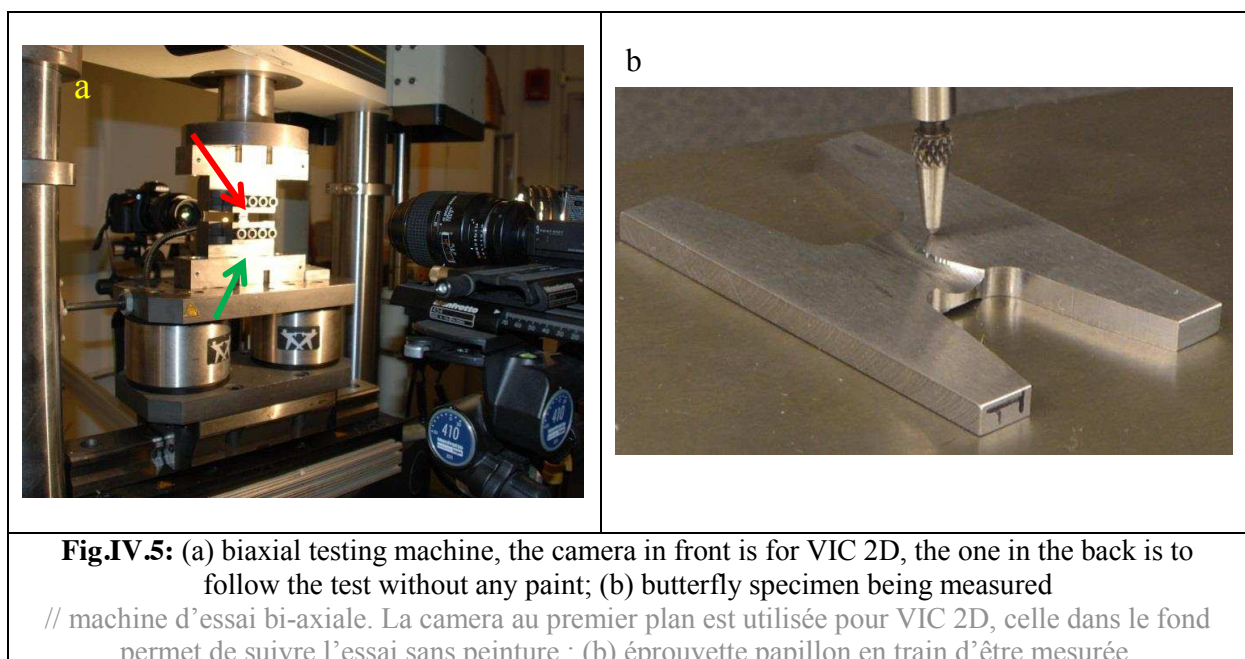


IV. 2 Core material

This part shows the mechanical characterization of the core material using two types of specimens. First, butterfly specimens are used to test the material at low, even negative triaxiality. It reproduces the stress state undergone by the material of a tooth. In a second stage, notched and grooved tensile tests are carried out to test the material at higher stress triaxiality.

IV. 2. 1 Low stress triaxiality characterization

The butterfly specimens were tested on a biaxial machine in the Impact and Crashworthiness laboratory at MIT. **Fig.IV.5** (a) is a picture of the biaxial testing machine; **Fig.IV.5** (b) illustrates a butterfly specimen. One can see the two wider areas and the thinned gage central one. The wider areas are called “shoulder” and are gripped by the jaws. The red arrow on **Fig.IV.5** (a) shows the upper jaw, which moves vertically. It enables to add compression or tension. The green arrow shows the lower jaw; it is linked to the horizontal axis and controls the shear displacement.



The measurement of the butterfly specimen is particularly tricky because of its shape, but mandatory since any error on the geometry corrupts the experimental results. This study is introduced in Appendix IV.1. The gage thickness is 1.15mm.

IV. 2. 1. a Experimental methodology

Four distinct loading conditions are chosen (-10° , 0° , $+5^\circ$ and $+90^\circ$). The angle refers to the direction of the solicitation as it results from the combination of horizontal displacement of the lower jaw (shear, 0°) and vertical displacement of the upper jaw (tension or compression, 90°). The first three conditions are close to the stress state met by the failed material in the tooth failure (FE study is done in Chapter 5). They are pure shear, shear with a bit of compression and shear with a bit of tension. The latter represents the crack opening stress state. These will give three experimental data points within a close range of stress triaxiality to better characterize the material. Displacements are imposed; axial velocity is about 1 mm/min, slow enough to have enough VIC pictures to apply the displacements correction. For every loading condition, displacements are controlled. Tests are recorded with VIC camera to assess the real displacements. Thus, the specific paint spot pattern is applied on the whole surface on the front side of the specimen. A High Definition camera records the opposite side where no paint is applied to observe the initiation of failure. Specimens were tested under quasi-static conditions: velocity is about 1 mm/min.

Fig.IV.6 plots the experimental curves for the pure shear tests. Three tests were done to check the repeatability. It is rather accurate, shear force curves are superimposed until 1.8 mm displacement. At the beginning of the experiment the slopes of shear force curves are very low. This is due to the compliance of the machine. Once the stiffness is offset, the slope increases linearly. This confirms that real displacements must be assessed through DIC system VIC®. There are some slight instabilities on the curves within the first 6 kN: these are due to possible sliding of the shoulders in the jaw. Those will be removed from the VIC displacement because displacement will be extracted from the pictures. A vertical force of -1.2 kN max (compression) is observed. Horizontal displacement is applied to the lower jaw, the upper one is fixed with a zero displacement condition. Because of the Poisson effect, there are vertical forces toward the specimen induced by the section reduction.

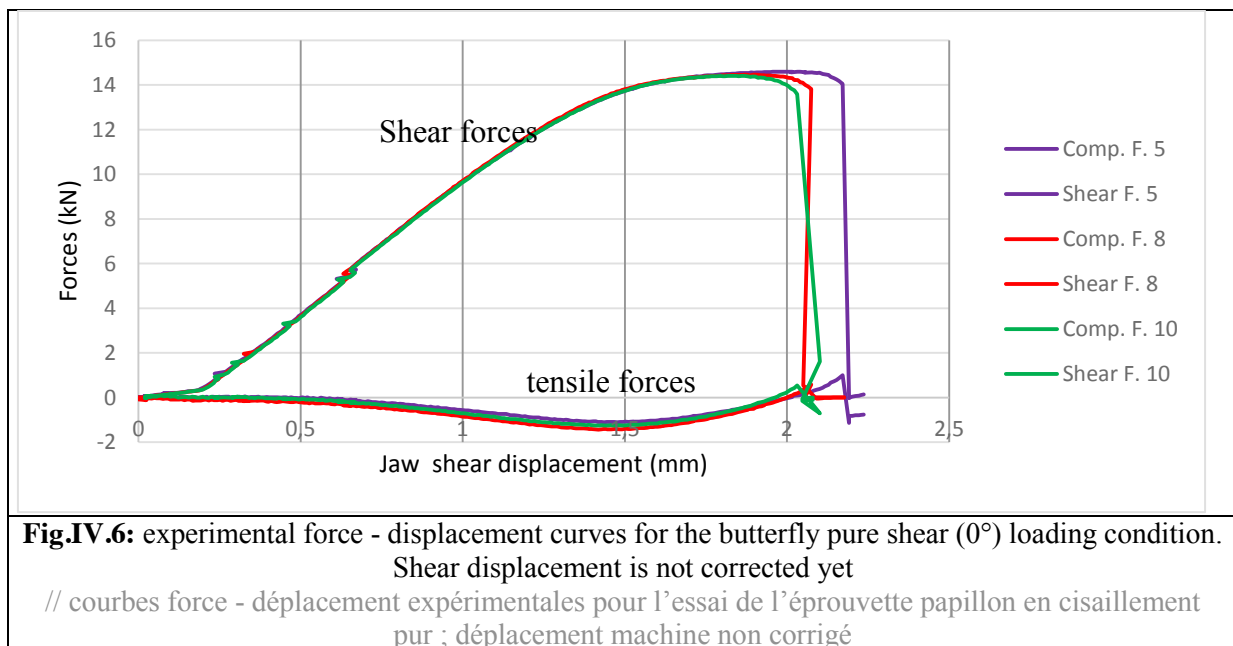


Fig.IV.7 (a) illustrates a butterfly specimen at the beginning of the test. The paint spot pattern is applied on the whole observed surface. However, it is mandatory that the shoulders have no paint otherwise the friction inside the jaws would be lower and the grip less efficient. Six points are selected on the same picture; displacement will be extracted at these 6 points to check whether there is any spurious rotation of the specimen around Z. **Fig.IV.7** (b) plots the displacement along Y calculated using DIC. The displacement gradient is localized in the middle of the gage section, thus gradient is locally quite high. DIC strain spatial resolution is not excellent because the paint spot pattern is rather coarse (see [K. Wang & Wierzbicki, 2015] for finer patterns). In particular the maximum strain, next to initiating cracks, may not be accurate enough, this is why it will also be calculated numerically.

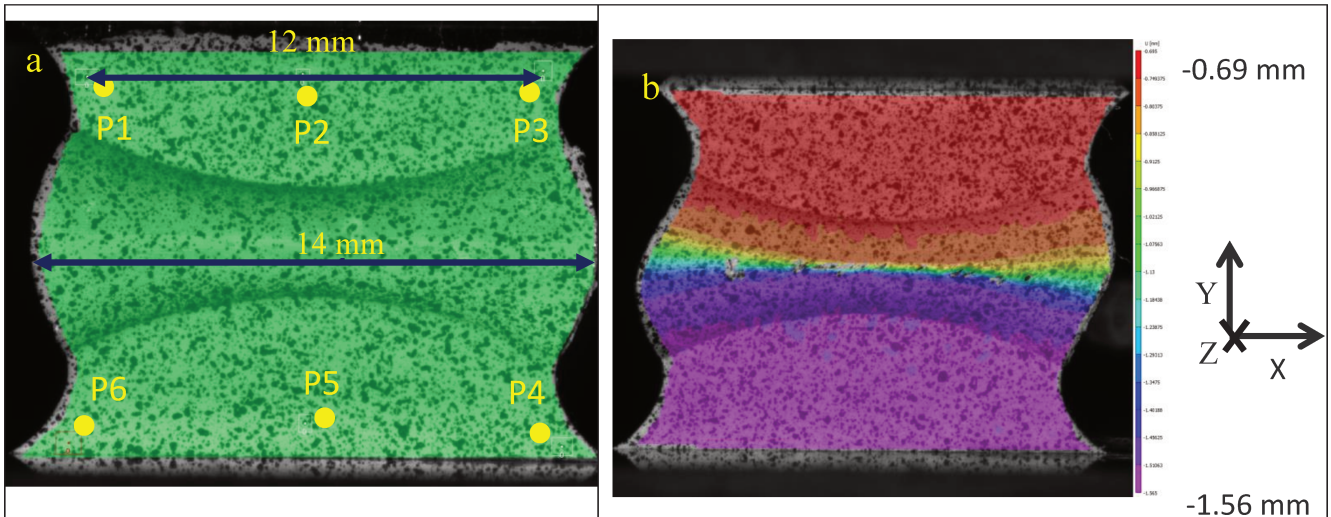


Fig.IV.7: butterfly specimen, pure shear loading condition (a) localization of the 6 points where displacements are extracted; (b) shear displacements (along X) are plotted (red: -0.69 mm, purple: -1.56 mm), the upper jaw is fixed, the lower one moves toward the left side.

// éprouvette papillon, condition de chargement en cisaillement pur (a) localisation des 6 points où les déplacements seront déterminés par VIC ; (b) visualisation du déplacement de cisaillement (en X) (couleur rouge : -0.69 mm, couleur violette -1.56 mm), le mors du haut est fixe, celui du bas bouge vers la gauche.

Fig.IV.8 (a) and (b) plot the displacement of the six points respectively along X and Y. There is no scatter in terms of displacement along X: the displacements of points P1, P2 and P3 are superimposed, as for 4, 5 and 6. For the displacement along Y, there is a slight difference of at most 0.08 mm between P1-P3 and P4-P6. The distance between these points is about 12 mm. This gives a rotation angle of less than 0.4° around Z, which is considered negligible. For the next specimen, relative displacement will be equal to the displacement of P2 minus the one of P5.

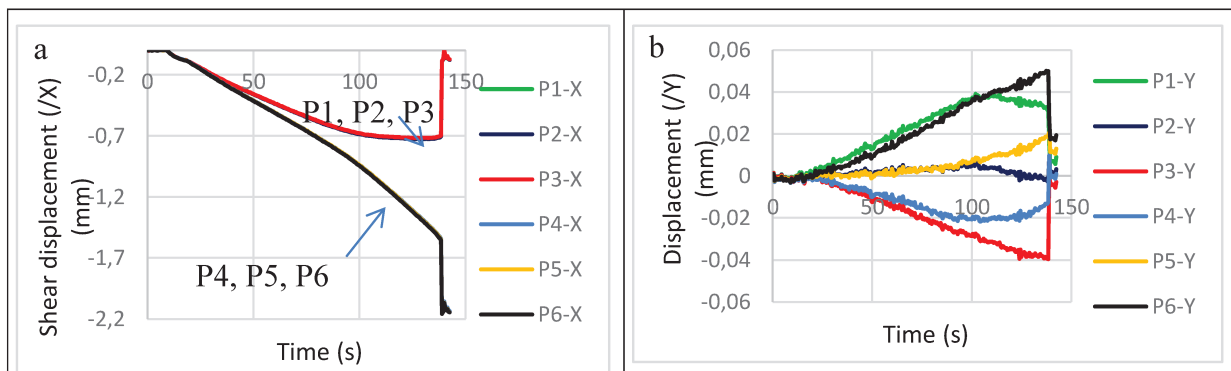


Fig.IV.8: Displacements of points P1 to P6 selected in **Fig.IV.7**, (a) along X; (b) along Y
// déplacements des points P1 à P6 indiqués sur la **Fig.IV.7**, (a) selon l'axe X; (b) selon l'axe Y

Fig.IV.9 plots the force - shear displacement curves for the 2 cases with the highest discrepancy (tests #10 and #5, see Figure IV.6). The third one (#8) lies in between these two. Before 0.6 mm displacement, shear force curves are superimposed. Then there is a difference of 9 % in terms of displacement to fracture (0.77 and 0.84 mm). Such displacements to fracture will induce different value of strain to fracture and it is thus important to account for this variability. The low tensile forces ($F_{y,max} \sim -1\text{kN}$) are due to the Poisson effect (material is extended in the axial direction and shrinks in the other 2 directions). A part can be due to the aforementioned small specimen rotation around Z axis.

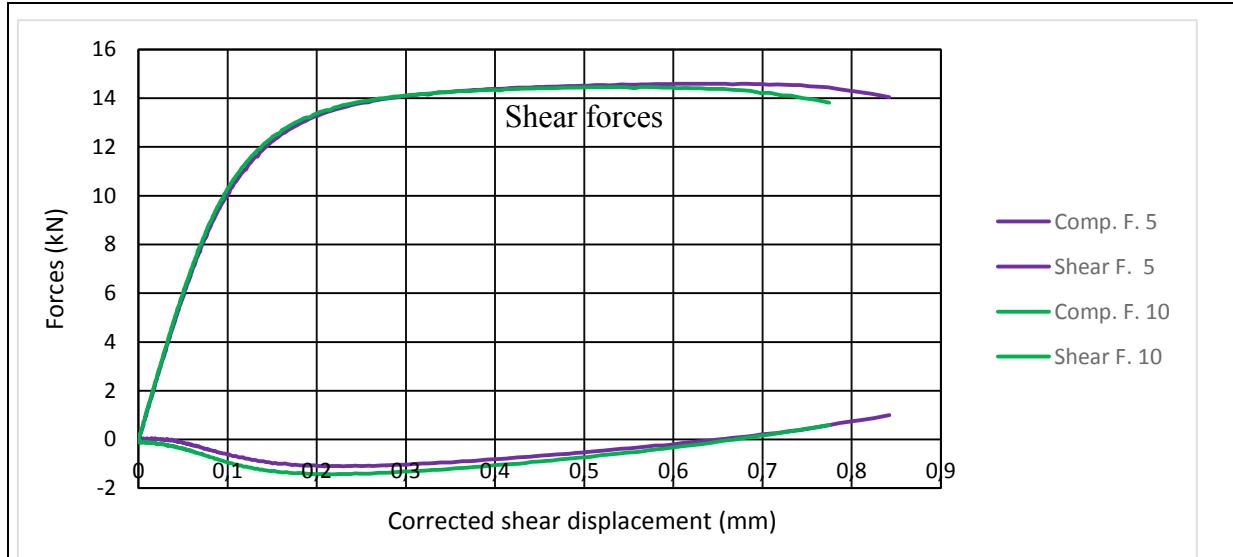


Fig.IV.9: evolution of the shear and tensile forces as a function of the corrected shear displacement
 // évolution des efforts de cisaillement et de compression en fonction des déplacements corrigés.

From the above analysis of the first results, the experimental methodology may now be precisely described. Due to the machine compliance, real displacements will be extracted from DIC data. They will be compared to the numerical simulations in Chapter 5. Because of the strain localization in a thin band (which is the aim of the double curvature geometry), deformations cannot be measured accurately: the resolution of the paint spot pattern is too low. VIC calculation of strain would give a value averaged at the scale of the resolution, rather than the needed local value. Deformation will thus be calculated with numerical simulations.

IV. 2. 1. b Experimental results

Four distinct loading conditions were applied on the butterfly specimen (-10° , 0° , $+5^\circ$ and $+90^\circ$). The last one corresponds to tensile stress state and will be detailed in the next section (IV. 2. 2) dealing with the characterization of the material at high level of stress triaxiality.

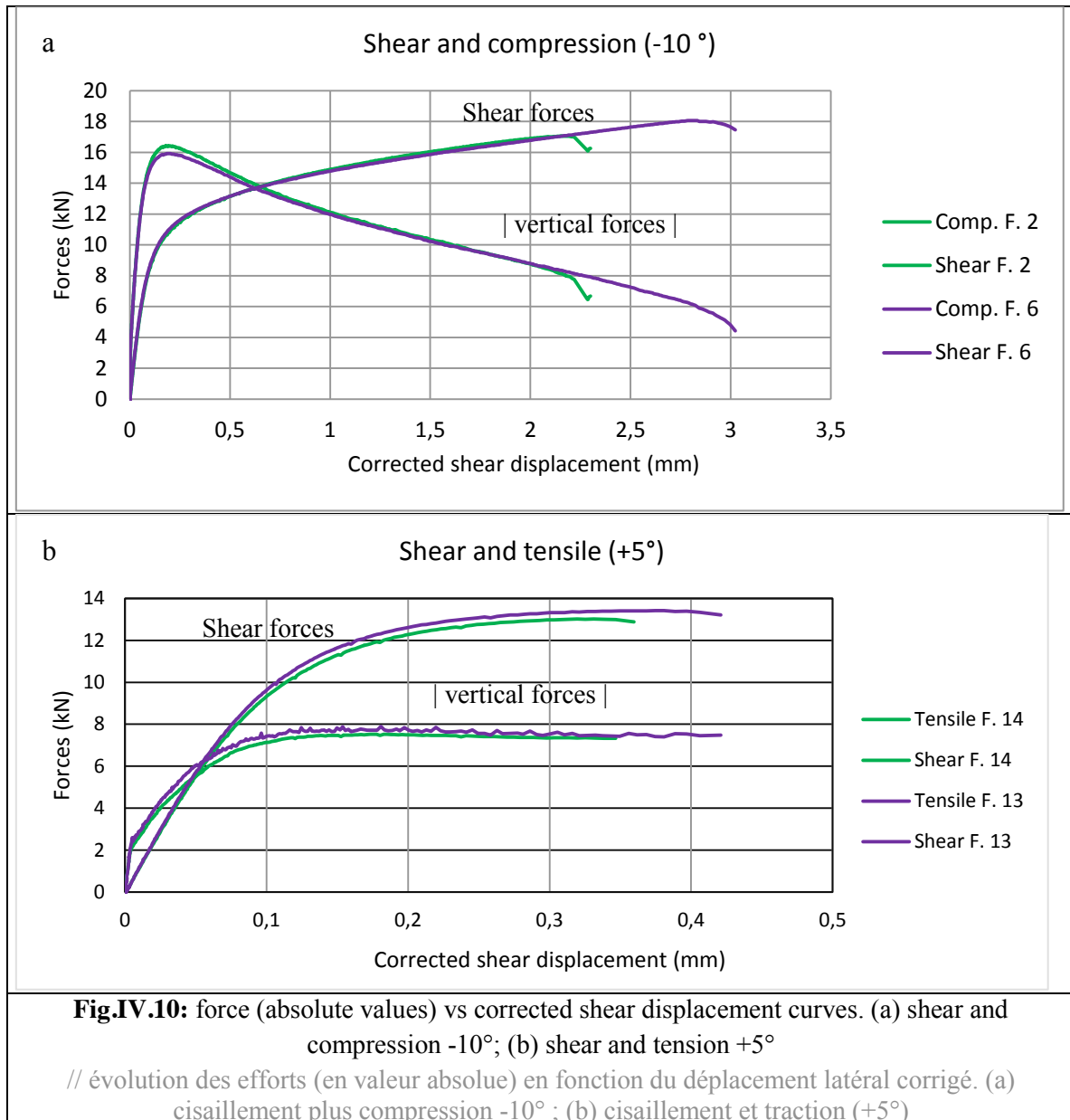


Fig.IV.10 (a) plots the evolution of the forces as a function of the corrected shear displacement for the shear case with compression. The compressive forces were multiplied by “-1” to make their reading easier on the same graph as the shear forces. The displacement to fracture increases a lot between the pure shear and the shear + compression tests (+300%). Material ductility must follow the same evolution.

The repeatability of the experimental curves with raw displacement is shown in Appendix IV.1. Note that until 2 mm displacement, the curves are almost superimposed. However, in terms of displacement to fracture, the scatter is significant with a difference of 33 % (2.28 and 3.04 mm). The plotted curves are the extrema ones. Displacements correction was done only on those, but the behavior of the two others tests for the repeatability (with raw displacements) can be seen in Appendix IV.1. **Fig.IV.10** (b) plots the force-displacement curves for the shear and tensile tests. Scatter of the displacement to fracture is about 17 %. The dispersion decreases to 9% for pure shear. The geometric measurements of these specimens did not show any machining defect that could explain the discrepancies. Surface roughness, which is directly linked to the machining process, could be questioned. Indeed a higher roughness may give locally stress concentration and accelerate crack initiation; such roughness is

usually a bigger issue for fatigue crack initiation. These cracks will propagate very quickly through the whole section because of the design of the specimen. Machining process of these butterfly specimens is tricky and is one of their main drawbacks. It is however difficult to quantify rigorously the influence of this default on the variability issue.

IV. 2. 1. c Fracture surfaces study

The study of the fracture surfaces is important: on such specimens, the stress state at failure is not homogeneous on the whole fracture surface. By looking at the dimple size and shape, one can check which mechanism is dominant (shear or tension).

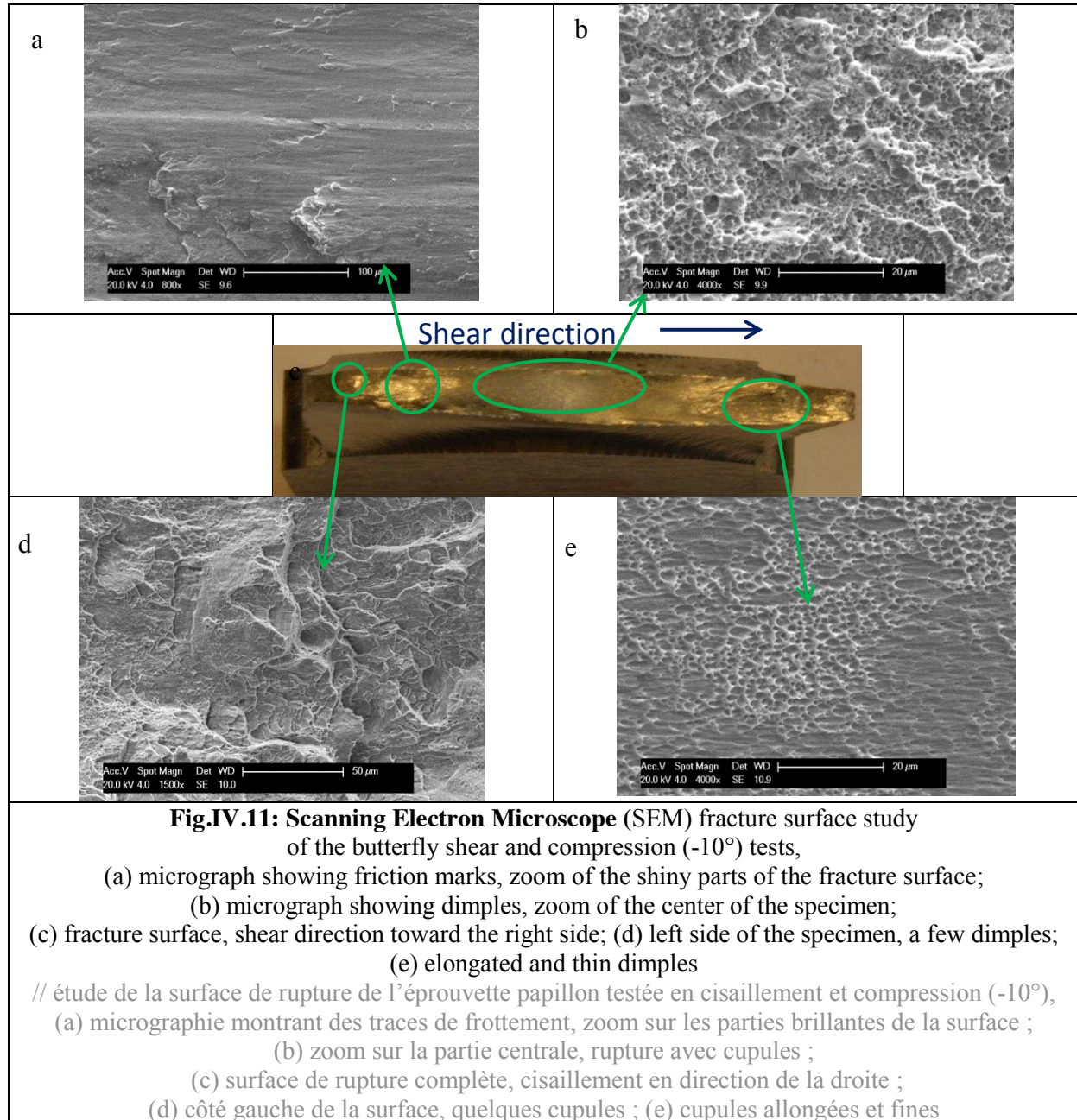


Fig.IV.11, Fig.IV.12 and Fig.IV.13 illustrate the fracture surface of the butterfly specimen respectively in shear with compression (-10°), pure shear and shear with tension ($+5^\circ$). As expected, there are dimples on the three fracture surfaces, meaning ductile fracture. They can be thin and

stretched toward the shear direction as in **Fig.IV.11** (e), **Fig.IV.12** (b). This characterizes a shear dominated fracture mode. This was indeed the expected stress state at failure. However, in some other areas, friction marks between the two parts of the specimen prevent from seeing the dimples. It can be seen on the three specimens (**Fig.IV.12** (a), **Fig.IV.13** (a and d) and **Fig.IV.11** (a)), but it is more noticeable on the specimen with compression since it increases friction areas after failure. It can be seen without SEM: some areas are very shiny on **Fig.IV.11** (c), suggesting low roughness.

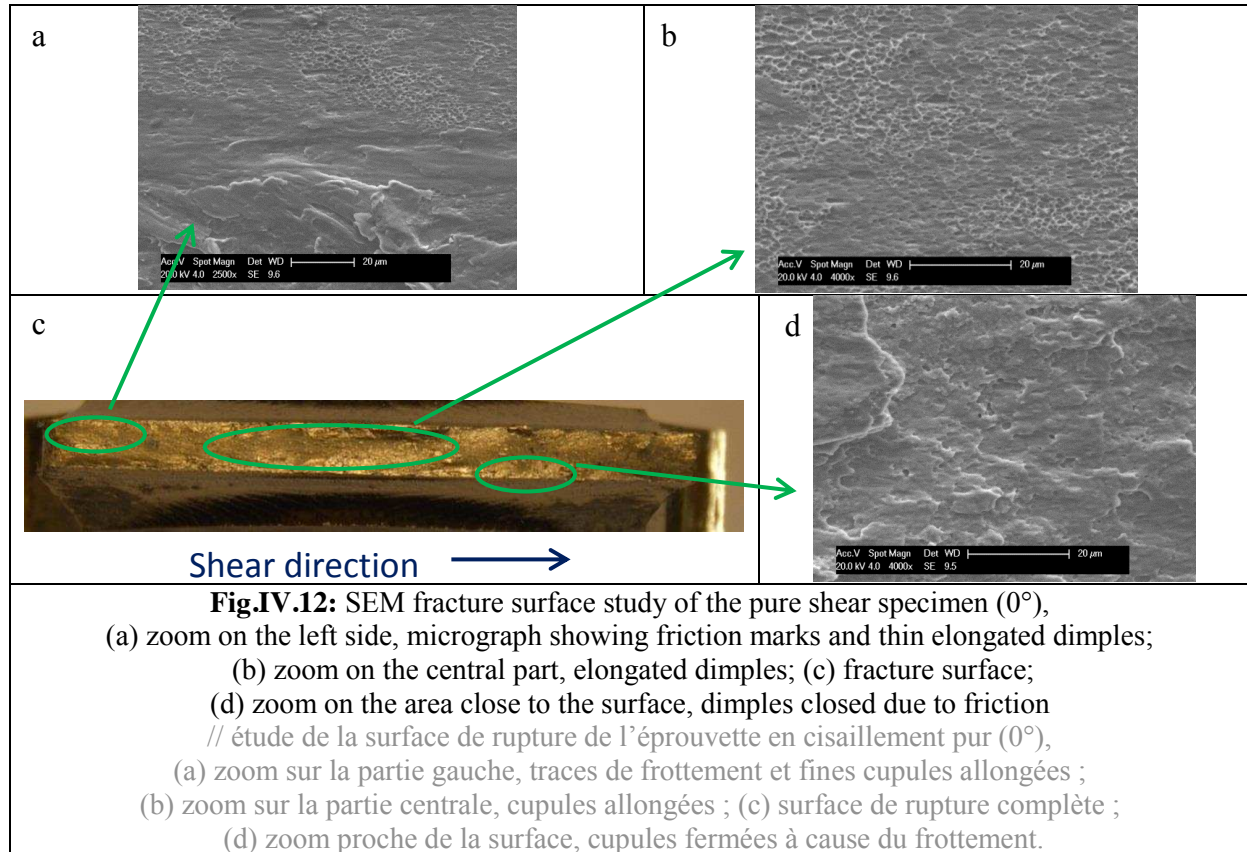
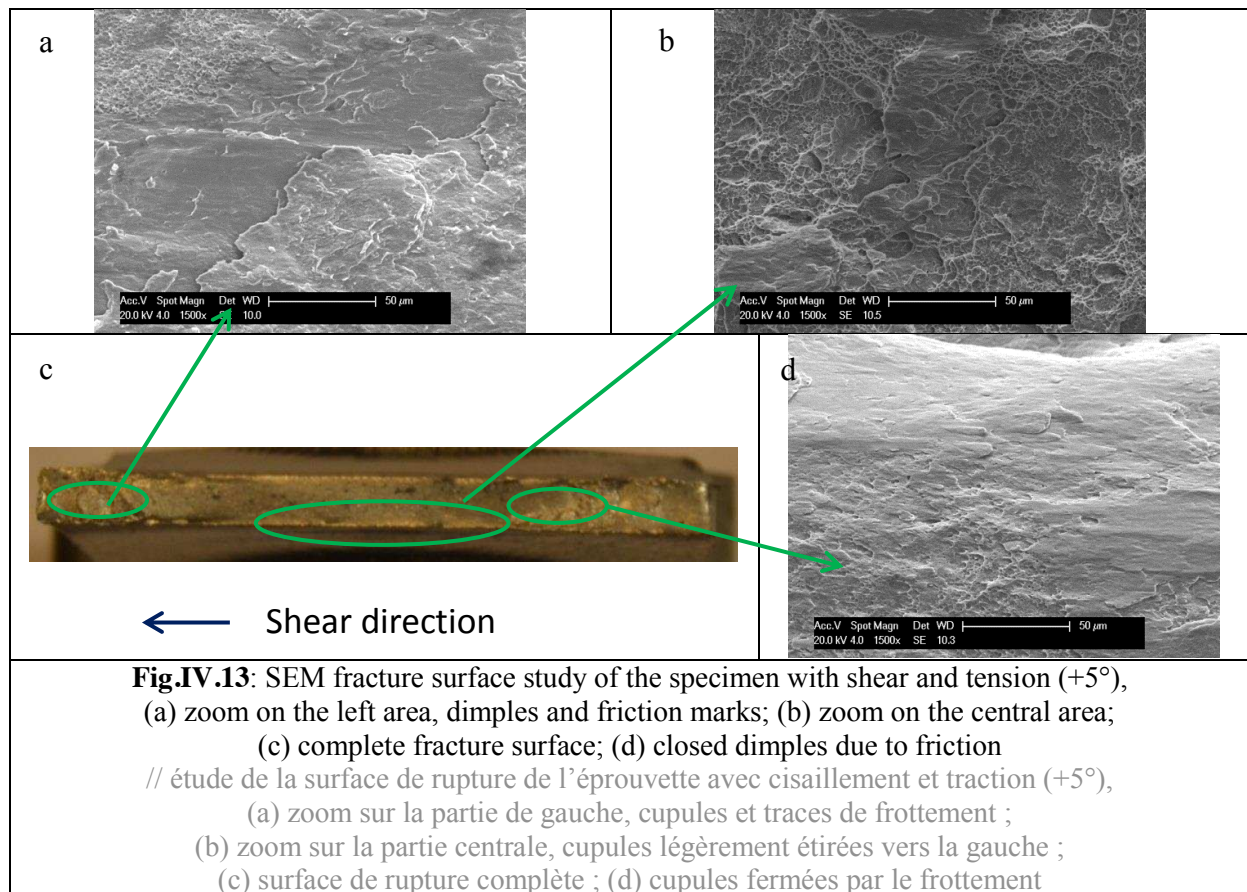


Fig.IV.11 (e), **Fig.IV.12** (d) and **Fig.IV.13** (d) dimples were partially closed due to friction. On the other hand, on **Fig.IV.11** (d) dimples are less stretched and bigger. This shows this area fails in a stress state closer to tension. This area is located on the rear side of the shear direction. Because the displacement to fracture is high, the deformation in the gage area is quite high as well. Then, sides can be submitted to tensile stress state. This is the main drawback of the induced shear specimen, even though strain homogeneity is improved thanks to the double curvature: decreasing triaxiality, compression increases at the same time the displacement to fracture so much that the rear side is stretched and the stress state ends up tensile.



IV. 2. 1. d Discussion

Material was characterized in a stress state range close to shear. Adding either compressive or tensile stresses enables to represent the stress state met by the material during tooth failure:

- before the crack opens, the material is sheared due to the displacement imposed by the tool. (shear and compression and pure shear tests),
- during crack propagation, at the tip of the opening crack, shear and tension coexist .

Adding compressive stress increased a lot the displacement to fracture, thus the material ductility must increase as well when stress triaxiality is negative. Until fracture, repeatability of the tests is very good; curves are often superimposed. However, results showed a large scatter of the displacements to fracture. Specimen dimensions were checked and their repeatability is good. This is confirmed by the repeatability of the curves until fracture. Specimens with machining imprecisions would have differences in terms of plastic behavior. This scatter is likely to be due to a possible roughness induced by the machining or to the presence of microdefects or inclusions in the useful area, which is relatively small. Indeed, the little grooves formed by the drill can create locally a stress concentration and accelerate crack initiation. Thus, the highest value will be used. This will be accounted for in the final discussion for the application to tooth failure.

Fracture surface analysis carried out on the three loading cases shows surfaces with elongated dimples. This is typical for shear fracture. On some other areas, dimples were closed or even totally smeared covered due to the friction between the two parts of the specimen. Finally, areas with bigger and wider opened dimples showed that failure occurred in stress state close to tension. Due to the localization of the deformations and the brutality of the crack propagation, DIC can neither assess crack initiation

locus, nor follow the crack propagation through the whole specimen. However, due to the double curvature design we are confident that failure initiates at the center of the specimen.

IV. 2. 2 High triaxiality characterization

The core material was characterized at low stress triaxiality with the butterfly specimens. It is mandatory to complete its characterization at high level of stress triaxiality. This is done with flat notched and grooved tensile tests. **Fig.IV.14** shows the design of the test. **Fig.IV.14** (a) shows the well-known flat tensile specimen widely used for mechanical characterization. **Fig.IV.14** (b) illustrates the notched tensile specimens; the notch depth is in the width direction of the specimen. There are three distinct notched specimens (TN7, TN7-2 and TN9; the number refers to the radius of curvature); the notch radius and the width between the notches vary to give three different stress states. Notch dimensions are detailed in **Table.IV.2**. **Fig.IV.14** (c) illustrates the grooved tensile tests, grooves are machined in the thickness. There are two grooved specimens (TG1 and TG7, dimensions in **Table.IV.2**). Final stress triaxiality and Lode angle parameter are given in the table as well. Stress triaxiality at failure for all the tests ranges from 0.58 to 1.1. These values are obtained by simulation using the Hollomon behavior law given by Faurecia at the beginning of the project. The identified material behavior law identified later on will give slightly different value, and stress triaxiality and Lode angle parameter evolution will be plotted versus plastic strain in **Fig.V.9**. Therefore, a wide stress state range can be covered with tensile tests.

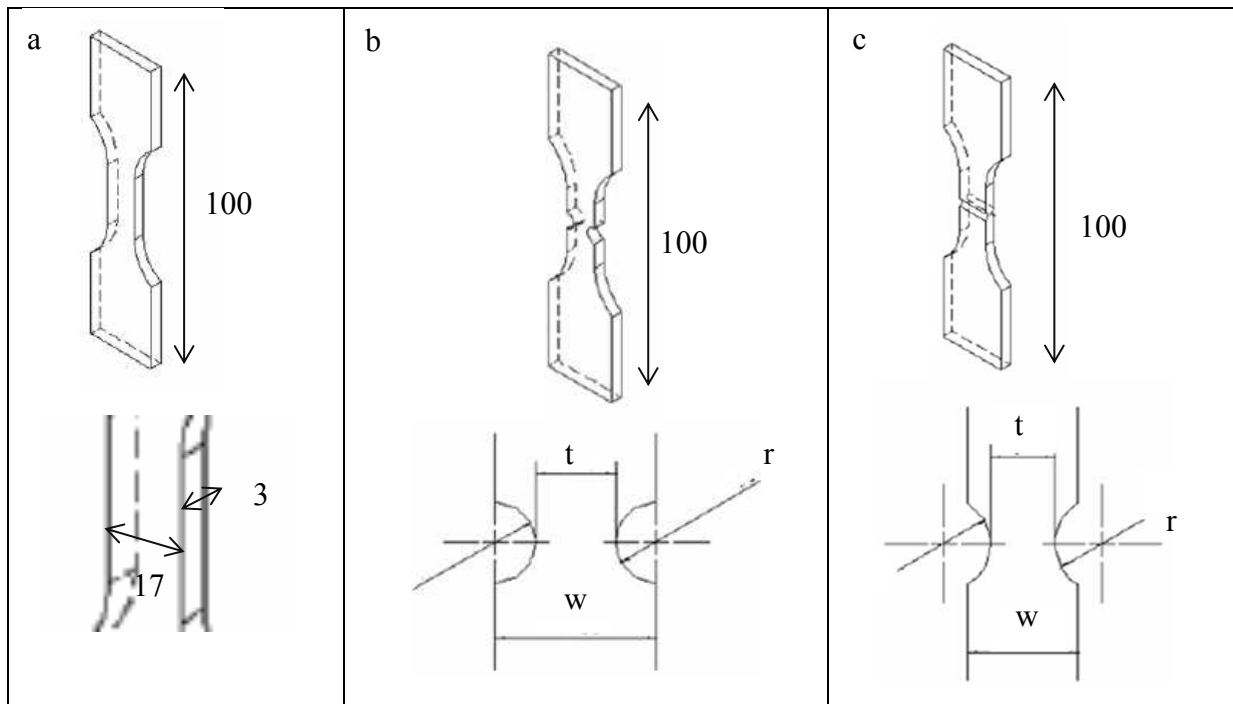


Fig.IV.14: tensile test specimens, (a) flat tensile specimen (dimensions in mm);
 (b) notched tensile specimen (notch in the width, TN7, TN7-2, TN9), the notch dimensions are given in **Table.IV.2**; TN7-2 differs from TN7 by its deeper notch
 (c) grooved tensile specimen (groove in the thickness TG1, TG7), the groove dimensions given in **Table.IV.2**

// éprouvettes de traction, (a) traction plane (dimensions en mm) ;
 (b) éprouvette de traction entaillée dans la largeur (TN7, TN7-2, TN9), entaille détaillée sur le second dessin et dimensions données dans le **Table.IV.2**; noter l'entaille plus profonde de TN7-2 par rapport à TN7 ; (c) éprouvette de traction entaillée dans l'épaisseur (TG1, TG7), entaille détaillée sur le second dessin et dimensions données dans le **Table.IV.2**

	T0	TN7	TN7-2	TN9	TG1	TG7
t (mm)	x	7	5	12	1.5	1.5
w (mm)	x	17	17	17	3	3
r (mm)	x	7	7	9	1.5	7
stress triaxiality	0.58	0.73	0.76	0.75	1.1	0.81
Lode angle parameter	0.59	0.06	0.51	0.1	0.01	0

Table.IV.2: notch and groove dimensions, values of stress triaxiality and Lode angle parameter at failure

// dimensions des entailles, valeurs de la triaxialité et paramètre de Lode à rupture.

IV. 2. 2. a Experimental method

Specimens are tested on a universal testing machine MTS Landmark 250. Hydraulic jaws are used to grip the specimen. 3D DIC VIC® system is used to measure the real displacements, correcting for the machine compliance. **Fig.IV.15** (a) shows the experimental set up. Two cameras and two spotlights point to the specimen being tested. Paint spot pattern is applied on the active part of the specimens. It is mandatory that no paint is applied on the surfaces where the jaws grip the sample. **Fig.IV.15** (b) shows four tensile specimens without any paint; **Fig.IV.15** (c) illustrates a TN7 specimen with random paint spot pattern applied on it. The holes were used for the machining process to ensure a good repeatability for the setting up on the machine. They do not alter the tests since they are located under the jaws.

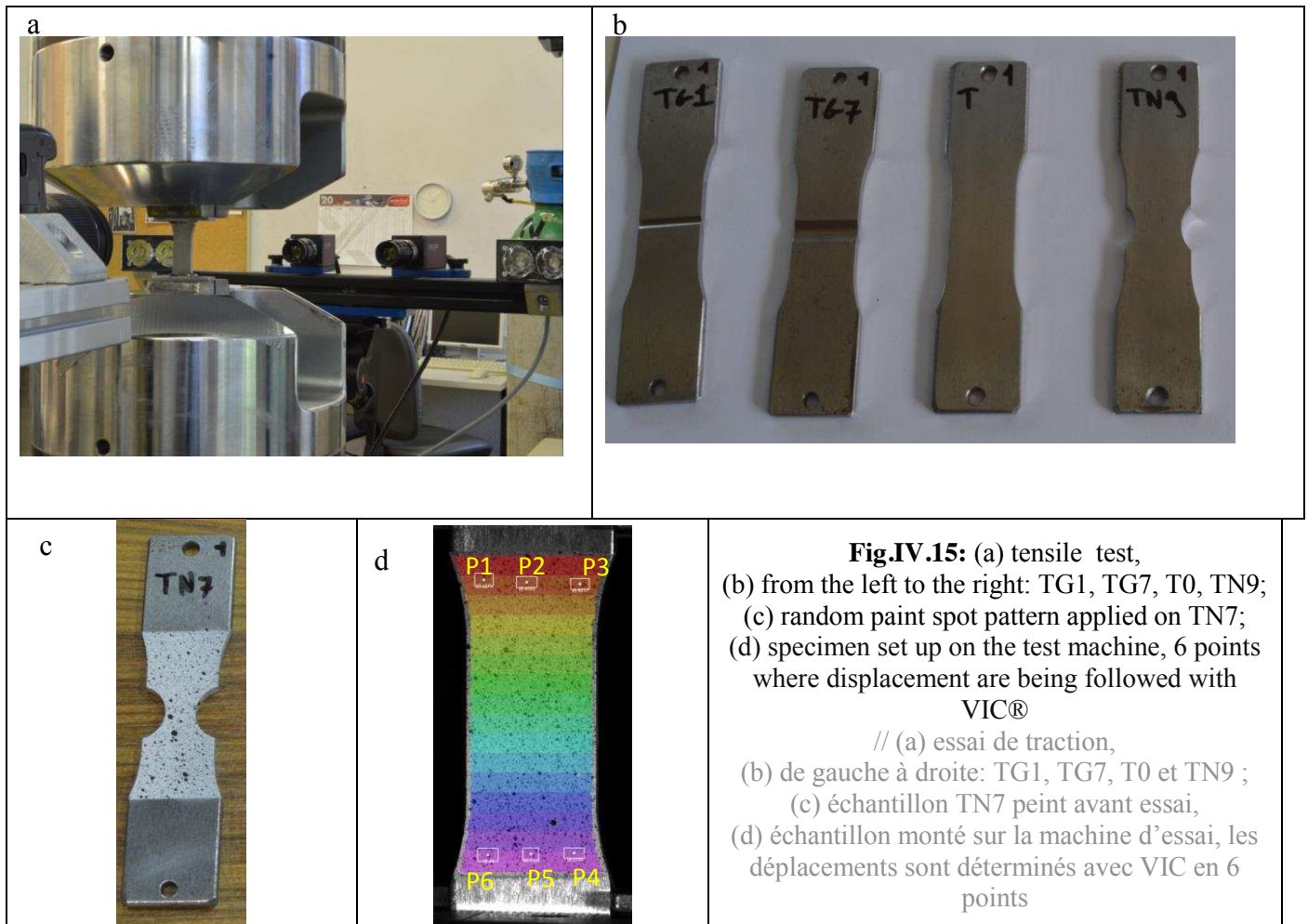


Fig.IV.16 plots the evolution of the force as a function of the uncorrected jaw displacement. Repeatability is very good. The small displacement oscillations are due to the acquisition system. Test T0-4 has a light gap at 0, but it will be fixed by using the corrected displacement.

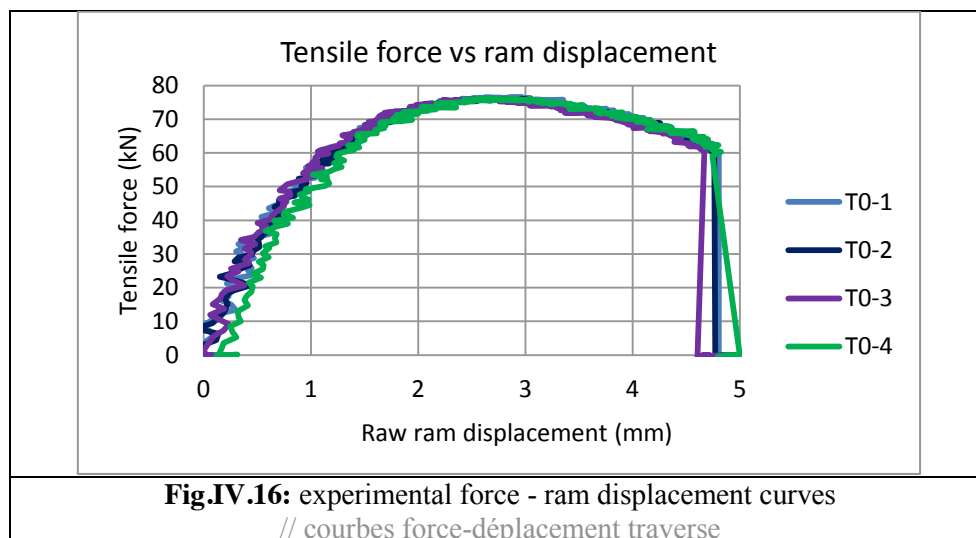
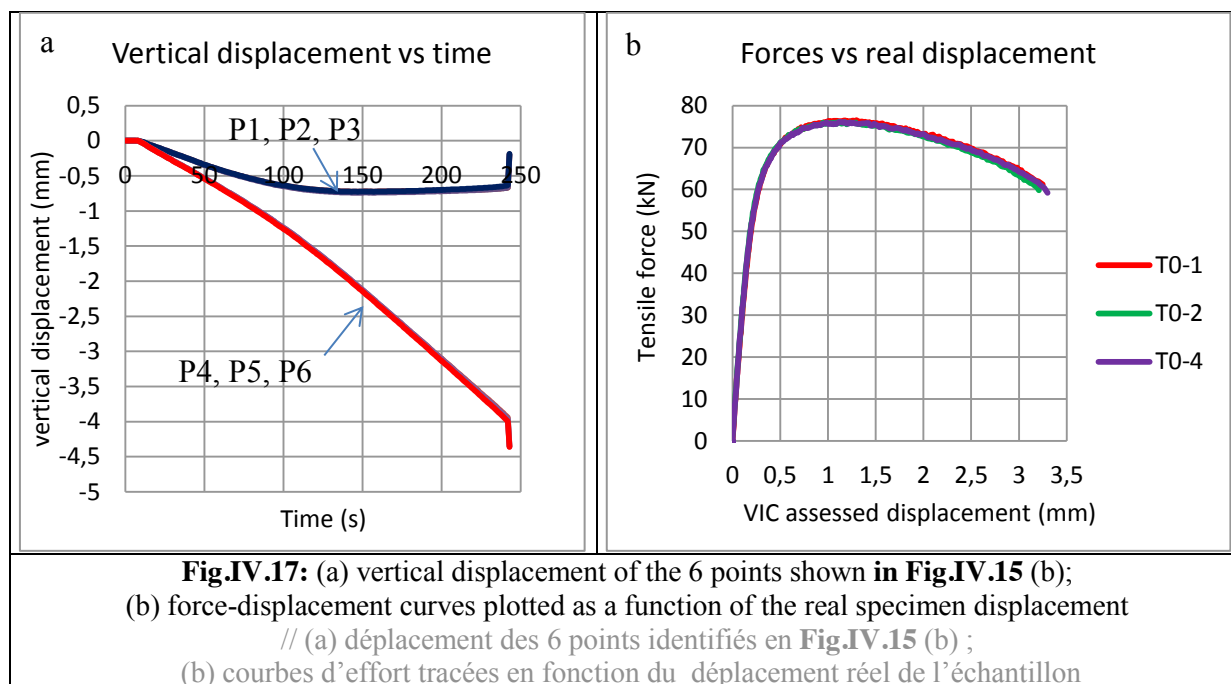


Fig.IV.15 (d) is a picture extracted from the VIC analysis. Displacements are determined in six points. These points are as far as possible from the center, very close to the jaws so that they undergo no strain. These displacements will serve as boundary conditions for the numerical simulations shown in Chapter 5. **Fig.IV.17** (a) plots the vertical displacement of the six points identified in **Fig.IV.15** (d). There is no discrepancy between the displacements; the lower jaws are mobile. The upper jaws are supposed to be fixed, but they move because of the machine stiffness (spurious displacement of about 0.7 mm). Finally, **Fig.IV.17** (b) plots the forces evolution as a function of the corrected displacement. Repeatability is very good, curves are superimposed; displacement to fracture varies from 3.21 (T0-2) to 3.29 mm (T0-4), a scatter lower than 3%. This level of repeatability was expected since this type of specimen requires the least machining. There is indeed no groove or notch; therefore there is no machining variability issue. Anyway, all the specimens were measured before being tested, details are shown in Appendix IV.2.



The same methodology is applied to assess the displacement on the other shapes of tensile tests. The points must be far enough from the grooved or notched areas to have no plastic deformation. Displacements measured will be compared to the numerical ones.

IV. 2. 2. b Experimental results

Fig.IV.18 (a-e) plots the evolution of the force as a function of the corrected displacement for the tensile specimens. Repeatability is very convincing, either in terms of plastic behavior or displacement to fracture. **Table.IV.3** gathers the minimum and maximum displacements to fracture. Scatter is inferior to 7 % and equal to or lower than 5% in most of the tests. This ensures an accurate characterization of the material.

	T0	TG1	TG7	TN7	TN7-2	TN9	Butt-T
min displacement to fracture (mm)	3.21	0.26	0.4	1.02	0.97	1.18	0.13
max displacement to fracture (mm)	3.29	0.28	0.42	1.07	0.99	1.25	0.153
(max-min)/min *100	2.5	7	5	5	2	6	17

Table.IV.3: minimum and maximum displacements to fracture for the tensile and butterfly-T tests (pure tension)

// déplacements minimum et maximum à rupture pour les essais de traction et butterfly-T (traction pure)

Fig.IV.19 plots the evolution of the force-displacement curve for the butterfly specimen tested in tension. Experimental curves with jaw displacement are in Appendix IV.1. The repeatability on the vertical force is good. The **raw displacements** to fracture are 0.84 (Tensile 9), 0.99, 1.04 and 1.07 mm (Tensile 16). Scatter is a bit high due to the specimen 9. Indeed, on the three others, scatter is about 7 %. The specimen 16 is the one with the highest displacement to fracture. On the **corrected displacement**, a 7 % scatter decreases the corrected displacement from 0.153 to 0.148 mm. So the displacement to fracture of 0.15 mm is retained for the specimen. As seen in Table.IV.3, the scatter of the displacement to fracture due to specimen 9 is higher than for the tensile tests, reaching 17%. This confirms the difficult machining process of the butterfly specimen is the critical factor for the test reproducibility. The shorter displacement of the specimen 9 is likely due to a machining defects.

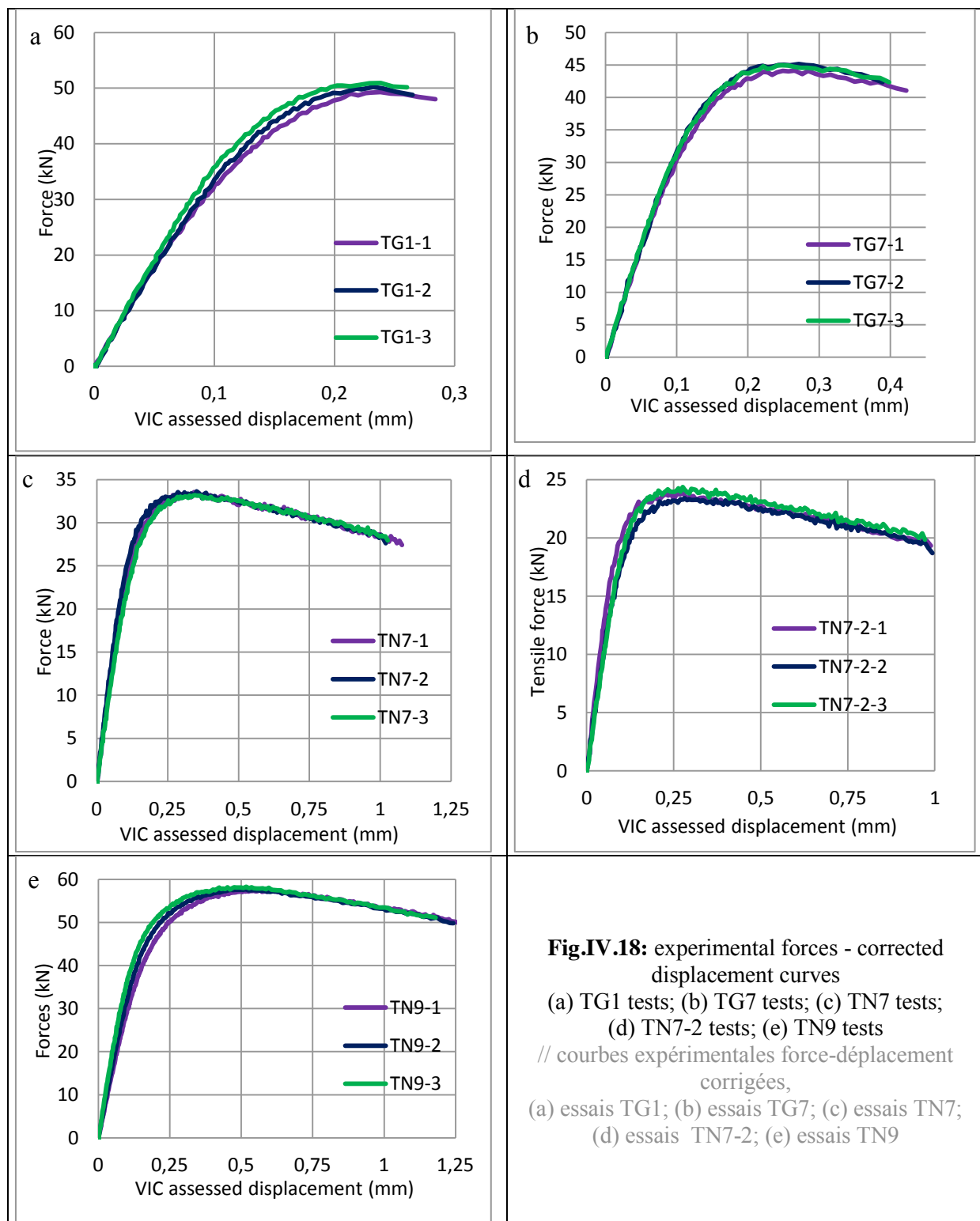
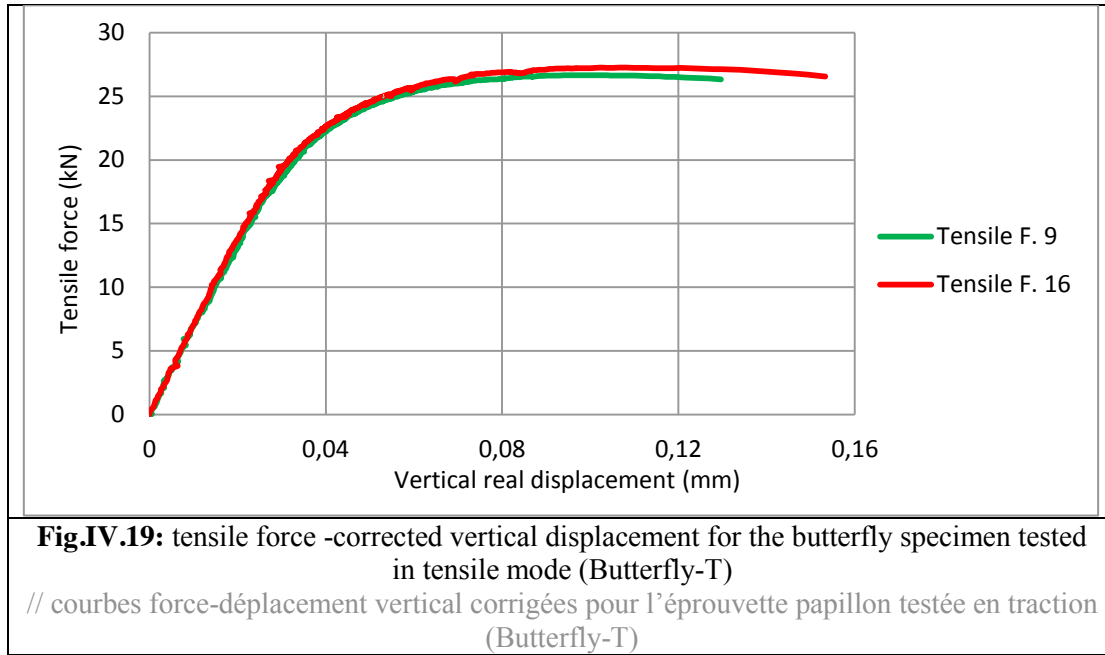
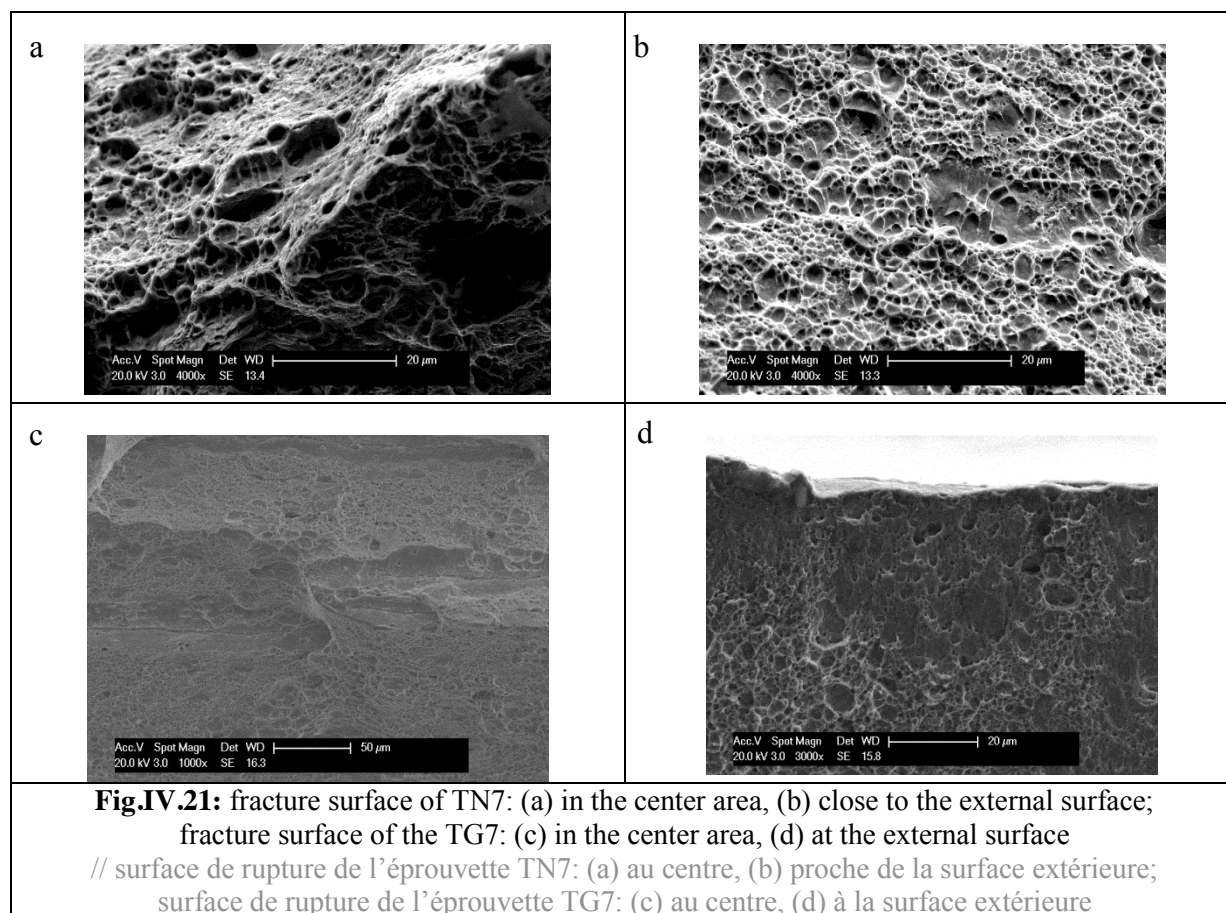
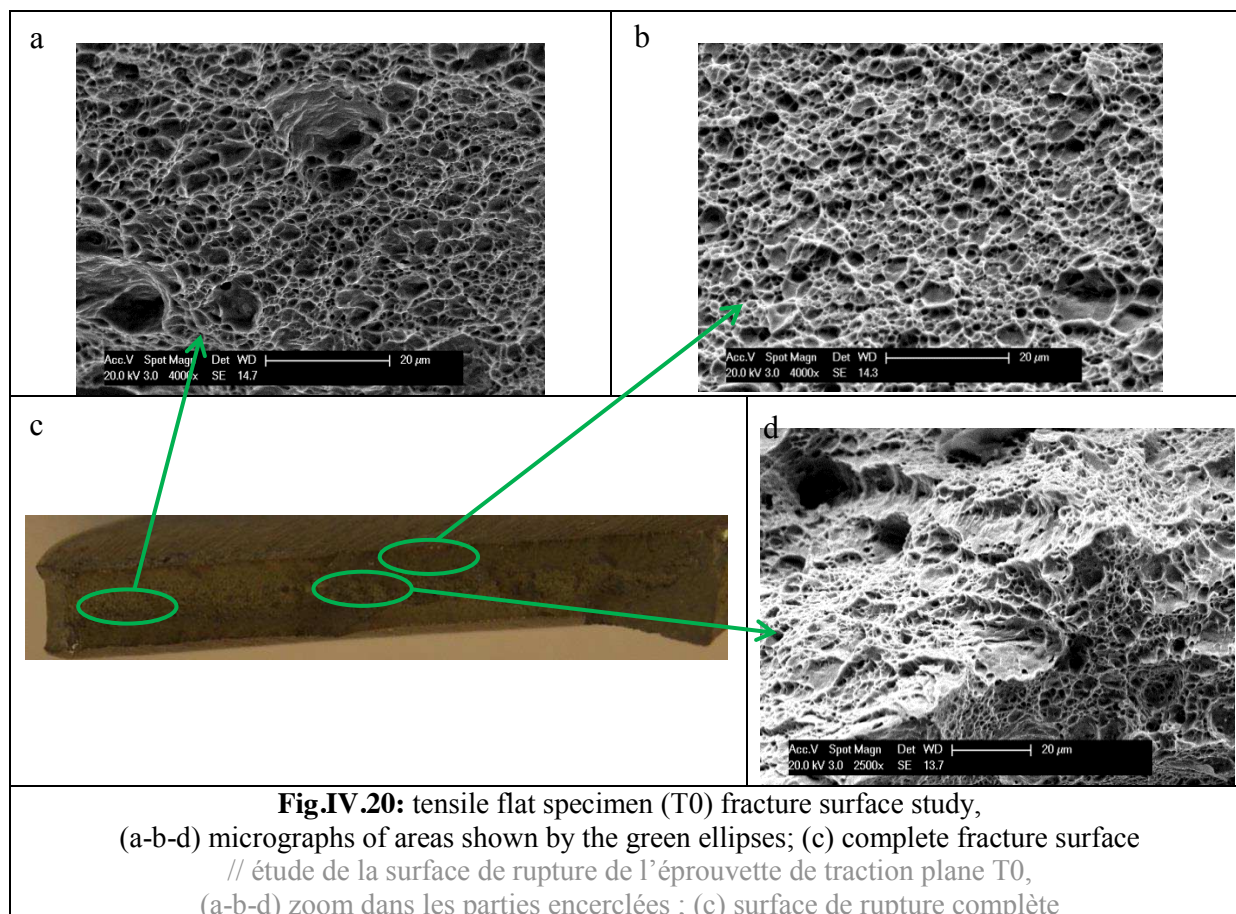


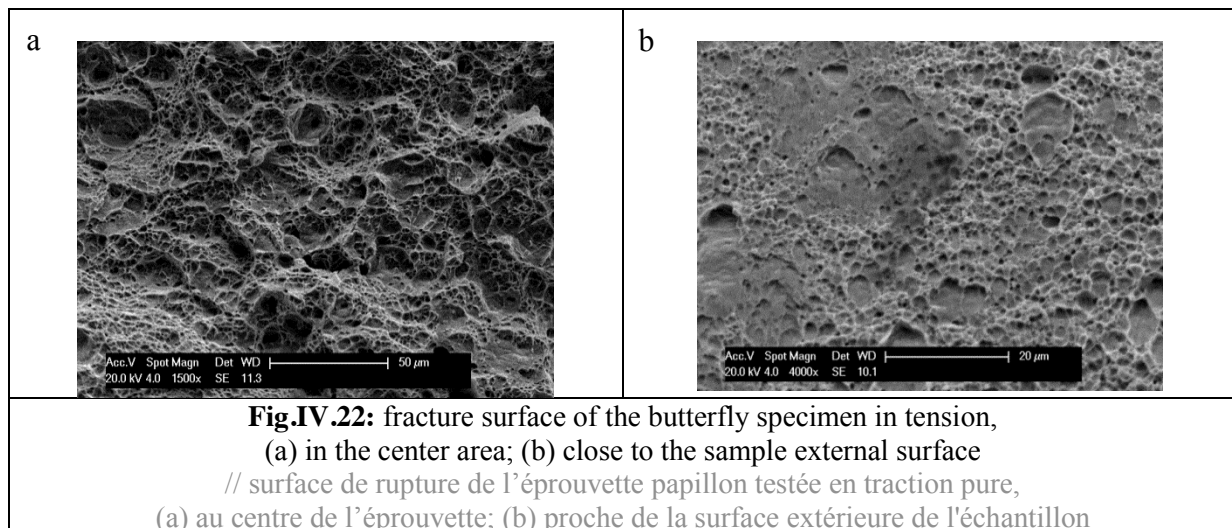
Fig.IV.18: experimental forces - corrected displacement curves
 (a) TG1 tests; (b) TG7 tests; (c) TN7 tests;
 (d) TN7-2 tests; (e) TN9 tests
 // courbes expérimentales force-déplacement corrigées,
 (a) essais TG1; (b) essais TG7; (c) essais TN7;
 (d) essais TN7-2; (e) essais TN9



IV. 2. 2. c Fracture surface Analysis

Tensile tests cover stress states where the triaxiality at failure varies from 0.58 for the flat tensile specimen until 1.1 for the grooved specimen with the lower radius (TG1). It is interesting to check whether this influences the fracture surfaces and how. Micrographs of the fracture surfaces are seen on **Fig.IV.20** and **Fig.IV.21**. Surfaces are covered by dimples of homogeneous size. One can notice they are quite elongated close to the external surfaces of the sample (in the notch for TN7), and rather open and oriented toward the normal to the surface at the center. Dimples elongation comes from the necking stage where material is sheared. This is why it is seen on the areas close to the surface of the specimen (**Fig.IV.20** (b), **Fig.IV.21** (b and d)). One must account for the magnification difference between the **Fig.IV.21** (c and d). The same remark can be done for the fracture surface of the butterfly in tension (see **Fig.IV.22**): dimples are very elongated close to the sample surface (in the notch) (**Fig.IV.22** (b)) and wide open in the central area (**Fig.IV.22** (a)).





IV. 2. 2. d Discussion

Material has been characterized at a high level of triaxiality with tensile specimen and butterfly-T specimen. Repeatability of the tests is good. Most of the curves are superimposed for the elastic and plastic part. Scatter of the displacements to fracture is small except for the butterfly tensile specimen where the scatter reaches 17%. Fracture surfaces are covered by open dimples in the central area and elongated ones close to the surface due to the necking process.

IV. 2. 3 Conclusion

The core material has been characterized at low and high levels of stress triaxiality. It shows a very high level of ductility for a heat treated material, especially at low triaxiality. Multiple tests are done to cover a wide range of stress state, from the shear with a bit of compression up to tensile specimens with low radii to increase the stress triaxiality ratio. It is however difficult to see the influence of the Lode parameter on the fracture surface, this is why nothing is said about it here. Its influence will be characterized and discussed in Chapter 5 where it is an output of FE simulations. This gives ten data points to assess the parameters of the failure criterion of the core material.

The external layer must be characterized as well and this is the topic of the next section.

IV. 3 Characterization of the CN layer

The characterization of the external layer is trickier because it is impossible to obtain a bulk material with only the CN layer. Tests must thus be done with the complete CN material (FCN = CN layer + core material). Bending tests are widely used to characterize graded and coated materials as seen in Chapter 2. Unlike three point bending test, the four point bending test (4PBT) submits the material to a homogeneous tensile stress state on the external side. Its intensity varies in the thickness of course, but between the loading cylinders, at a given thickness, stress is homogeneous in the two in-plane directions. Thus the test is adapted to characterize the external layer in tension.

In addition, tensile tests are performed with the whole core + CN layer material. These tests will be compared to the flat tensile test done previously to characterize the core material. So, the influence of the CN layer on fracture in tensile stress state will be quantified.

These specimens are extracted from 3.5 mm thick rolled 20MnB5 sheets; CN treatment is following the extraction; remember the total thickness of the CN layer is 400 μm . The final step is the machining: tensile specimens section is reduced to create the active area; long edges are machined on the 4PBT to better see the cracks propagation. Unfortunately, the supplied specimens were not perfectly flat due to the cutting processes used: most of them were slightly bent and some of them were also twisted. These imperfections may make the final interpretation more difficult.

IV. 3. 1 4PBT

IV. 3. 1. a Experimental method

The 4PBT aims at characterizing the failure mechanism of the CN layer. It is a brittle material, so cracks will likely go through the whole CN layer and stop inside the transition area. In order to characterize the CN layer fracture one needs to assess the stress level at the onset of failure, and the propagation depth of cracks. Tests are not done until complete failure of the specimen since the core material was characterized previously. They are stopped before, when displacements are high enough to have cracks visible at the surface. In order to check cracks propagation, multiple tests were done from a displacement of 8 until 20 mm.



Fig.IV.23 (a) shows the experimental test bench set up on a tensile test machine. Specimen is in contact with four ground cylinder rods, made out of cemented steel; their length is 50 mm and their diameter 10 mm. The span between the loading cylinders is 50 mm and 120 mm between the two lower ones. Specimens dimensions are 220x35x3.5 mm. Width has been reduced from 45 mm: 5 mm were ground and polished on each side. Therefore, CN layer and the core material can be observed, together with crack propagation in the material.

IV. 3. 1. b Results

Fig.IV.24 plots the force-displacement curves. A ramp displacement is imposed; elastic spring back is controlled as well. Ten specimens are tested. While loading, sharp noises are heard after 8 mm displacement. This can be due to the initiation and propagation of cracks in the external layer.

Some specimens are cut to check the presence of cracks and measure their depth. **Table.IV.2** collects the results. The observed samples are taken out of the center area of the bending specimen where stress state is homogeneous, using a laboratory micro cutting machine. No crack is observed on the specimen with the lowest displacement (8 mm). At 9 mm, a few cracks are initiated, but crack density remains very low. **Fig.IV.25** (a) shows a crack issued from the specimen tested at 9 mm displacement. A crack, initiated at the surface, propagated until 90 μm depth. Furthermore, one can see some little cracks deeper under the blue circle. They are visible up to 200 μm deep. It is hard to say if these small cracks are due to coalescence of microvoids or are an extension of the major crack that cannot be seen correctly in this particular cutting plane. Due to the stress repartition in a bending specimen, the second hypothesis is more likely. Polishing may have smeared the thinner part of the crack.

Fig.IV.25 (b) illustrates two cracks observed on the specimen with the highest displacement, 20 mm. On this specimen, cracks density is obviously higher with roughly one crack every 3 mm. The left crack is wide open (about 20 μm width) and has propagated until 260 μm deep. The one on the right is thinner (a few microns) and shorter. Crack depth reaches an average of about 230 μm .

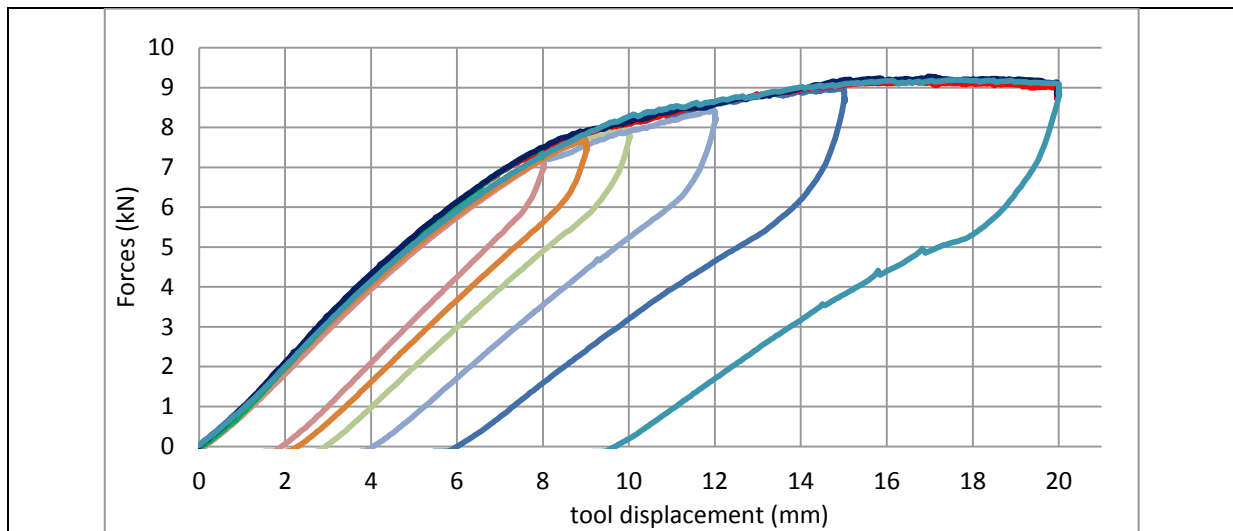


Fig.IV.24: force-displacement curves for the four point bending specimens.

// courbes force-déplacement pour les essais de flexion 4 points

Max displacement (mm)	8	9	12	20
Crack density (number crack/mm)	0	0.1	0.25	0.3
Number of cracks	0	2	6	8
Average depth (μm)	0	90	231	227
Standard deviation (μm)	0	16	9	15

Table.IV.4: Cracks initiation and propagation study on four point bending specimens

// étude de l'initiation et de la propagation des fissures sur les échantillons de flexion 4 points

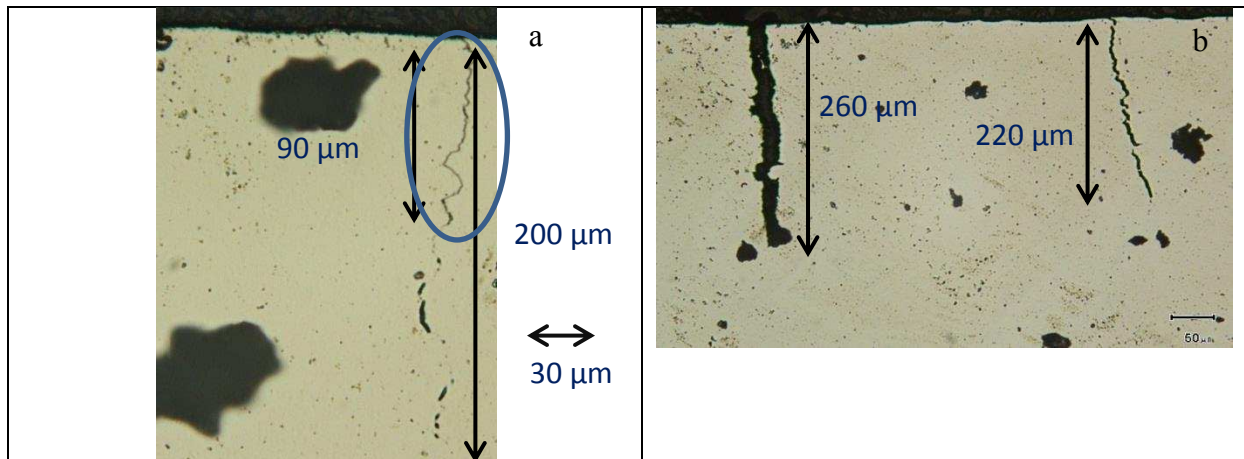


Fig.IV.25: cracks observations after four point bending tests,
 (a) after 9 mm displacement, (b) after 20 mm displacement
 // observations de fissures sur éprouvettes de flexion 4 points,
 (a) après 9 mm de déplacement; (b) après 20 mm de déplacement

There is a change of direction in the fracture surface. It is not perpendicular to the loading direction anymore, there is an angle and then it is the ductile fracture of the core material. This phenomenon has been described in the literature on nitrided steel ([Firrao & Ugues, 2005]) and in our own 4PBT as illustrated with **Fig.IV.26**. It shows a crack in the CN layer slightly propagating in the transition layer. It must be noticed that these specimens were submitted to a longer CN treatment than the one applied to previous 4PBT specimens. Indeed, applied treatment corresponds to the one applied on the flange, the other CN part of the recliner. Treatment is longer to have deeper penetration of the carbon and nitrogen atoms, and thus thicker hard surface for the contact resistance. This is why the depth of the observed crack is about 390 μm. The angle formed by the bifurcation is about 45°. The crack depth cannot be compared to the ones observed here, but the mechanism can. Especially the crack bifurcation when it reaches the more ductile area (same phenomenon was being observed in the II.1.3 part dealing with the damage of FGM).

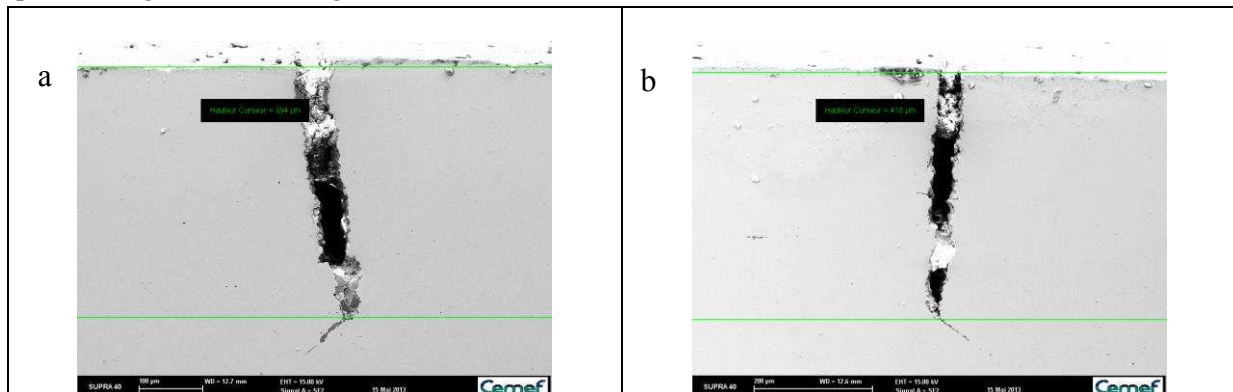


Fig.IV.26: 4PBT specimen, with a longer CN treatment, tested until complete failure 62 mm displacement, SEM observation of a crack in the CN layer. CN treatment is longer on these tests (105' instead of 60')

// échantillon de flexion 4 points, avec un traitement de CN plus long, testé jusqu'à rupture complète déplacement de 62 mm, observation MEB d'une fissure dans la couche CN. Le traitement sur ces échantillons est plus long (105' au lieu de 60')

IV. 3. 1. c Discussion

This test aims at characterizing the fracture process of the external layer in tensile mode. It shows an array of cracks visible through the whole width of the specimens (see **Fig.IV.27**). As a brittle material, cracks propagate through the whole CN layer abruptly (thickness and width). They are initiated

between a tool displacement of 8 and 9 mm. Sharp noises started at the same displacement and popped until 20 mm of displacement. If the two are related, this shows the continuous evolution of the cracks initiation and opening. Cut and polished sections of the specimens show cracks whose initial depth seems to start around 90 μm as seen on **Fig.IV.25** (a) (black spots are grains removed due to cutting and polishing).

Note that it is mentioned in the literature that cracks in CN material may initiate not at the surface but deeper at the interface between the CN layer and the core material due to martensite formation sequence and residual stresses ([Kanchanomai & Limtrakarn, 2008]). It was observed on fatigue tensile tests. However, in the 4PBT, the external layer undergoes the highest stress level. So the abovementioned crack initiation process is not likely to occur here. It is difficult to judge whether cracks are smeared by the polishing process or if a few of them initiate locally deeper due to stress concentration. But the first phenomenon is more likely to occur. The bending is still quite low (9 mm, including machine compliance, vs 120 mm span between the 2 cylinders) and so is the strain. Thus crack opening depth is very small, and only the wider areas are visible.



Finally crack depth reaches an asymptote: there is no crack longer than 270 μm . The average is about 230 μm . So, this depth represents the external CN layer and a part of the transition area where the ductility increases and cracks are stopped. Cracks get wider as the deformation is increasing. On **Fig.IV.25** (b), the wider one opened before the thinner one.

It must be noticed that no crack was observed on the surfaces in compression or at the corners of the hardness tests either. It means the material can undergo a certain amount of plastic strain in compressive stress states.

Numerical simulations of the four point bending test in Chapter 5 will help identifying the critical stress for CN layer cracking in tension. The observed specimens show crack arrays with homogeneous distances between cracks. This means that the first crack opens once the critical stress is reached. Then the stress is relaxed on both sides (cracks are going through the whole width of the specimen). Next crack initiates once the critical stress is reached again.

IV. 3. 2 Tensile tests

Tensile tests are carried out on the complete CN components. As for the 4PBT, the CN layer is submitted to tensile stress that will make it crack. This test will give another experimental data to assess the stress state at failure. It will be compared to the one assessed thanks to the 4PBT.

IV. 3. 2. a Experimental methodology

The total length of the specimen is 100 mm, the thickness 3.5 mm, and the width of the active area (outside the grip by the jaws) is 17 mm. The methodology is basically the same as for the tensile tests performed with CMO. The corrected specimen displacements are post-processed with VIC®. But another High Definition camera is used to record the face where no paint is applied. It is used to observe the evolution of cracks pattern and correlate it with the displacement. Three tests are carried

out until complete failure of the specimen (TF-1, TF-2 and TF-3). Two interrupted tests are carried out until a displacement of 0.2 mm (TF-4) and 0.27 mm (TF-5) in order to check the presence of cracks by dye penetrant inspection (also called Liquid Penetrant Inspection) (see **Fig.IV.27**); TF-4 and TF-3 were cut to allow SEM observations.

IV. 3. 2. b Results

Fig.IV.28 plots the evolution of the force as a function of the corrected displacement. Repeatability is good, and displacements to fracture on the three specimens vary between 1.2 and 1.22 mm, i.e. a scatter lower than 2%.

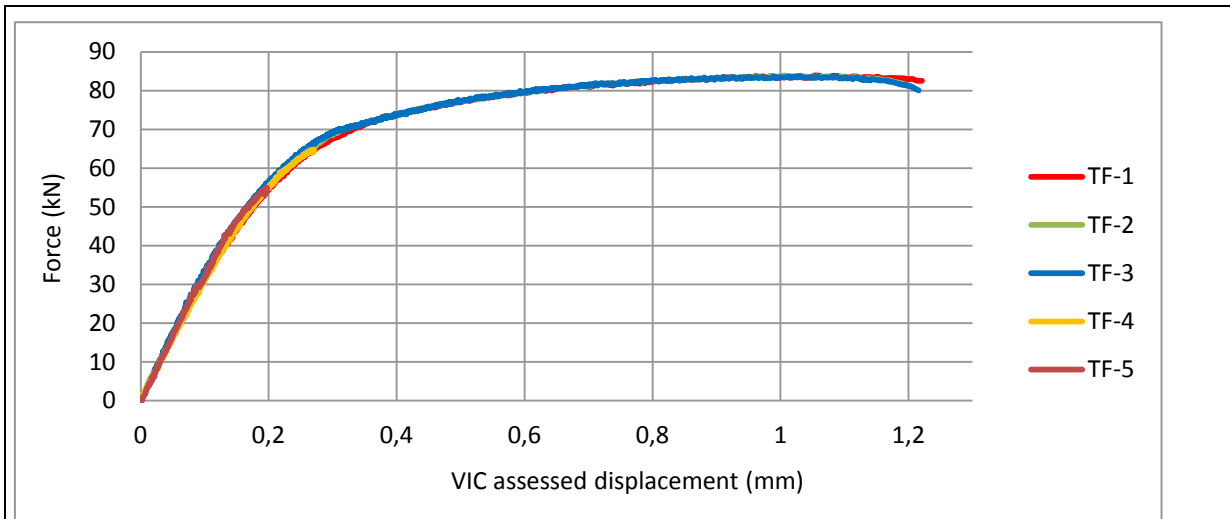


Fig.IV.28: forces vs corrected displacement curves for the tensile test on FCN component
// courbes force-déplacement corrigé pour les essais de traction sur le matériau CN complet

Dye penetrant inspection performed on the two specimens stopped before failure shows no crack on the first one (0.2 mm corrected displacement), and 9 on the one tested at 0.27 mm corrected displacement (crack density of about 0.2 crack /mm). These cracks, visible along the whole specimen width (see **Fig.IV.29** (a)), and perpendicular to the loading direction, seem to initiate between 0.2 mm and 0.27 mm displacement.

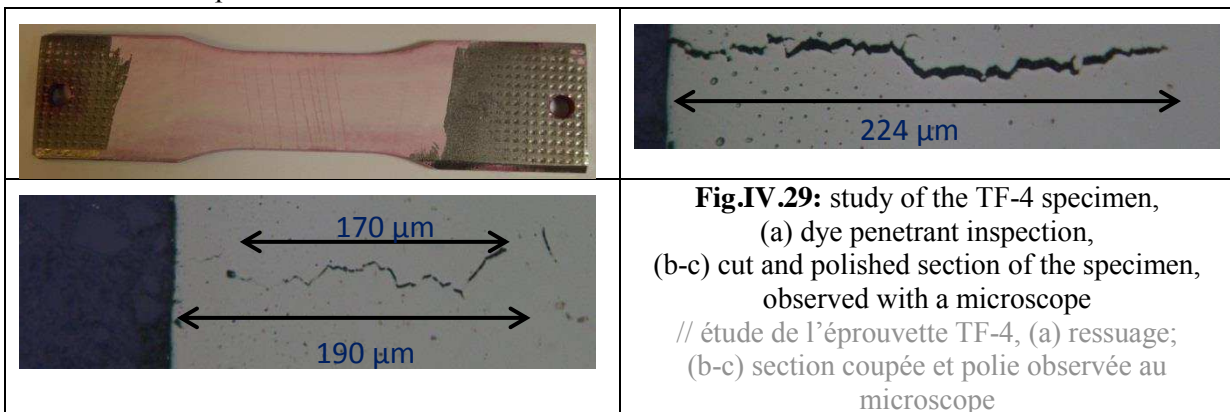


Fig.IV.29: study of the TF-4 specimen,
(a) dye penetrant inspection,
(b-c) cut and polished section of the specimen,
observed with a microscope
// étude de l'éprouvette TF-4, (a) ressuage;
(b-c) section coupée et polie observée au
microscope

Numerical simulations presented in Chapter 5 will allow assessing the corresponding stress state range. **Fig.IV.29** (b-c) illustrate two cracks: the first one has a depth of 224 μm and reaches the free surface. The second one does not seem to propagate until the surface and seems to have been initiated deeper. As discussed in the previous section, polishing can cover the thinnest part of the cracks, and make them invisible on the observed surfaces. Furthermore, one can guess the crack path close to the surface (between the surface and the left part of the arrow) on the **Fig.IV.29** (c). One can notice crack

paths are not straight lines; they are saw-tooth like which is consistent with the intergranular mechanism as can be checked at higher magnification.



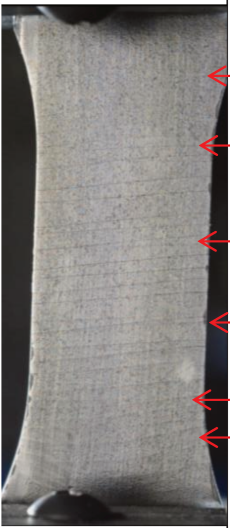

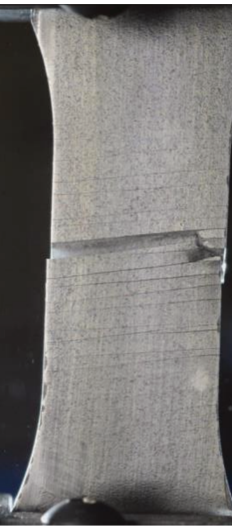
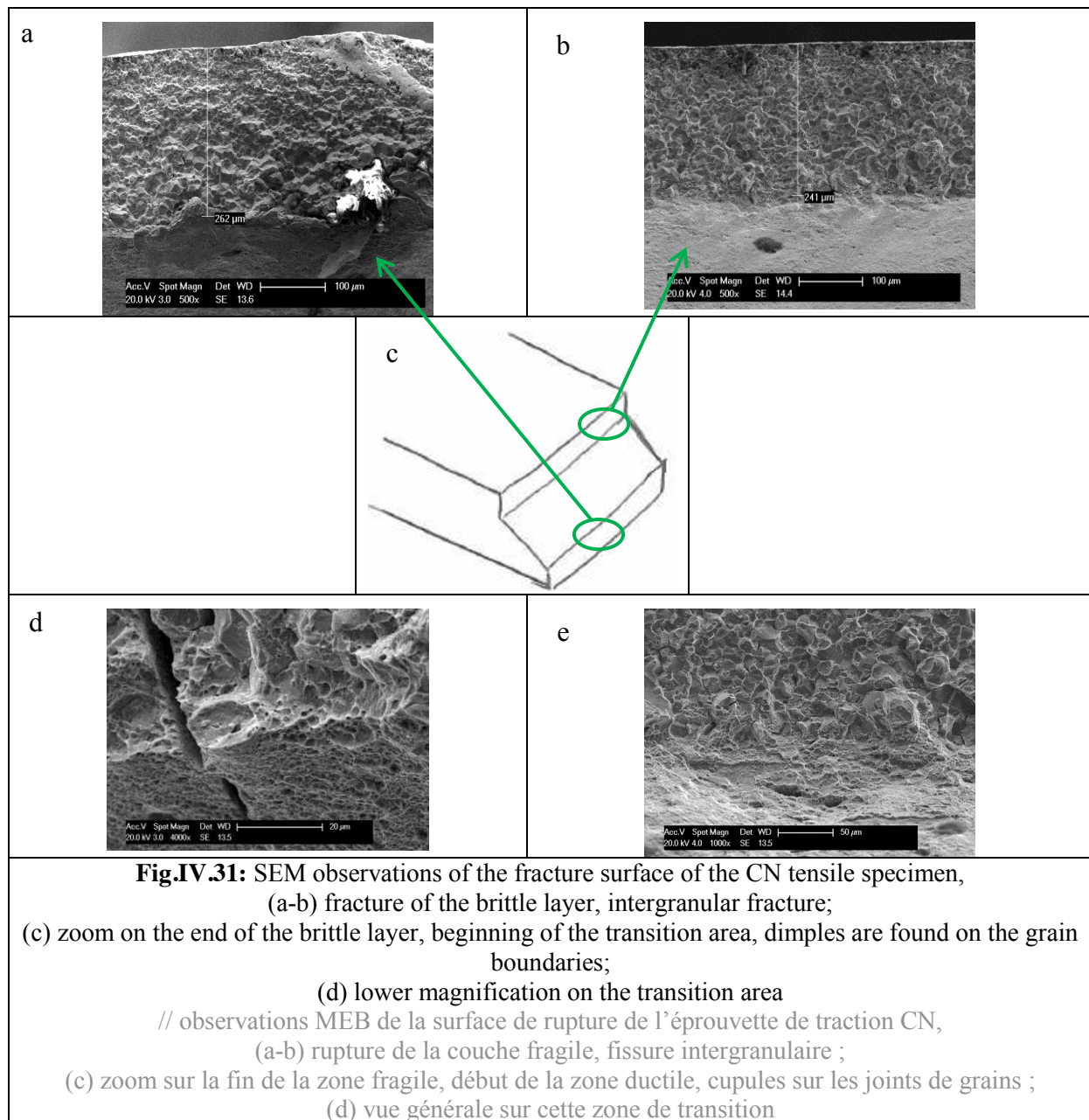
0.46 mm	0.7 mm	0.9 mm	1.1 mm	1.2 mm
				
19 cracks	22 cracks	28 cracks	30 cracks	complete failure
<p>Fig.IV.30: external crack opening sequence as a function of the corrected displacement. The red arrows show the cracks opening between 0.7 and 0.9 mm displacement</p> <p>// séquence de fissuration de la couche externe, en fonction du déplacement corrigé. Les flèches rouges indiquent la position des nouvelles fissures apparues entre 0.7 et 0.9 mm déplacement.</p>				

Fig.IV.30 illustrates the sequence of cracking during the test. An array of cracks is formed in the active area. The red arrows show the location of the new cracks appearing. It must be noticed that these cracks are parallel but not strictly horizontal (i.e. perpendicular to the loading direction), they have a slight angle. This was observed on all tested specimens.

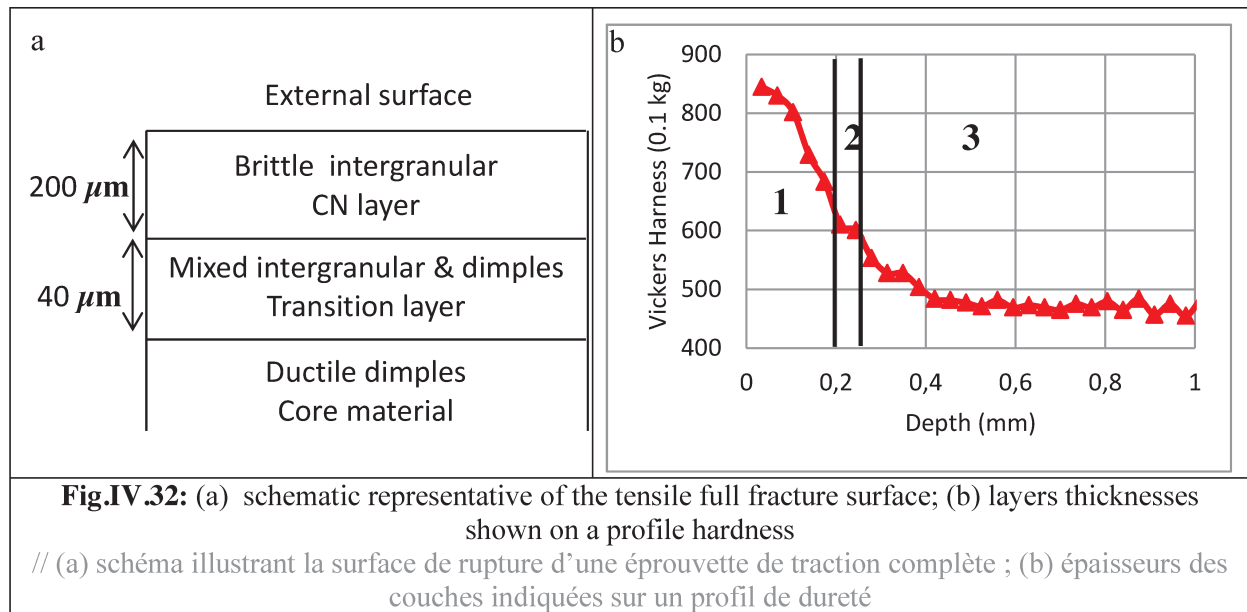
Fig.IV.31 (a-b-d-e) illustrate the failure of the brittle layer with SEM observations of the fracture surface. **Fig.IV.31** (a-b) shows two fracture planes with intergranular failure respectively 260 and 240 μm long. **Fig.IV.31** (c) is a schematic representation of the fracture surface, which is divided into three parts: the two brittle external areas and the central ductile part. The former are perpendicular to the surface (and consequently to the loading direction), the latter is not. It is represented as a plane on the scheme even though it is slightly curved. The depth of the brittle parts corresponds to the depth of the cracks observed in the 4PBT. We can conclude that both tests give the same brittle / ductile transition depth. **Fig.IV.31** (d) is very interesting because it shows little dimples on grain boundaries. So, it is a mixed failure mode between intergranular brittle failure and ductile failure in the so-called transition area beyond 250 μm from the surface. **Fig.IV.31** (e) is a view of this transition area with a lower magnification. The thickness of this area is about 40 μm . **Fig.IV.32** (a) is a representative schematic of the fracture surface of a tensile full specimen. The external part has a thickness of about 200 μm and corresponds to the CN layer with the intergranular brittle failure (fracture mechanism is illustrated in **Fig.IV.31** (a)). Then there is the transition layer, where the two failure mechanisms are present. This layer is about 40 μm thick; it is illustrated in **Fig.IV.31** (e). And to finish there is the core material with a ductile failure mode.



IV. 3. 2. c Discussion

This test induces the creation of an array of cracks in the external layer. These cracks are parallel to one another and are visible through the whole width of the specimen. They show a slight angle with respect to the horizontal line. It cannot be due to the misalignment of two jaws because it was observed on all the specimens. It can be due as well to the untwisting effect when setting up the specimen on the bench. Indeed specimens were slightly curved along their main direction. This curvature is a result of the shearing process used to produce these specimens.

The average crack depth is about 230 μm . Cracks do not propagate in straight lines, they are rather sawtooth-like: they propagate at the grain boundaries. **Fig.IV.32** (b) represents the layers thickness observed in this part on a hardness profile. It can be seen that hardness is evolving in the three identified areas. The critical tensile displacement at which cracks initiate is between 0.2 and 0.27 mm. Critical stress state will be assessed with numerical simulations in the following chapter.



The transition area was illustrated with pictures where little dimples can be observed on grain shapes. Ductility is progressively increasing; in the transition area both failure mechanisms are occurring. Grain boundaries are still brittle due to the martensite grains and its incapacity to be strained, so failure occurs here. However, dimples present on grain boundaries prove a ductile failure mode. Therefore, it seems that microstructure is not fully martensitic, and that residual austenite also exists. Bainitic microstructure or martensite with lower carbon content should start just below the transition area with a fully ductile failure. This needs to be confirmed with a microstructure study. The thickness where the two failure mechanisms are coexisting is about 40 μm .

The same bifurcation is being observed at the end of the crack on the fracture surface on the FCN tensile specimen (**Fig.IV.31**) and on 4PBT (**Fig.IV.26**). It is not only specific to the tensile test but to the CN treated material. It was not observed on 4PBT specimens with the usual CN treatment (60 min instead of 105 min) only because the displacement applied to these specimens was not high enough. So, this bifurcation appears between a displacement of 20 and 62 mm. This corresponds to a level of plastic strain higher than 8% in the core material. Whereas it appears for a strain level of 27 % for the tensile test (value of EPS in the element of the core material at the interface with the CN layer for a 1.2 mm displacement corresponding to the displacement to fracture). Differences are due to the treatment duration. Details of the simulation are given in Chapter 5.

IV. 3. 3 Conclusion

The fracture of the external layer is characterized. Critical displacement at failure is identified using interrupted tests. The numerical simulations in Chapter 5 will allow comparisons of stress states at failure. An array of parallel cracks is formed, of which the density increases progressively with time. On these specimens, cracks open at the surface and extend through the width. As expected, crack propagation through the martensite layer is instantaneous, typical of brittle failure. Average crack depth is homogeneous and around 230 μm in both tests. On the fracture surfaces, there is an area where brittle intergranular fracture and ductile one with dimples are observed together. Its thickness is about 40 μm and corresponds to a part of the transition area. This area would be the limit between the martensitic with high carbon content microstructure with residual austenite and either a bainitic microstructure or a martensitic one with lower carbon content with ferrite. At the end of this layer, the crack path is changing to form a 45° angle with respect to the initial crack direction.

The next part is dedicated to the comparison of the tensile tests done on the complete CN material and on the core material only. This comparison was already done in the previous Chapter dedicated to tooth failure. But this time it will be carried out on a better controlled test with easier understanding and interpretation.

IV. 4 Influence of the external layer on the behavior and failure mechanism in tension

Tensile tests were performed on specimens with the Core Material Only (CMO) and with both the CN layer and the core material (Full CN component - FCN). Thus, the influence of the CN layer can be measured and quantified. Based on the hardness tests performed, it is assumed that the core material is the same on the specimens with CMO and FCN. The FCN tensile specimens are thicker (3.5 mm) than the ones with just the core material (3 mm). The specimens with the CMO are thinner because 0.25 mm was grounded off the two surfaces to remove the layer with the lower hardness obtained with the anti-diffusion paint. It was more rigorous to remove this layer and to have only the core material for this study. Otherwise, geometries are identical, and the thickness difference will not influence the fracture behavior, just the force.

IV. 4. 1 Influence on the strength and ductility

Fig.IV.33 plots the force - real displacement for 2 specimens, FCN vs CMO. The increase in terms of maximal load is due both to the increased thickness of the specimen and to the presence of the CN “harder” layer. The difference in terms of displacement to fracture is really significant (1.25 mm for the FCN vs 3.18 mm for the CMO, i.e. 160 % difference). Scattering on those values is quite low (2 % for the FCN and 3 % for the CMO). The cracks in the external layer of FCN create locally areas of high stress concentration, which seem to accelerate failure in the core part of the specimen. This is surprising because there is almost no influence of the CN layer on the tooth displacement to fracture.

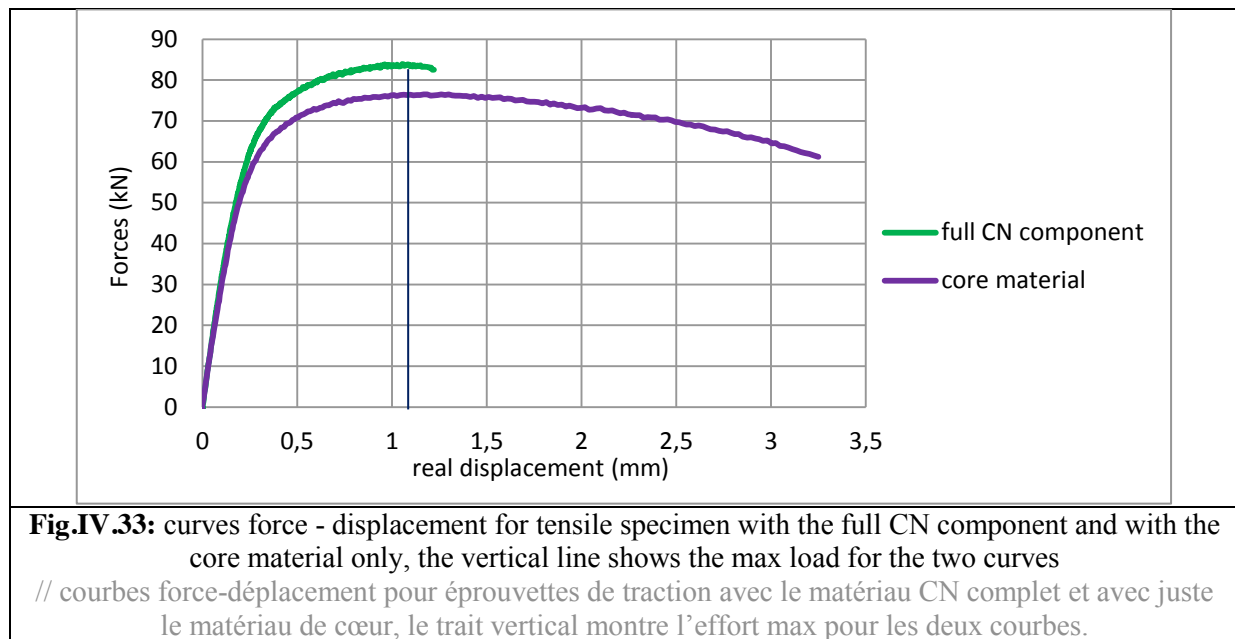
The peak load is higher for the specimen with the complete CN material, so is the section (3.5 vs 3.0 mm). But, they occur at the same displacement (1.1 mm). Neglecting necking, the maximum stress can be computed for both specimens:

- Full CN component: $\sigma_{\max CN} = \frac{83.5}{17 \times 3.5} = 1.40 \text{ GPa}$
- Core material only: $\sigma_{\max core} = \frac{76.3}{17 \times 3} = 1.49 \text{ GPa}$

With the assumption that necking can be neglected, the material with only the core material is more resistant because the maximum stress sustained is a bit higher (only 3.5 %). This suggests that if the two specimens had been given the same thickness, the forces would have been very close. The stresses calculated are averaged on the whole section. They are close to the real value for the CMO but for the FCN the real ones are different. Indeed, the stress sustained by the CN layer is higher until fracture. This is due to the distinct behavior laws (see Chapter 5). However, the calculated stresses confirm one of our previous conclusions: the CN treatment is intended to improve contact resistance and fatigue limit; it is not improving quasi-static failure limits. In this case, quenching without the carbon and nitrogen diffusion process seems to be more efficient in terms of critical stress limit for quasi-static failure, but the difference is very low.

In the end, fracture toughness of CMO is much higher than FCN. It must be noted however that such a difference is observed in simple tension whereas the difference was much smaller in shearing

condition, as seen in tooth failure (See Chapter 3). One could hypothesize the failure in mode II (shear) is less sensitive to the high stress concentration areas created by the numerous cracks in the CN layer than the mode I (tensile).



IV. 4. 2 Influence of the CN layer on the failure process

Fig.IV.34 (a-e) illustrates the fracture process of both specimens. Looking at **Fig.IV.34** (a, b and c), the first one is V shaped (illustrated in **Fig.IV.34** (b)), V center is in the middle of the specimen thickness. On the second one, fracture surface starts with 2 flat surfaces perpendicular to the specimen loading direction: these are the failure in the brittle CN layers. Inside, the fracture plane is inclined (see representative schematic **Fig.IV.31** (c)).

Looking at the other two pictures (**Fig.IV.34** (c and f)):

- on the first one, the necking is very pronounced, and the only crack is inclined 60° with the loading direction and at $\sim 45^\circ$ in the thickness direction (V shaped);
- on the second one, there is no necking, multiple cracks can be observed and the final crack is quasi-horizontal in the CN layer (a plane defined by the normal direction and the slightly slanted crack direction). Because of the failure inclined in the core material, one cannot see the light between the two parts of the broken specimen; however the **Fig.IV.34** (e) is the last picture of the test after complete failure: i.e. no load is sustained anymore by the specimen. Indeed, the cracks in the CN are first being opened and then failure propagates into the core material in shear, at $\sim 45^\circ$ as well in the thickness direction.

The presence of the CN and transition layer thus induces a double failure mechanism, with cracks formed early and quasi-horizontal in the CN layer and late cracks slanted in both transverse and normal direction in the core material. Residual stresses could be responsible as well since they are present in the FCN specimen but not in the CMO one.

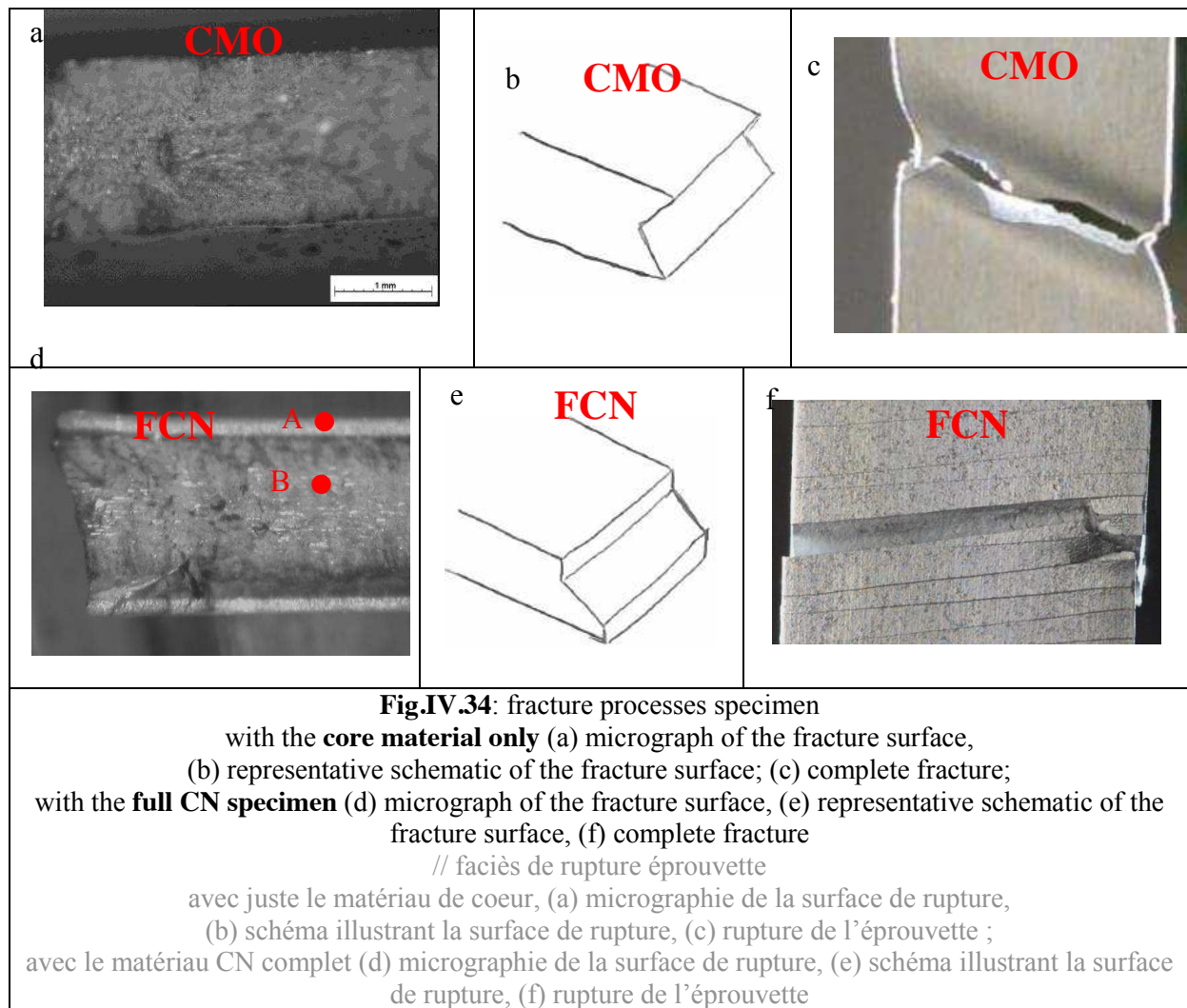
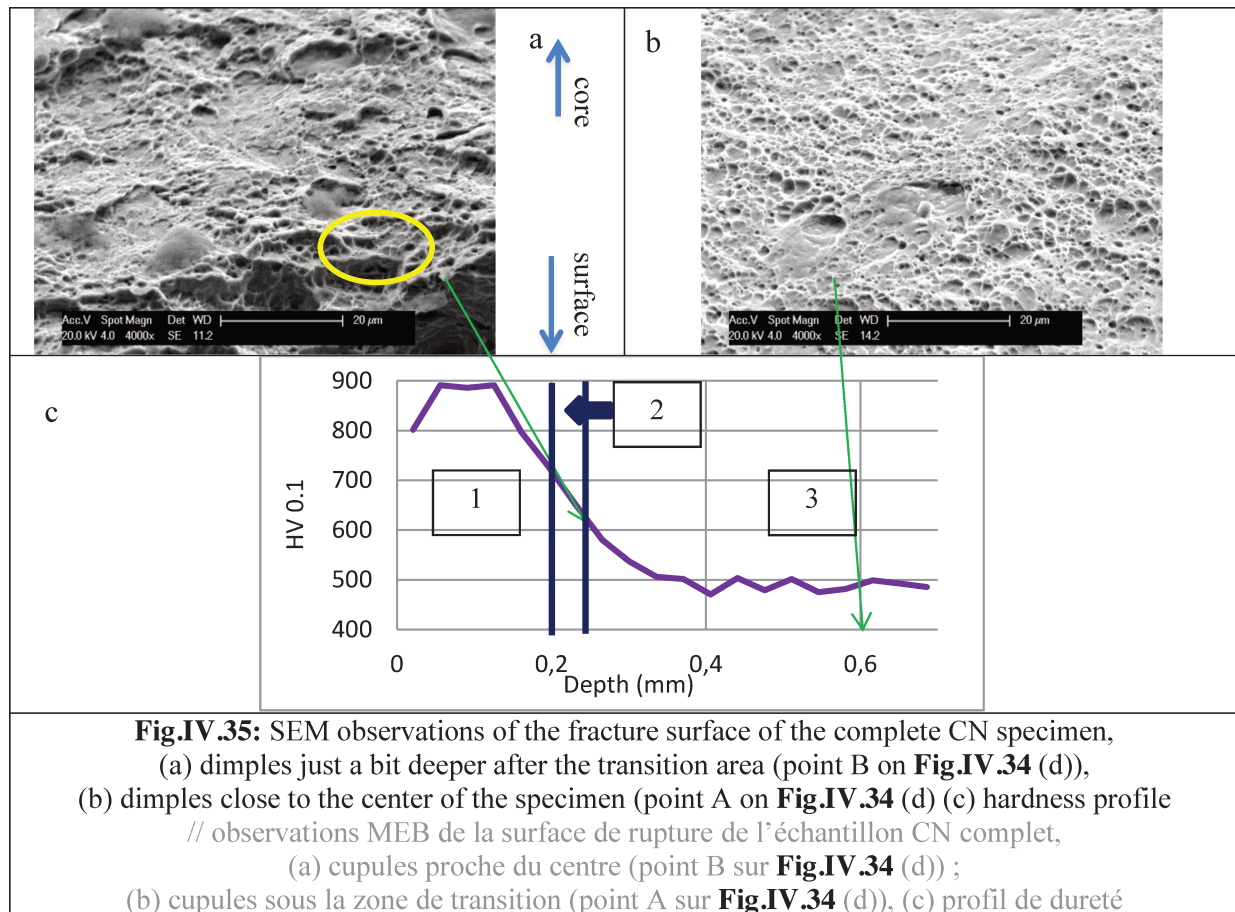


Fig.IV.35 (a-b) illustrate the fracture surface of the full CN specimen at higher magnification. The first one represents the fracture surface just below the transition area (point A on **Fig.IV.34** (d)), the second one (b) the core material at the center of the specimen (point B on **Fig.IV.34** (d)). One can see dimples with homogeneous sizes, elongated as for shear failure. The position of these two zones is given in **Fig.IV.34** (d) and **Fig.IV.35** (c) gives their associated hardness. The picture with sheared dimples (**Fig.IV.35** (b)) is located in the area of constant hardness (the area defined as “3” is the core material). **Fig.IV.31** (a) is an overall view of the fracture surface of the area defined as “1”, the external brittle layer. **Fig.IV.35** (a) is located just deeper the transition area, defined as “2”. The thickness of this second layer is about 30 – 40 μm , where the two failure mechanisms are seen. However, if one looks more closely at **Fig.IV.35** (a) (the surface of the material is toward the bottom of the micrograph), there are grain shaped holes (one is circled in yellow). It must be a sort of residual intergranular failure where whole grains left as for a brittle failure. However this shape is full of dimples due to presence of more ductile particles. These shapes are located at the crack bifurcation, so at the end of the transition layer. Fracture surface of the specimen with the core material only was studied previously (**Fig.IV.20**) and showed dimples of various sizes, proving an evolving stress state within the fracture surface.



IV. 4. 3 Discussion

The influence of the CN layer has been addressed for tensile specimens. Its presence does not increase the mechanical resistance of the material; a slight decrease is observed compared to the quenched steel. This was observed by determining the global stress at peak load. Calculation was done assuming that cross section variation can be neglected at the point of maximum load (i.e. before necking), which is a fair approximation.

In addition, the CN layer decreases a lot the ductility of the FCN material (- 60 %). Indeed, an array of cracks initiating pretty soon during the tensile test (displacement lower than 0.27 mm) can be observed. By cracking, it creates locally areas with high stress concentration at crack tips. This induces a much faster failure of the core part of the specimen. It reduces as well the section locally, and explains the decrease of σ_{max} . It is here assumed that the core materials of the FCN specimen and the CMO ones are the same; they have the same hardness level. The necking process is prevented by the incapacity of the CN layer to undergo deformation. For CMO, there is a significant necking and then a classical failure for such a ductile material in tension with shear localization at $\approx 45^\circ$.

SEM observations show fracture surface with dimples for both specimen in the core material. But, they are different. They are indeed wide open and oriented toward the normal of the fracture surface on the center of the tensile CMO (**Fig.IV.20** (a and d)) showing material was strained in a direction normal to the fracture surface. Whereas on the FCN tensile specimen, dimples are less open and are oriented along the fracture surface (see **Fig.IV.35** (a and b)). This shows a fracture occurring in a mode mixed between shear and tension.

With the observations, the following hypotheses on the FCN tensile specimen can be done. At first, cracks in the external CN layer initiate as soon as the material reaches the critical stress. They open at the free surface and then propagate toward the core material, perpendicularly to the loading direction. They are stopped in the transition area. This can be justified by the external cracks observed. Then, as soon as the critical plastic strain is reached in the core material at the tip of the external cracks, the final crack propagates through the core material. This hypothesis cannot be fully supported by our observations though but numerical simulations of the complete tensile test will confirm this process in Chapter 6.

One major question remains though. It is shown on the tensile test that carbonitriding strongly reduces the overall ductility of the specimen (displacement to fracture, but strain to fracture in the core area has to be analysed). However, the same comparison between full CN specimen and CMO specimen was carried out on the semi-industrial test, and ductility was approximately the same in both cases. Further analysis should be carried out to understand the influence of the type of loading on the brittle-ductile transition in these carbonitrided specimens.

IV. 5 Conclusion of chapter IV

This chapter describes the characterization methodology set up for the CNed steel analysis. As it was not possible to obtain specimen of carbonitrided layer only, the methodology adopted was the following. First, a study of the core material alone by using the same thermomechanical treatment but with a specific paint preventing diffusion of carbon and nitrogen atoms. Then a study of full CN components both in bending and tension.

Fracture of the core material will be predicted with a failure criterion accounting for the stress triaxiality and the Lode angle parameter. Introduced in Chapter 2, this method relies on a set of mechanical tests used to assess its criterion parameters. The material must be tested under proportional loading conditions, and tests must cover a wide range of stress triaxiality and Lode angle. Special attention has to be paid to stress states close to the main one undergone by the teeth during failure. The semi-industrial test showed the main crack in the core material was a shear dominated crack. Shear tests were thus performed to characterize the core material. A literature review showed a number of induced shear tests. It was seen that failure often initiates on the side of the specimen, and consequently in tensile stress state or mixed shear / tension state rather than in pure shear as required. Butterfly-type specimens were chosen for two reasons. First, their double curvature geometry induces failure initiation at the center of the gage section. Secondly, it is tested on a biaxial testing machine with two independent axes, which enables to apply shear combined with tension or compression. Thus, core material was tested in pure shear, and then shear with a bit of compression (loading angles -5° and -10°) and shear with a bit of tension (loading angle $+10^\circ$). This represents the stress state in the tooth at the beginning, before the main crack propagates. To complete the characterization, tensile tests were performed to get experimental data at high level of triaxiality. Multiple radii of notches and grooves enable to vary the stress triaxiality. Thus, core material was tested within a triaxiality range of -0.15 until 1.1 .

It is being hypothesized that the scatter of the butterfly specimens is due to machining issue, and more especially to the surface quality. This issue can be improved by polishing. However, polishing the gage is tricky and even impossible by mechanical processes. Electrolytic polishing can be the solution to remove the little grooves at the surface and thus decrease the surface roughness leading to a smaller scatter. However, this could change the sharpness of the geometry (sides of the gage) and

influence the stress state field. Optical measurements would be mandatory to check this particular point after the polishing.

As seen previously, it is assumed that the CN layer fails in tensile stress state in the tooth. Thus its characterization is achieved thanks to 4 point bending tests and tensile tests performed on specimen with the full CN material. These tests induce an array of cracks in the CN layer; cracks propagate through the whole width of CN layer very quickly. The cracks average depth is about 230 μm , they stop in the transition layer. On fracture surfaces, an area is seen with both brittle and ductile failure mechanisms: dimples on grains boundaries. This coexistence represents a part of the transition area. It is thus possible to simplify the whole failure mechanisms in two main steps:

- brittle fracture of the CN layer with cracks propagating (almost) instantaneously through the whole CN layer and stopping in the transition area;
- ductile fracture of the core material starting from the tip of one of the CN layer multiple cracks.

The influence of the CN layer on the failure of a bulk part was studied thanks to tensile specimens. While no significant difference was observed in terms of maximum stress, a major overall ductility loss was observed on tensile specimen with CN layer (-60 % in terms of displacement to fracture). This is explained by its progressive superficial cracking that forms, at the end, an array of cracks. Because it fails early in the test, the external layer cannot sustain any load. Furthermore, cracks induce areas with high stress concentration at their tip. Once the deformation reaches the critical value for this area, a crack initiates and propagates through the whole core material. These cracks array are not observed on the CMO specimen. This explains the lower displacement to fracture for the FCN specimen. It must be noted however that such a ductility decrease was not observed when applying the same methodology to the semi-industrial tests. The main difference between both tests is the shear type failure mode for the semi-industrial test whereas a pure mode I failure mode is expected for the tensile test. This would suggest that stress concentrations induced by cracks in the CN layer do not have the same impact on ductile failure in both failure modes. This may also be explained by the fact that strain to fracture is much lower for high stress triaxiality (tensile mode) than for almost zero stress triaxiality (shear mode). This will be analyzed in more details in Chapter 6.

The CN layer changes the fracture process of the core material as well. There were no wide open dimples on the core fracture surface, but elongated dimples suggesting a crack propagating in mode II. This confirms what was seen in Chapter 3 while comparing the tooth failure with or without the CN layer. Two phenomena can explain this:

- firstly, no necking is observed on the specimen with the FCN. It is explained by the limited capability of the CN layer to strain. Indeed, due to its high flow stress, it prevents the core material to strain and form the neck. Thus the material is strained along the loading direction, so tensile. In this stress state, the CN layer fails pretty soon, by definition of a brittle material.
- then the cracks in the CN layer create areas with high stress concentration, increasing very locally the triaxiality and thus decreasing the ductility of the material in these areas (material cannot undergo as much plastic strain as it is without any crack). Final crack cutting the specimen in half initiates from one of them. And not from the thickness center as it occurs for the CMO specimen.

One can wonder why this difference between CMO and FCN is so obvious on the tensile test but not on the semi industrial test. The reason is the stress state. It is known brittle materials fails in tensile stress state. Even though the core material is quite ductile in tensile stress state (flat tensile specimens

with CMO have a high displacement to fracture)) the machining of a low radii groove reduces a lot its capability to undergo plastic strain before failure (failure of TG1 specimen). So the cracks in the CN layer accelerate the failure of the tensile specimen. Then failure is at $\sim 45^\circ$ as on the CMO because material is ductile. Whereas in the tooth failure, core material is submitted to shear stress. Even though the CN layer fails due to tensile stress, the core material still resists due to a lower triaxiality stress state. One can see the difference in terms of displacement to fracture of the butterfly pure shear and the pure tensile. The teeth are less sensitive to the earlier failure induced by the external cracks due to the stress state. This is obviously a good point regarding the global resistance of the recliner.

Chapter V : Parameters identification

Contents

V. 1	Plastic behavior for the core material.....	126
V. 2	Fracture criteria for the core material.....	129
V. 2. 1	Analysis of strain, stress triaxiality and Lode parameter at fracture	129
V. 2. 2	Test of criteria from the literature	137
V. 2. 2. a	Identification based on strain sensors	137
V. 2. 2. b	Improved estimation of the loading paths.....	139
V. 2. 2. c	Improved identification of damage model parameters	141
V. 2. 3	Proposition of a new exponential criterion.....	144
V. 2. 4	Fracture criterion reduction	148
V. 2. 5	Discussion	149
V. 3	Fracture criterion for the CN layer	152
V. 3. 1	4PBT.....	153
V. 3. 2	Tensile tests.....	154
V. 3. 3	Discussion	156
V. 4	Summary	157

Résumé en Français

Ce chapitre présente l'identification des paramètres des critères de rupture ainsi que de la loi de plasticité du matériau de cœur. L'identification se fait grâce aux essais effectués dans le précédent chapitre.

La calibration de la loi de comportement se fait avec l'essai de traction plat. Différentes lois sont testées, mais c'est la loi de Voce qui représente le mieux le comportement du matériau à tous les niveaux de déformation. Les paramètres sont identifiés par analyse inverse ; la loi de comportement est vérifiée sur les autres essais réalisés et à chaque fois la corrélation des courbes force-déplacement numériques et expérimentales est de bonne qualité. C'est un point important car les essais balayaient un vaste panel d'états de contraintes. Une fois la loi d'écrouissage calibrée, il est possible de déterminer le critère de rupture.

Les essais réalisés avec les éprouvettes « butterfly » et de traction couvrent un large éventail d'états de contraintes. La méthode d'identification est la suivante : on se place sur les simulations au déplacement expérimental à rupture. Dans un premier temps, on recherche l'élément dans le maillage ayant la déformation plastique la plus élevée. On extrait sur cet élément le trajet de chargement, c'est-à-dire l'évolution de la triaxialité et du paramètre de Lode en fonction de la déformation plastique. Cette démarche est répétée sur les dix essais. Puis, par analyse inverse avec le logiciel MOOPI, on identifie les paramètres des critères de rupture. Une fois la première identification effectuée, la démarche est répétée avec l'élément dans les maillages ayant la valeur de D (paramètre d'endommagement) la plus élevée. In fine, dès que le premier élément dans le maillage est supprimé, la fissure se propage très rapidement jusqu'à la rupture finale. Les critères de rupture trouvés dans la littérature n'ont pas donné satisfaction sur les 10 essais ; il y a à chaque fois un état de contrainte où la rupture est mal prise en compte. Cela a nécessité l'écriture d'un nouveau critère de rupture ; cette fois-ci la rupture est bien modélisée sur les 10 essais. Ce critère prend en compte le paramètre de Lode via une fonction exponentielle. En effet, il a été remarqué que son influence est très faible pour une valeur inférieure à 0,8. En revanche, une fois passé 0,8, son influence est très importante et bien prise en compte par la fonction exponentielle. Le critère de rupture ainsi identifié exprime une valeur critique de la déformation plastique en fonction de l'état de contrainte, i.e. triaxialité et paramètre de Lode.

Un critère de rupture plus simple est utilisé pour la couche CN ; il comprend une valeur critique de la première contrainte maximale principale ainsi que la pression ($p = -\frac{1}{3}(\sigma_I + \sigma_{II} + \sigma_{III})$), le dernier paramètre permet de prendre en compte l'influence des seconde et troisième contraintes principales. L'identification est effectuée grâce aux essais de flexions 4 points ainsi qu'aux essais de traction réalisés sur le matériau CN complet. Deux jeux de paramètres distincts sont trouvés sur chaque géométrie d'échantillon ; rien ne nous permet de trancher en faveur de l'un ou de l'autre. Les valeurs critiques retenues correspondent à la moyenne des 2 jeux. Nous soupçonnons une différence de contraintes résiduelles initiales due au processus de découpe des échantillons. En effet, les éprouvettes de flexion étaient vrillées dans leur longueur. Les critères de rupture ainsi identifiés vont être utilisés pour modéliser la rupture complète d'une dent dans le prochain chapitre.

Introduction

Chapter 5 deals with the numerical methodology used to calibrate both material behavior laws and failure criteria. First, focus is on the core material. The choice of the plastic hardening law stress-strain curve, an important preliminary stage ahead of fracture criterion calibration, is discussed and followed by the identification of its parameters. Once the hardening law is calibrated, the loading paths for all 10 mechanical tests can be assessed.

This is the first step of the fracture criterion identification. The latter is based on the definition of a damage variable $D(\epsilon_f, \eta, \theta)$ which must be equal to 1 at the displacement where fracture is observed in experiments:

$$D = \int_0^{\epsilon_f} \frac{d\bar{\epsilon}_p}{f(\eta, \theta)} = 1 \quad \text{Eq.V.1}$$

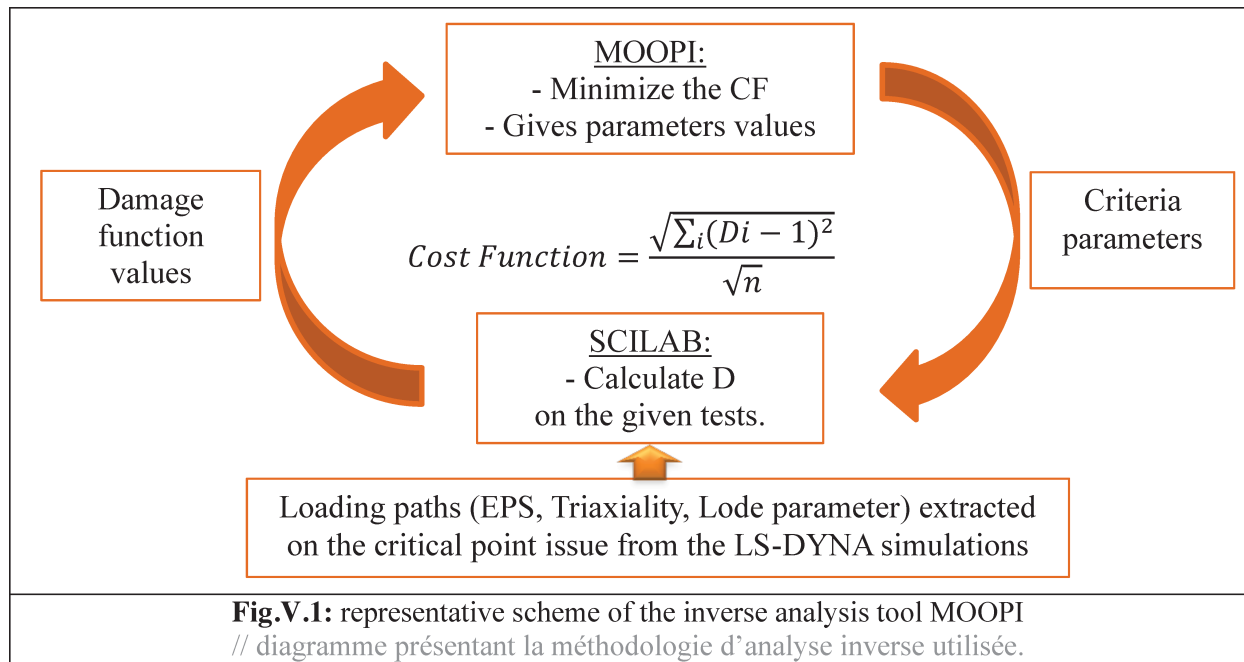
It embeds a $\epsilon_f = f(\eta, \theta)$ fracture criterion, a phenomenological, uncoupled ductile failure model as discussed previously (Chapter 2). As explained later on in this chapter, ϵ_f must be taken at the point most liable to see fracture initiation. The relation $D(\epsilon_f) = 1$ for all 10 tests is obtained by minimization in the least square sense of the following cost function:

$$\text{Cost Function} = \frac{\sqrt{\sum_i (D_i - 1)^2}}{\sqrt{n}} \quad \text{Eq.V.2}$$

where D_i ($i = 1 \dots n$) are damage functions for each test and n is the number of tests chosen for the calibration stage.

The inverse analysis tool used to perform this minimization is called MOOPI (MOdular software dedicated to Optimization and Parameters Identification), and is based on an evolution strategy algorithm and a Kriging Metamodel developed by [Roux, 2011] at CEMEF. SCILAB® is used to calculate the damage functions D_i with the parameters given by MOOPI. This calculation can be done thanks to the loading path (equivalent plastic strain $\bar{\epsilon}$, Triaxiality and Lode parameter) extracted from the simulation at the critical point (maximum strain or maximum damage). The process is being illustrated in **Fig.V.1**. The integration achieved in the SCILAB® subroutine is based on all the stress and strain history saved at the location of fracture initiation and thus obtained using finite element simulations of the tests. Then the value of the cost function is calculated in MOOPI (see Eq.V.2) and MOOPI gives a new set of parameters that improves the metamodel description of the cost function at each iteration corresponding to a new generation. The best result is the one with the lowest value of the cost function.

The methodology followed to assess the loading paths is accurate and is detailed as well in [J. Papasidero, Doquet, & Mohr, 2013].



The strain to fracture ϵ_f and the stress path $\eta(\bar{\epsilon})$, $\theta(\bar{\epsilon})$ are determined by a two-stage procedure. First, a numerical simulation of each test is performed until displacement of experimental failure, to give the abovementioned characteristics at the point of maximal strain (as the damage function is not yet known). A first set of damage parameters is thus obtained using MOOPI and Scilab® as explained above. With this preliminary set of parameters, a second simulation of all tests is carried out calculating the damage function. This time, the point with maximum damage (rather than strain) can be selected as the probable locus of fracture initiation, ϵ_f and the stress path $\eta(\bar{\epsilon})$, $\theta(\bar{\epsilon})$ are selected there, and the second, final identification of the damage function parameters can be performed.

This complex procedure has been repeated for several fracture criteria from the literature (Lou and Huh, Bai & Wierzbicki, Johnson-Cook). Two of them will be detailed, and it will be shown that their predictions are not satisfactory, i.e. D significantly differs from 1 for several tests. A more accurate criterion will therefore be proposed, based on the experimental features of fracture obtained for our material.

The third part of this chapter addresses the failure criterion for the CN layer. The selected criterion relies on the critical value of the first maximum principal stress, assessed with the 4PBT and the tensile test. An additional pressure threshold was also added to this criterion to be more representative of experimental failure of the CN layer.

V. 1 Plastic behavior for the core material

Identification of the material law parameters is the first step in the procedure of the fracture behavior determination. Indeed, the stress state at failure in the material depends on its plastic behavior.

❖ Yield criterion

The von Mises yield criterion is assumed for the material. It states that yielding occurs when the second invariant of the deviatoric stress tensor (J_2) reaches a critical value ([von Mises, 1913]).

$$J_2 = R(\alpha) \quad \text{Eq.V.3}$$

where $R(\alpha)$ is a function of the hardening internal variable(s) α . This model is widely used for its simplicity. It was shown by [Hencky, 1924] that the von Mises criterion can be seen as a condition of maximum distortion energy: yielding occurs when this energy reaches a critical value.

❖ Stress-strain relation

The material characterized in this work seems to have a high level of ductility. The mathematical formulae used for the stress-strain curve must consequently be adapted for a good description of the material behavior at high plastic strain. For instance power hardening laws such as Swift's (Eq.V.4) ([Swift, 1952]) or Hollomon's (Eq.V.5) ([Hollomon, 1945]) may not be the most adapted for high plastic strain:

$$\sigma = \sqrt{3}K(\varepsilon_0 + \bar{\varepsilon}_p)^n \quad \text{Eq.V.4}$$

$$\sigma = K\bar{\varepsilon}_p^n \quad \text{Eq.V.5}$$

where σ is the flow stress; $\bar{\varepsilon}^p$ the equivalent plastic strain and K, ε_0, n material parameters. These laws are often calibrated for relatively small strain using a tensile test and then extrapolated for higher plastic strain. However, due to their mathematical form, they often overestimate hardening at high plastic strain. For specific alloys, a plastic law with a strain hardening saturation is required. Eq.V.6, through Eq.V.9 are examples from the literature of material laws with saturation (respectively Voce's law ([Voce, 1955]), the modified Voce law by [Cao, 2013], Brown's law ([Brown, 1989]) and the law used by the steelmaker ArcelorMittal, SMATCH:

$$\sigma = \sigma_{p0} + (\sigma_{ps} - \sigma_{p0})(1 - e^{-n\bar{\varepsilon}_p}) \quad \text{Eq.V.6}$$

$$\sigma = \sigma_{p0} + (\sigma_{ps} - \sigma_{p0} + K_2 \bar{\varepsilon}_p)(1 - e^{-n\bar{\varepsilon}_p}) \quad \text{Eq.V.7}$$

$$\sigma = \sigma_{ps} - \left[(\sigma_{ps} - \sigma_{p0})^{1-a} + (a-1) * \left(\frac{H_0}{\sigma_{ps}^a} \right) \bar{\varepsilon}_p \right]^{\frac{1}{1-a}} \quad \text{Eq.V.8}$$

$$\sigma = \sigma_{p0} + (K_1 + K_2 \bar{\varepsilon}_p)(1 - K_3 e^{-b\bar{\varepsilon}_p}) \quad \text{Eq.V.9}$$

where σ is the flow stress; $\bar{\varepsilon}_p$ the equivalent plastic strain; $\sigma_{p0} = \sigma(\bar{\varepsilon}_p = 0)$ the yield stress; $\sigma_{ps} = \sigma(\bar{\varepsilon}_p \rightarrow \infty)$; K_1, K_2, K_3 (MPa), a, b, H_0 (MPa), n are material parameters. The modification of the Voce law consists in adding a parameter K_2 which, multiplied by $\bar{\varepsilon}^p$, better accounts for the residual material hardening at high plastic strain. So there is no saturation (horizontal asymptote) like in the first Voce law, but a linearly increasing line with slope K_2 . Brown's law has two parameters (a, H_0) to account for the necking point. Nevertheless, the modified Voce law has been chosen in this work to represent the plastic behavior of the core material after comprehensive testing has shown it to best predict the force – displacement curves and in particular the post-peak behavior (see e.g. **Fig.V.2**). It can be noticed that the modified Voce law and the SMATCH one behave similarly if $K_2 = 0$ and $K_3 = 1$.

Parameters identification is achieved by inverse analysis. This method consists in minimizing a cost function, Eq.V.10:

$$CF = \frac{\|F^e - F(P)\|}{\|F^e\|} = \sqrt{\frac{\sum_{i=1}^N (F_i^e - F_i(P))^2}{\sum_{i=1}^N (F_i^e)^2}} \quad \text{Eq.V.10}$$

where F^e are experimental data, $F(P)$ the numerical data obtained with the set of parameters P . Here the unknowns are the set of parameters of the material behavior law. The data used for the analysis

need to be chosen carefully. The force – displacement curve in tension tests is widely used for the calibration of behavior laws. However, the test must be adequately chosen: its repeatability must be excellent and the material must reach high plastic strain. For instance, the TG1 tensile test and the butterfly test in tension are not accurate for this purpose: since triaxiality is high, the material fails at low plastic strain. The butterfly test in shear and compression could have been chosen, but it has a rather large experimental scatter. This is why the tensile test of flat specimen with only the core material is chosen. The scatter is lower than 2 % ,which makes it a reliable test.

σ_{p0} (MPa)	σ_{ps} (MPa)	K_2 (MPa)	n
1088	1570	30	175

Table.V.1: identified hardening parameters for the modified Voce law
// Les paramètres identifiés pour la loi d'écrouissage de Voce modifiée

Faurecia is using the Hollomon hardening law identified in [C. Moussa, 2012] (**Fig.V.2** (a) in red). In this work, the material law parameters were identified with hardness tests. Interested readers can read [Moussa et al., 2011] to get more precise information. As it is seen in **Fig.V.2** (b) in red, the fitting is not accurate and required to identify a new plastic law. Modified Voce law was chosen to model the plastic behavior of the core material. **Fig.V.2** (a) plots the identified stress-strain curve in purple, the parameters of which are listed in Table.V.1. It reaches quite quickly the necking point ($\bar{\epsilon} = 0.025$). **Fig.V.2** (b) plots the force - displacement curve for the experimental test (green curve) and the numerical simulation (purple one). Simulations are done with the FEA software LS-DYNA with linear hexahedron elements. The mesh size is 0.1 mm. The fit of the curve obtained with the Voce law is quite good.

However, to be validated, the stress-strain relation must describe accurately the plastic behavior not only in tension and in shear. Thus it is tested on all ten tests to be validated. The comparison between the experimental and the numerical curves of the nine other tests is given in Appendix V.1. The fit is good on all tests, especially the ones with potentially high plastic strain (butterfly -10° and butterfly pure shear). It is interesting to see a behavior law coupled with the von Mises yield criterion fitting such a high number of tests with a wide range of stress states (from shear with compression until pure tensile). It usually requires anisotropic yield criteria or of enhanced yield criteria accounting for both J2 and J3 ([Cao, 2013], [Gachet, 2013]). The rather flat stress hardening seems to well represent the behavior of the material at high plastic strain. However, it can be noticed that the force is slightly overestimated compared to the experimental one at the onset of plasticity. For instance, it can be seen on **Fig.V.2** (b) that the numerical curve (purple one) is a bit higher than the experimental one (green one). But, the two curves are crossing at 1.5 mm displacement and then the numerical curve slightly underestimates the force. This behavior can be seen on the other curves in Appendix V.1. Difference is just a few percent, but it has to be accounted for regarding final discussions on tooth failure correlation.

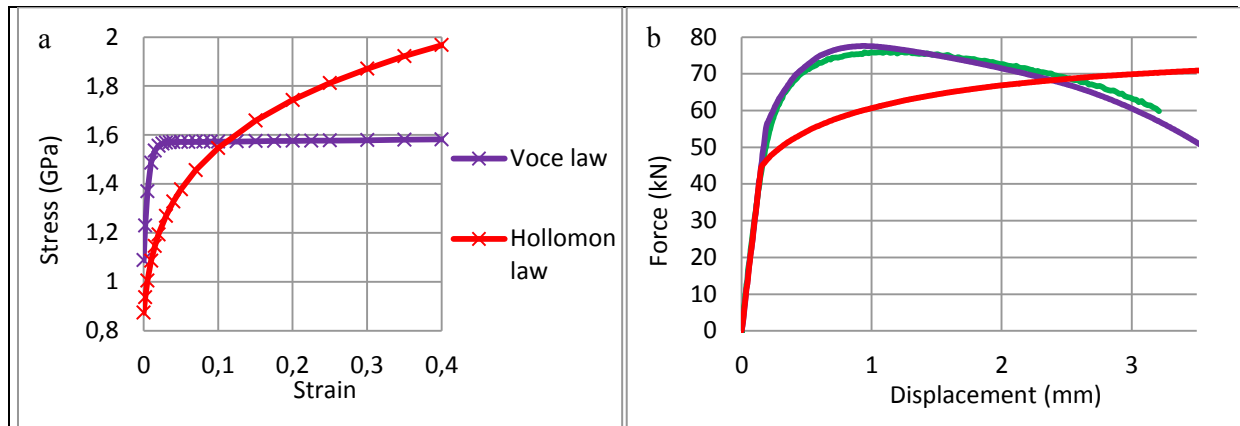


Fig.V.2: Simulation of the tension test on flat samples.

(a) the modified Voce law identified (purple curve), the Hollomon law (red curve) ;

(b) comparison of the experimental (green curve) and numerical (purple and red curves) force - displacement curves

// simulation de l'essai de traction sur éprouvettes planes T0.

(a) en violet : la loi d'écrouissage de Voce modifiée identifiée, en rouge : la loi de Hollomon ;

(b) comparaison entre les courbes force-déplacement expérimentale (verte) et numériques (violette et rouge)

The plastic behavior is thus identified; next step consists in determining the stress state at failure.

V. 2 Fracture criteria for the core material

V. 2. 1 Analysis of strain, stress triaxiality and Lode parameter at fracture

The first step is to determine the loading paths for each tests i.e. the evolution of the three important mechanical variables impacting fracture (Equivalent Plastic Strain, Stress triaxiality ratio and Lode parameter). Numerical data must be extracted from the element which fails first in the simulation. It is common to take the element with the highest plastic strain at the experimental displacement to fracture [Papasidero, 2014]. However, here, once the failure criterion will have been determined, simulations will be run again and the element with the highest D value at displacement to fracture will be used for the identification process. A better precision is expected from this two-stage procedure ([Papasidero et al., 2013] [Cao et al. , 2013]).

T0	TG1 – TG7	TN7 – TN7-2 – TN9
a	b	c

Fig.V.3: Nomenclature of the tensile specimens used.

(a) flat tensile specimen T0 , (b) grooved tensile specimen, 2 radii 1.5 (TG1) and 7 (TG7) mm, (c) notched specimen, there are 2 radii 7 and 9 mm, and TN7-2 has a thinner gage 5 instead of 7 mm

// nomenclature des éprouvettes de traction utilisées.

(a) éprouvette plate T0, (b) éprouvette entaillée, 2 rayons différents 1.5 (TG1) et 7 (TG7) mm, (c) éprouvette entaillée, 2 rayons différents 7 et 9 mm, et TN7-2 a une partie centrale plus fine, 5 au lieu de 7 mm

❖ Simulation of loading paths

All the simulations are run with 8-node hexahedra reduced integration with the FEA software LS-DYNA®. No symmetry plane is used: even when the tests are geometrically and kinematically symmetric, the fracture mode may be asymmetrical. The mesh size, if not specified, is 0.1 mm. **Fig.V.3** illustrate the shape of the specimen regarding their name in the manuscript.

Fig.V.4 (a-b-c) illustrate the stress state at experimental displacement to failure in the T0 (a), TG1 (b) and TN7 (c) tensile specimens (see Figure 4) for the nomenclature). Contours are plotted on a cross section in the middle of the specimen. The selected element is the one at the gravity center of the specimens, the one with the highest strain for these particular tests. The strain pattern is however somewhat different depending on the test. On the flat specimen, it is a circular area around the gravity center. Necking is very pronounced in the middle of the section, which has been observed experimentally as well, as discussed in the previous chapter. Regarding TG1 specimen, the strain localization is a thin line in the median plane of the observed section. This change of behavior is due to the machined groove which forces localization from the beginning, preventing the occurrence of the slip line seen on tensile flat specimen (**Fig.V.4**).

One can notice the stress triaxiality evolving the same way as the strain does, with a maximum at the gravity center of the specimen. This comforts the assumption that failure should initiate in that particular element.

Fig.V.5 (a) and (b) plot the variation of the equivalent plastic strain with respect to respectively the stress triaxiality and the Lode parameter. The curves are stopped when the simulations reach the experimental displacement to fracture. First, one notices the very high plastic strain at fracture for the T0 specimen. A critical plastic strain higher than 100% in a tensile stress state is considerable for such high strength steel (The global engineering strain to failure is about 0.08). This shows its high ductility. Secondly, the stress triaxiality and the Lode parameter evolve a lot during a test. For instance, the triaxiality increases from $1/3$ to 0.8 for T0. Rigorous parameters identification cannot account for the loading path with only one value (be it the initial, the average, or the final value of the triaxiality or the Lode parameter). This is why the whole loading path will be accounted for in the calibration methodology.

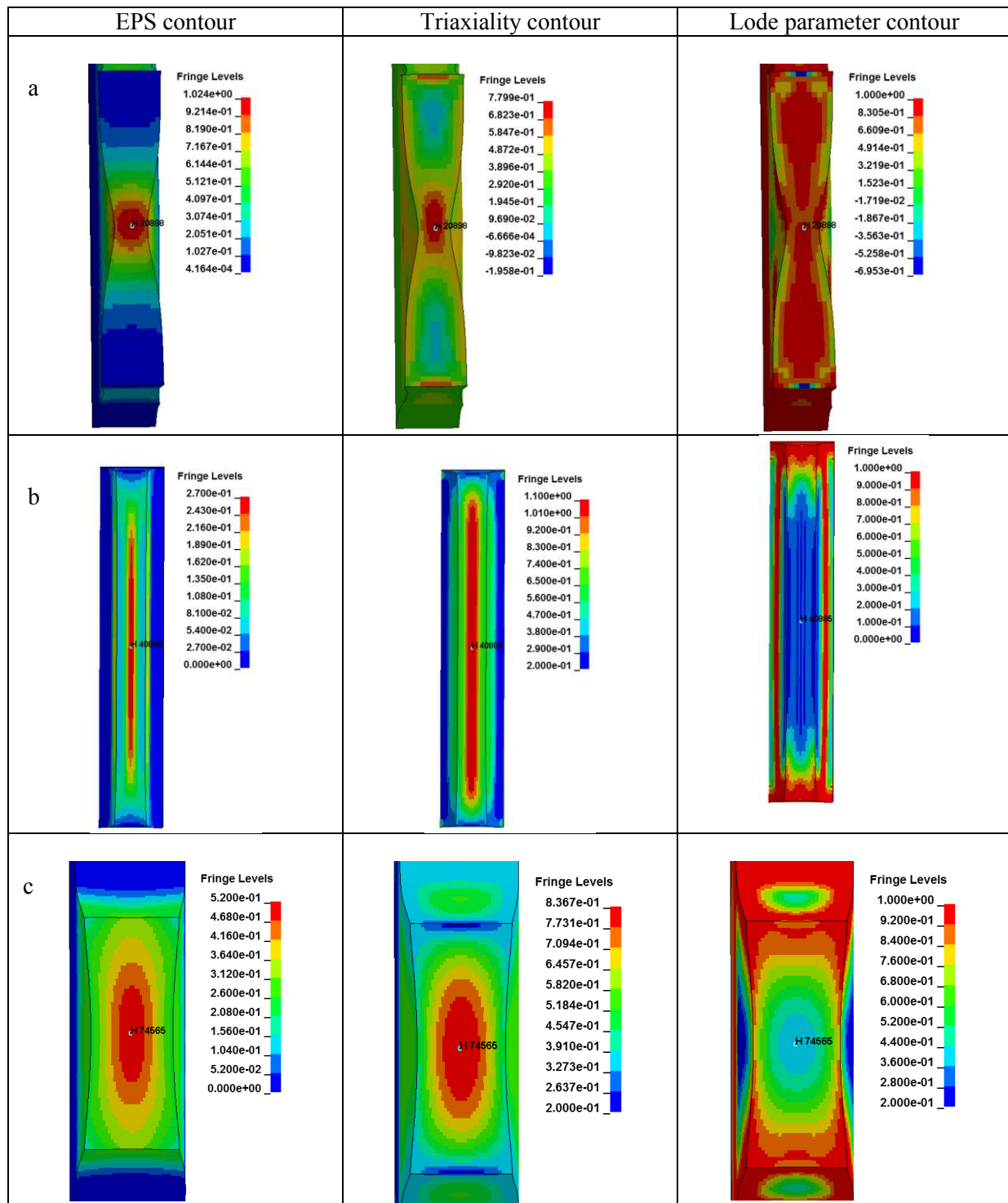


Fig.V.4: Tensile tests, computed stress and strain in cross sections of the specimen, at the time of the experimental displacement to fracture.

(a) Flat tensile T0; (b) grooved tensile TG1; (c) notched specimen TN7.

Equivalent plastic strain (first column), stress triaxiality (second column) and Lode parameter (third column) are shown. The selected element (H 74565) is at gravity centre.

// Simulation des essais, contraintes et déformation calculées dans la section de l'éprouvette à l'instant de la rupture expérimentale.

(a) traction sur éprouvettes plates T0 ; (b) traction entaillée TG1 ; (c) traction entaillée TN7.

Déformation plastique équivalente (1^{ère} colonne), triaxialité (2nd colonne) et paramètre de Lode (3^{ème} colonne) dans le plan médian des éprouvettes.

L'élément sélectionné (H 74565) correspond au centre de gravité,

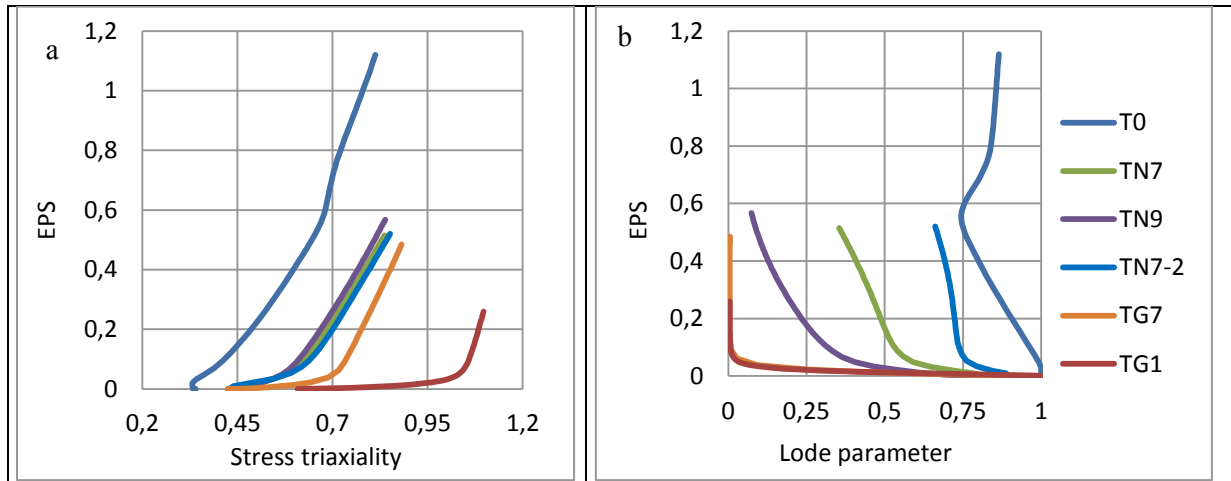


Fig.V.5: loading paths for the six tensile specimens,
 (a) evolution of the Stress triaxiality; (b) evolution of the Lode parameter
 // trajets de chargement pour les six essais de traction,
 (a) évolution de la triaxialité des contraintes ; (b) évolution du paramètre de Lode

Fig.V.6 (a-b) illustrates the fracture parameters contours at displacement to fracture for the butterfly -10° and pure shear. The cross-section is taken where the maximum strain is reached. The same is done on **Fig.V.7** (a-b) for the butterfly +5° and pure tension. Here the cross-sections are in the middle plane of the specimen. For the moment, the selected elements are the ones with the highest strain at the displacement to fracture. These elements are in the middle of the section, either at the surface (pure shear and +5°) or at the center (-10° and pure tension). This is a result of the double curvature geometry. They are not especially where the triaxiality is the highest (butterfly +5°).

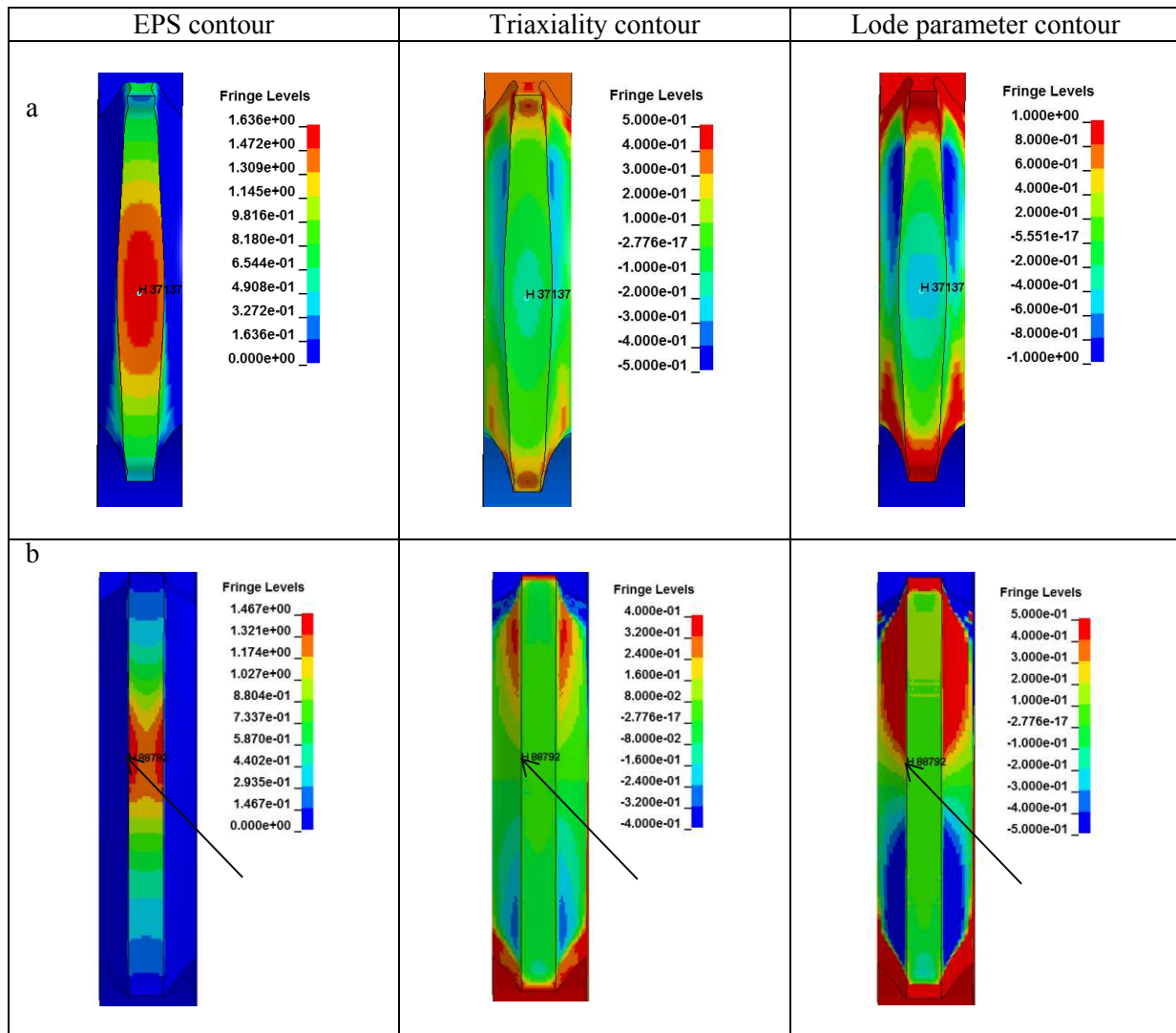


Fig.V.6: Butterfly tests, computed stress and strain in cross sections of the specimen, at the experimental displacement to fracture.

(a) butterfly -10° ; (b) butterfly pure shear.

Strain (first column), stress triaxiality (second column) and Lode parameter (third column) are shown.

The selected element corresponds to the element with the highest EPS at displacement to fracture.

// Simulation des essais

(a) butterfly -10° ; (b) butterfly cisaillement pur.

Déformation plastique équivalente (1^{ère} colonne), triaxialité (2nd colonne) et paramètre de Lode (3^{ème} colonne) dans le plan médian des éprouvettes.

L'élément sélectionné correspond à celui avec l'EPS le plus élevé au déplacement à rupture.

Fig.V.8 (a-b) plot the loading paths for the four butterfly specimens. Note the high plastic strain at failure for the butterfly -10° and pure shear, already seen with the T0 specimen and showing the high ductility of the material. On the other hand, for the butterfly $+5^\circ$, the strain at failure decreases a lot compared with the pure shear specimen. Fitting of the failure for the butterfly pure shear and $+5^\circ$ will be difficult because of the drop of strain at failure without having a huge variation of the triaxiality and the Lode parameter. The loading for the pure shear is proportional, neither triaxiality nor Lode parameter evolves during the test (after the elastic stage). This remark can be extended to the three butterfly tests in the positive triaxiality space. Indeed, after the elastic stage, neither triaxiality nor Lode parameter evolves during the test; this contrasts with tensile tests.

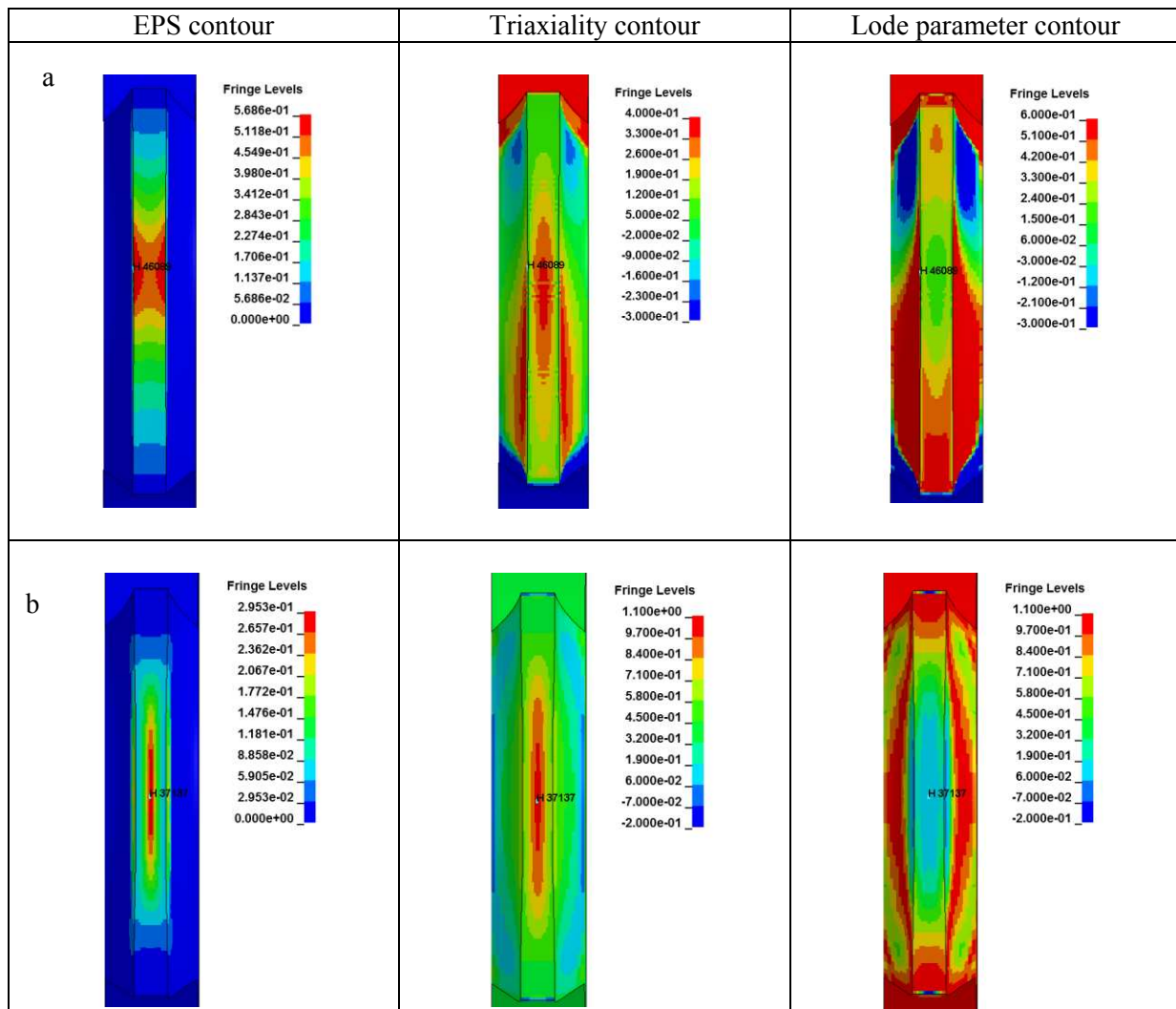


Fig.V.7: Butterfly tests, computed stress and strain in cross sections of the specimen, at the time of the experimental displacement to fracture.

(a) butterfly +5°; (b) butterfly pure tensile.

Strain (first column), stress triaxiality (second column) and Lode parameter (third column) are shown,
// Simulation des essais

(a) butterfly +5° ; (b) butterfly traction pur.

Déformation plastique équivalente (1^{ère} colonne), triaxialité (2nd colonne) et paramètre de Lode (3^{ème} colonne) dans le plan médian des éprouvettes.

L'élément sélectionné correspond à celui avec l'EPS le plus élevé au déplacement à rupture.

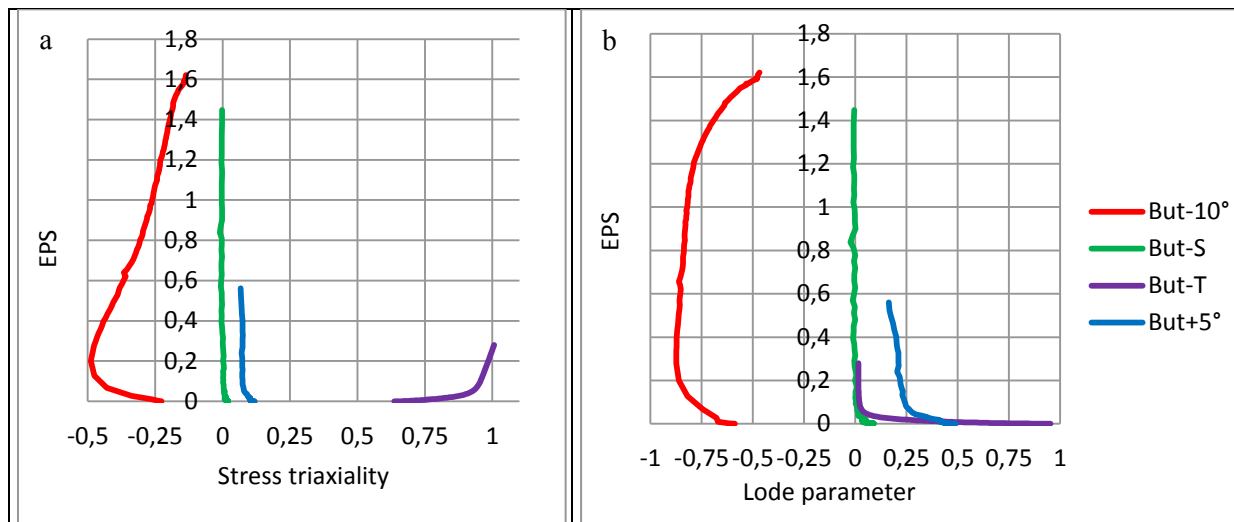


Fig.V.8: loading paths for the four butterfly specimens,
 (a) evolution of the Stress triaxiality; (b) evolution of the Lode parameter
 // trajets de chargement pour les quatre essais butterfly,
 (a) évolution de la triaxialité des contraintes ; (b) évolution du paramètre de Lode

Fig.V.9 (a-b) gather the loading paths for all 10 mechanical tests, whereas Table.V.2 compares the final and average values of the stress triaxiality and Lode parameter. They cover a wide range of stress state. The average triaxiality varies from -0.28 to 1.06, and the Lode parameter from -0.58 to 0.84. Three specimens are close to shear conditions (But-10°, But-S and But+5°). There is however an undesired big gap in the triaxiality variation between But+5° and T0. It is explained by the assessment of the geometries for the tensile specimen and the loading conditions of the butterfly specimens with the initial Hollomon law. If this study would have been done with a more precise law, notches and grooved designed would have been different.

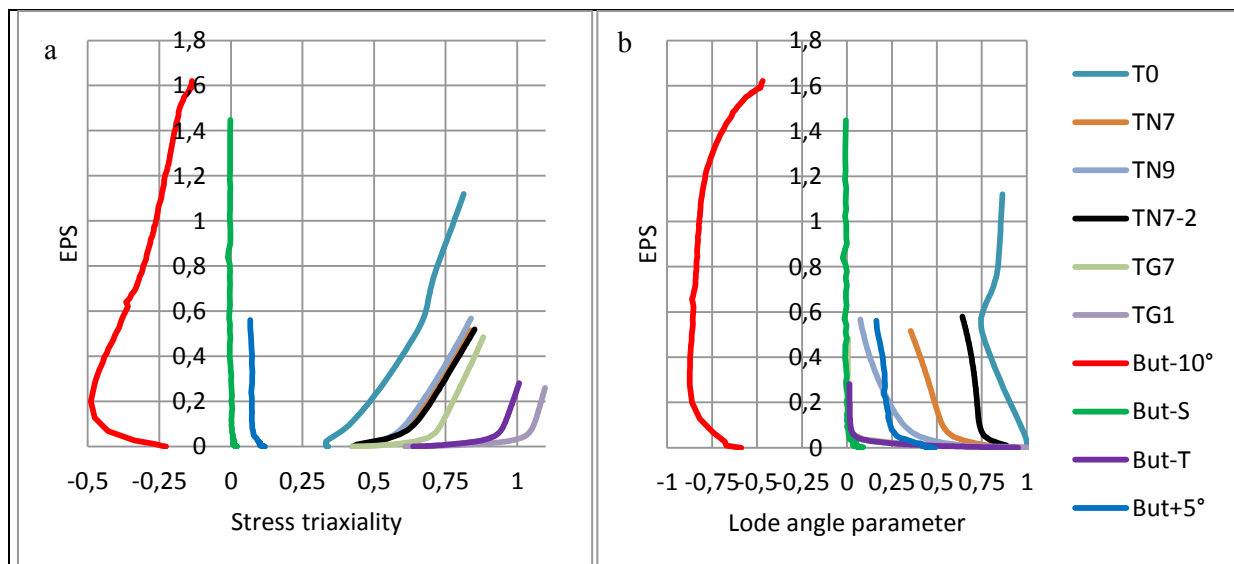


Fig.V.9: loading paths for the complete set of tests, (a) evolution of the Stress triaxiality; (b) evolution of the Lode parameter
 // trajets de chargement pour les dix essais, (a) évolution de la triaxialité des contraintes ;
 (b) évolution du paramètre de Lode

	T0	TG1	TG7	TN7	TN7-2	TN9	But-10°	But-S	But+5°	But-T
final triaxiality	0.83	1.1	0.88	0.84	0.84	0.84	-0.13	0	0.06	1
final Lode	0.86	0.01	0.02	0.36	0.66	0.07	-0.47	0	0.16	0.01
average triaxiality	0.66	1.06	0.79	0.72	0.73	0.71	-0.28	0	0.07	0.96
average Lode	0.84	0.07	0.04	0.48	0.72	0.22	-0.58	0	0.01	0.06

Table.V.2: comparison of final and average values of stress triaxiality and Lode parameter

// Comparaison des valeurs finales et moyennes de la triaxialité des contraintes et du paramètre de Lode

❖ Mesh size sensitivity analysis

For all numerical simulations, the mesh size is a parameter which can have influence on the results. The initial mesh size used by Faurecia for simulations of recliners is 0.25 mm. It can however be decreased to 0.1 mm for specific requests (it goes down to 0.07 mm for the CN layer). For such a material with gradient behavior, finer meshes are required for better prediction. Thus all the parameters identification in this work is done with a mesh size of 0.1 mm (0.07 mm for the CN layer). It is however mandatory to study the influence of this decrease of mesh size on the loading paths and fracture strain.

This sensitivity analysis was conducted with the tensile tests. **Fig.V.10** (a, b) plot the evolution of EPS for T0 and TG1 tests with the two mesh sizes (blue curves 0.1 mm ; red ones 0.25 mm). One can see the influence is quite limited on the T0 specimen (**Fig.V.10** (a,b)); there is a 10 % discrepancy on the EPS at experimental displacement to fracture. For TN7 the discrepancy is 7 %, TN9 14% and TN7-2 5 %. Those tests are in the same range. However, for TG1, the influence is 48 % and 41 % for TG7. Influence is higher here due to the strong necking process on the two latter tests.

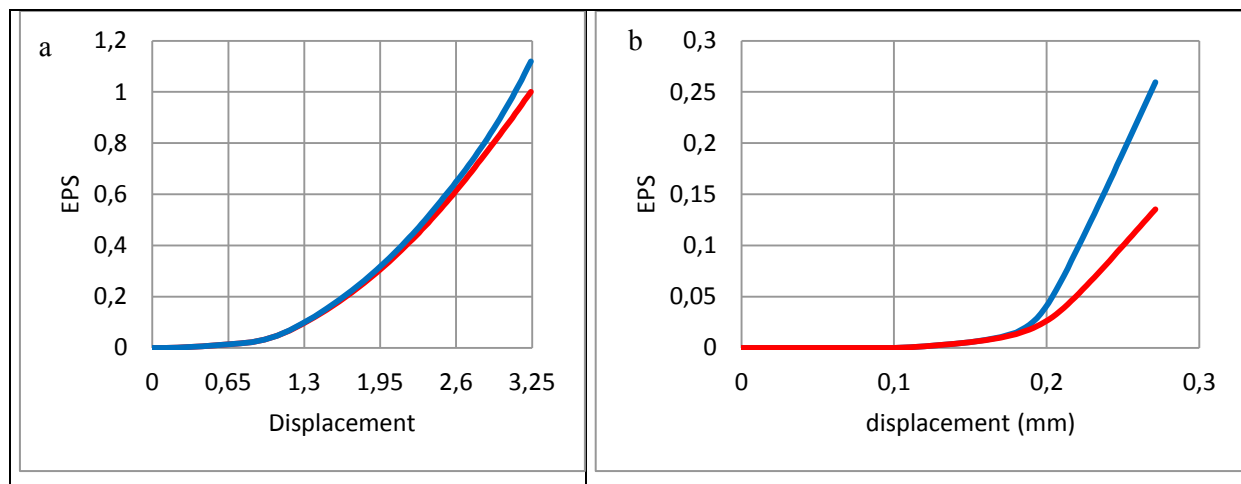


Fig.V.10: Influence of the mesh size on the variation of the EPS as a function of the displacement for (a) T0 and (b) TG1; blue curves mesh size 0.1mm; red ones 0.25 mm

// Influence de la taille de maille sur l'évolution de l'EPS pour (a) T0 et (b) TG1 ; courbes bleues taille de maille de 0.1 mm ; courbes rouges 0.25 mm

One could have tested this influence with a smaller mesh size (0.025 mm for instance) but it would not have been possible to use this mesh size for the tooth simulations at the end. However, there are already 15 elements in the width of the TG1 numerical specimen, which was considered to be enough

to have accurate description of the strain field. In addition, it was checked that there were no influence of the mesh size on the triaxiality nor the Lode parameter for a given EPS.

V. 2. 2 Test of criteria from the literature

V. 2. 2. a Identification based on strain sensors

Several phenomenological, uncoupled criteria from the literature have been tested (Modified Xue and Wierzbicki [Gachet, 2013], Bai and Wierzbicki [Bai & Wierzbicki, 2008] , Lou and Huh [Lou et al., 2012], Johnson-Cook [Johnson & Cook, 1985]). Only the identification of the Bai and Wierzbicki ([Bai & Wierzbicki, 2008]) and Lou and Huh ([Lou et al. , 2012]) criteria are detailed here.

❖ Bai and Wierzbicki

The Bai and Wierzbicki failure criterion was presented in Chapter 2, section 2.c, Eq.II.18. Symmetry with respect to $\theta = 0$ is assumed here ($D_1=D_5$ and $D_2=D_6$). There is just one point in the negative θ range, which is not enough to rigorously assess the behavior there. The criterion thus becomes:

$$\bar{\epsilon}_f(\eta, \bar{\theta}) = [D_1 e^{-D_2 \eta} - D_3 e^{-D_4 \eta}] \bar{\theta}^2 + D_3 e^{-D_4 \eta} \quad \text{Eq.V.11}$$

Table.V.3 gathers the set of identified parameters for the Bai and Wierzbicki criterion. **Fig.V.11** (a) plots the fracture locus in the (η, θ) space. **Fig.V.11** (b) plots the final value of the damage D parameter for the 10 tests obtained with the assessed criterion and identified set of parameters. Fitting is not satisfactory. For instance, it predicts premature failure for T0 but delays it considerably for Butterfly + 5°.

D_1	D_2	D_3	D_4
1.36	0.396	1.31	1.48

Table.V.3: set of parameters for the Bai and Wierzbicki criterion
// paramètres identifiés du critère de Bai & Wierzbicki

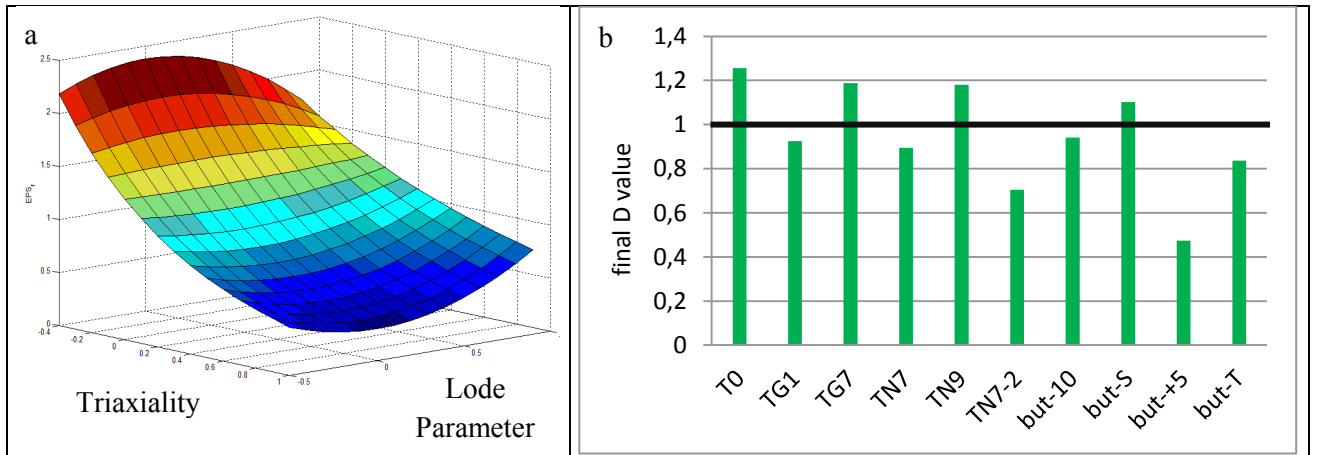


Fig.V.11: Assessment of the Bai and Wierzbicki criterion

(a) fracture locus in the (stress triaxiality, Lode parameter) plane;

(b) final value of the Damage function D for the 10 tests.

The apparent asymmetry comes from the Lode parameter interval represented, $[-0.5; 1]$

// Identification du critère de Bai et Wierzbicki,

(a) surface de rupture dans l'espace (triaxialité, paramètre de Lode);

(b) valeurs finales du paramètre d'endommagement D sur les 10 essais.

La dissymétrie apparente provient de l'intervalle représenté pour le paramètre de Lode, $[-0.5; 1]$

With its mathematical form (see Eq.V.12), this criterion prevents any failure when $\eta < -0.3$. This induces a large error on the butterfly -10° where the average triaxiality is -0.28. Thus, it was decided to change the expression of the criterion for negative triaxiality as in Eq.V.14:

$$\frac{1}{C_3} \int_0^{\bar{\epsilon}_f} \left(\frac{2}{\sqrt{3}} \cos\left(\frac{\bar{\theta}\pi}{6}\right) \right)^{C_1} \left(\frac{\langle 1 + 3\eta \rangle}{2} \right)^{C_2} d\bar{\epsilon} = D(\bar{\epsilon}) \quad \text{Eq.V.12}$$

$$\bar{\epsilon}_f(\eta, \bar{\theta}) = C_3 \left(\frac{2}{\sqrt{3}} \cos\left(\frac{\bar{\theta}\pi}{6}\right) \right)^{-C_1} \left(\frac{\langle 1 + 3\eta \rangle}{2} \right)^{-C_2} \quad \text{for } \eta \geq 0 \quad \text{Eq.V.13}$$

$$\bar{\epsilon}_f(\eta, \bar{\theta}) = C_3 \left(\frac{2}{\sqrt{3}} \cos\left(\frac{\bar{\theta}\pi}{6}\right) \right)^{-C_1} C_5 \left(\frac{1}{C_5 + \eta} \right)^{-C_6} \quad \text{for } \eta < 0 \quad \text{Eq.V.14}$$

where $C_3 = 2^{C_2} C_5^{C_6}$ for continuity between the two triaxiality domains. This same modification was done by [Gachet, 2013] on the Xue and Wierzbicki criterion at negative triaxiality to better fit the material fracture behavior.

Table.V.4 gathers the set of parameters for the identified Lou and Huh criterion. **Fig.V.12** (a) plots the fracture locus in the (η, θ) space. Once again, the fitting is not very good; failure is predicted too late for the butterfly specimens (except pure shear).

C_1	C_2	C_3	C_4	C_5	C_6
8.52	0.905	2.18	5.33	15.99	0.377

Table.V.4: set of parameters for the adapted Lou and Huh criterion
// Paramètres identifiés pour le critère de Lou et Huh modifié.

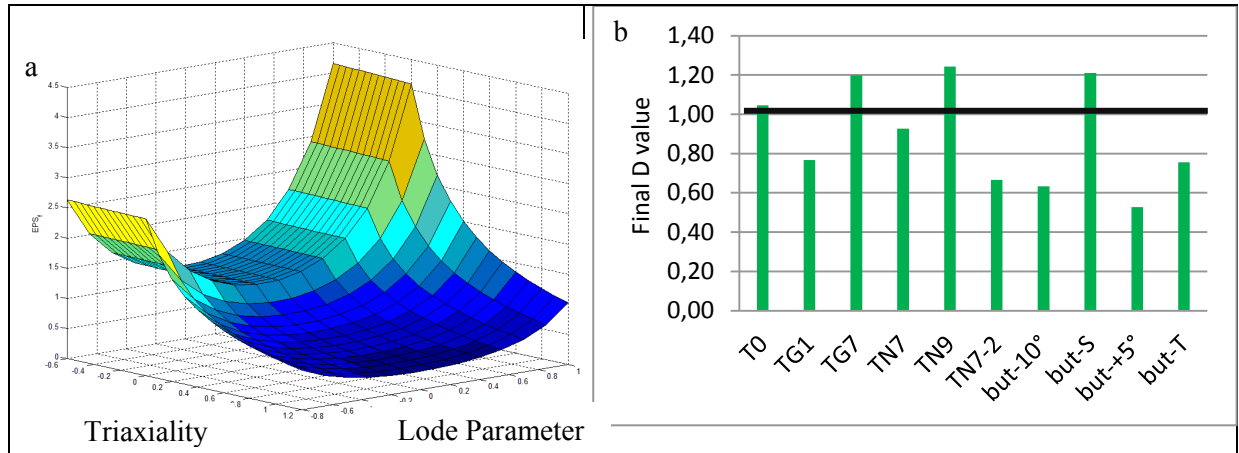


Fig.V.12: Assessment of the Lou and Huh adapted criterion
(a) fracture locus in the (stress triaxiality, Lode parameter) plane;
(b) final value of the Damage function D for the 10 tests.

The apparent asymmetry comes from the Lode parameter interval represented, $[-0.5; 1]$

// Identification du critère de Lou et Huh modifié,

(a) surface de rupture dans l'espace (triaxialité, paramètre de Lode) ;

(b) valeurs finales du paramètre d'endommagement D sur les 10 essais.

La dissymétrie apparente provient de l'intervalle représenté pour le paramètre de Lode, $[-0.5; 1]$

However, because this criterion is supposed to be good for shear failure prediction, simulations of the butterfly tests are run to check the choice the elements for the loading path. So far, the elements with the highest strain at experimental displacement to fracture were chosen, whereas fracture occurs when a critical damage is reached. Simulations of the tests are therefore re-run with the failure models implemented, looking for the element with the largest D value. It is a two steps method.

V. 2. 2. b Improved estimation of the loading paths

For the tensile tests, nothing has changed; the element at the gravity center has both the highest strain and the highest damage D. However, things change for the butterfly tests except for the one in pure tension. **Fig.V.13** illustrates this change respectively for the butterfly -10° (**Fig.V.13 (a)**), butterfly pure shear (**Fig.V.13 (b)**) and butterfly $+5^\circ$ (**Fig.V.13 (c)**). The orange arrows (resp. the green arrows) show the element with the highest strain (resp. highest damage parameter D) at displacement to fracture. The orange and green curves (**Fig.V.13**) plot the evolution of the D parameter for the two positions of elements (showed by colored arrows) as a function of its strain. Both green and orange curves are stopped at experimental displacement to fracture. Thus, the last point corresponds to the critical failure plastic strain.

On the butterfly -10° , the two elements are not in the same section: the section pictured is the one containing the element with the highest D value (this is why there is no orange arrow showing the element on the **Fig.V.13 (a)**). The elements with the highest strain was at the gravity center, here the maximum damaged element is located 0.4 mm lower and on the surface.

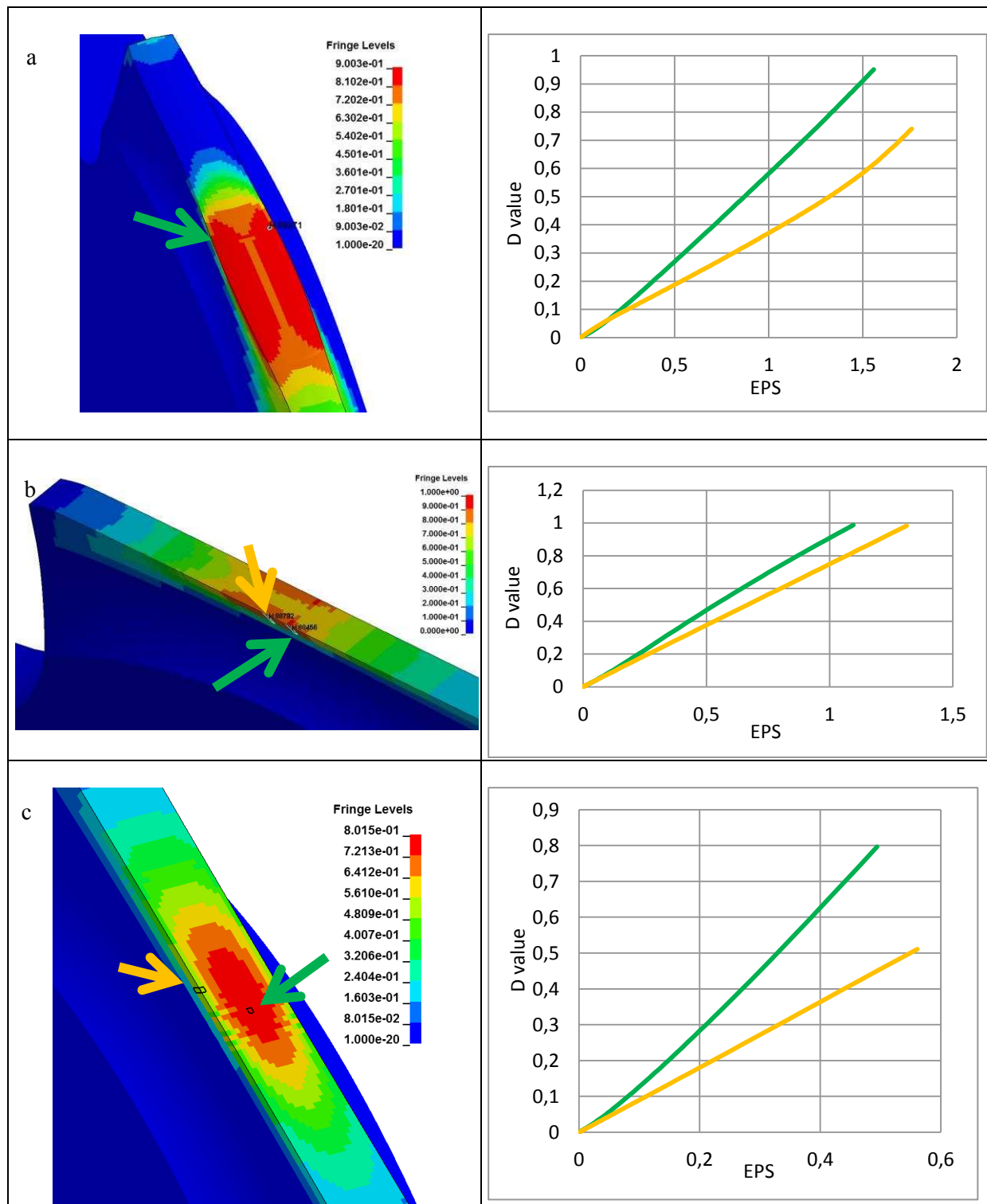


Fig.V.13: butterfly simulations with Lou and Huh criterion.

(a) butterfly -10° ; (b) butterfly pure shear; (c) butterfly $+5^\circ$.

For each simulation, 3D contour plots of D are given at the experimental displacement to fracture.

Orange curves and arrows are for the elements with the highest strain,
the green ones for the elements with the highest D

// simulations des essais butterfly avec critère de rupture de Lou et Huh,

(a) butterfly -10° ; (b) butterfly cisaillement pur ; (c) butterfly $+5^\circ$.

Pour chaque simulation, visualisation 3D du paramètre d'endommagement D au déplacement à rupture. Courbes et flèches oranges indiquent l'élément avec le plus de déformation;
en vert, celui qui a le paramètre d'endommagement le plus élevé

Even though these elements are not far from each other, this is enough to change the loading paths (see **Fig.V.14** (a-b)). The curves with crosses represent the previous loading paths, the ones without are the updated ones. There is no change for the butterfly pure tension. Whereas strain at failure is lowered for the butterfly -10° and pure shear, triaxiality is increased for the butterfly $+5^\circ$. The Lode parameter increases for the butterfly -10° . **Table.V.5** gathers the final and average value of $(\eta, \bar{\theta})$.

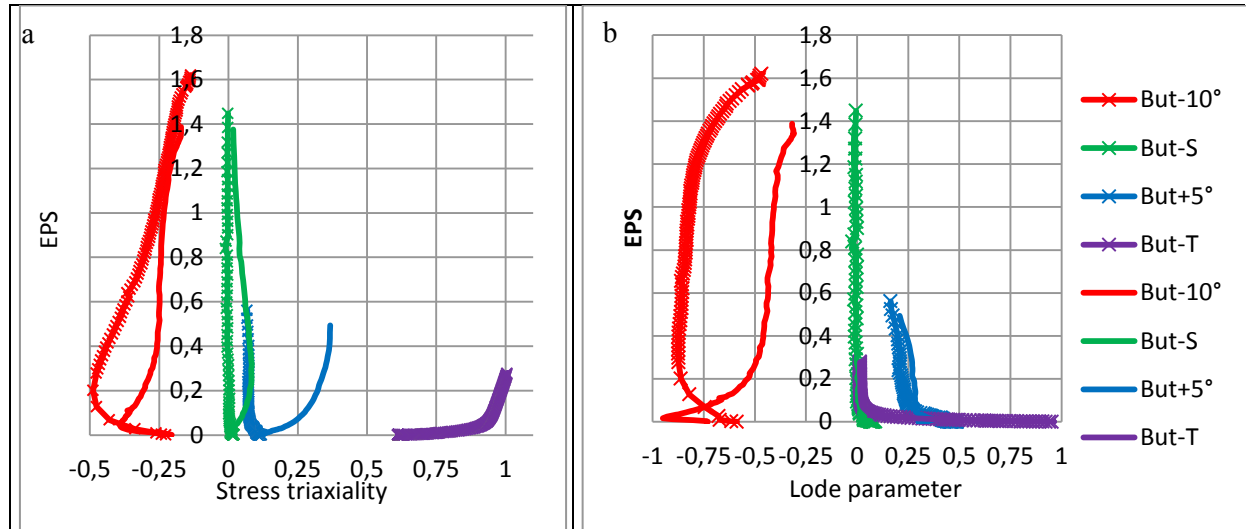


Fig.V.14: updated loading paths for the butterfly specimens, (a) stress triaxiality; (b) Lode parameter
 // trajets de chargement mis à jour pour les éprouvettes butterfly, (a) triaxialité des contraintes ; (b) paramètre de Lode

	T0	TG1	TG7	TN7	TN7-2	TN9	But-10°	But-S	But+5°	But-T
final triaxiality	0.83	1.1	0.88	0.84	0.84	0.84	-0.17	0.02	0.37	1
final Lode	0.86	0.01	0.02	0.36	0.66	0.07	-0.31	0.02	0.2	0.01
average triaxiality	0.66	1.06	0.79	0.72	0.73	0.71	-0.24	0.05	0.32	0.96
average Lode	0.84	0.07	0.04	0.48	0.72	0.22	-0.46	0.01	0.26	0.06

Table.V.5: average and final triaxiality and Lode parameter for the ten tests
 // valeurs moyennes et finales de la triaxialité et du paramètre de Lode pour les dix essais

V. 2. 2. c Improved identification of damage model parameters

Now the loading paths have been updated, and correspond to the elements with the highest damage parameter, new identifications can be done.

❖ Bai and Wierzbicki

Symmetry with respect to $\theta = 0$ is still assumed here, Table.V.6 gathers the identified set of parameters.

D ₁	D ₂	D ₃	D ₄
5.83	2.38	1.15	1.41

Table.V.6: improved parameters set of the Bai and Wierzbicki criterion
 // jeu de paramètres amélioré pour le critère de Bai et Wierzbicki

Fig.V.15 (a) plots the fracture surface in the $(\eta, \bar{\theta})$ space; **Fig.V.15** (b) shows the final value of the D parameter on the ten tests. Note that the curve is very different from the one assessed previously (**Fig.V.11**). Indeed, at $\eta < 0$, the EPS increases a lot in the updated case, whereas it was decreasing with the first set of parameters. This enables to see the limit of the method which consists in choosing the element with the highest EPS at experimental displacement to fracture, instead of the one with the highest D. However, failure prediction is not accurate on the tests at low triaxiality, it predicts failure too early for TG7 and TN9 for instance and too late for but-10°, but+5° but-T and TN7-2.

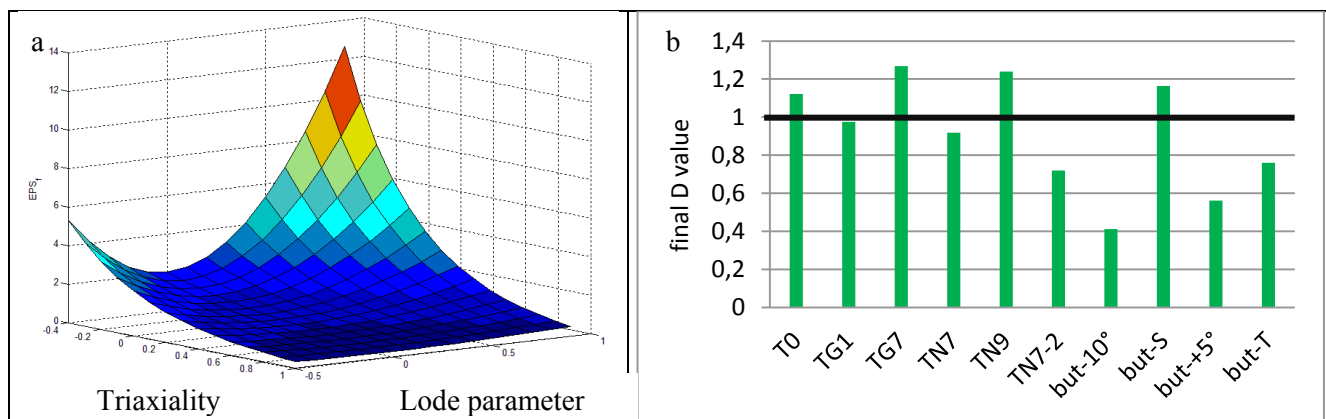


Fig.V.15: Updated Bai and Wierzbicki criterion

(a) fracture locus in the (stress triaxiality, Lode parameter) plane;

(b) final value of the Damage D function for the 10 tests.

Apparent asymmetry comes from the Lode parameter interval represented, $[-0.5; 1]$.

// critère de Bai et Wierzbicki ré-identifié,

(a) surface de rupture dans l'espace (triaxialité, paramètre de Lode);

(b) valeurs finales du paramètre d'endommagement D pour les 10 essais.

La dissymétrie apparente vient de la représentation sur l'intervalle du paramètre de Lode $[-0.5; 1]$.

❖ Lou and Huh

Table V.7 gathers the set of parameters for the Lou and Huh criterion. **Fig.V.16** (a) plots the fracture surface in the $(\eta, \bar{\theta})$ space; **Fig.V.16** (b) shows the final value of the D parameter on the ten tests. Unlike the Bai & Wierzbicki criterion, the criterion is less sensitive to the choice of new elements: the global shape of the curve is the same than the one assessed previously **Fig.V.12**. Failure prediction remains not very accurate for most of the tests.

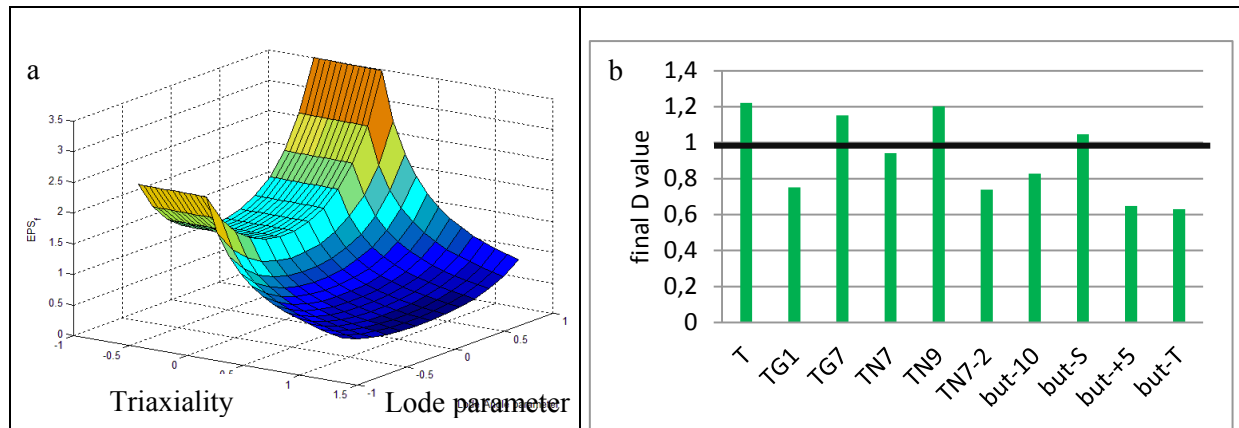


Fig.V.16 : Lou and Huh updated criterion,
 (a) fracture locus in the (stress triaxiality, Lode parameter) plane;
 (b) final value of the Damage D function for the 10 tests.
 Apparent asymmetry comes from the Lode parameter interval represented, [-0.5; 1].
 // critère de Lou et Huh ré-identifié,
 (a) surface de rupture dans l'espace (triaxialité, paramètre de Lode);
 (b) valeurs finales du paramètre d'endommagement D pour les 10 essais.
 La dissymétrie apparente vient de la représentation sur l'intervalle du paramètre de Lode [-0.5 ; 1].

C ₁	C ₂	C ₃	C ₄	C ₅	C ₆
6.44	0.984	1.75	2.29	8.44	0.070

Table.V.7: improved set of parameters for the Lou and Huh criterion
 \\ jeu de paramètres amélioré pour le critère de Lou et Huh

❖ Discussion

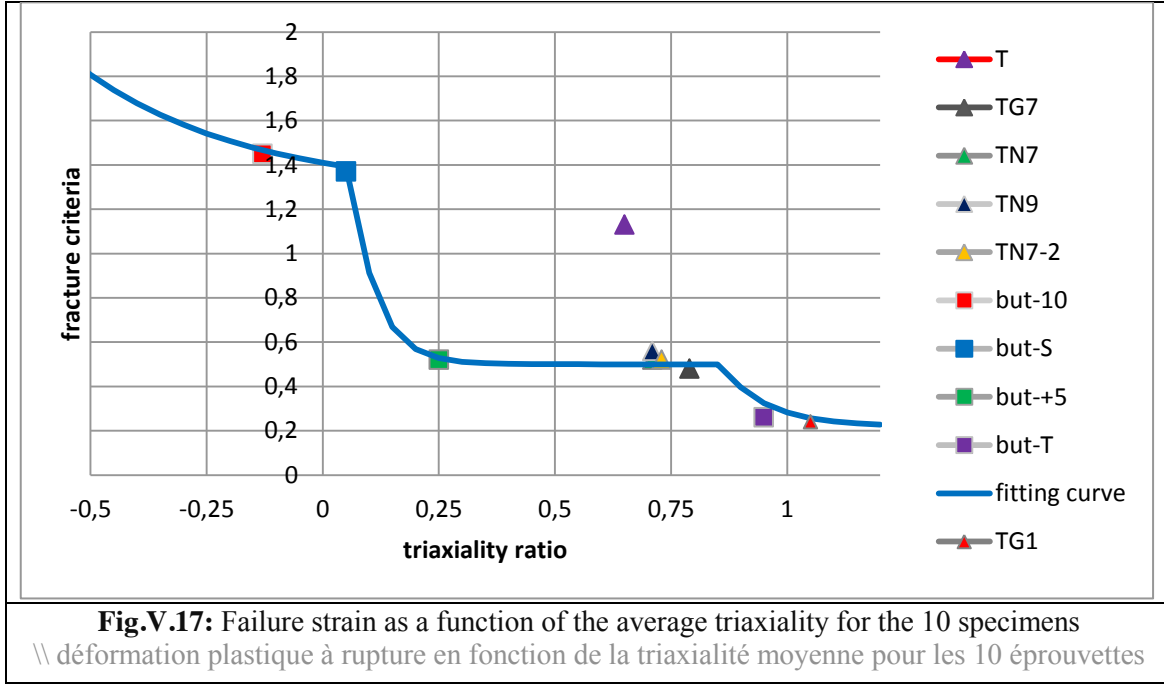
Other (triaxiality, Lode parameter)-based criteria have been tested, for instance Xue and Wierzbicki criterion, but the fit was not good either. The inaccuracy comes from the mathematical formula of these criteria, namely the dependence on Lode parameter is too restrictive. If one looks at **Fig.V.9** (b), the tensile tests (except TG1) have a triaxiality varying from 0.66 to 0.79. The Lode parameter varies from 0.04 to 0.84. For these five tests, at this level of stress triaxiality around 0.7, the Lode parameter has a weak influence on most of its domain. Only at $\theta > 0.8$ (higher than TN7-2) is its influence significant, and in fact huge (as shown by the T0 specimen). This cannot be accounted for by a degree two power law as in the Bai and Wierzbicki criterion, or by a power of a cosine function as in the Lou and Huh model. Those criteria are phenomenological and have no physical meaning. The mathematical form of the criteria was written to predict aluminum alloy fracture, it could be less efficient for our heat treated steel.

In addition, it must be noted that many papers in the literature never show the final D value at displacement to fracture for all tests such as in **Fig.V.16** (b). It is then difficult to judge the accuracy of their models once the set of parameters identified.

Based on these poor results using established failure criteria, it was decided to define a new criterion derived from the Johnson-Cook model ([Johnson & Cook, 1985]).

V. 2. 3 Proposition of a new exponential criterion

The idea is to propose a new failure criterion with an adapted mathematical formula for the core material. As noticed previously, the Lode parameter has a weak influence on the failure behavior for $\theta < 0.8$. Therefore a first approach of the material failure can be done without accounting for it. **Fig.V.17** plots on the same graph the ten points corresponding to the fracture loci in the (η_{av}, ϵ_f) plane. The loading paths correspond to the updated ones, **Fig.V.14**. It can be seen that all the points except the one corresponding to T0 can be fitted on a single curve. The curve is the merge of three exponential branches, the formula of which is given in Eq.V.15.



❖ First set of parameters

A new phenomenological fracture locus is written based on our experimental data. The stress triaxiality axis is divided into three domains. In each domain, the stress triaxiality is accounted for through:

$$f_{\eta}(\eta) = C_1 + C_2 * e^{-C_3 * \eta} \quad \text{Eq.V.15}$$

The exponential function to account for the triaxiality comes from the Rice and Tracey criterion [Rice & Tracey, 1969]. To obtain the observed very sharp increase around $\theta = 0.8$, the Lode parameter influence is also given an exponential form through $f_{\bar{\theta}}(\bar{\theta}) = L_1 + L_2 * e^{L_3 * |\bar{\theta}|}$. The complete fracture locus is thus:

$$\epsilon f(\eta, \bar{\theta}) = (C_1 + C_2 * e^{-C_3 * \eta}) * (1 + L_1 * e^{L_2 * |\bar{\theta}|}) \quad \text{for } \eta \leq 0.05 \quad \text{Eq.V.16}$$

$$\epsilon f(\eta, \bar{\theta}) = (C_4 + C_5 * e^{-C_6 * \eta}) * (1 + L_1 * e^{L_2 * |\bar{\theta}|}) \quad \text{for } 0.05 \leq \eta \leq 0.8 \quad \text{Eq.V.17}$$

$$\epsilon f(\eta, \bar{\theta}) = (C_7 + C_8 * e^{-C_9 * \eta}) * (1 + L_1 * e^{L_2 * |\bar{\theta}|}) \quad \text{for } 0.8 \leq \eta \quad \text{Eq.V.18}$$

where $C_1, C_2, C_3, C_4, C_5, C_6, C_7, C_8, C_9, L_1, L_2$ are material parameters. There are continuity conditions on some of the parameters, see Eq.V.19 and Eq.V.20.

$$C1 = (C_4 + C_5 * e^{-C_6*0.05}) - C_2 * e^{-C_3*0.05} \quad \text{Eq.V.19}$$

$$C_8 = \frac{(C_4 - C_7 + C_5 * e^{-C_6*0.8})}{e^{-C_9*0.8}} \quad \text{Eq.V.20}$$

$$D = \int_0^{\epsilon_f} \frac{d\bar{\epsilon}_p}{f(\eta, \theta)} = 1 \quad \text{Eq.V.21}$$

Table.V.7 gathers the identified parameters for the exponential criterion. **Fig.V.18** (a) plots the fracture surface in the $(\eta, \bar{\theta})$ space and **Fig.V.18** (b) illustrates the final value of the D damage parameter. One sees the failure prediction is much better than the previous fitting. The exponential function accounting for the Lode parameter fits well the material behavior to fracture. Thus, L_1 is quite low to account for the Lode parameter only at higher value than 0.75.

C1	C2	C3	C4	C5	C6	C7	C8	C9	L1	L2
1.2	0.13	2.8	0.5	2	18	0.22	4134	12	10^{-5}	13.92

Table.V.7: identified parameters for the exponential criterion;
C1 and C8 are obtained using continuity conditions
// jeu de paramètres identifiés pour le critère exponentiel ;
C1 et C8 sont obtenus à partir des conditions de continuité

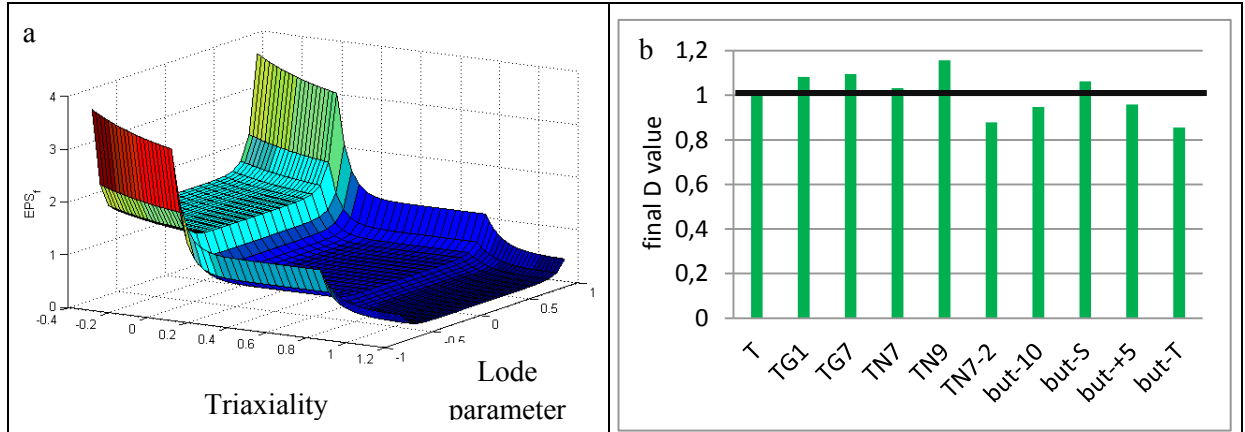


Fig.V.18: exponential criterion (a) fracture locus in the stress triaxiality and Lode parameter; (b) final value of the Damage D function for the 10 tests

// critère exponentiel, (a) surface de rupture dans l'espace triaxialité et paramètre de Lode ; (b) valeurs finales du paramètre d'endommagement D sur les 10 essais.

❖ Identification of the new updated loading paths

However, it is mandatory to make another study of the damage localization in the butterfly simulations. Indeed, the fracture locus has changed, and that may change the localization of the element with the highest damage at fracture and the stress and strain paths.

Simulations with the identified exponential criterion are done to check the localization of the highest damage elements. There is no modification for the butterfly pure tension and pure shear. **Fig.V.19** illustrates the modification for the butterfly-10° (**Fig.V.19** (a)) and butterfly+5° (**Fig.V.19** (b)).

Modification is very weak for the butterfly +5°, the two elements are located nearby and the loading paths are very close.

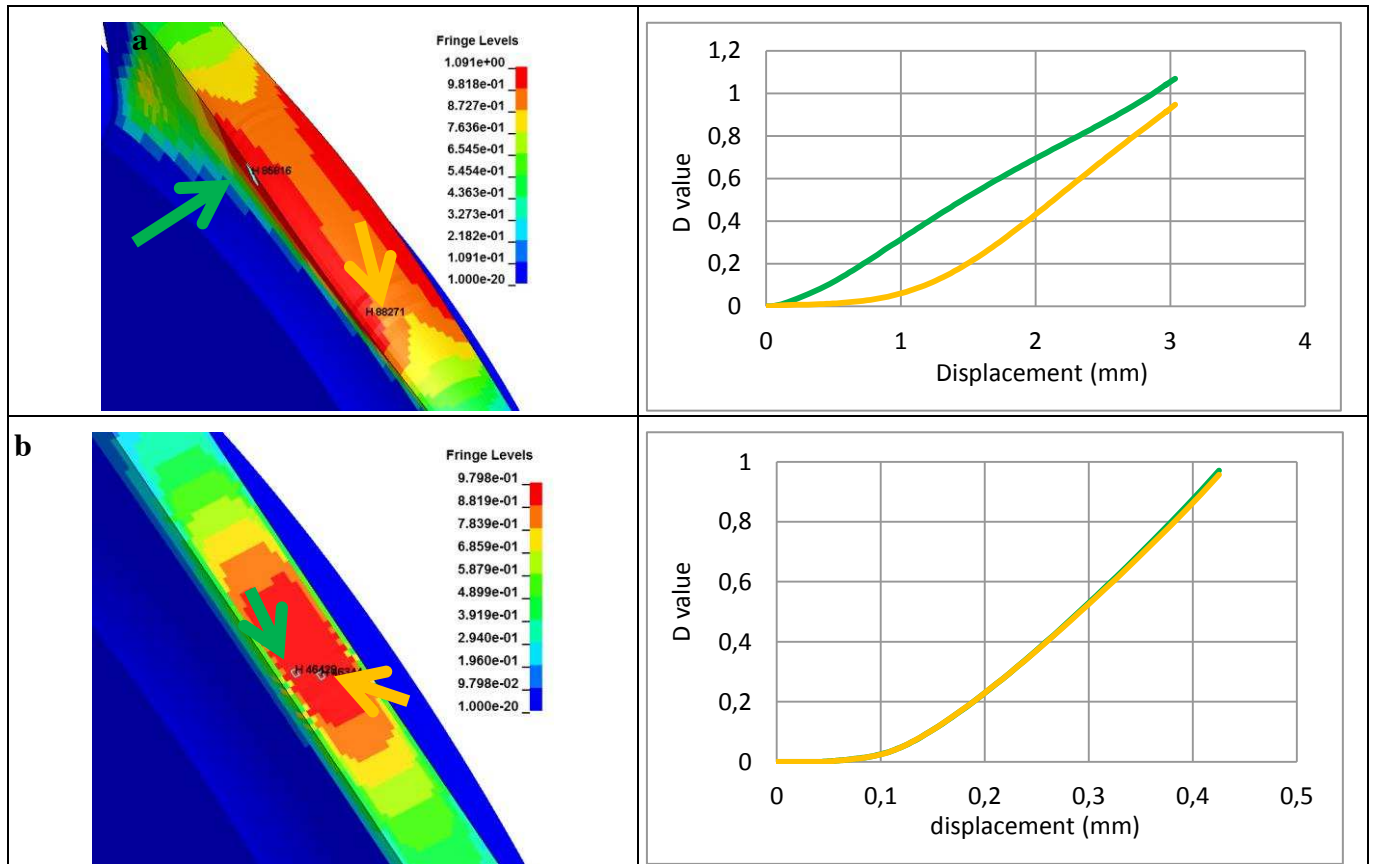


Fig.V.19: butterfly simulations with exponential criterion.

(a) butterfly -10°; (b) butterfly +5°.

For each simulation, 3D contour plots of D are given at the experimental displacement to fracture. Blue curves and arrows are for the elements with highest strain, the green ones for the elements with highest D

// simulations des essais butterfly avec critère de rupture exponentiel,

(a) butterfly -10° ; (b) butterfly +5°.

Pour chaque simulation, visualisation 3D du paramètre d'endommagement D au déplacement à rupture.

Courbes et flèches bleues indiquent l'élément avec le plus de déformation;

en vert, celui qui a le paramètre d'endommagement le plus élevé,

For the butterfly -10°, elements seem far away, but they are at quasi-symmetrical positions. **Fig.V.20** (a-b) illustrate the updated and final loading paths for butterfly tests. Table.V.8 shows the final and average values of the stress triaxiality and the Lode parameter. The discrepancy between the final value and the average is not that significant (except for But-10°) showing that after the establishment of the stress state, it is rather proportional.

	But-10°	But-S	But+5°	But-T
final triaxiality	-0.17	0.02	0.29	1
final Lode	-0.31	0.02	0.21	0.01
average triaxiality	-0.13	0.05	0.25	0.96
average Lode	-0.53	0.01	0.29	0.06

Table.V.8: average and final triaxiality and Lode parameter for the butterfly tests

// valeurs moyennes et finales de la triaxialité et du paramètre de Lode pour les échantillons butterfly

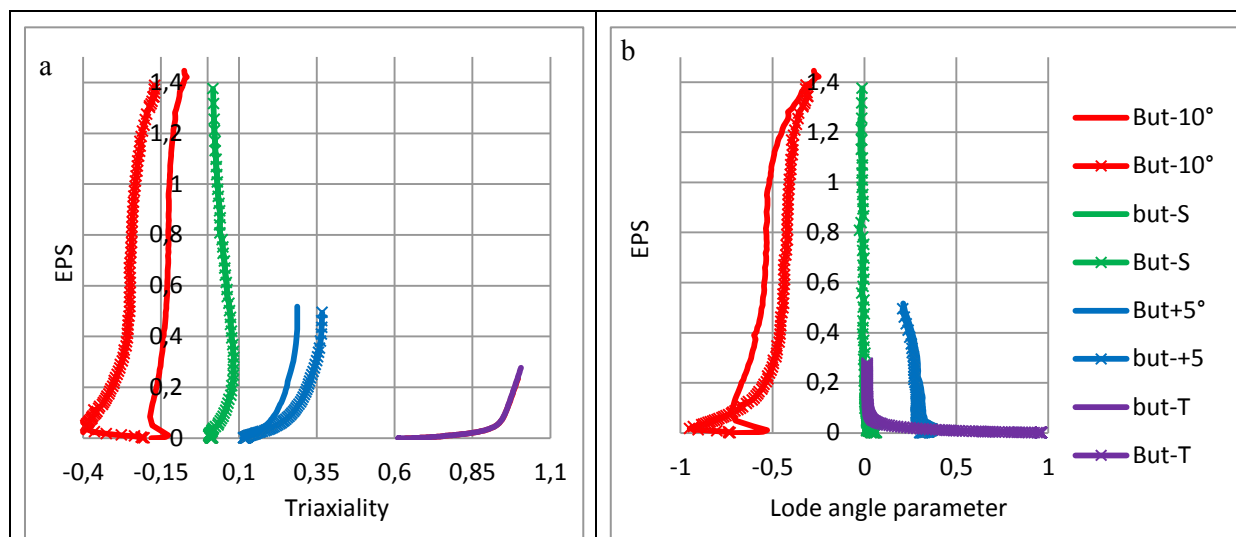


Fig.V.20: updated loading paths for the butterfly specimens; curves with crosses are the previous paths,

(a) stress triaxiality ; (b) Lode parameter

// trajets de chargement actualisés pour les éprouvettes butterfly ; les courbes avec croix sont les anciens trajets,

(a) triaxialité des contraintes ; (b) paramètre de Lode

Finally, the parameters identified with the new loading paths for the new fracture criterion are gathered in Table.V.9. **Fig.V.21** (a) illustrates the fracture locus in the $(\eta, \bar{\theta})$ space and **Fig.V.21** (b) illustrates the final value of the D damage parameter.

C1	C2	C3	C4	C5	C6	C7	C8	C9	L1	L2
1.41	0.12	2.8	0.5	2.5	18	0.22	1245	10.5	10^{-5}	14.05

Table.V.9: final set of parameters for the exponential criterion

// jeu de paramètres finaux pour le critère exponentiel

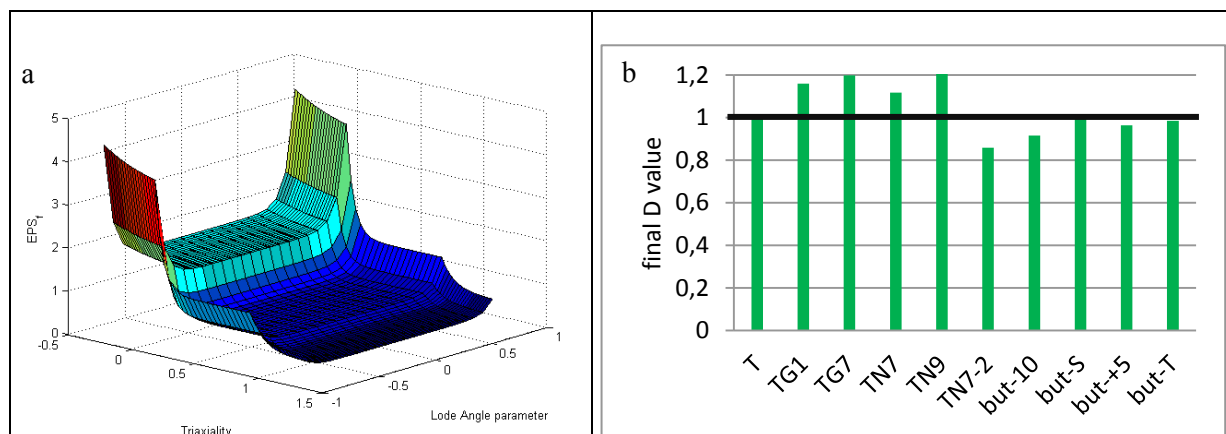


Fig.V.21: exponential criterion

(a) fracture locus in the stress triaxiality and Lode parameter;

(b) final value of the Damage D function for the 10 tests

// critère exponentiel,

(a) surface de rupture dans l'espace (triaxialité, paramètre de Lode);

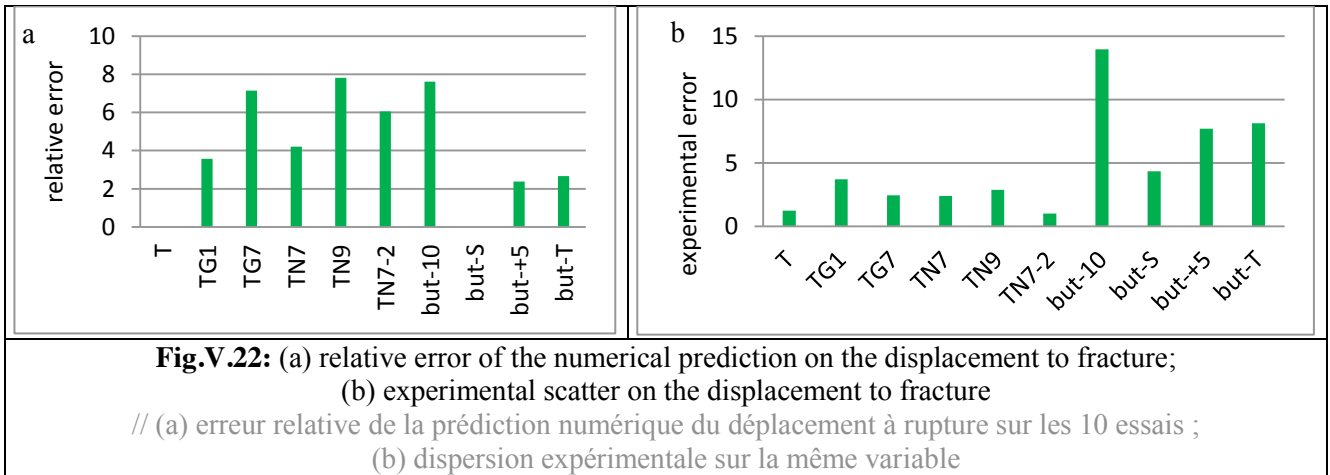
(b) valeurs finales du paramètre d'endommagement D sur les 10 essais.

❖ Discussion

The failure criterion of the core material is finally identified. **Fig.V.21** (b) shows the final value of the damage D parameter at experimental displacement to fracture. Fitting is good for the tests submitting the material to shear stress state, which is important for gear tooth behavior. There is in average 8% discrepancy on the D value, to be compared with 21 % for the Lou and Huh and 24 % for the Bai & Wierzbicki: failure prediction has been improved.

However, one can wonder how much this difference means in terms of displacement to fracture. Thus, the relative error on the predicted displacement is calculated on the 10 tests ($\frac{|d_{exp}-d_{num}|}{d_{exp}} * 100$) and illustrated through **Fig.V.22** (a). The error on the displacement to fracture is lower than the error on the D final value. Indeed, the increase of the D value is not linear regarding the displacement, for instance, **Fig.V.19** (b) plots the variation of D as a function of the displacement. One can see it increases faster than the displacement at the end. Its variation is linked to the plastic strain, by its mathematical definition. For the TN9 specimen, the final value of D is 1.21, therefore an error of 21%, whereas it is only 8% in terms of displacement. Furthermore, this is the test with the highest error on the failure prediction. The average error on the displacement is about 4%, over ten tests; this is rather convincing.

Finally, this must be compared with the experimental scatter. **Fig.V.22** (b) plots the relative error on the experimental displacements to fracture ($\frac{d_{max}-d_{average}}{d_{average}} * 100$). It is higher than the numerical discrepancy on the failure prediction for most tests. This is especially true for the butterfly specimens: for instance the butterfly -10° reaches a relative error of 14%. The average relative error is 5%, it decreases to 2.3 with only the tensile tests specimen. So the error on the failure prediction is relevant in regard of the experimental discrepancy.



V. 2. 4 Fracture criterion reduction

Within the context of industrial use of this criterion, the identification of 9 parameters may appear to be too cumbersome. Therefore, a simplified version with fewer parameters is defined here. The Lode parameter dependence is removed since it has an influence only for $\bar{\theta} > 0.8$, whereas teeth fail mainly in shear. For the same reason, the last domain of $\eta > 0.8$ can be removed as well. In that case, the criterion is a curve depending only on η .

$$\varepsilon f(\eta, \bar{\theta}) = (C_1 + C_2 * e^{-C_3 * \eta}) \text{ for } \eta \leq 0.05 \quad \text{Eq.V.22}$$

$$\varepsilon f(\eta, \bar{\theta}) = (C_4 + C_5 * e^{-C_6 * \eta}) \text{ for } 0.05 \leq \eta \quad \text{Eq.V.23}$$

C1	C2	C3	C4	C5	C6
1.41	0.12	2.8	0.5	2.5	18

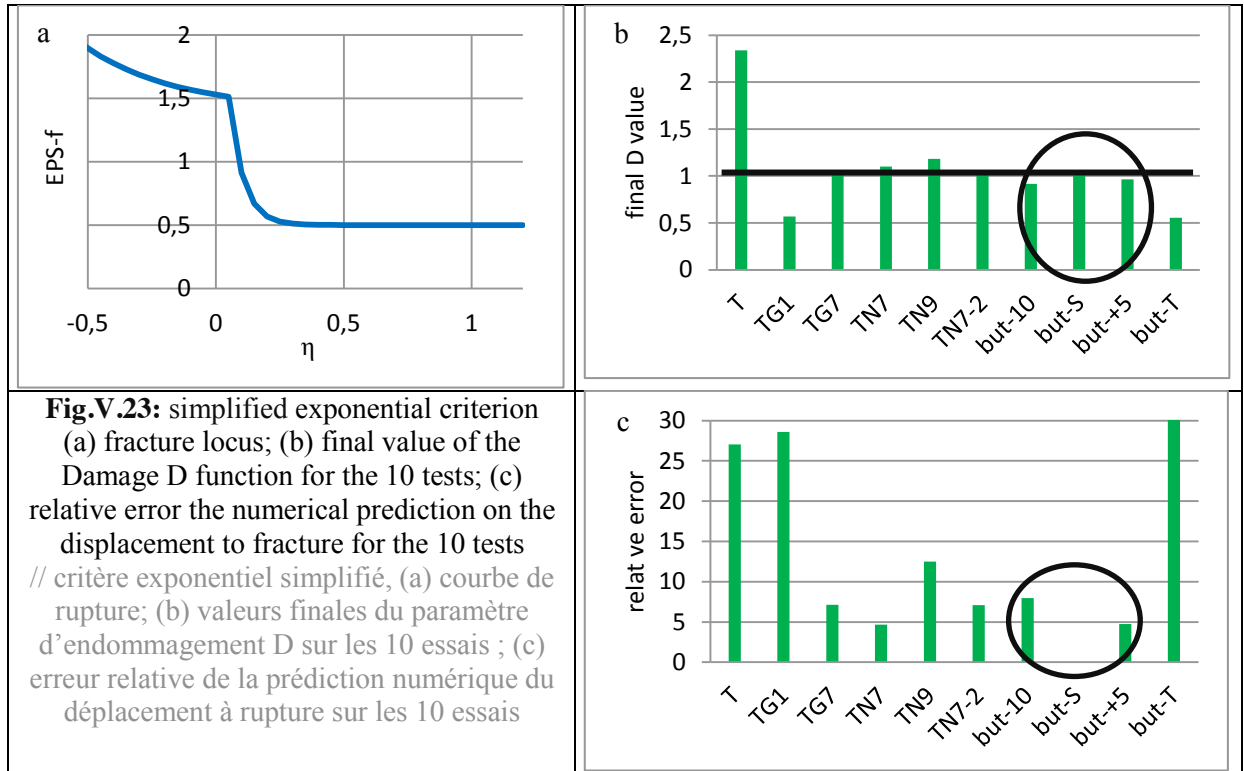
Table.V.10: identified parameters of the simplified criterion

\ \ paramètres du critère simplifié identifiés

Parameter C1 is fixed for continuity between the two ranges, it is being expressed as a function of the other parameters as in Eq.V.24:

$$C_1 = C_4 + C_5 * e^{-C_6 * \eta} - C_2 * e^{-C_3 * \eta} \quad \text{Eq.V.24}$$

Parameters have been re-identified (Table V.11). **Fig.V.23** (a) Plots the fracture locus in the triaxiality domain. **Fig.V.23** (b) plots the final value of the D parameter. Of course, failure prediction is less efficient for the tensile flat specimen where the Lode parameter has most of its influence. Damage is here strongly overestimated, i.e. fracture is predicted much too early. And because the last domain of triaxiality has been removed, prediction is degraded for the tests at high triaxiality (TG1 and butterfly T). But in the range of stress triaxiality and Lode parameter observed during teeth failure in critical areas, the prediction is rather good (tests in this range are circled in black). The relative error on the displacement to fracture is indeed quite low in this range (see **Fig.V.23** (c)).



V. 2. 5 Discussion

Failure criterion of the core material was identified thanks to a method using both experimental and numerical data. It consists of measuring the numerical plastic strain reached at experimental displacement to fracture. This methodology requires an accurate identification of the material behavior

law. Even though this method is efficient, there are obviously some elements which are usually not detailed in the literature and which must be accounted for.

- Firstly, it was seen in Chapter 4 there is some experimental scatter on the fracture displacement. This is especially the case on the butterfly specimens where the machining is tricky due to the complex shape and low thickness of the useful part. It induced up to 30 % discrepancy on the displacement to fracture. Thus, the strain to fracture ranges between 1.06 and 1.45, a 40 % scatter. The difference is higher on the strain since it increases faster than the displacement due to the localization before fracture. This example is the worst case with the highest experimental scatter. But it has to be taken into account; furthermore, it is impossible to avoid scatter in experiments. However, another test inducing shear stress state with less scatter should be found for further studies.
- Secondly it is difficult to detect precisely the beginning of the fracture process (crack opening) on the specimens. It is well known that in the tensile test, cracks appear at the gravity center, but it is more difficult to predict for the butterfly specimen. It is likely, but not certain, that failure will appear in the middle thanks to its specific gage section. This is why the method has been coupled with the FEM simulation. Once fracture is implemented, the first element which reaches the critical value of the damage variable is the one where failure is supposed to start. This is valid only if the fracture criterion is correct. However, experimental fracture could have appeared on the sides of the specimen, especially for the pure shear and the butterfly-10° where sides are submitted to tensile stresses. According to the simulation, it is not the case, but it might have occurred, considering the machining issues. The only way to be sure is to record the specimen with high speed cameras and high resolution lenses focused on the gage section. This device was unfortunately not available.
- The behavior law of the core material fits accurately the ten specimens on a wide range of stress state. This is a good result considering the use of an isotropic behavior law. At low level of plastic strain, the load slightly is overestimated; at high level, it is the opposite. Obviously, the difference is just a few percent, but it has to be discussed. Indeed, for the failure, the part after the necking matters most because it is where the strain increases most. Inaccuracies during the fitting stage will induce inaccurate prediction of necking, and thus modify the strain at fracture and more generally the loading path.
- Furthermore, an uncoupled method is used to account for fracture here. Some more advanced models for which damage can be coupled to material behavior could be used as seen in the literature part, Chapter 2. Using such models would induce a softening of the material in the damaged area; i.e. strain localization should occur faster. This would increase the strain at failure. However, this method is time consuming to set up and may induce localization issues leading to mesh dependency; this is why the uncoupled method was chosen for this work.
- Another point is the calculation of the strain itself through the integration points, and the elements. It is indeed mandatory to check the homogeneity of the strain field within the critical area. If the mesh is of poor quality, or extremely distorted in the end, this can create a false local extremum. This is why nonlocal methods have been developed based on the definition of a regularized variable. The latter account for the average damage in a vicinity of a material point; it avoids the deletion of one element based on a bad calculation due to a highly distorted mesh. But no such method is available in LS-DYNA for 3D meshes.
- The last point is the variation of the triaxiality and the Lode parameter during loading. This method of uncoupled behavior law is very precise when the loading path is proportional. However, with few exceptions, it is hardly ever the case. This is why the damage variable accounts for the whole loading path, and not just the initial or average or final value of the

triaxiality and Lode parameter. This enables to better determine the damage variable D despite the evolution of the aforementioned parameter. This can be illustrated with the T0 specimen; for the calculation of the D parameter at experimental displacement to fracture, the initial, average, or final values of the triaxiality may be considered. Respectively, they give $D = 0.17$, 1.05 and 1.1 ; whereas it is equal to 1.00 when the complete loading path is accounted for. Note that the difference is not that high when average or final values are used, because that is when damage accumulates as triaxiality grows during the test.

In the end, the highest source of variability is the butterfly specimen. It was used to submit the material to stress states close to shear. Another possibility would have been to perform other induced shear tests with a simple tensile test machine. Machining would have been easier, but for such highly ductile materials, failure is likely to occur on the side of the analyzed area, and therefore in tension stress states. Another shear specimen has been designed during this PhD, an evolution of the double shear specimen proposed by [Gachet, 2013], with curved gauge sections instead of square ones. However, the machining was not a success, because initial sheets were bent and twisted because of the industrial cutting process and the inherent distortion coming from the carbonitriding treatment. Therefore, the scatter of the experimental curves was quite high, and it was decided not to use these results. With flat sheets, it would have been interesting to compare these results to the butterfly in pure shear mode.

Failure criterion of the core material is now identified once the previous remarks are accounted for. A new criterion has been derived because none of the criteria available in the literature matched the whole set of tests, due to their too restrictive mathematical form.

Indeed, the mechanical characterization reveals two special features.

- The first one is the weak influence of the Lode parameter for $\bar{\theta} < 0.8$ for our material. Indeed, all the tensile tests except TG1 have average stress triaxiality around 0.7 . In the meantime, the average Lode parameter varies from 0.04 for shear to 0.84 for the flat specimen tension test T0. Except for T0, the failure is weakly influenced by $\bar{\theta}$. The critical plastic strain is about 0.5 for $0.04 < \bar{\theta} < 0.72$ but reaches 1.17 for T0 with an average $\bar{\theta} = 0.84$. This abrupt increase of the influence of the Lode parameter cannot be taken into account with any second order power law or through a cosine-based function. It requires higher exponent or an exponential function. This strong increase of strain to fracture for the T0 specimen was a surprise. Such a result was not seen in the literature for other materials. This is why this test was checked carefully and the same results were obtained again.
- The other specific feature is the strong increase of the material ductility between the butterfly $+5^\circ$ and the butterfly pure shear. Indeed, the strain to failure is multiplied by 2.6 between the two tests. Mathematical formulae of criteria from the literature cannot capture this behavior. This is why the new criterion was developed, with the three stages along the triaxiality axis. It matches accurately the fracture behavior of all the specimens, at low as well as high triaxiality.

Indeed, if one looks at the error between the experimental displacements to fracture and the predicted ones, it is lower than the experimental scatter (4.15% vs 10%).

However, nine parameters to be identified can be a bit too much for industrial R&D. The aim is to model the tooth failure; it was shown that it occurs in a stress state close to shear (this will be confirmed in chapter 6). So the last domain of triaxiality ($\eta > 0.8$) does not matter a lot. Furthermore, the Lode parameter has an influence only for high values $0.8 < \bar{\theta}$, which should not be reached

during tooth failure (this also will be confirmed in chapter 6). This is why a simplified criterion is written by removing the Lode parameter dependence and the last domain of stress triaxiality. That leaves only 5 parameters to be identified. The failure prediction is obviously less efficient for the tests at high Lode parameter (T0), or at high triaxiality, which could be removed from the set of tests to perform. Otherwise, the failure prediction is accurate for the other cases. It will be compared to the other criteria (Bai and Wierzbicki, exponential criterion with 9 parameters) to model the failure of a tooth in Chapter 6.

V. 3 Fracture criterion for the CN layer

The plastic and the fracture behavior of the core material are now characterized. Next, the properties of the CN layer must be identified. As it is not possible to work on homogeneous carbonitrided material only, we had to work on “full specimen”, i.e. core + CN layer. This is possible since the core material was characterized before. We thus assume that the core material of the full specimen has the same behavior and fracture properties as the one obtained using the anti-carbonitriding paint on its surface during heat treatment.

Observations done with the Four-point Bending Test (4PBT) and the tensile test confirm the brittle behavior of the CN layer. Thus a criterion based on the principal stresses is chosen. It is composed of a critical value of the first principal stress (Eq.V.25) and a maximum value of the hydrostatic pressure (Eq.V.26). Therefore failure occurs if the two following conditions are fulfilled:

$$\sigma_I \geq \sigma_{Ic} > 0 \quad \text{Eq.V.25}$$

$$p = -\frac{1}{3}(\sigma_I + \sigma_{II} + \sigma_{III}) \leq p_c < 0 \quad \text{Eq.V.26}$$

The former accounts for the tensile stress, which induces the failure of such brittle materials and governs the crack orientation. The latter ($p = -\frac{1}{3}(\sigma_I + \sigma_{II} + \sigma_{III})$) introduces a second condition for failure, assuming an influence of stress triaxiality. It accounts for the case of compressive σ_{II} and σ_{III} which could delay failure, even if σ_I has reached the critical value. Elements will be deleted only when the two conditions are met. Those two values (σ_{Ic}, p_c) are identified with the 4PBT and checked afterwards with the tensile full test. The method consists in detecting experimentally the displacement at which first cracks occur, then simulating the tests to determine the state of stress at the same displacement. This method has been used in [Picqué, 2004].

The thickness of the external layer must be defined as well. From the tests, the average crack depth is about 0.23 mm (see **Fig.IV.35** depth of crack related to the hardness profile). However, near the crack tip, the opening is very narrow, a few microns only. With the mesh size chosen, and due to the erosion element technique, the numerical crack is necessarily wider. This is why, in order to keep some stiffness numerically, the external layer thickness (representing the brittle, martensitic zone) is 0.2 mm (the layer is numerically decreased by 0.03 mm). It is discretized with three elements in the thickness.

Strain hardening has been assessed in a previous work using micro-indentation ([C. Moussa, 2012]). This method was used as well for the core material. It shows its limit at high plastic strain, which will not be reached here by the CN layer since it is brittle. Even though the stress state is quite different between hardness tests and a tensile stress (tension or bending), the aforementioned law is assumed accurate. Material will not reach high level of plastic strain anyway, so that should not have a first order influence. The material behavior is thus modeled through Hollomon's law with: $K=5.01 [GPa]$,

$n=0.15$ and $\sigma_y = 2.646 \text{ GPa}$. Flow stress is quite high but corresponds to a surface hardness of 850 HV0.1 due to the CN treatment (850HV 0.1), by the $HV = 3 \sigma_y$ rule (Tabor's rule). Final discussions at the end of this section will account for the material law used.

V. 3. 1 4PBT

Experimental results have been presented in Chapter 4. Cracks appear between tool displacements of 8 and 9 mm. So a simulation of the test is done here. The four cylinders in contact with the bending specimen are modeled as rigid bodies. Dimensions of the specimen are 35x3.5x220 mm; the cylinders are 50 mm long and their diameter is 10 mm.

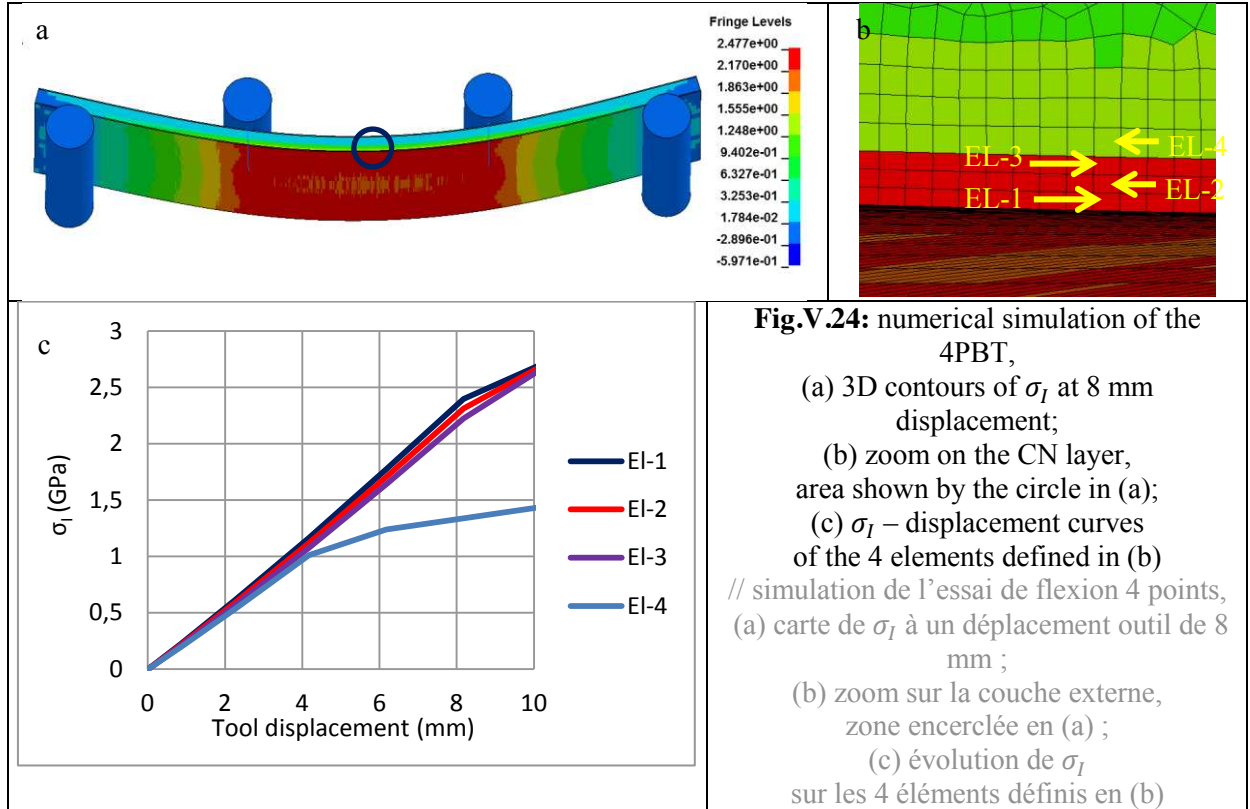


Fig.V.24 (a-c) show the numerical simulation results of the 4PBT. **Fig.V.24** (a) is a 3D plot of σ_I on the whole mesh. It can be seen that stresses are quite uniform between the two internal loading cylinders. **Fig.V.24** (b) is a zoom on the CN layer. The modeling of the CN steel is binary (without a transition zone), this is why there is such a jump of the stress. σ_I is higher than 2.17 GPa in the CN layer, whereas it is around 1.3 GPa in the core material. **Fig.V.25** (a) plots the variation of σ_I as a function of the depth at a displacement of 8 mm (the thin vertical red line shows the boundary of the CN layer). It decreases very quickly from the CN layer until the core material, losing almost 1 GPa between 0.13 mm and 0.3 mm depth. Beyond the specimen center (thick vertical dark line), stress is compressive so that the largest principal stress is close to zero.

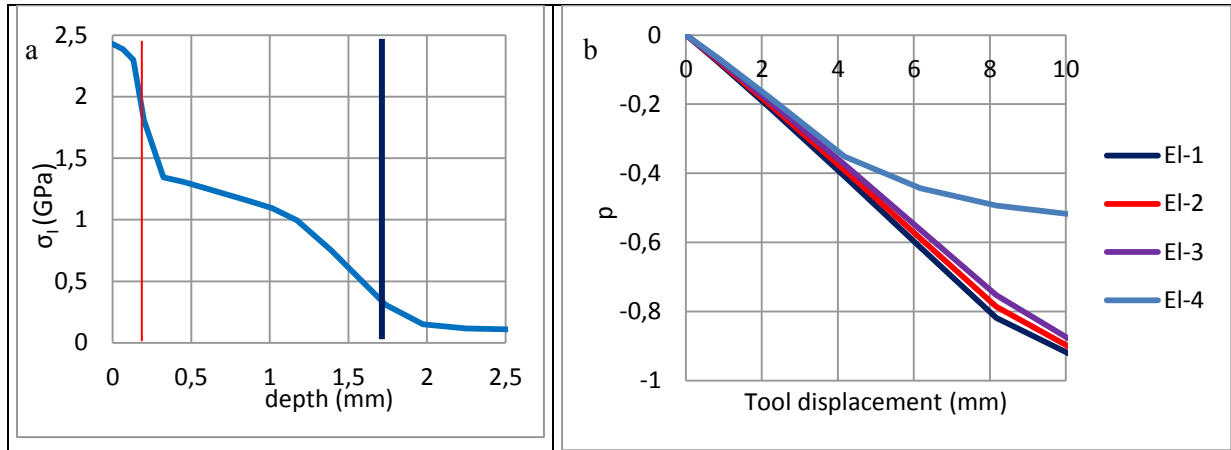


Fig.V.25: (a) σ_l as a function of the depth, the thin vertical red line shows the boundary of the CN layer the thick vertical blue line shows the middle of the thickness, tool displacement of 8 mm;
 (b) evolution of the hydrostatic pressure p as a function of the tool displacement (mm) on the elements defined in **Fig.V.24** (b)

// (a) évolution de σ_l en fonction de la profondeur, la ligne rouge montre la fin de la couche CN, la ligne noire montre le milieu dans l'épaisseur, le déplacement des outils est de 8 mm ;
 (b) évolution de la pression hydrostatique p en fonction du déplacement outil (mm) sur les éléments définis en **Fig.V.24** (b)

In the experiments, cracks appear between 8 and 9 mm displacements. As seen in **Fig.V.24** (b) at 8 mm, the material is still in the elastic domain ($\sigma_l = 2.34 \text{ GPa}$). However, it is in the plastic range at 9 mm ($\sigma_l = 2.52 \text{ GPa}$). The critical stress is between these two values. $\sigma_{lc} = 2.44 \text{ GPa}$ is chosen as the critical value (it corresponds to a 8.2 mm displacement). Values are taken on the elements, so averaged on the 8 integration points.

The same method is followed to assess the critical pressure $p_c = -0.818 \text{ GPa}$.

The meaning of this pressure is the following. At 8.2 mm displacement, $\sigma_{eq} = 2.44 \text{ GPa}$ on EI-1. The ratio $-p_c / \sigma_{eq}$ is equal to the stress triaxiality by definition. Its value is 0.34. Thus it means that the triaxiality on the element must be higher than 0.34 for failure to occur. Noting that the stress triaxiality in pure tension is 1/3, the second line of the criterion eqs (V.24 – V.25) means that the point must be at least in a pure tension state while σ_l must be higher than σ_{lc} .

These values will next be checked with the tensile test on full specimen where the CN layer is submitted to a very similar stress state.

V. 3. 2 Tensile tests

Experimental tests prove that cracks in the external layer appear between displacements of 0.2 and 0.27 mm. The same method as above is used to assess σ_{lc} and p_c . The same mesh size than the 4PBT is used in the thickness and width for the CN layer.

Fig.V.26 (a) illustrates σ_l in the tensile specimen at 0.27 mm displacement. It is quite homogeneous in the central area. The areas close to the fillet have a higher level of σ_l ; however, no cracks were observed here, they are all in the central area. So the σ_{lc} is determined using the central area. **Fig.V.26** (b) plots the evolution of σ_l on the four elements defined in **Fig.V.26** (c). Plasticity in the core material is reached a bit after 0.2 mm displacement, but it is still the elastic domain for the CN layer: at 0.27 mm displacement, $\sigma_l = 1.46 \text{ GPa}$. There is no difference within the elements of the CN layer.

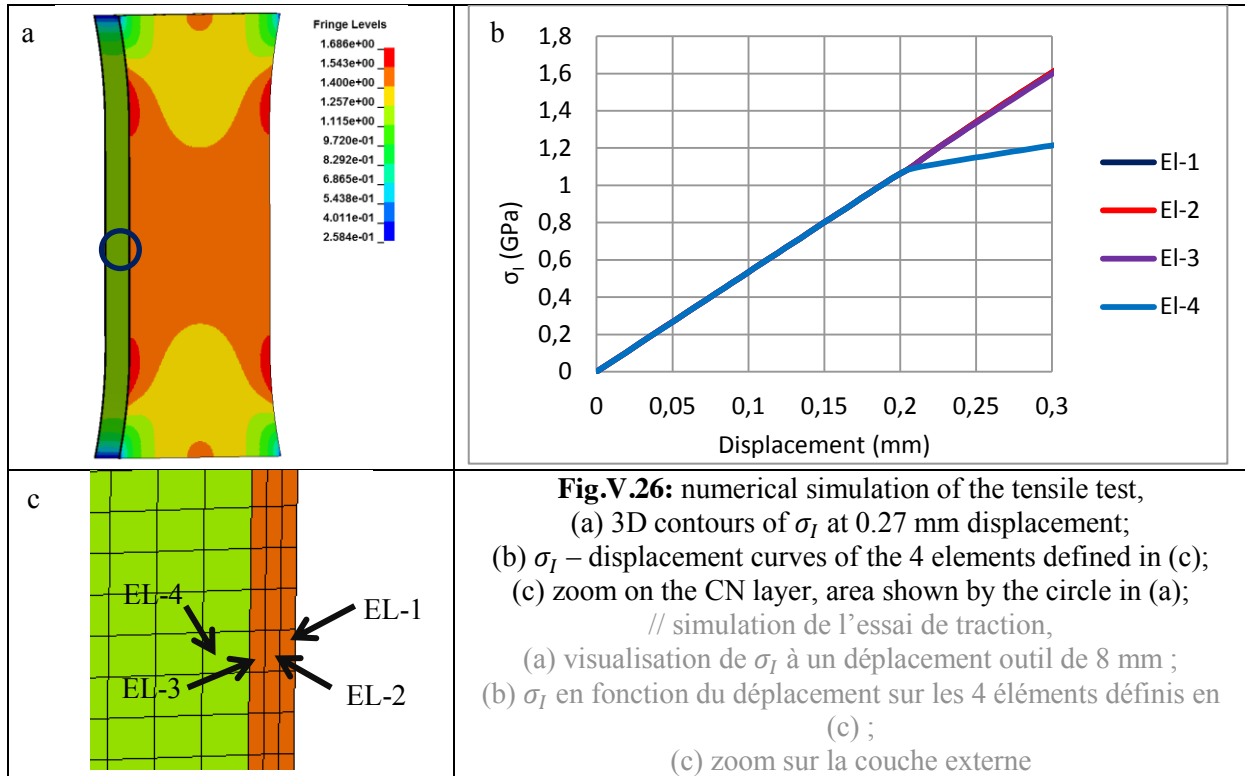
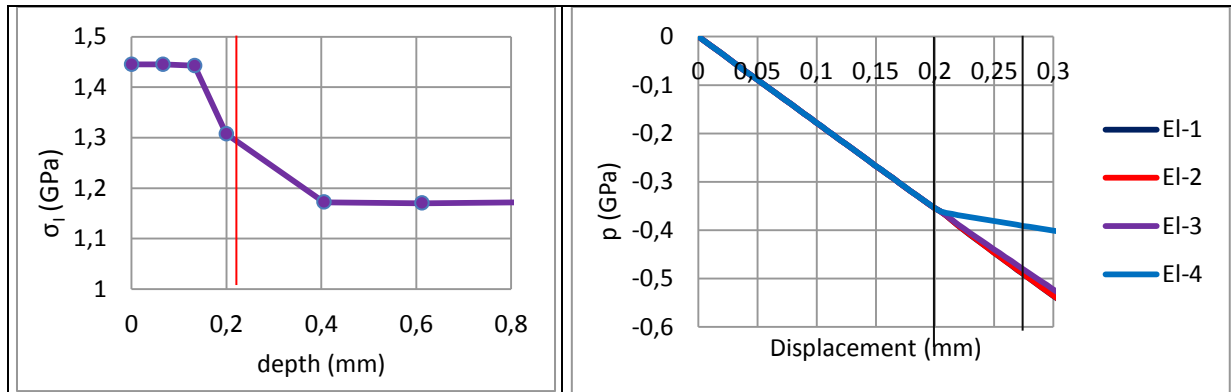


Fig.V.27 (a) plots the evolution of nodal σ_l with depth at 0.27 mm displacement. It is obviously higher in the CN layer than in the core material (1.44 vs 1.17 GPa). The decrease is quite abrupt since there is only one node between the two values (nodes at the interface between the two materials) due to the absence of the transition layer.

The experimental data show that cracks appear between a displacement of 0.2 and 0.27 mm displacement. This is a relatively wide range (35%) where σ_l evolves from 1.06 GPa to 1.44 GPa, and the hydrostatic pressure from -0.36 GPa to -0.48 GPa. Because of the sudden character of the brittle failure, $\sigma_{lc} = 1.44$ GPa and $p_c = 0.48$ GPa are selected.



V. 3. 3 Discussion

These two tests (4PBT and tensile test) submit the CN layer to tensile stress states, leading to early fracture. Numerical simulations give the critical values of σ_{Ic} and p_c , gathered in Table.V.11.

GPa	4PBT	Tensile
σ_{Ic}	2.44	1.44
p_c	-0.818	-0.48

Table.V.11: critical values of σ_{Ic} and p_c
// valeurs critiques de σ_{Ic} and p_c

Values are very different between the two tests, although the ratio $-\frac{p_c}{\sigma_{Ic}}$ is around 1/3 for both. As the state of stress is quasi-uniaxial, the value of σ_{Ic} is close to σ_{eq} , respectively 2.38 and 1.42 GPa in the two tests. Thus the triaxiality is 0.34 for the 4PBT and 0.32 for the tensile test. This was expected since the external layer of the 4PBT is known to be submitted to homogeneous, quasi-monoaxial tensile stress state. So the stress state cannot explain such a difference.

Part of it may be due to the quality of the specimens. Indeed, none of the tensile specimens or the bending specimens was perfectly flat; they were all bent along the main direction. For instance, the 4PBT specimen tested until 9 mm had an initial deflection of 2.7 mm for a length of 220 mm. Deflection was measured just before doing the test, so after the CN treatment. Moreover, specimens were cut with shears before the CN treatment (so unwanted internal stresses induced by the shears stress), which further deformed the specimen. Machining the sample instead of cutting them by shears would indeed have been better. This would have removed the internal stresses induced by the cutting process. Obviously, the CN treatment can induce curvature because of 2 reasons. Firstly, heating in austenitic phase releases the initial residual stresses. Secondly, if the treatment is slightly asymmetrical on the surfaces, the obtained material will not be the same afterwards. This difference will induce a torque, and thus specimen bending as well as residuals stresses.

A similar remark can be done for the tensile test specimen. While setting up the specimen in the jaws, there were unbent first.

These remarks explain that the specimen had strong undesired initial stresses, partly due to the manipulation discussed above and, partly to the residual stresses induced by the CN treatment itself (the last point is true only in case of material asymmetry).

However it could be interesting to account for the residual stresses in the simulations for a better understanding of the mechanics. Since they are strongly compressive in the external layer (likely -800 MPa), accounting for them in the simulations would lead to decrease the critical stress to failure. To study them, the first step would be to measure the residual stresses field through the thickness for this specific steel (20MnB5). It should be close from the ones found in the literature, but variations can be expected depending on the alloying elements. Then the second step would be to calculate the stresses due to the cutting process. Those could be quickly estimated: for instance the specimen with the initial deflection of 2.7 mm over 220 mm, $\sigma_{xx} = 0.7 \text{ GPa}$. If those are added to the residual stresses found in the literature, the external layer to be put in tension must have an initial stress state of about -100 MPa (specimens were tested in the same direction of the initial curvature). Thus the critical principal stress according to the 4PBT would be $\sigma_{Ic} = 2.34 \text{ GPa}$. By assuming the initial stresses in the tensile specimen are only due to the CN treatment, $\sigma_{Ic} = 2.24 \text{ GPa}$. Thus, the discrepancy is reduced. This study could be performed it has not been done during the PhD due to the lack of time.

Another point is that the stresses values accounted in this chapter are the ones on the elements and not on the integration points. This can explain the difference between the values obtained from the 4PBT and the ones from the tensile tests. There is indeed a high gradient in the first case whereas in the second one stress field is quite constant.

The difference could also show the limit of the choice to model the CN material with 2 distinct layers: external and core materials. In the reality, the evolution is smoother with an intermediate layer composed of materials with evolving properties. This is the key point to fully understand and model the CN material. It would require very thin mesh and the capability to characterize their properties. One can imagine the external layer would still be brittle, but the added layers could undergo plastic deformation: thus plastic and fracture behavior would have to be identified. The idea of the hardness tests performed by Moussa is very interesting to test the plastic behavior since it enables to easily reach the material deeper in a progressive way. However, it showed serious limitations since the material is not being tested to a high level of strain, even though it is not a big issue regarding the strain capability of the CN material. However there are other ideas, but more time consuming. The 4PBT is a test easy to perform where the stress state is known and homogeneous. The idea is to prepare specimens on which a layer corresponding to the external layer is grounded (0.2 mm). Then the so-called intermediate layer would be at the surface and could be tested. If a priori the residual stress field is measured, and the specimen flat, this study should bring interesting answers.

In the meantime, based on our observations, it is not possible to say which one of the tests is closer to the real values. They would require additional experiments on perfectly flat specimen. This is why the average values are taken $\sigma_{Ic} = 1.93 \text{ GPa}$ and $p_c = -0.64 \text{ GPa}$. An estimation of the effect of the uncertainty interval has been carried out on the tooth failure and is shown in Chapter 6.

V. 4 Summary

Thanks to the teeth failure observation, it was decided to divide the CN component into two materials: the CN layer and the core material. The former is hard and brittle, and the latter is ductile with a high toughness. Chapter 4 introduced the mechanical characterization of the two materials. This chapter 5 deals with the identification using a numerical approach.

The first step was the identification of the material behavior of the core material. The modified Voce law was chosen; its modification enabled to better account for the material behavior at high level of deformation. A set of parameters was identified on the tensile flat specimen, the test with the lowest experimental scatter. Then, the aforementioned law was validated on the 10 mechanical tests. On each of them, fitting was rather good. The stresses are a bit overestimated at low deformations, but for higher strain the fitting is excellent.

The second step was the identification of the core material failure criterion. Multiple criteria issued from the literature have been tested. However, none of them correctly fits all the tests. They cannot account for the ductility increase between the butterfly $+5^\circ$ and the pure shear one. It was also proved that for the present material, the Lode parameter has a weak influence on failure for $\bar{\theta} < 0.8$. The mathematical form of these criteria is not adapted to this experimental feature. This is why a new criterion has been defined; the stress triaxiality range is divided into three domains, in each domain stress triaxiality is accounted for through the Johnson-Cook criterion from which the influences of strain rate and temperature have been removed. Failure prediction is reasonably accurate on the whole set of tests. The average error on the displacements to fracture is about 4%, which is lower than the experimental scatter.

One can wonder why this material has a weak Lode parameter influence for values lower than 0.8. It can be related to the microstructure itself. Indeed, the Lode parameter influence was highlighted in [Bai & Wierzbicki, 2008] to explain the fracture behavior of materials for which stress triaxiality only was not satisfactory. However, these studies were performed on Aluminum alloy initially. Its microstructure is obviously different from the one of the CNed material. Indeed, it shows a Fe matrix with a few precipitates. Its homogeneity could explain its capability to undergo such huge amount of strain in shear stress state. Whereas the aluminum alloy (2024 T-351) has obviously an Al matrix with Cu precipitates. Microstructures are different, so would be the influence of the Lode parameter. However, this behavior has not been met in other studies on steel (e.g.: [Gachet, 2013], [T. S. Cao, 2015]). Other test with a high Lode parameter (>0.7) should be done to check this behavior.

The last step is the assessment of the failure properties of the CN layer. Due to its brittle behavior, failure is predicted through principal stresses. The latter have been determined with the 4PBT and the tensile test introduced in Chapter 4. However, the two tests gave two distinct sets of critical values. Differences are supposed to be due to spurious initial stresses and imperfect shape of the specimens. Indeed, they were cut with shears, which deforms a lot the specimens. Therefore, they were not flat but curved before testing; setting them up in the jaws flattens them but induces corresponding elastic stresses, which add up with the tension stresses properly speaking. Moreover, the strong residual stresses due to the CN treatment itself should be implemented

These initial stresses have not been introduced in the simulations to determine if they have a significant impact on the identified critical fracture stresses; the uncertainty on the latter is therefore large. Thus, average values between 4PBT and tension are chosen. A proper identification would require perfectly flat specimens and the measurement of the residual stresses to take them into account as an initial stress state in the simulation. The latter has not been done by lack of time.

Even though the critical values of σ_{Ic} and p_c from 4PBT or tensile test are different, the overall fracture behaviors are the same. In both cases, external cracks open at the free surface and propagate toward the core material but are stopped in the intermediate layer. Indeed, the ductility increases with depth, therefore the capability of the material to resist crack propagation. As the load is increasing, a single crack propagates through the core material until complete fracture. It could be interesting to characterize the fracture of the CN layer in another stress state, for instance shear with a rigorous induced shear test. Indeed, the material is submitted to strong shear stress in the tooth failure process, even though the CN layer seems to fail in tension (by bending in certain areas, or at 45° to the shear direction). It would give further information about the material behavior and failure properties for shear loading conditions.

Failure criteria have been determined with tests submitting the materials to homogeneous stress state. They must now be checked with the tooth failure semi-industrial test. This is done in Chapter 6, where experimental tests are compared to their numerical simulations.

Chapter VI : Models validation: tooth failure

Contents

VI. 1	Failure implementation in LS-DYNA	161
VI. 1. 1	Core Material: power-law damage function defined through GISSMO	161
VI. 1. 2	Carbonitrided layer: critical stress implementation.....	163
VI. 2	Semi-industrial tests simulation - methodology	163
VI. 3	Experiment – simulation comparison with the core material only (CMO)	165
VI. 3. 1	Force-displacement curves.....	165
VI. 3. 2	Fracture process	167
VI. 3. 2. a	Overall observation	167
VI. 3. 2. a	Shear crack analysis.....	170
VI. 3. 3	Comparison with Faurecia's previous method	175
VI. 3. 4	Discussion	176
VI. 4	Experiment – simulation comparison with the complete CNed component	179
VI. 4. 1	Force displacement curves	179
VI. 4. 2	Fracture process	180
VI. 4. 2. a	Overall facture process.....	180
VI. 4. 2. b	Shear crack propagation – comparison with the CMO	182
VI. 4. 3	Comparison with Faurecia's previous method	190
VI. 4. 4	Discussion	191
VI. 4. 4. a	Impact of variations of the CN behavior	191
VI. 4. 4. b	Influence of mesh size	195
VI. 4. 4. c	Simplified ductile fracture criterion – Lou & Huh criterion	197
VI. 5	Conclusion.....	199

Résumé en Français

Ce dernier chapitre correspond à la comparaison des ruptures de dents numériques vs expérimentales. Cela permet d'utiliser les outils numériques identifiés durant le projet et mesurer leur performance pour la simulation d'un système complexe.

La première comparaison est effectuée sur les dents avec le matériau de cœur seulement. Elle est très satisfaisante en termes d'effort maximal, avec une différence de 8 % pour le cas le plus éloigné. Cependant, les déplacements à rupture sont surestimés. En ce qui concerne le processus de rupture, les fissures sont bien représentées au bon endroit : la première fissure reste dans la couche externe et s'arrête rapidement dans la zone de transition. Puis la rupture finale a lieu par la propagation d'une fissure de cisaillement.

La seconde comparaison est effectuée sur le matériau CN complet. Elle est moins satisfaisante que sur le matériau de cœur, l'écart entre les courbes numériques et expérimentales est plus important. Les efforts ainsi que les déplacements à rupture sont globalement sous-estimés numériquement. De plus, le faible écart entre les courbes expérimentales avec et sans couche CN n'est pas prédit par les simulations. Nous avons pu confirmer que la couche CN est là pour augmenter la résistance à la fatigue de contact ; c'est le matériau de cœur qui apporte la résistance mécanique. Cependant, le processus de rupture de dent numérique correspond bien au processus expérimental, les fissures sont au bon endroit.

L'étude locale réalisée sur ce chapitre permet d'expliquer les raisons des écarts trouvés plus haut. La première est la modélisation du matériau CN en deux zones : couche externe et matériau de cœur. En réalité, il y a un gradient de propriétés entre ces deux zones. Ainsi, la ductilité augmente progressivement depuis la couche CN pour atteindre son maximum dans le matériau de cœur : l'évolution est continue. Numériquement, la modélisation en deux matériaux impose un saut des propriétés qui ne représente pas la réalité et cause une suppression prématurée des éléments de la couche CN. Cette suppression prématurée d'éléments induit une diminution du volume de matière soutenant l'effort, donc une moins bonne répartition de la contrainte. Cela crée aussi des zones de concentrations de contraintes qui n'existent pas expérimentalement : ces deux facteurs ont une part importante dans le fait que la simulation numérique sous-estime les déplacements à rupture et les efforts maximaux. Une perspective pour pallier ce problème est d'introduire dans la modélisation une couche de transition entre les deux matériaux. Cette couche serait définie comme ductile, donc avec une loi de comportement et un critère de rupture en déformation plastique. Bien sûr, sa ductilité serait moindre par rapport au matériau de cœur. Un autre élément pouvant expliquer l'écart est la technique de propagation de la rupture utilisée. La suppression est la seule technique disponible en 3D dans LS-DYNA mais elle reste grossière avec une taille d'éléments de l'ordre de 70 μm . Elle induit un état de contrainte en pointe de fissure différent de l'état réel et surtout supprime de la matière, ce qui n'a pas lieu en réalité. Des techniques plus récentes évoquées chapitre 4, comme le CZM ou même la suppression d'élément mais avec une taille de maille plus fine et avec du remaillage, permettraient de mieux représenter l'expérience.

Introduction

Chapter 6 aims at validating the material law and fracture criteria with the semi-industrial test by comparison of the experimental tests and the numerical simulations. The latter are done with the FEM analysis software LS-DYNA; failure has been implemented for the core material through the GISSMO model. The first part of this chapter introduces the reader to the way failure can be implemented in LS-DYNA. Then, the six configurations are studied: three with the core material only (CMO) and three with the full CNed material (FCN). The three engagement depths are analyzed and compared. The CMO model enables to check the accuracy of the Voce behavior law and exponential fracture criterion for the core material. Attention is paid to the experimental scatter issue raised in Chapter 3. Then, comparisons using FCN is made to check the accuracy of the CN failure criterion. The differences observed between numerical prediction and experimental observations are discussed and related to the necessary hypotheses that were made for modeling such a complex failure process. These numerical simulations help getting a better understanding of the failure process of such a graded material.

VI. 1 Failure implementation in LS-DYNA

This part describes how failure can be modeled in the software LS-DYNA. Firstly the method to predict failure of the core material is introduced; implementation is done through the model GISSMO. This model is quite versatile to implement any fracture criterion as soon as the strain to failure depends on the stress triaxiality and the Lode parameter. Therefore, the failure criteria described in Chapter 5 can be implemented. For the CN layer, the critical stress criterion implementation is done without using the GISSMO model, but standard options of LS Dyna.

VI. 1. 1 Core Material: power-law damage function defined through GISSMO

GISSMO (Generalized Incremental Stress State dependent damage MOdel) is a phenomenological model which has been extended to account for the Lode parameter in [Basaran et al., 2010]. In the present work no coupling between damage and plastic behavior was used.

The damage parameter (D) is defined through Eq.VI.1:

$$D = \left(\frac{\varepsilon_p}{\varepsilon_f} \right)^n \quad \text{Eq.VI.1}$$

where n is the damage exponent, ε_p is the equivalent plastic strain (EPS) at a given time t and ε_f is the strain at fracture. The integral form is defined in Eq.VI.2:

$$D = \int_0^{\varepsilon_f} \frac{n}{\varepsilon_f(\eta, \bar{\theta})} D^{\frac{n-1}{n}} d\varepsilon_p \quad \text{Eq.VI.2}$$

The exponential failure criterion accounting for the Lode parameter will be used. In this study, the damage exponent n is set to 1, as seen in most studies dealing with fracture criteria of metallic materials. Nevertheless, it could be interesting to check the influence of this exponent. If equal to 2 for instance, it enables to account more for the last part of the loading path, and less for the first part

during which stress state is evolving because of the necking process for instance for the tensile specimens. This is a topic for further study.

The fracture surface is implemented as a table: for each value of the Lode parameter corresponds a curve $\varepsilon_{f\theta}(\eta)$. Both triaxiality and Lode parameter are discretized with 0.05 steps. That way, any mathematical formula of the failure criteria can be used as soon as ε_f is expressed as a function of the stress triaxiality and the Lode parameter. Neither the mathematical formulae nor the parameters need to be written in GISSMO; only the curves $\varepsilon_{f\theta}(\eta)$ are needed.

GISSMO is a quite versatile tool to implement failure in LS-DYNA. The fracture parameters are defined through the material card *MAT_ADD_EROSION, see **Fig.VI.1**. There are numerous parameters to model failure, from the simplest criterion with a single critical value and no damage parameters to more complex criteria depending on severable variables that need to be identified. **Fig.VI.1** is extracted from the input data of the semi-industrial test. A lot of variables are equal to 0, which means they are not used. For instance, MAXPRES is a criterion involving just a maximum pressure at failure; MNEPS is a criterion working with the minimum EPS at failure. Failure occurs when the values of the selected parameters reach the critical value. Those criteria are obviously not used for the core material; the value is equal to 0. This is why the criteria depending on the stress state are implemented.

*MAT_ADD_EROSION_TITLE								
core-failure								
\$#	mid	excl	mxpres	mneps	effeps	voleps	numfip	ncs
	2	0.000	0.000	0.000	0.000	0.000	8.000000	1.000000
\$#	mnpres	sigpl	sigvm	mxeps	epssh	sigth	impulse	failtm
	0.000	0.000	0.000	0.000	0.000	0.000	0.000	0.000
\$#	idam	dmgtyp	lcsdg	ecrit	dmgexp	dcrit	fadexp	lcregd
	1	1.000000	31	10.000000	1.000000	1.000000	0.000	0.000
\$#	sizflg	refsz	nahsv	lcsrs	regshr	rgbiar		
	0	0.000	14.000000	0	0.000	0.000		
\$#	lcfld	epsthin		engcrt	radcrt			
	0	0	0.000	0.000	0.000			

Fig.VI.1: material card used in LS-DYNA to define GISSMO parameters for the core material

// carte matériau utilisée dans LS-DYNA pour définir les paramètres de GISSMO

pour le matériau de cœur

Here are the definitions of the parameters used:

- NUMFIP: this enables to choose how many integration points in one element must fulfill the condition for the element to be deleted. The elements used have 8 integration points. It was chosen to wait until all the integration points fulfill the condition, in order to better account for the gradient of stress.
- NCS: this sets the number of conditions the integration point must fulfill for the element to be deleted. For the core material it is only one, but for the CN layer it is two (as detailed in the next section).
- IDAM: this is to select the damage model being used, 1 stands for GISSMO.
- DMGTYP: this is to activate the element erosion technique.
- LCSDG: this is the ID of the table where the curves $\varepsilon_f(\eta, \bar{\theta})$ are recorded.
- ECRIT: this is to couple the failure with the material behavior law. The value represents the critical value of the EPS (the plastic strain) above which the material law starts being softened. It has been set up to 10, to be sure there will be no coupling in the simulations. Indeed, we

chose in this work to avoid material softening due to inherent damage localization and consequently mesh dependency that would result from such softening.

- DMGEXP: this is the damage exponent, here $n = 1$.
- DCRIT: this is the threshold value leading to fracture, here $D_c = 1$.
- NAHSV: this selects how many outputs are being saved during the simulation in the output files to be studied afterwards.

VI. 1. 2 Carbonitrided layer: critical stress implementation

Failure of the CN layer is modeled in LS-DYNA without using GISSMO. It is however the same material card as the one used to define GISSMO (*MAT_ADD_EROSION) except that IDAM = 0.

*MAT_ADD_EROSION_TITLE								
CN failure								
\$#	mid	excl	mxpres	mneps	effeps	voleps	numfip	ncs
	1	0.000	0.000	0.000	0.000	0.000	8.000000	2.000000
\$#	mnpres	sigp1	sigvm	mxeps	epssh	sigth	impulse	failtm
	-0.640000	1.930000	0.000	0.000	0.000	0.000	0.000	0.000
\$#	idam	dmgtyp	lcsdg	ecrit	dmgexp	dcrit	fadexp	lcregd
	0	0.000	0	0.000	0.000	0.000	0.000	0.000
\$#	lcfld		epsthin	engcrt	radcrt			
	0	0	0.000	0.000	0.000			

Fig.VI.2: material card used in LS-DYNA to define failure parameters for the CN layer
 // carte matériau utilisée dans LS-DYNA pour définir les paramètres de rupture
 pour le matériau de la couche CN

Less parameters are being used than for the core material. The criterion for the CN layer is simpler since it does not depend on the triaxiality nor the Lode parameter.

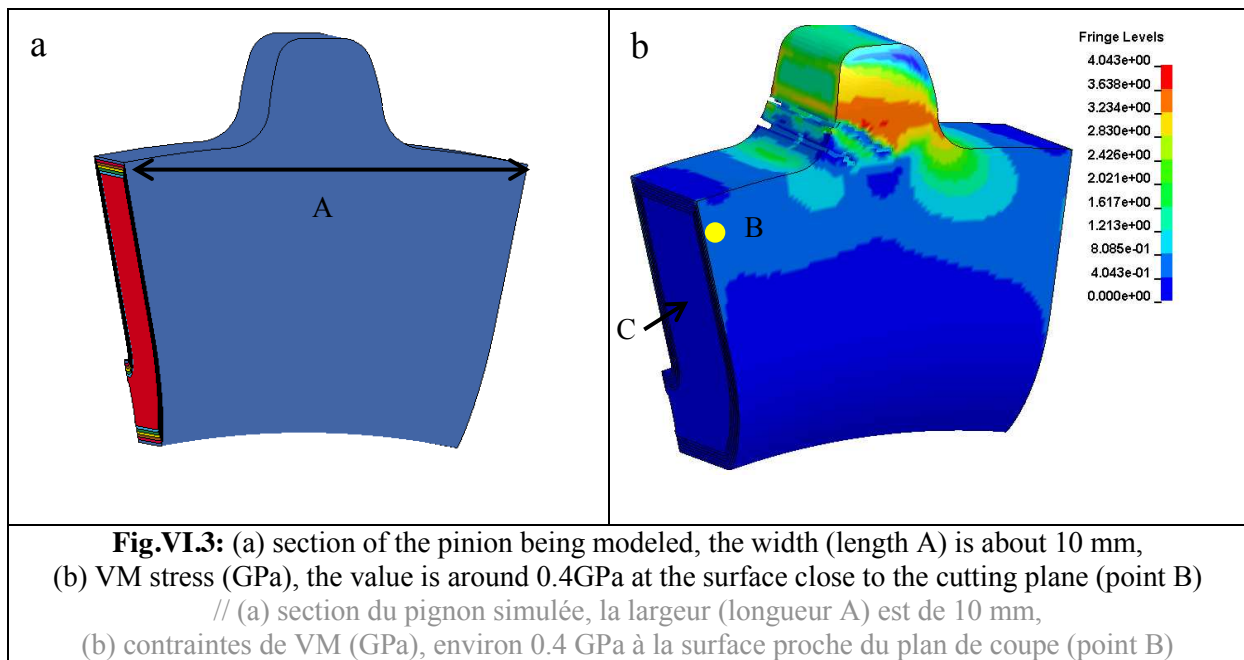
- NUMFIP: the conditions of failure must be fulfilled by the eight integration points of one element to trigger its failure, as for the core material.
- NCS: this time, two conditions must be fulfilled to delete one integration point:
 - MNPRES: this is the value of the minimum pressure at failure (negative = depressive). Absolute value of the hydrostatic pressure must be higher than 0.64 for failure to be triggered
 - SIGP1: this is the critical principal stress at failure, σ_1 must be higher than 1.93 GPa for failure to be triggered.

VI. 2 Semi-industrial tests simulation - methodology

The simulations of the tooth failure enable to validate the numerical models assessed in this work. This is a complex 3D multi-domain failure configuration and the methodology is set up step by step. Firstly, simulations of the tooth failure with the CMO are carried out. The numerical force-displacement curves are compared to the experimental ones and so is the failure process (crack propagation). It was seen previously in Chapter 3 that the core material was sustaining most of the load. Then simulations of the complete CN component are performed and numerical laws to model the CN layer behavior and fracture are tested.

❖ The tooth section

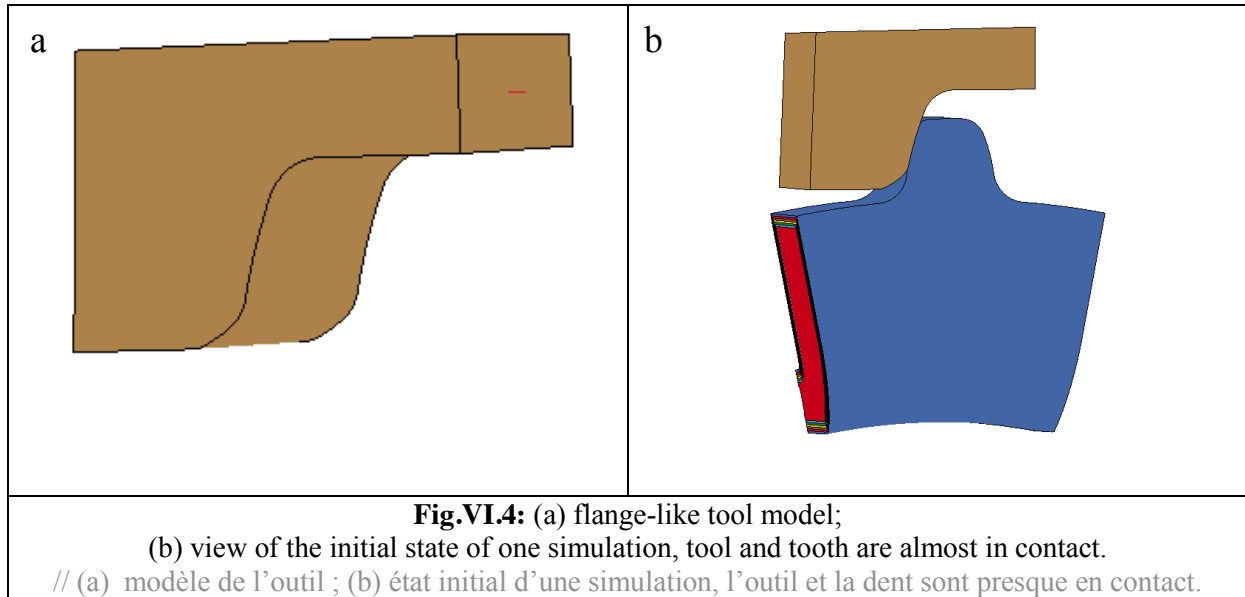
As seen in Chapter 3, and for instance in **Fig.III.3**, the test is performed on a complete pinion on which two teeth out of three have been ground away. The tested pinions thus have only 11 teeth out of the initial 33 teeth of a complete pinion. Even for one-tooth simulation, we cannot mesh the whole pinion; it would be too time consuming. Furthermore, it is easy to assume that the rest of the pinion, far from the tested tooth, is not submitted to significant stress. This is why the model of the semi-industrial test is just a section of the pinion. It is of course wider than one tooth, **Fig.VI.3 (a)**. Indeed the section width is about 10 mm (length A), whereas a tooth measured root to root is about 4 mm. **Fig.VI.3 (b)** illustrates a simulation at an advanced damage state; the intensity of the von Mises (VM) stress is about 0.4 GPa close to the cutting plane. The strain induced with this level of stress (0.2% of elastic strain) is low enough to assume that boundary conditions on these surfaces have no significant influence on the tooth failure. This is why boundary conditions have been applied there. Nodes on these surfaces (the one shown by C and the one on the other side of the section) are constrained in the 3 directions (no translation, no rotation).



❖ The tool

To reduce the simulation cost, only a part of the tool is modeled (see **Fig.VI.4 (a)**), as a rigid solid; it is thus assumed there is no elastic and plastic strain on the tool. This assumption makes sense: by its geometry, the 5 mm thick tool is more rigid than the tested tooth. Furthermore it is harder than the CN material. The shape of the tool active part (the one in contact with the tooth) is the same as the flange (part in contact with the pinion in the full recliner). It was also checked, using a profile projector, that this geometry was still the same after the test campaign. This profile projector also enabled to check that the profile of the numerical tool was accurate. **Fig.VI.4 (b)** illustrates the simulation at the initial state. The tool is close to the tooth (0.01 mm) and the engagement corresponds to the medium one. Experimentally, displacement was applied to the pinion. But in the end, both parts were moving as seen in Chapter 3. So the numerical simulation has to account for the displacements of the two parts. It was thus decided to impart the tool with the experimental relative displacement between the two parts.

The method applied is described in Chapter 3; **Fig.III.9** plots the relative displacement of the tool in regard of the pinion. Simulations are carried out with a friction coefficient $\mu = 0.17$ (given by Faurecia). A sensitivity analysis should be conducted to study the influence of friction.



VI. 3 Experiment – simulation comparison with the core material only (CMO)

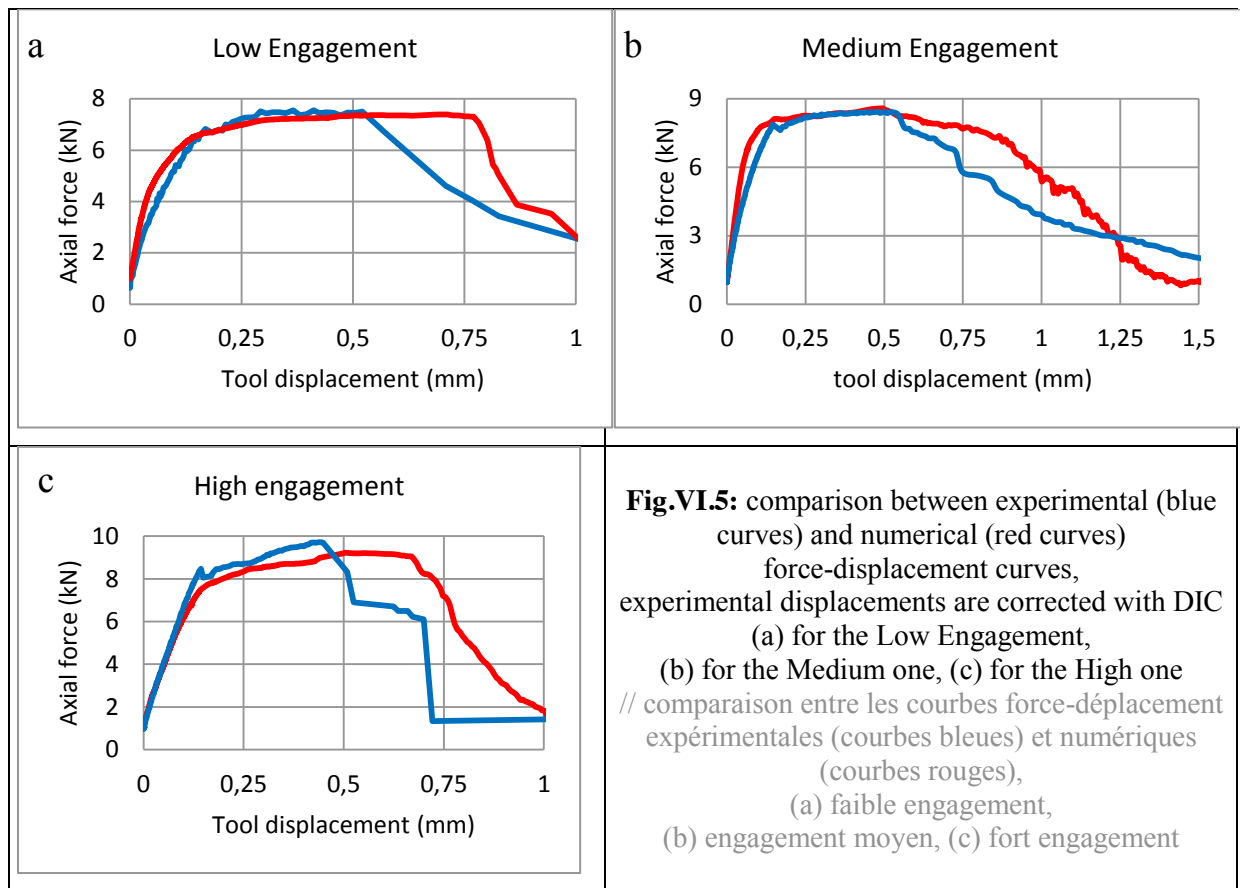
The first step of the final comparison is to work with the CMO. Both material behavior law and failure criterion are results from the Chapter 5. The three engagement depths are studied. First, the force-displacement curves are compared before detailing the fracture process. Then, the results are compared to the previous Faurecia methodology explained in section VI.3.3.

VI. 3. 1 Force-displacement curves

Fig.VI.5 (a-c) plots the curves for the three engagement cases; **Table.VI.1** summarizes the peak loads and the displacements to peak load for the simulations and the experiments. One can notice the peak load increases when the engagement depth increases, this was expected. It can also be seen that the higher the engagement, the higher the force increase between the first load drop corresponding to the opening of the first crack and the max load.

	Displacement to peak load (mm)		Peak load (kN)	
	Simulation	Experiment	Simulation	Experiment
Low Engagement	0.77	0.52	7.4	7.5
Medium Engagement	0.52	0.52	8.5	8.5
High Engagement	0.55	0.45	9	9.8

Table.VI.1: displacements to peak loads and peak loads for the simulations and the experiments
 // déplacements à effort max et valeurs d'efforts maxi pour les simulations et les essais



❖ Peak load

For the low and medium engagement, correlation is very good in terms of maximum load sustained, whereas for the high engagement, the experimental maximum load is higher by 8 % than the numerical one.

Except for the high engagement, simulation is stiffer in the elastic regime. This may come from the fact that the numerical analysis is performed on a reduced domain or from the choice of using a rigid tool which therefore cannot deform elastically. The overall comparison is however good enough to tolerate such hypotheses.

❖ Displacement to peak load

For the low engagement case, the numerical curve overestimates the fracture displacement by 0.2 mm. But it can be noticed the fracture process is quite fast for both the numerical and the experimental tooth failure.

Regarding the medium engagement, the numerical displacement to peak load is in very good agreement with the experimental one: 0.52 mm.

For the high engagement case, there is a first experimental load drop which occurs earlier. The final load drop is however at the same displacement experimentally and numerically, at 0.7 mm. There is however a difference in terms of behavior: the load decreases in two steps experimentally, the first one at 0.4 mm and the second one at 0.7 mm.

It must be noticed that elements deletion modifies the contact areas and thus the sustained force. Furthermore, experimental displacements are extracted from VIC analyses corresponding to the experimental configuration, which therefore incorporate in this particular case the first fracture

occurring at 0.4 mm displacement. So every remark done on the simulations at a displacement higher than the one to experimental fracture must be done with caution.

The differences between the experiments and the simulations will be explained by the observation of the failure process in the following section. But the choice which was made for butterfly specimens and which conducted to use the higher experimental displacement to failure may be a plausible explanation for overestimating tooth failure displacement.

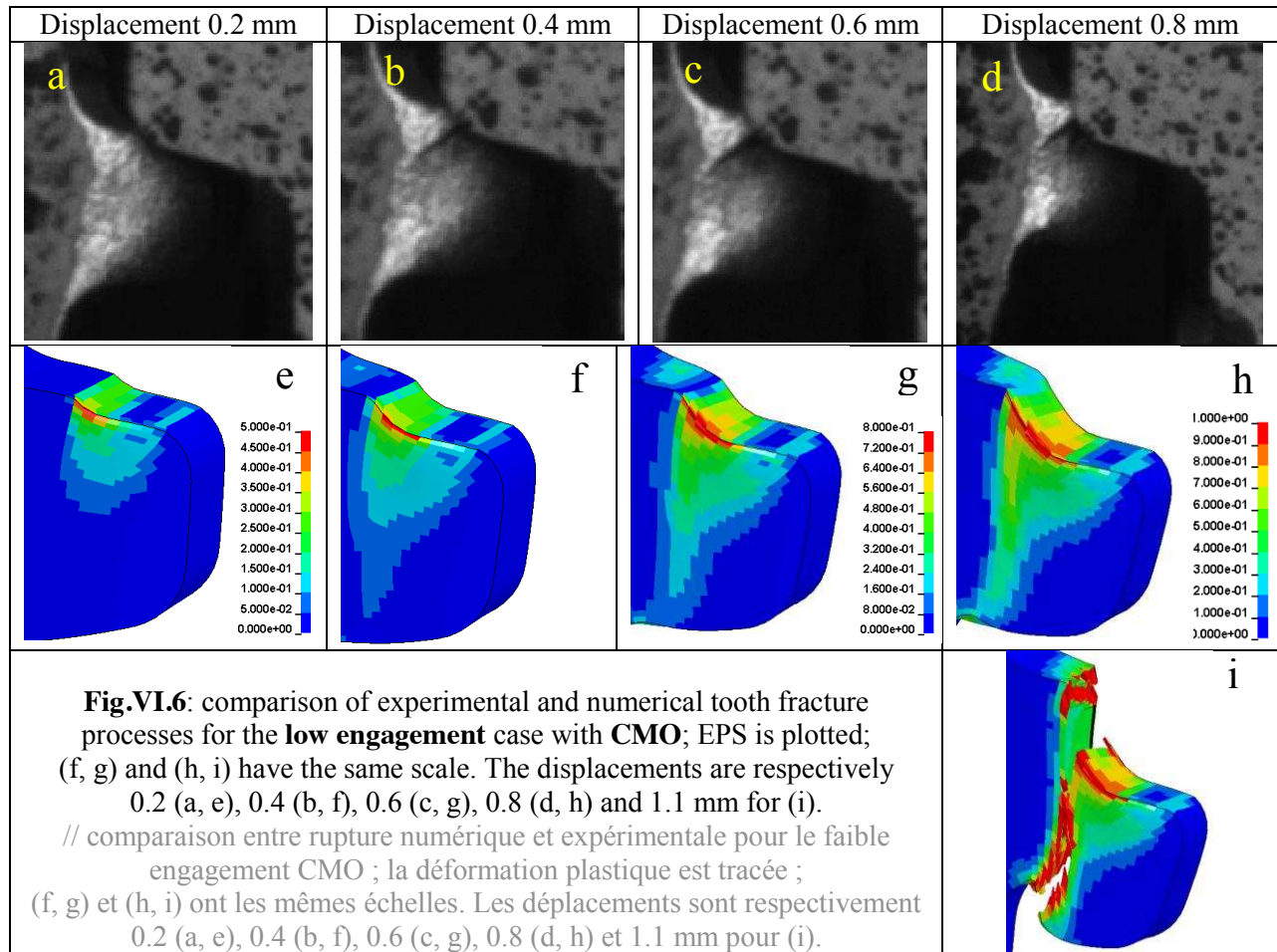
The hypothesis of a crack opening on the opposite side of the one in contact with the tool was raised in Chapter 3. It was however impossible to conclude if there was a crack opening and propagating toward the tool, or just the parts of the tooth splitting. Simulations will enable to conclude on that point.

VI. 3. 2 Fracture process

VI. 3. 2. a Overall observation

This section compares the experimental and numerical tooth fracture processes. **Fig.VI.6**, **Fig.VI.7** and **Fig.VI.8** show respectively the cases for the Low (LE), Medium (ME) and High (HE) Engagements.

For the LE, the force-displacement curves suggest the first crack at 0.17 mm, as studied in Chapter 3. It cannot be seen on **Fig.VI.6 (a)** because of poor contrast. However, remember the CMO has a 0.1 mm softer external layer which is not accounted for in the simulations (250 HV0.1 for the subsurface layer). There is no numerical crack at that displacement, but the equivalent plastic strain (EPS) is building up and one can see the progressive formation of the shear line in the tooth. EPS is increasing faster on the edge at the surface; this is because the contact with the tool is occurring there first. Indeed, the tooth section is variable (between the front side and the rear side) because of the blanking process. Strain is building up in the shear band until it reaches the critical plastic strain to failure. Then the crack is opening and propagating through the whole tooth.



The experimental observations do not allow checking the opening of a crack on the opposite side. The simulation does not represent this crack propagating toward the tool though.

The same failure process is observed as well on **Fig.VI.7**. There is a crack opening at the edge of the contact surface with the tool experimentally at 0.18 mm displacement; it remains a short, superficial crack as seen in Chapter 3. It propagates around 1 mm at the observed surface, but does not propagate more than 0.3 mm in the core material. However it propagates at the surface of the tool, in the plane perpendicular to the observed one. Then the shear band is building up (green arrow on **Fig.VI.7** (c)). The simulation confirms the shear band is progressively developing from 0.2 mm displacement. However, the crack observation is not easy on this side of the tooth since it opens on the other side where first contact occurs. This will be developed in VI. 3. 2. a.

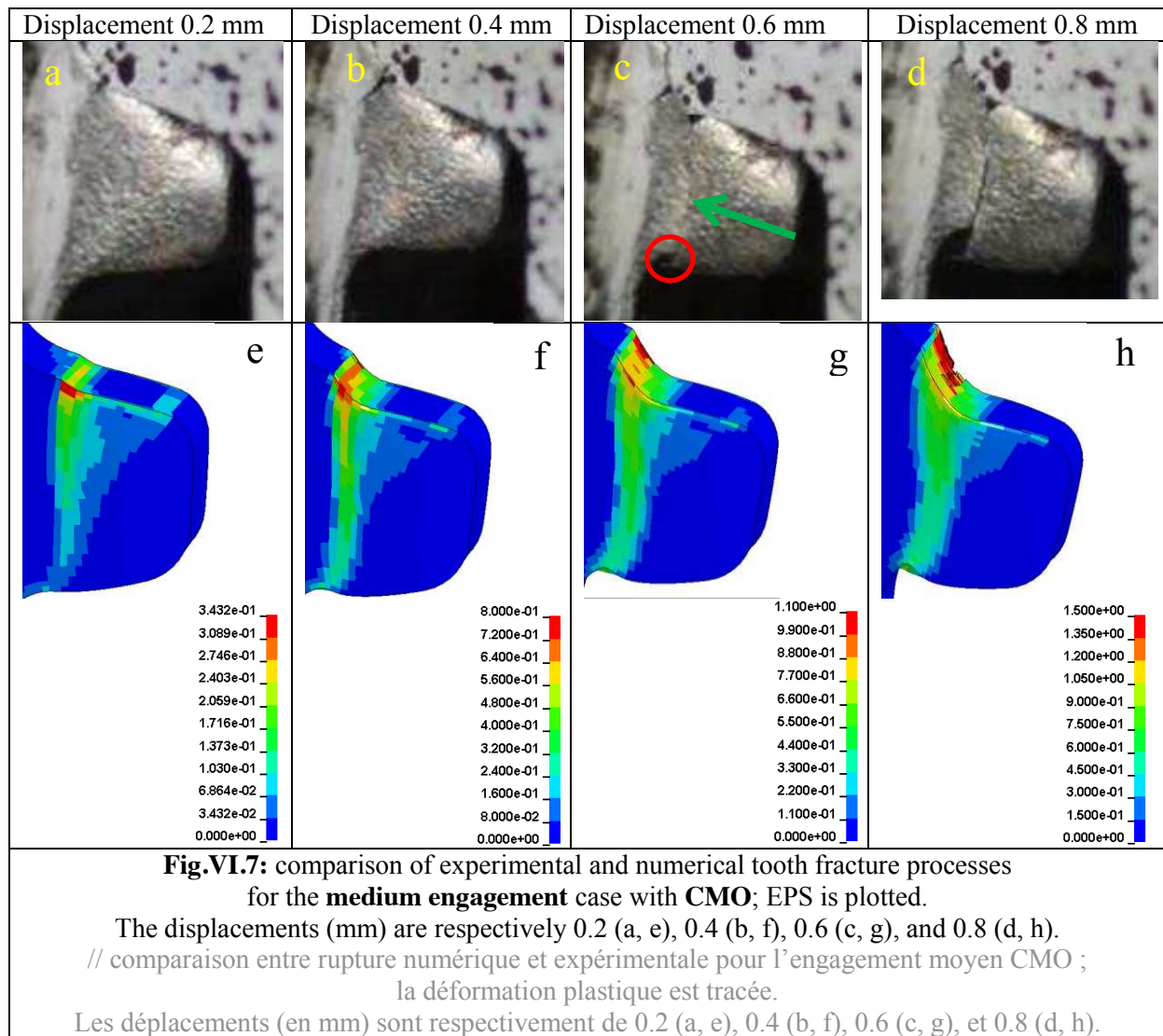
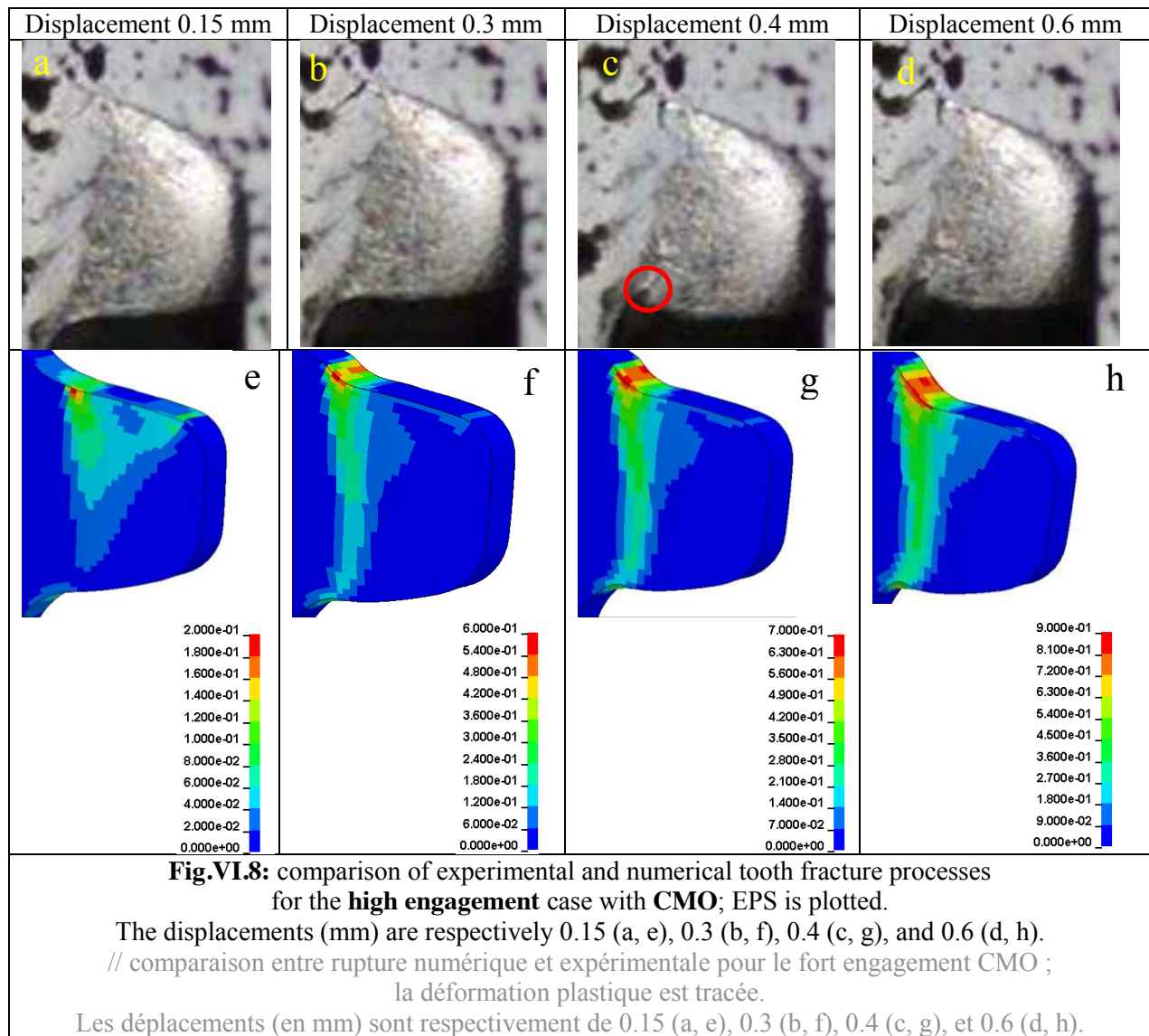


Fig.VI.7 (c) could show the opening of a crack on the opposite side of the tooth (red circle). It is however not being seen in the simulation.

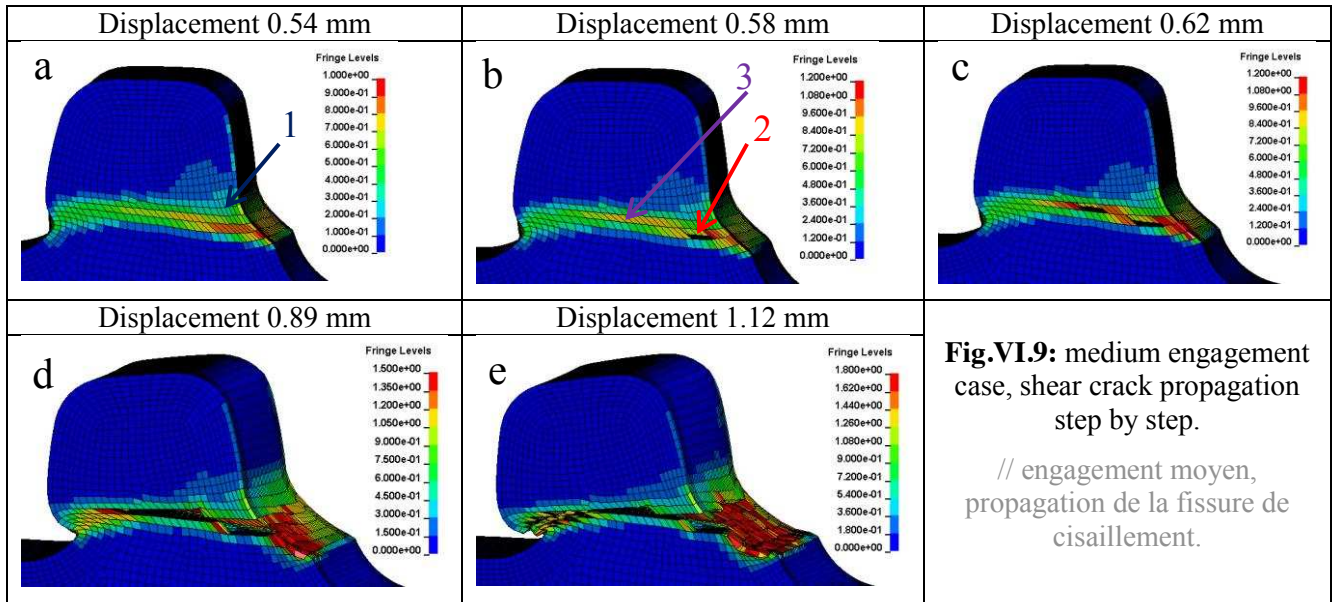
Fig.VI.8 compares the fracture processes for the HE case. As for the previous configurations, the shear band is expanding. One can notice it is thinner on the high engagement case than for the others. Crack initiation is being delayed compared to the experimental tooth fracture. One can hypothesize that the failure criterion overestimates the plastic strain to failure in this stress state, thus delaying fracture. This will be developed in next section. **Fig.VI.8** (c) seems to indicate there is the initiation of a crack on the opposite side of the tooth (red circle). It is however not being seen in the simulation. Interrupted tests could be a good way to be sure that such a crack can initiate on the tooth back side.



VI. 3. 2. a Shear crack analysis

The tooth failure is due to the propagation of a main shear crack going through the whole section. Because it is a fast phenomenon, it is difficult to observe with DIC cameras (they are not high speed cameras). However, numerical simulation enables a detailed analysis of this shear failure process. Furthermore, the evolution of the parameters describing the stress state (Triaxiality and Lode parameter) can be analyzed to explain it. **Fig.VI.9** (a-e) shows the crack propagation in the numerical simulation for the medium engagement case. It is on the inner side of the test bench, opposite to the camera, invisible but where contact occurs first. So no rigorous comparison can be done. However, it looks like what has been observed experimentally. The crack is opening at the bottom of the contact surface with the tool and propagates through the section. **Fig.VI.9** (d, e) show there is no crack opening on the opposite side of the tool in the simulations. Parameters describing the stress state are extracted from three elements inside the crack. The first one (#1, on **Fig.VI.9** (a) in blue) is the first element being deleted in the simulation. It is located inside the tooth material (0.34 mm depth, not at the surface), below the contact with the tool. The second one (#2 on **Fig.VI.9** (b) in red) is on the side of the tooth, at the surface, and on the path of the crack. The last one (#3 on **Fig.VI.9** (b) in purple) is inside the tooth. **Fig.VI.10** (a) plots the evolution of the damage parameter D on the three aforementioned elements, and **Fig.VI.10** (b) plots the stress triaxiality ratio. Damage (D) is increasing

faster for element 1 than for the others; it starts after 0.2 mm displacement until it reaches the critical value of 1 at 0.5 mm. Triaxiality on this element is positive at the beginning, around 0.2. It shows this area is submitted to tensile stress state because it is below the contact surface with the tool, which is pushing the upper part of the tooth upwards. Once it is deleted, other elements nearby are deleted due to the abrupt change of stress state. This can be noticed by the change of triaxiality and Lode parameter of the other two elements, especially #2: its triaxiality increases from 0.04 to 0.58.



As shown in **Fig.VI.10** (c), elements 2 and 3 stress triaxiality is close to 0 and element 1 triaxiality remains moderate (~ 0.25 , i.e. close to tension). These elements experience a pure shear stress state quite proportional along the loading path. This proportional loading path is observed as well for the Lode parameter (**Fig.VI.10** (d)). This is confirming the stress state chosen to be reproduced with the butterfly specimens in pure shear mode. Lode parameter and triaxiality evolve a lot for very low EPS (data points are on the abscissa line). This is not disturbing the damage parameter since it is integrated on the EPS evolution. This can be observed on **Fig.VI.10** (c) and (d) where stress state is plotted as a function of EPS on the elements and not the tool displacement as in **Fig.VI.10** (b). Element 3 exhibits a pure shear stress state with almost zero values for triaxiality and Lode parameter. Only at the end does this stress state change because of the crack propagation and the progressive deletion of elements.

The same observation can be done on the other two depth engagements. **Fig.VI.11** and **Fig.VI.12** plot the D parameter and the triaxiality as a function of the tool displacement (respectively a and b). Loading paths are plotted on respectively c and d.

It can be noticed that triaxiality is lower for the high engagement than for the other cases. Indeed, the crack path is closer to the tooth root, thus the bending movement of the upper part of the tooth is quite limited compared to the other engagement depths.

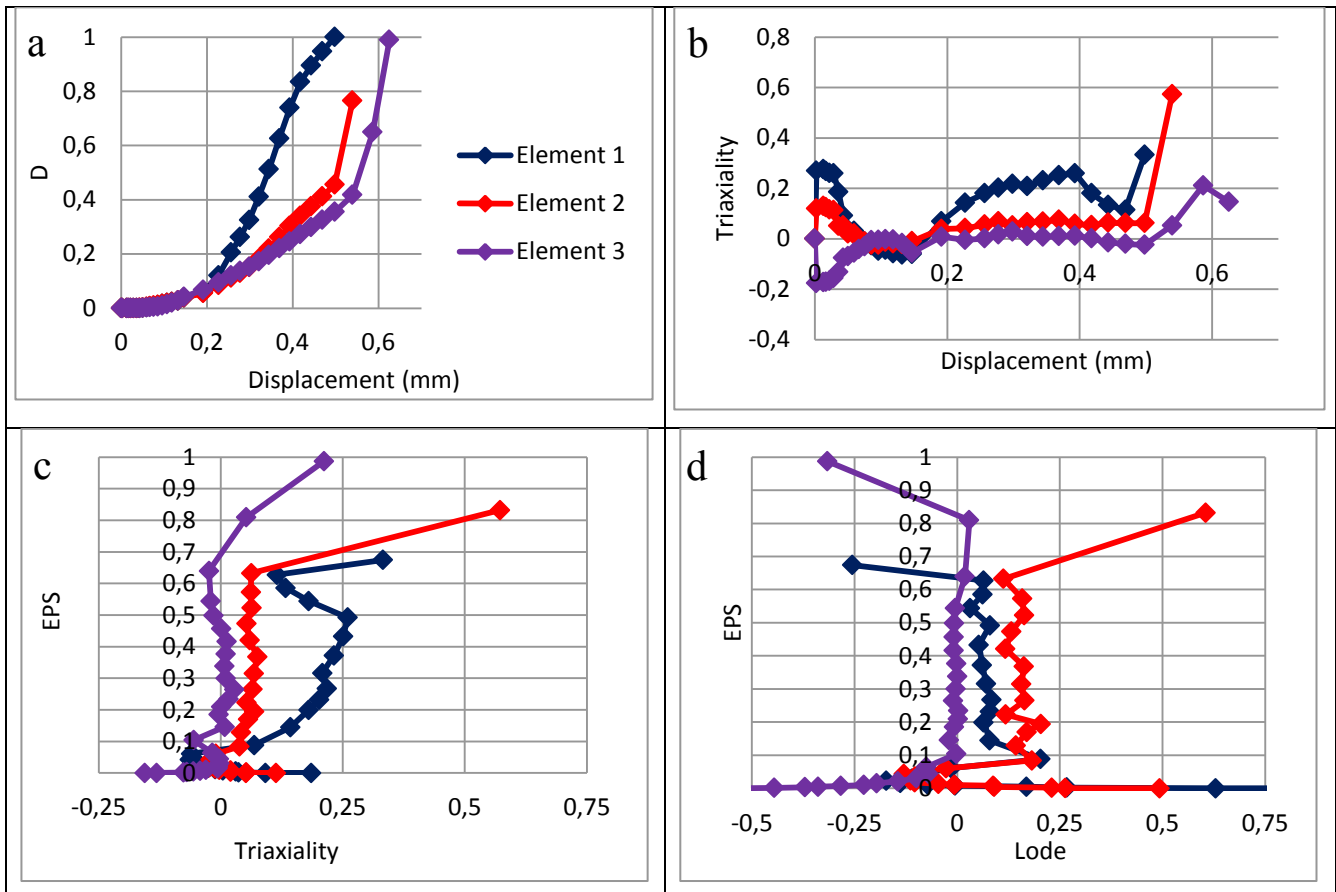


Fig.VI.10: Parameters describing the stress state extracted from 3 elements defined in **Fig.VI.9**, **medium engagement case**.

(a) evolution of the damage variable D ; (b) triaxiality ;

(c) and (d) loading paths, respectively the triaxiality and the Lode parameter vs plastic strain.

// paramètres caractérisant l'état de contrainte tracés sur les 3 éléments définis en **Fig.VI.9** ;
engagement moyen.

(a) évolution du paramètre d'endommagement D ; (b) triaxialité ;

(c) et (d) trajets de chargement, respectivement la triaxialité et paramètre de Lode.

Once the element deletion has started, the stress state evolves a lot on the elements nearby. Indeed, stress triaxiality increases, which accelerates the damage accumulation and thus the failure initiation. The triaxiality increase, in that specific case, should be considered regarding the element size. Indeed, in the reality, crack tip is thinner, which creates very locally a volume with a high level of stress concentration. Whereas here, volume submitted to a high stress concentration is higher, but with a lower value. However, element deletion creates free surfaces, which do not exist in the reality. Part of this triaxiality increase may be physical, because of crack opening. However, the erosion element technique implies the deletion of an element and a loss of volume at the crack tip, which clearly influences significantly the stress state as well. This is one of the drawbacks of this robust technique for failure modeling. This means that post-failure behavior is subject to caution and may depend on mesh size.

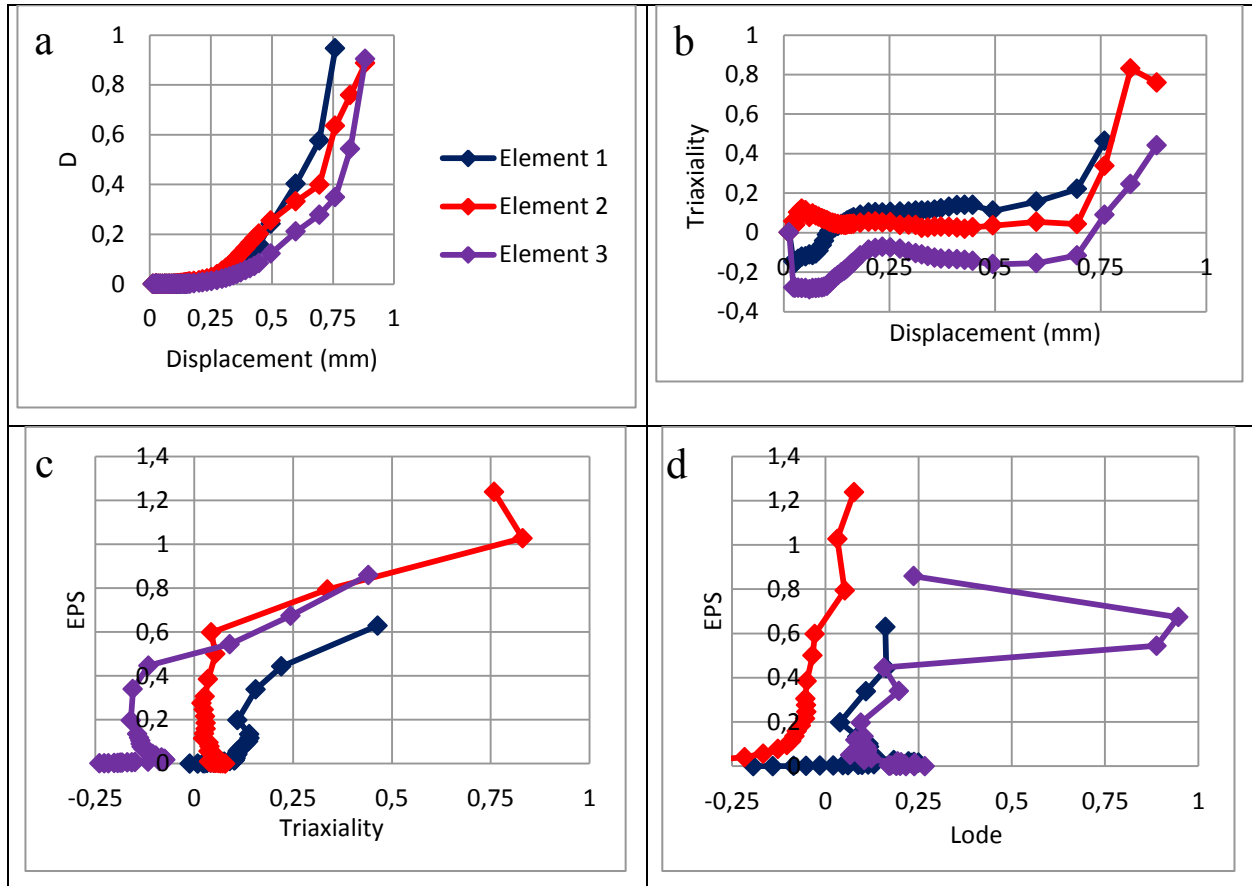


Fig.VI.11: Stress state parameters extracted from 3 elements defined in **Fig.VI.9**; **high engagement** case.

(a) evolution of D; (b) triaxiality;

(c) and (d) loading paths, respectively triaxiality and Lode parameter vs strain.

// paramètres caractérisant l'état de contrainte tracés sur les 3 éléments définis en **Fig.VI.9**; **engagement fort**.

(a) évolution de D ; (b) triaxialité ;

(c) et (d) trajets de chargement, respectivement triaxialité et paramètre de Lode.

Fig.VI.13 plots the force displacement curves for the experiments and the numerical simulation for the three engagements. The blue color corresponds to experimental curves and the red one to numerical curves. The smallest displacement to numerical max load corresponds to the medium engagement (0.47 mm), whereas the longest is for the low one. The high engagement reaches its max load and sustains it for 0.08 mm. The medium engagement is the one where failure process starts first and this can be explained by the stress state evolution of element 1.

Fig.VI.10 (c) illustrates the triaxiality of the first element increases to a value higher than 0.2 after 0.3 mm of tool displacement; this corresponds to $\bar{\epsilon} = 0.20$. On the low engagement (see **Fig.VI.12** (b and c)), triaxiality is mainly higher than 0.2 after a displacement of 0.1 mm. However, the EPS is lower for the low engagement: a displacement of 0.5 mm corresponds to $\bar{\epsilon} = 0.25$, whereas for the medium engagement, a displacement of 0.5 mm corresponds to $\bar{\epsilon} = 0.5$. This is why the damage variable is increasing faster, and so the failure appears sooner.

The high engagement (see **Fig.VI.11** (b and c)) has the quickest increase of the triaxiality on the three studied elements. One can notice that element 3 on the low engagement case (red curves **Fig.VI.12** (b and c)) has an abrupt increase of the triaxiality from 0.05 to 0.27 at a displacement of 0.76 mm. This is due to the propagation (and thus progressive elements deletion) of the crack.

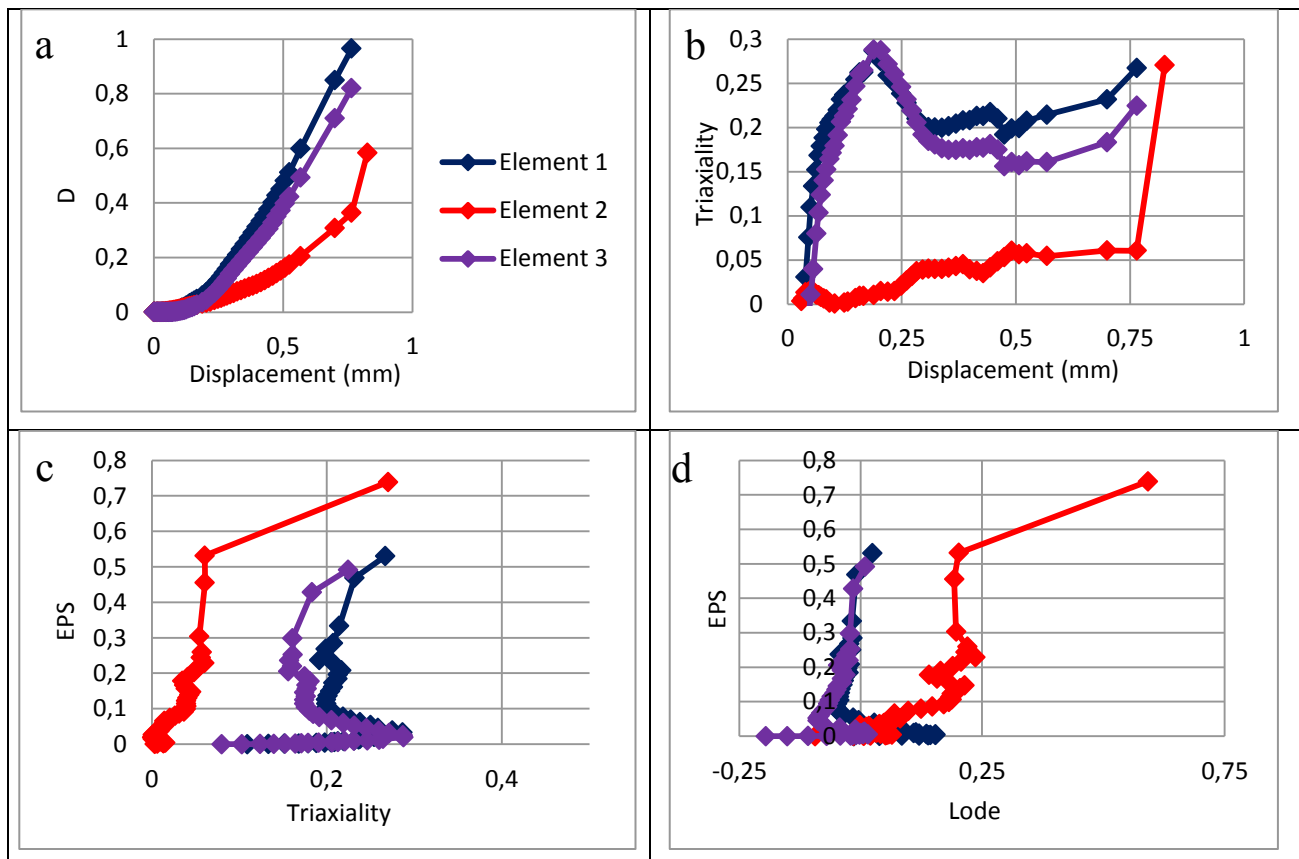


Fig.VI.12: Parameters describing the stress state extracted from 3 elements defined in Fig.VI.9; **low engagement case.**

(a) Evolution of D; (b) triaxiality;

(c) and (d) loading paths, respectively triaxiality and Lode parameter vs strain.

// paramètres décrivant l'état de contrainte tracés sur les 3 éléments définis en Fig.VI.9 ;
engagement faible.

(a) évolution de D ; (b) triaxialité ;

(c) et (d) trajets de chargement, respectivement triaxialité et paramètre de Lode.

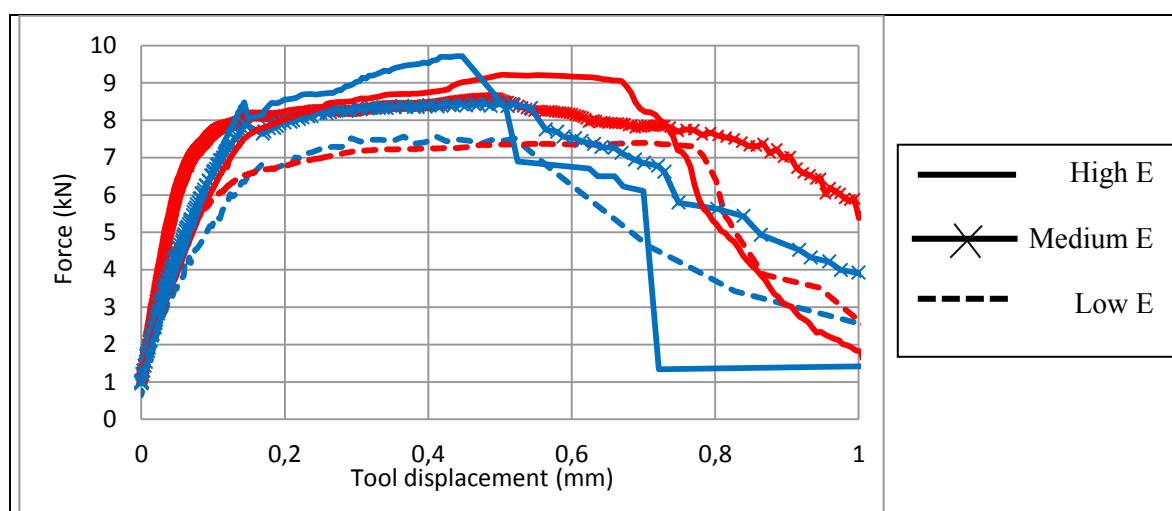
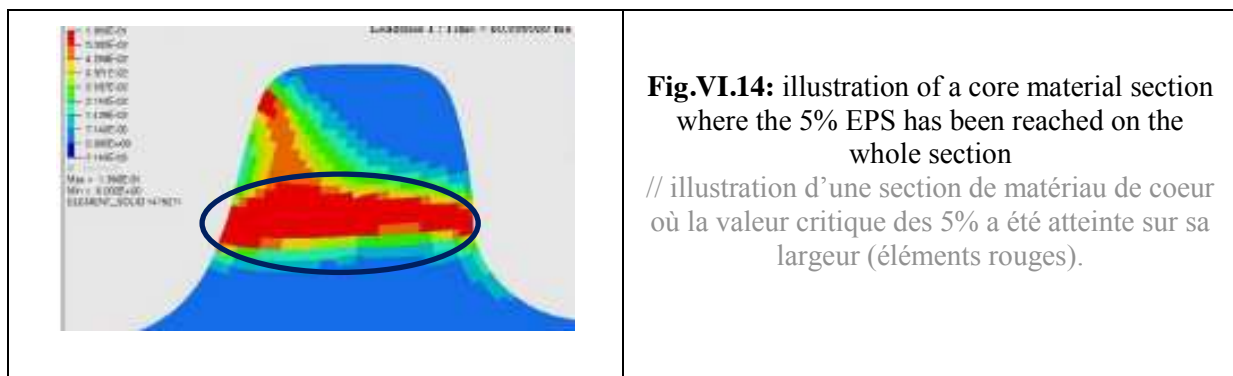


Fig.VI.13: Comparison of the force-displacement curves experimental (blue curves) and numerical (red curves) for the three engagements

// Comparaison des courbes forces-déplacement expérimentales (courbes bleues) et numériques (courbes rouges) pour les trois engagements.

VI. 3. 3 Comparison with Faurecia's previous method

In this section, the results obtained with the methodology developed within this PhD work are compared with the results obtained by Faurecia with its own method at the beginning of the PhD. Faurecia's modeling of carbonitrided parts failure was based on a critical equivalent plastic strain (EPS) criterion. Computations were run without element deletion and a tooth was considered as failed if EPS was exceeding 5% in the whole section of the core material and EPS was exceeding 2% for the external carbonitrided layer on the whole section as well. **Fig.VI.14** illustrates a core material section where failure is declared. The red elements in the circled area have an EPS higher than 5%, so failure is declared on those elements. Since they are on the whole width of the section, failure of the tooth is concluded. This technique is numerically robust since failure is not modeled. Computations are carried out until the end without any failure and at the end EPS is checked to identify at which displacement fracture should have occurred based on EPS values in the mesh. This methodology remains limited though since there is no influence of the stress state on the critical plastic strain values.



In addition, it was not possible with this approach to study any post-failure behavior. This last point may be important when working on the complete pinion if one wants to study the successive failure of multiple teeth. Indeed it was not possible to study the fracture of a complete mechanism; it would have required checking the EPS on the 33 teeth on all the tooth section. With the criterion it can be done because elements are being deleted when failure is reached.

Fig.VI.15 plots the comparison between the method used by Faurecia and the result of this PhD. Comparison is performed with the three engagements studied. The vertical red lines indicate fracture is reached according to Faurecia's method. It must be noticed that Faurecia uses another behavior law for the core material, it will not be discussed here for the sake of confidentiality.

For the low and medium engagements, Faurecia's method underestimates the displacement to fracture by respectively 43 and 65 %, whereas the method developed in this work overestimates by 40 % the displacement for the low engagement, but predicts accurately the failure for the medium engagement configuration. For the high engagement the two methods are overestimating displacement to fracture, even though the method developed here enables to predict accurately the second load drop (see **Fig.VI.15** (c)). This second load drop has been met on all the three tested teeth in high engagement situation (see **Appendix.IV.1**, **Fig.III.1.3**).

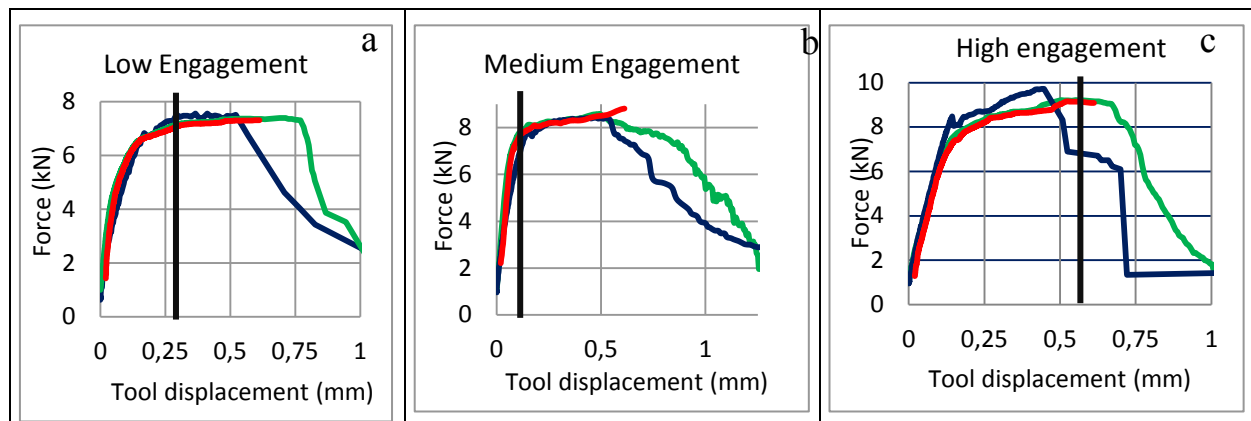


Fig.VI.15: Comparison between the Faurecia method to assess failure and the result of this work, (a) Low Engagement; (b) Medium Engagement; (c) High Engagement.

The vertical lines show where failure is reached according to the Faurecia method.

The blue curve is the experiment, the red curve is the simulation without element deletion, the green one with element deletion.

// Comparaison entre la méthode Faurecia (courbe rouge et ligne verticale noire) pour déterminer la rupture et le résultat du présent travail (courbe verte), la courbe bleue correspond aux mesures expérimentales ;

(a) engagement faible ; (b) engagement moyen ; (c) engagement fort.

Les lignes verticales indiquent que la rupture est atteinte selon la méthode de Faurecia

VI. 3. 4 Discussion

In this section, the accuracy of the numerical methodology developed in this PhD to model the behavior of the core material is discussed. Both plastic law and fracture criterion are checked on a quite complicated but realistic case. As seen in Chapter 5, models were quite accurate on quasi-proportional loadings obtained with butterfly and tensile specimens. The failure prediction with the exponential criterion is accurate for all tested specimens, and thus for a wide range of stress states (from shear with compression until notched tensile specimen).

Regarding semi-industrial tests, of the three engagements, the medium one shows the best correlation of load and displacement to fracture. Experimental and numerical curves are almost superimposed. For the low engagement case, the correlation between experimental and numerical load is accurate, difference is only a few percent, but the failure is predicted too late. For the high engagement case, the experimental load is slightly underestimated by the simulation (8%) and the numerical displacement to fracture is overestimated. The experimental load drop occurs in two stages, whereas the numerical curve fits only the second drop, in an accurate way though. These differences can be due to different reasons listed hereunder.

- The reason with the highest impact is the scatter of the experimental results on the butterfly specimen and the choice of test with the highest displacement to fracture to be accounted for in the loading path for the core material. This choice was done to prevent from any experimental mistakes which would tend to underestimate the displacement to fracture. The drawback is the overestimation of the displacement to fracture which delays the fracture prediction.
- The second reason is the way failure is accounted for in simulations. Modeling progressive failure of 3D components for large plastic strain in a robust way is still a current research topic. The easiest way (and possibly the only way for such complex configurations) is the element deletion technique. This is the only technique available in 3D meshes in LS-DYNA. Chapter 2 listed other techniques like cohesive zone models (CZM) for instance. This technique is quite powerful since it enables to create real cracks through the mesh thanks to a

traction-separation law at elements interfaces. However, its use is very limited so far, in particular when dealing with 3D configurations where failure path is not known a priori. Future developments on 3D CZM techniques or real discrete crack propagation techniques would be interesting to improve post-failure modeling of pinion teeth. One of the main drawbacks of elements deletion technique is related to the element size. Indeed, such a technique means that failure implies volume loss, which is directly related to elements size. Indeed, deleting one element does not induce the real stress state occurring at the crack tip. Experimental stress concentration is higher in the crack tip than in the numerical crack tip. This delays failure in the numerical simulation. Next section will compare the simulation with a coarser mesh. From an industrial point of view, simulations must run in 8 hours with a limited number of cores and it is thus impossible to use thin mesh as seen in the academic research. It is therefore necessary to accept a compromise in terms of accuracy to match this industrial requirement. Hopefully with increasing power of computers, thinner meshes could be used in the future for better accuracy.

- The third reason is the experiment.
 - Firstly the semi-industrial test bench: the objective of the industrial test bench was to study pinion teeth failure under loadings as close as possible to the industrial configuration ones. A lot of work was devoted at the beginning of the project to make this test bench as stiff as possible, keeping in mind that it had to allow direct observations with cameras, which may possibly decrease global stiffness. DIC observation shows there is a spurious movement of the tool of about 0.6 mm max in the direction of the tooth movement, due to the force applied on it. There is as well a spurious displacement of 0.2 mm max of the tool, which reduces the depth of engagement during the test. Those values are very low, but not negligible compared to the longitudinal displacement to fracture which is around 0.8 mm depending on the engagement. Thanks to DIC it was possible to apply exact displacements in numerical simulations. However, it must be noticed that such corrected displacements do not match anymore once failure occurs either experimentally or in numerical simulations. The bench stiffness should still be improved before any other test campaign or a simpler semi-industrial configuration should be designed.
 - Secondly, the engagement depth measurement: over the three studied cases, the engagement depth evolves from 2.0 to 2.4 mm. Micrometric screws were used to impose it precisely before doing the test but it was mandatory to check it with DIC to correct it if needed. The latter was difficult to do because of the darkness required by the DIC system. A 0.05 mm positioning error could be quite sensitive. A more reliable way to measure and impose the engagement should be found in the future to improve accuracy. Those remarks can be done also for the following section dealing with the comparison of the tooth failure for the complete CN material.
- CN paint protection: one can wonder what could be the influence of the specific paint used to prevent the Carbon and Nitrogen atoms to diffuse within the material during the treatment. Because the hardness is lower than the core material, one can hypothesize the carbon content is lower than initially in the material. However, no further studies were done in this material since it represents a thin layer of the treated material and is not present in the CN material.
- Questions about the residual stresses can be raised. In the CN material, since there are strong compressive residual stresses in the external layer, there are some tensile ones in the core material. According to the literature review, they were quite low, around 20 MPa ([Kanchanomai & Limtrakarn, 2008]). In the material studied in this part, there are no residual stresses in the core material. This can induce some differences.

- Reproducibility: as it is seen in Chapter 3 (see **Fig.III.24**) the scatter on the max load sustained by the teeth is lower than 5 %. For the displacement to max load, scatter is a bit higher especially for the low engagement where it is in between 1.05 and 1.32 mm (with raw displacements). A higher number of tests should be carried out to address the variability issue more precisely. This was not possible during the PhD due to very long tests analyses with DIC. Simplifying the tooth failure test should be considered to decrease variability as well.
- Damage coupling: one of the other drawbacks of this failure criterion methodology is that there is no coupling between the material behavior law and the damage increase. Damage models can be coupled to the behavior law [Cao et al., 2014], thus giving a better description of the progressive degradation of material properties. Such a coupling requires however longer calibration procedures and numerical issues, such as mesh dependency, which may require the use of non-local models. This is the main reason why uncoupled failure criteria are used most in industry.

Otherwise, results are rather convincing:

- Plasticity: the material behavior law assessed for the core material is the best compromise found to fit the butterfly and tensile tests (10 tests in the end). Fitting is accurate over all the tests performed, and discrepancy is about 7 % max in terms of load on the tooth failure. One must keep in mind it is rather difficult to model the behavior of the same material in both shear and tensile stress states with the same law using isotropic von Mises yield criterion (J2 plasticity). A Hill48 type anisotropic yield criterion was used in [Gachet, 2013]. Better results were obtained, but it was still difficult to find a good set of parameters for tensile and pure shear loading experiments. As shown in [Cao et al. 2014], modeling accurately the behavior of such steel grades for both tensile and shear loading configurations, the use of a J2-J3¹ plasticity criterion may be preferable.
- Failure criterion: the failure criterion used here defines failure as a critical strain depending on the stress triaxiality ratio and the Lode parameter. The combination of these two parameters enables a unique definition of the stress state. Damage is accumulated through the whole loading path and failure is triggered when $D = 1$. This technique is widely used in the failure modeling community thanks to its reasonable time for parameters identification. However, even though D is accumulated over the loading path, this technique is more efficient when loading remains as proportional as possible. This seems to be true in the simulations where stress state is close to shear and does not evolve much. Just at the end, the stress state changes because of the element deletion technique.

The different explanations detailed above may be interesting leads for future improvements of pinions failure prediction. As seen, these improvements may be both numerical and experimental. However, it must be highlighted that the methodology developed in this work significantly improves results compared to the initial solution used by Faurecia, in particular for the medium engagement configuration. For the future, an enhanced semi-industrial test with a better control of contact surfaces, rigidity and engagement depth would however be interesting.

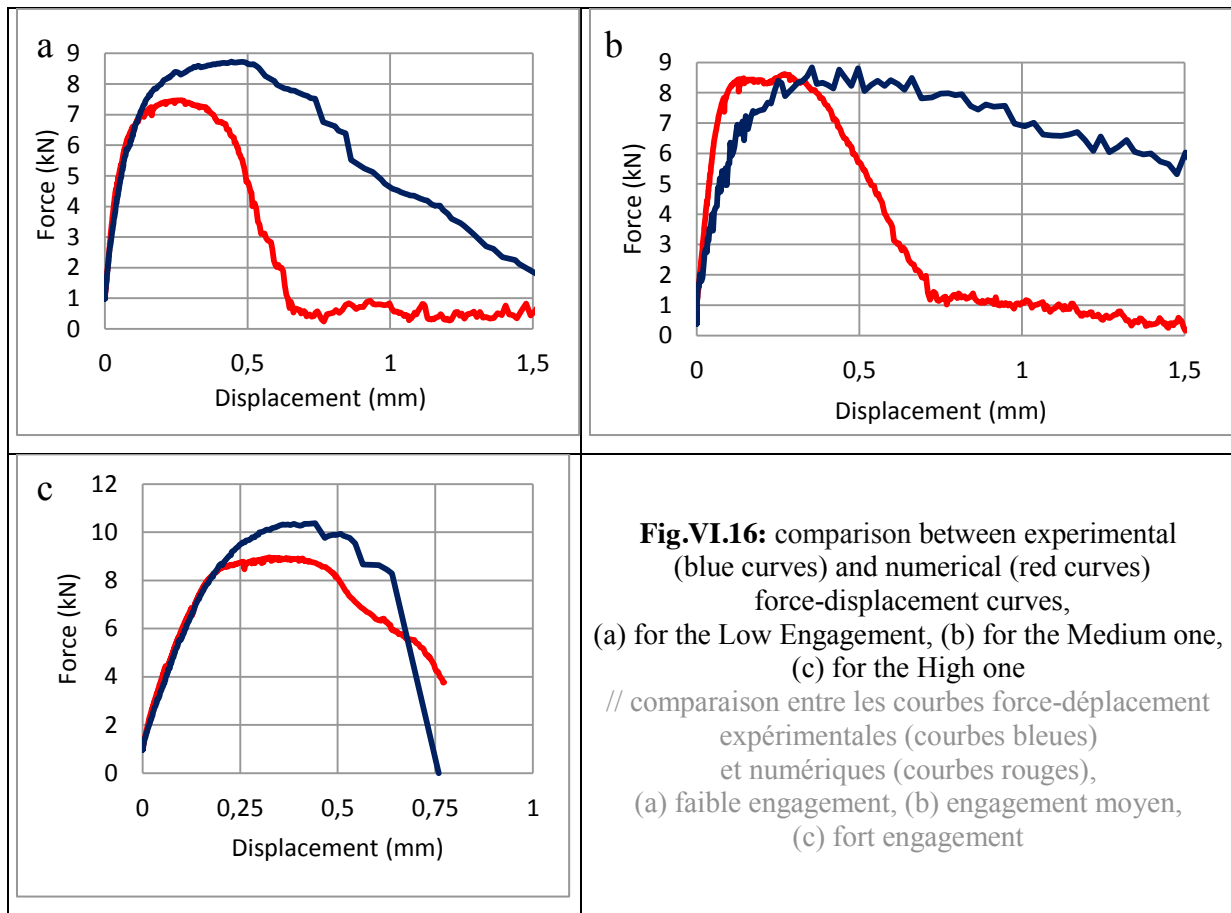
¹ J2 and J3 are respectively the second and third invariants of the deviatoric stress tensor.

VI. 4 Experiment – simulation comparison with the complete CNed component

Now that the models regarding the core material have been checked in the previous section, this part will check the models used for the CN layer. Failure in the CN layer is controlled by a stress-based criterion with the critical values given in section VI.1.2.

VI. 4. 1 Force displacement curves

The first step is the comparison of the force-displacement curves. **Fig.VI.16** (a-c) plots the three engagements. The agreement is globally less good than for the CMO.



For the low engagement, max load is underestimated by 13%, mainly because of premature failure in the CN layer. It is difficult to assess a displacement to fracture since the experimental process is progressive and the force measured at the end of the test is mainly based on the friction between the lower part of the tooth and the tool. However, an estimation about the max load gives 0.5 mm for the experiment and 0.25 mm for simulation, a 50% difference.

For the medium engagement, there is a good agreement (5%) in terms of max load but in the simulation the elastic loading is faster than in the experiment, even with the boundary conditions assessed with DIC. However, one must keep in mind this test exhibited experimentally a disagreement in terms of stiffness in the elastic part compared to the other engagements, so results must be taken with care.

For the high engagement, there is a good agreement in terms of displacement to max load (less than 10%) and the load is underestimated by approximately 11%.

Over those three cases, the behavior of the model is different, even though it tends to globally underestimate the load. The next section compares the fracture processes to try to understand this disagreement.

VI. 4. 2 Fracture process

The fracture process analysis is carried out in several steps. First, the overall process is studied using contour plots of the largest stress eigenvalue σ_I . Then the strain (EPS) contours will be studied by removing numerically the elements corresponding to the CN layer to evidence the state of the core material beneath. Finally, crack propagation will be studied by extracting parameters on chosen elements.

VI. 4. 2. a Overall fracture process

Fig.VI.17, **Fig.VI.18** and **Fig.VI.19** compare respectively the fracture process for the three engagements. On all the simulations, the crack at the lower edge of contact is predicted. This crack appears due to tensile stress states, which trigger the deletion of the CN layer elements. It remains in the external layer; it is stopped in the core material, more ductile. These cracks are shown by black arrows on the **Fig.VI.17** (e), **Fig.VI.18** (e) and **Fig.VI.19** (e). However, it propagates farther than it should. For instance, in the high engagement case **Fig.VI.19** (f and g) the crack propagates through the mesh whereas there is no crack observed experimentally at this point (crack is shown by a purple arrow). Even though it stays only in the CN layer, it can be a reason why the load sustained by the tooth is lower than in the experiment. There are however two inclined cracks at 45° in the experiment, near the side opposite to the contact, which are not modeled. There are also two areas with quite high level of tensile stress (yellow surfaces on the **Fig.VI.19** (g)). Stress is between 1.3 and 1.7 GPa, quite close to the identified critical stress.

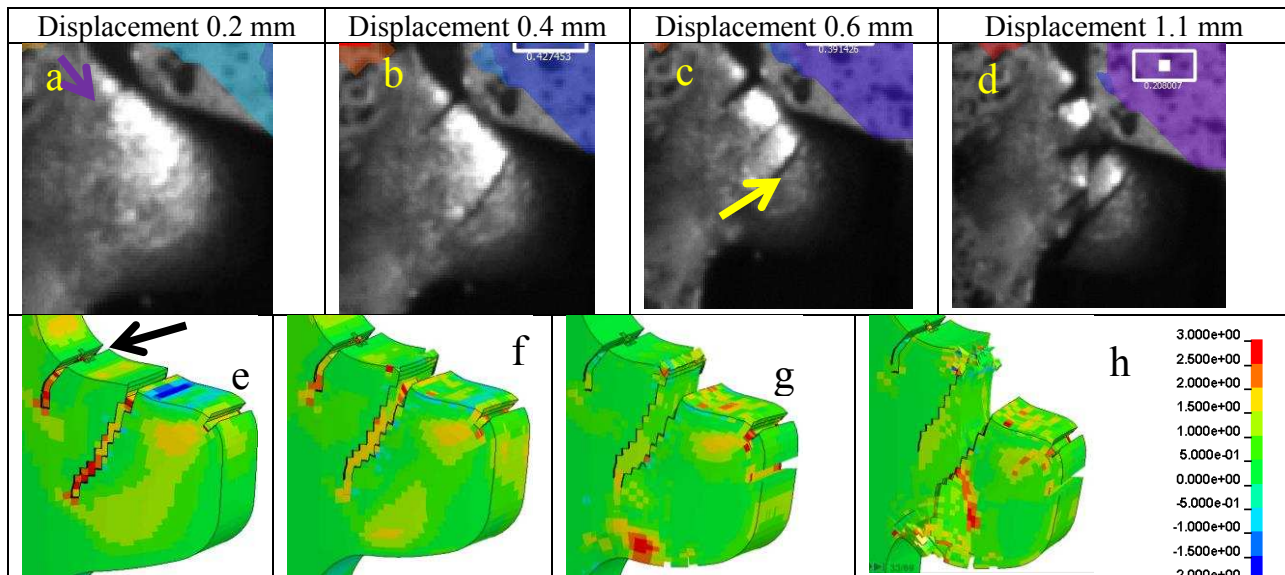


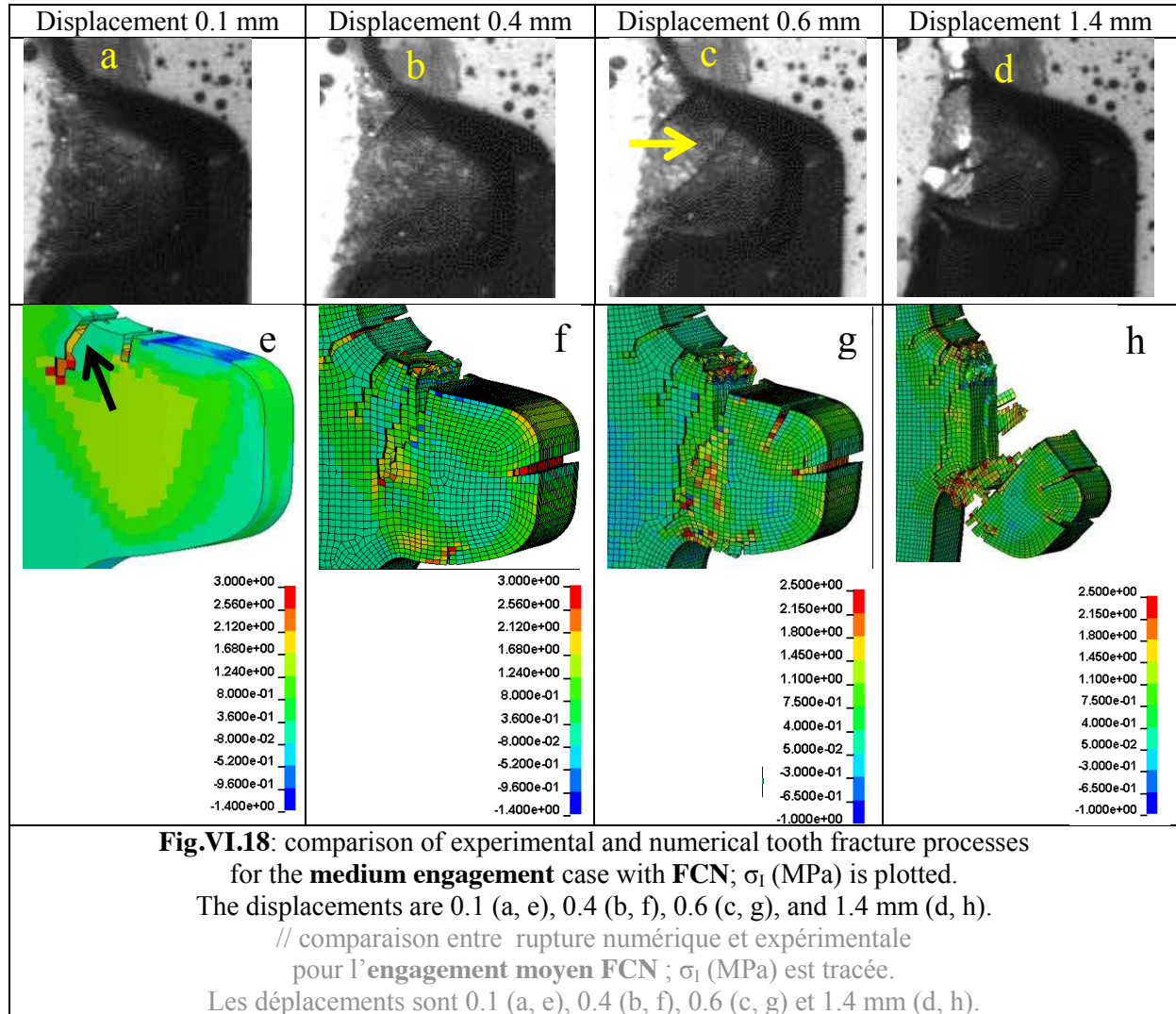
Fig.VI.17: comparison of experimental and numerical tooth fracture processes for the **low engagement** case with **FCN**; σ_I (MPa) is plotted.

The displacements are respectively 0.2 (a, e), 0.4 (b, f), 0.6 (c, g), and 1.1 mm (d, h).

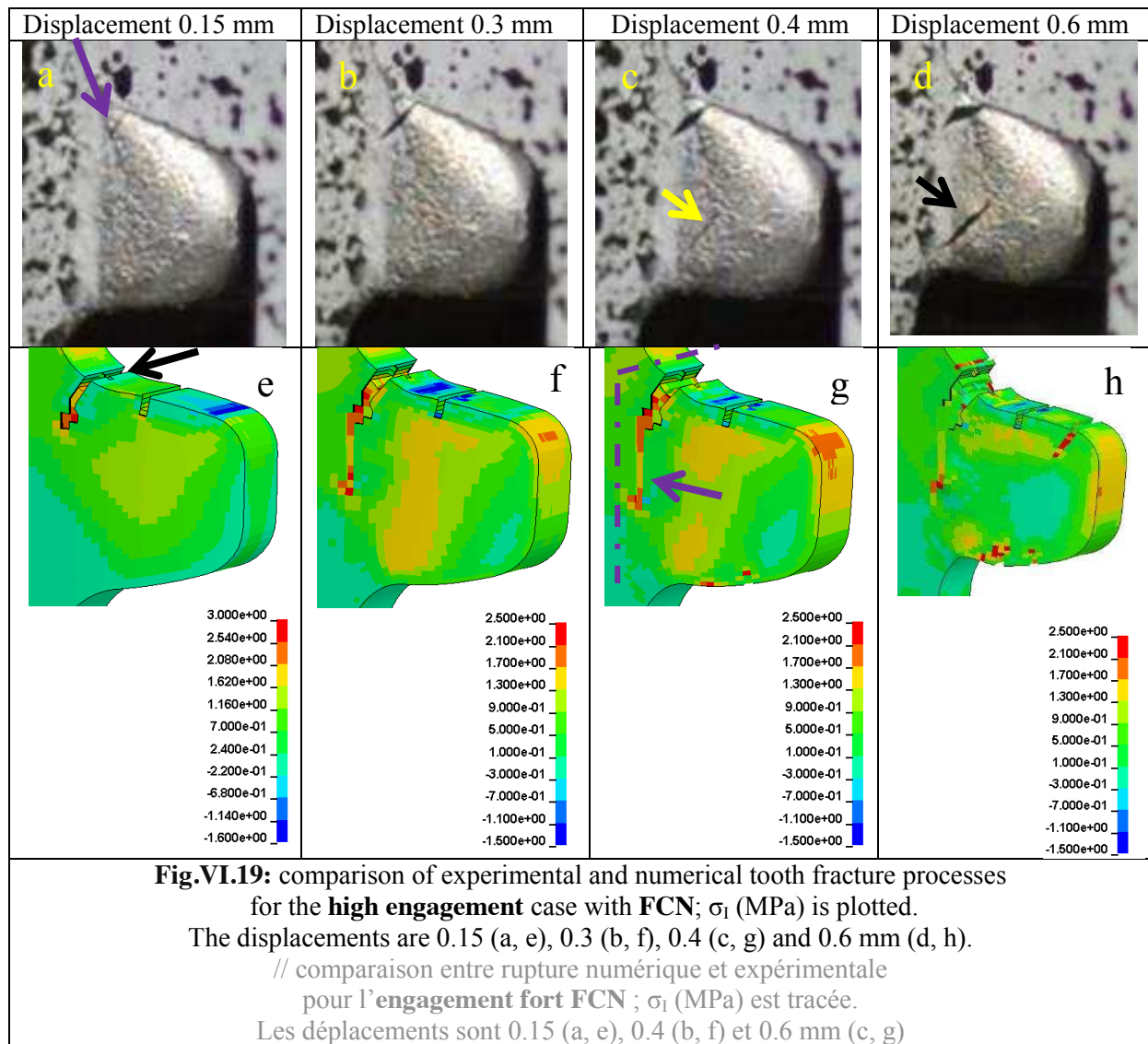
// comparaison entre rupture numérique et expérimentale
pour le **faible engagement** FCN ; σ_I (MPa) est tracée.

Les déplacements sont respectivement 0.2 (a, e), 0.4 (b, f), 0.6 (c, g) et 1.1 mm (d, h).

In the three cases, elements deletions are being observed on the opposite of the tool. It will be shown in the following part that this failure occurs only in the external layer.



Experimental cracks could have been triggered by defaults present at those locations. The final failure is occurring with the main shear crack. It is worth mentioning that the localization of this main shear crack in numerical simulations is in good agreement with observations. However, whatever the engagement, the numerical crack is propagating too early compared to the experiment. So the fracture criterion for the core material would underestimate the strain to failure. One must remind that the CN layer is being modeled through one single behavior, whereas in the reality there is a transition zone. Thus the numerical sharp interface created could have a negative influence on the failure prediction accuracy.

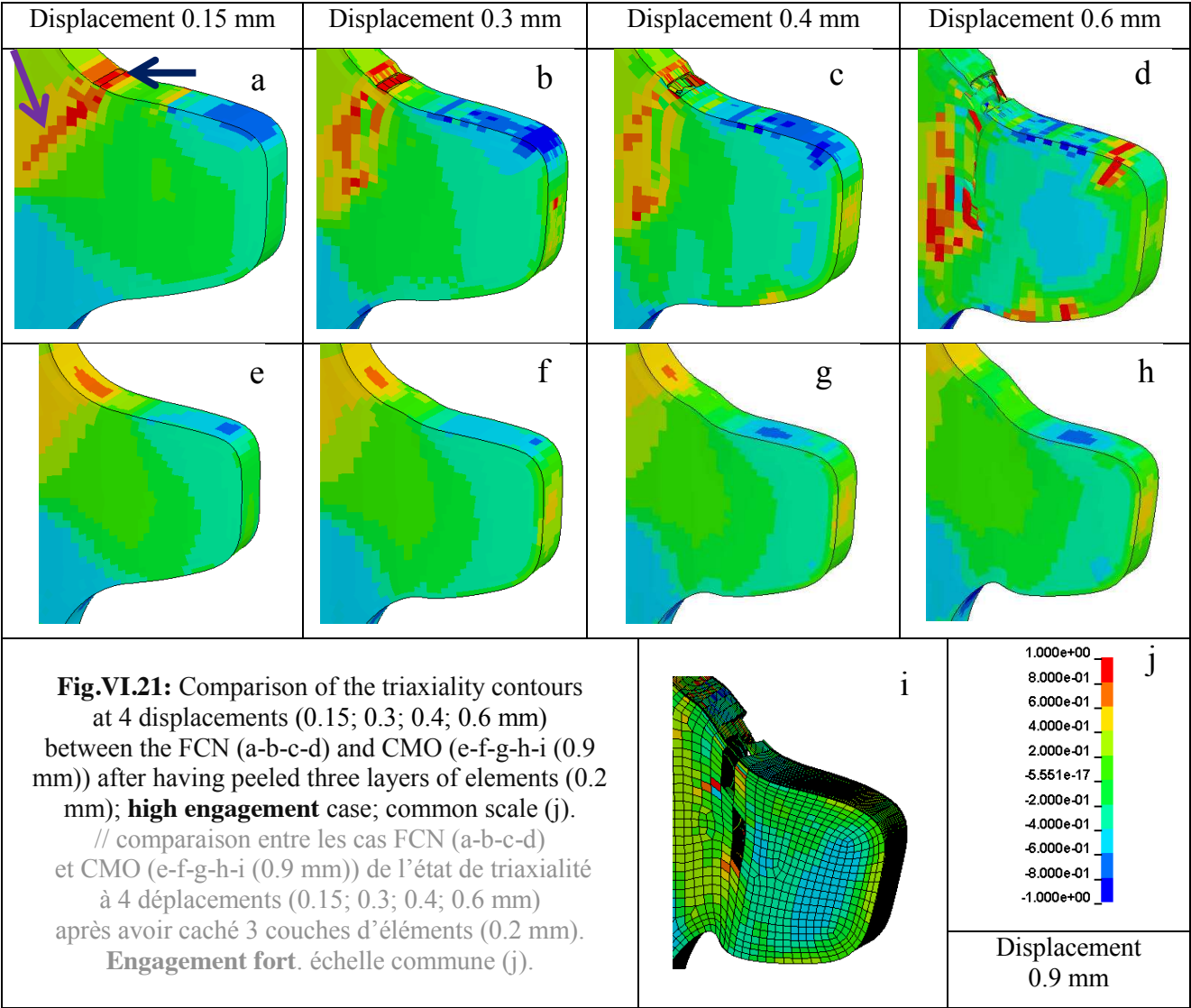
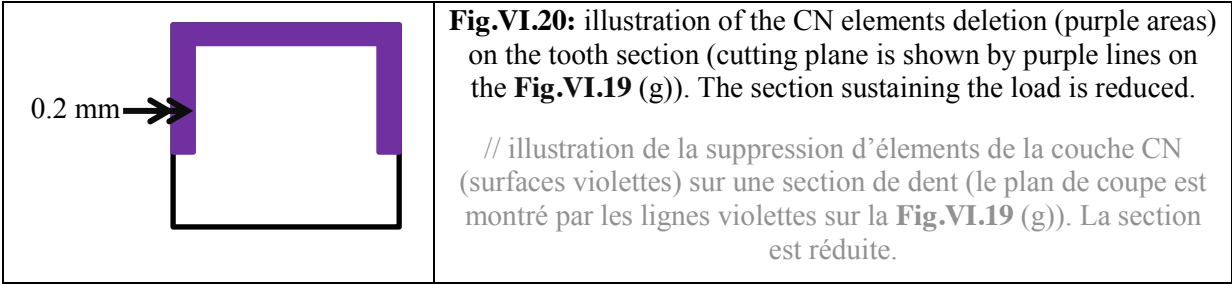


VI. 4. 2. b Shear crack propagation – comparison with the CMO

The observation of the shear crack is trickier than with the CMO because of the external layer. To better understand its propagation, it is mandatory to numerically peel the elements corresponding to the external layer (three layers of elements) and observe only the ones corresponding to the core material. Thus, influence of the CN layer on the core behavior can be studied. To be consistent, three layers of elements have been numerically peeled as well on the following pictures from the CMO. **Fig.VI.21** plots the evolution of the stress triaxiality contour at four distinct displacements. It can be seen that the triaxiality, and thus the stress state is different in the core material. Indeed **Fig.VI.21** (a-b-c) shows there is an influence of the first crack opening below the contact surface with the tool already from 0.15 mm displacement. Below the CN crack, there are core material elements where the stress triaxiality is quite high (>0.6 , purple arrow on **Fig.VI.21** (a)). It is even higher under the surface in contact with the tool (red elements shown by the blue arrow). This line of elements is being deleted before 0.4 mm displacement. Pictures must be observed together with **Fig.VI.19** where the whole mesh is present and the external surface (CN layer) can be studied. Indeed, the elements of the CN layer are deleted, which introduces high triaxiality stress state in the core material. This stress state is not present on the CMO tested tooth. By propagating in the CN layer, the crack concentrates the strain

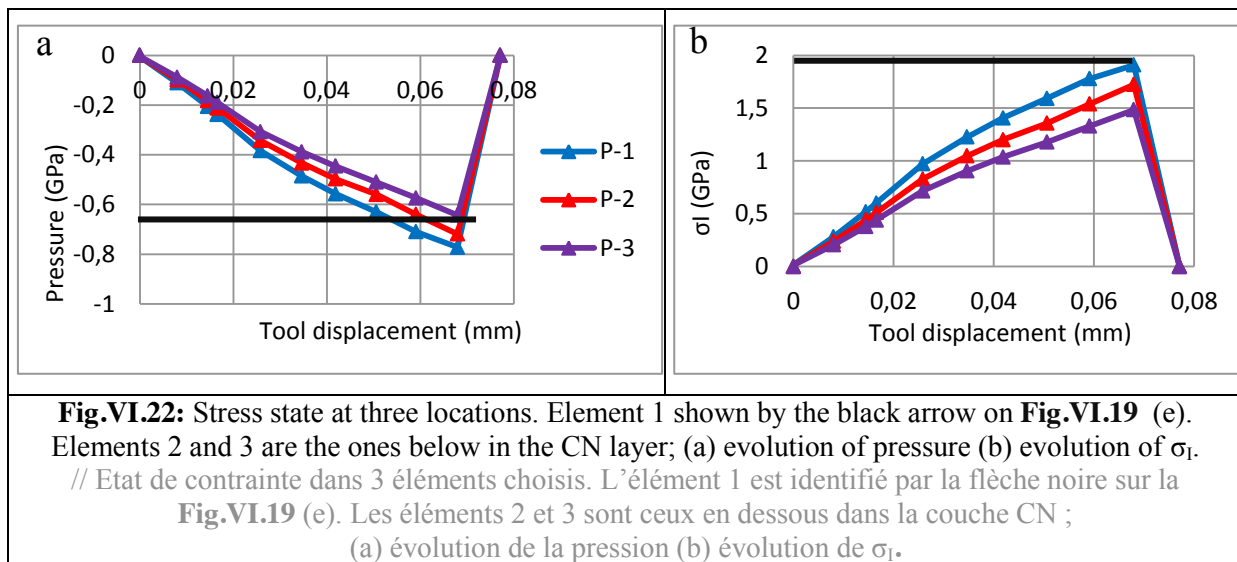
in the material which has the capability to strain, i.e. the core material. This phenomenon is due to a mechanical effect and a numerical one.

The mechanical effect comes from the CN elements deletion which reduces the available section capable of sustaining the load. Indeed, elements belonging to the CN layer are being deleted on a U-shaped surface (**Fig.VI.20**, purple area). There are therefore a section reduction of 0.2 mm on three surfaces out of four.. This is not observed experimentally: there is no material deletion, just crack opening.



The second effect is the formation of voids, corners, and new free surfaces due to the elements deletion. Those create numerically volumes with high stress concentration which lead to premature failure. Indeed because stress triaxiality is quite high, critical strain is reached very quickly. There is no such phenomenon on the CMO tooth since the whole tooth can undergo a higher level of strain. Especially the first three layers of elements can be strained plastically to absorb the energy due to the contact with the tool. More work is needed to weight the influence of the two effects.

Let us study now the evolution of those parameters on some selected elements. **Fig.VI.22** plots respectively the pressure (a) and the first principal stress σ_1 (b) on three elements belonging to the CN layer. They are displayed on the **Fig.VI.23** (a) (Elements 1, 2 and 3). Actually, element 1 is the first element deleted in the simulation (0.07 mm displacement). Its deletion leads to the deletion of the other two elements below on the same vertical line as well as all the elements on the same horizontal line. The calculation time step is 10^{-4} ms whereas the time interval corresponding to the stored results that can be visualized is 0.5 ms. There are 5000 calculation steps between two outputs shown on **Fig.VI.22**. If it was possible to save all the increments elements deletion would not look that fast.



The deletion of these elements creates the crack shown by the black arrow in **Fig.VI.19** (e). This is the crack at the tooth root, in tensile stress state; it runs through the contact surface and a short distance on both sides of the tooth, without penetrating the tougher core material. However, the element deletion continues at the interface with the core material, on the CN layer side. **Fig.VI.23** illustrates cross sections of the tooth root where the crack is opening. First the aforementioned elements 1, 2 and 3 are deleted and they trigger the deletion of the ones on the same line so that the crack extends from one side to the other. Then element 4 is deleted together with all the interfacial CN elements on the same line perpendicular to the surface shown. Those above (5 and 6) are not deleted because they do not reach the critical values of the failure criterion. And once failure propagates in the previous 4 elements, stress relaxation occurs in these elements. Furthermore, as it can be seen on both pictures, triaxiality is quite high in the core material as well (>0.8 below the crack opening). This is why the final crack is starting here.

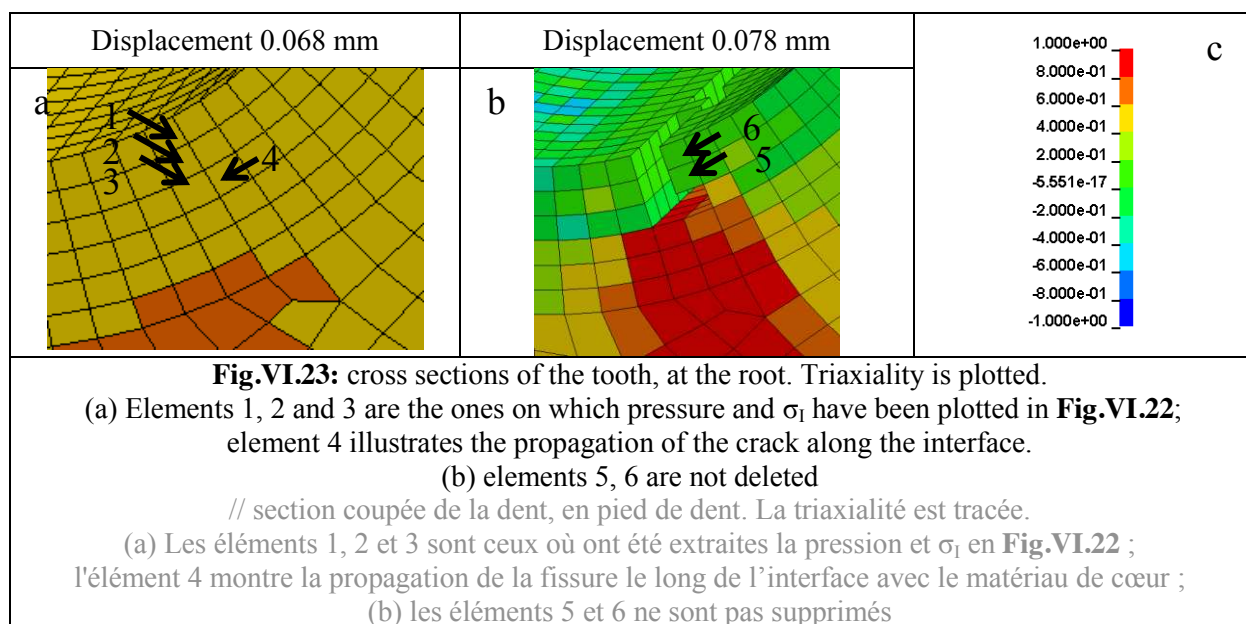


Fig.VI.24 plots the pressure and the first principal stress on elements 4, 5 and 6. Element 4 has been deleted because it has reached the critical value. It is difficult to observe this on the plots, this is due to the difference between calculation time step and the time between two data outputs. Once the elements forming the crack are deleted, the stress state changes immediately and the stress is decreasing: elements 5 and 6 have their stress state changed immediately, pressure goes from -0.8 to 0.04, the stress is released because they have free surfaces now.

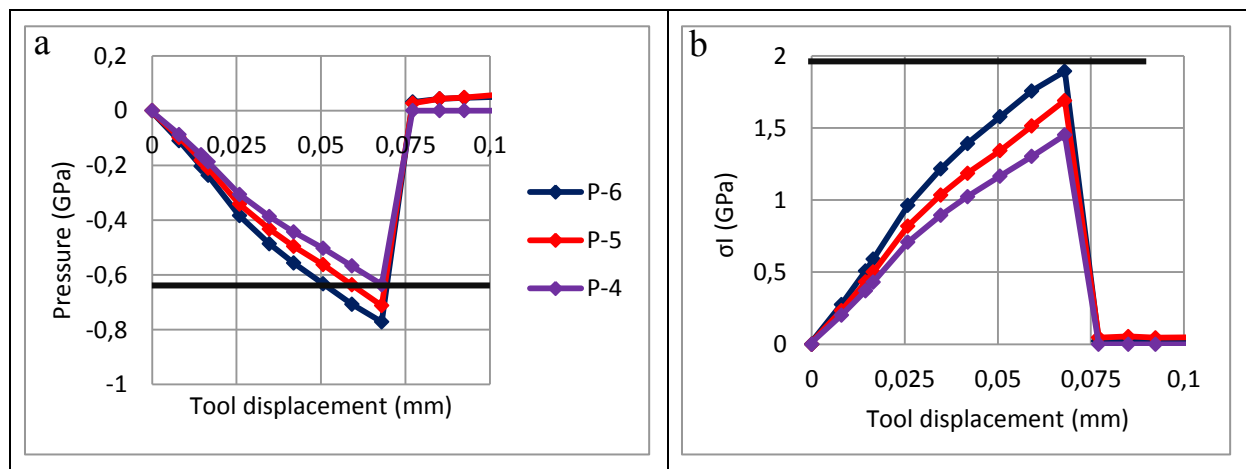


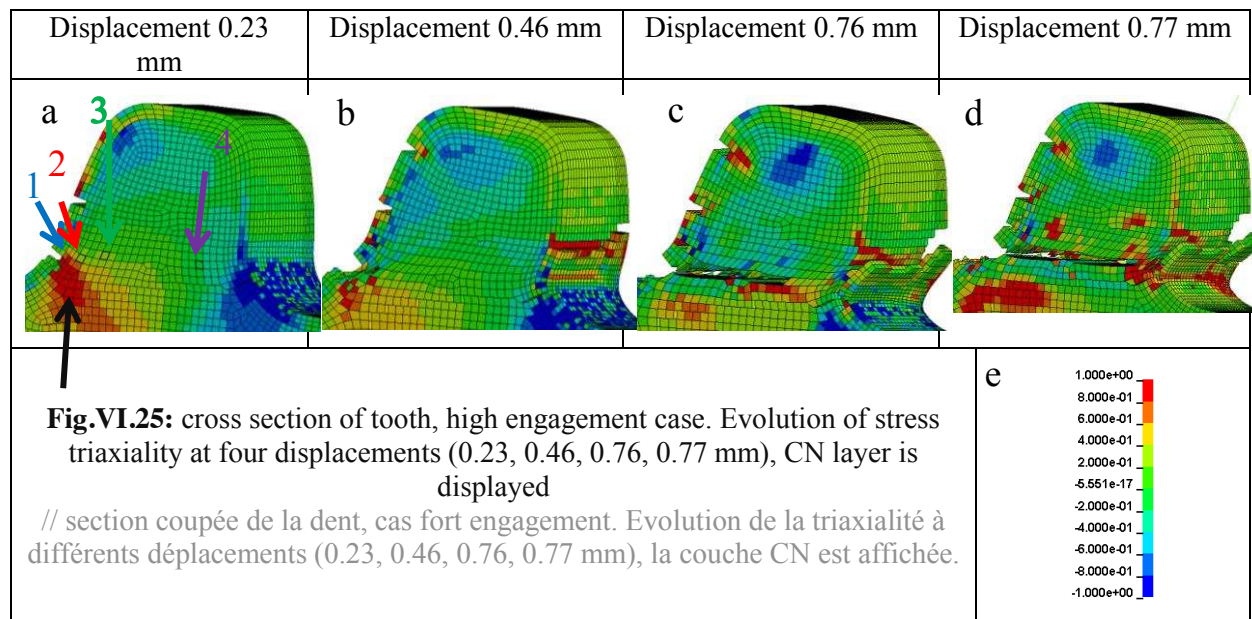
Fig.VI.24: stress state of elements 4, 5 and 6 shown in **Fig.VI.23** (a - b). Evolution of (a) pressure and (b) first principal stress as a function of the tool displacement.

// état de contrainte des éléments 4, 5 et 6 montrés en **Fig.VI.23** (a - b). Evolution de (a) la pression et (b) de la première contrainte max principale en fonction du déplacement outil.

Then, as the tool displacement is increasing, the stress and strain are increasing as well in the tooth. Once the critical strain is reached on the elements in the core material, a crack propagates within the tooth in a shear mode. This is illustrated in **Fig.VI.25** by a tooth cross section at four distinct displacements. First, triaxiality is high (>0.8) in the red area starting from the first crack downwards (black arrow in **Fig.VI.25** (a)). This high triaxiality lowers the critical strain to failure for the core material, and thus damage increases fast. This stress state is due to the contact with the tool as well as the crack in the CN layer.

Let us follow the evolution of fracture parameters on four elements to study this more precisely. Four elements are highlighted in **Fig.VI.25** (a) and shown with colored arrows. Element 1 in blue corresponds to one element in the core material but initially at the interface with the CN layer. It is located below the first crack. The second element, in red, is located 0.12 mm deeper. Elements 3 and 4, respectively in green and purple, are located on the same horizontal line of elements in the core material. Those four elements are on the shear crack path and illustrate the mechanism of the crack propagation.

Fig.VI.26 (a-b) plots the evolution of the damage parameter D and the triaxiality as a function of the tool displacement on the aforementioned elements.



The damage increase on the four elements is quite fast as the crack tip approaches, it is exponential. Looking at **Fig.VI.26** (b) it can be seen that stress triaxiality exhibits significant differences however.

The first and the second elements have a high triaxiality as soon as contact is made between the tooth and the tool. They are indeed located below the contact surface, hence submitted to tensile stress state. It is confirmed by the triaxiality of 0.5. Then there is an abrupt increase at 0.07 mm displacement, which corresponds to the crack opening in the CN layer. Triaxiality of element 1 increases from 0.5 up to 0.84, and for element 2 from 0.5 to 0.6. It is higher for the first element because it is an interfacial element which is located directly ahead of the crack tip from 0.07 until 0.2 mm displacement. Then, an element on the line is deleted (0.203 mm displacement), which creates a change of stress state; triaxiality drops to 0.37 close to pure tension where the element is deleted. It is unexpected that the element is deleted after the triaxiality drop, but $D = 0.88$ before the drop. It increases fast because triaxiality is high, but not enough to reach its deletion. This is why it is deleted after the drop. So in the end, the stress state on this element is highly tensile.

The second element has a lower triaxiality, but its average triaxiality at failure is 0.3.

The third and the fourth elements are deeper inside the tooth on the crack path. Their triaxiality evolves within the range $[-0.3; 0.3]$ on their loading path, and increases in the end. Tooth upper part is pushed forward which induces tensile stress state at the crack tip. This is why triaxiality for the two elements increases up to 0.36 and 0.46 at failure.

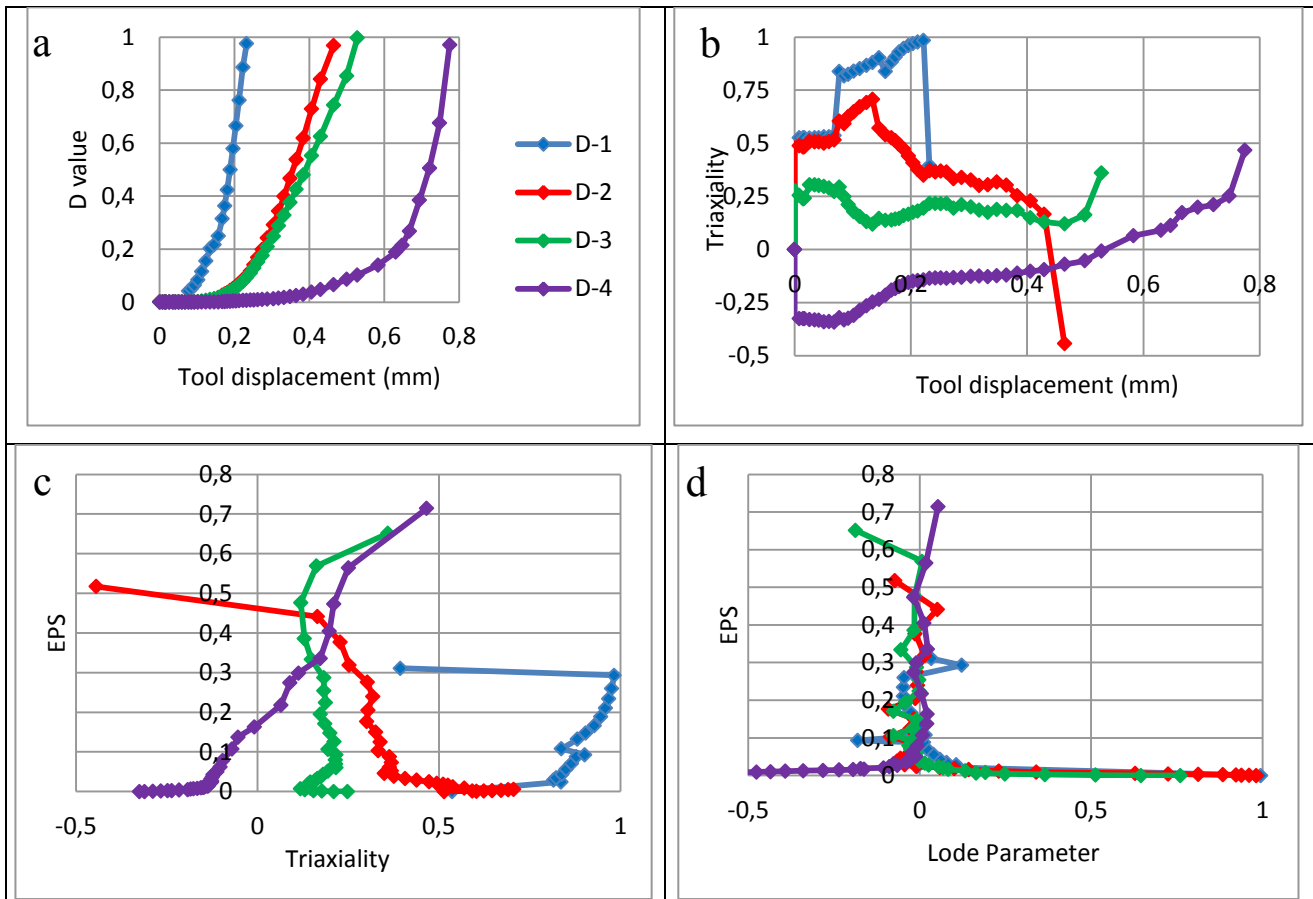


Fig.VI.26: Fracture parameters extracted on 4 elements defined in Fig.VI.25, **high engagement** case.

(a) Evolution of the D parameter; (b) triaxiality ;

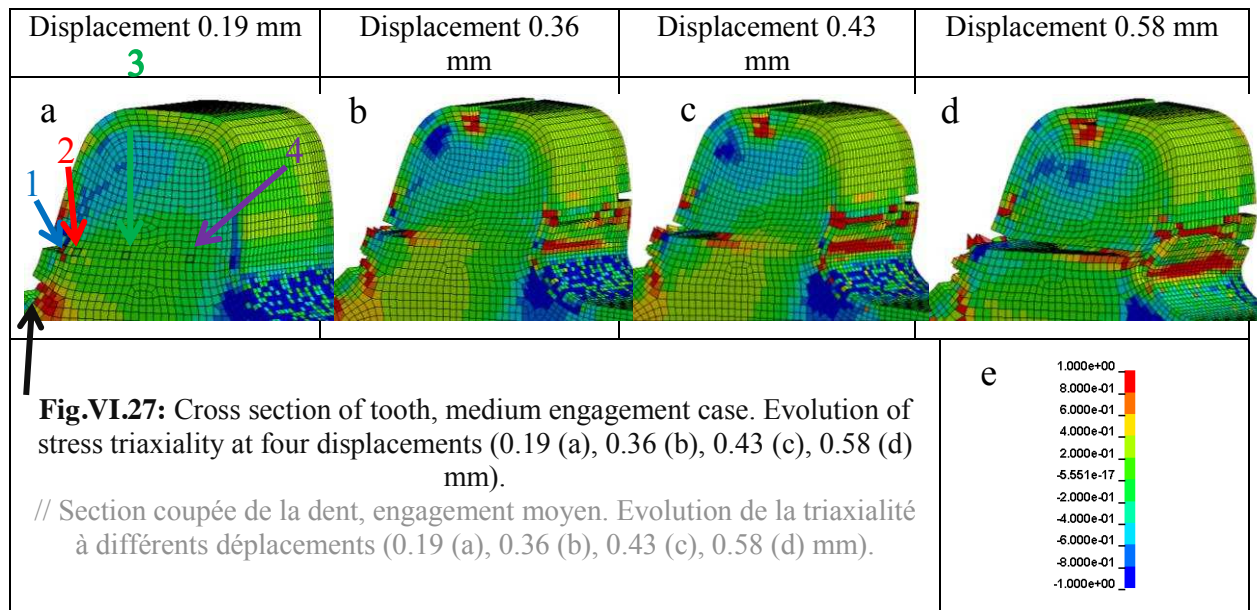
(c) and (d) loading paths, respectively the triaxiality and the Lode parameter vs strain.

// Paramètres de rupture tracés sur 4 éléments définis en Fig.VI.25, **engagement fort**.

(a) évolution du paramètre d'endommagement D ; (b) triaxialité ;

(c) et (d) trajets de chargement, respectivement triaxialité et paramètre de Lode en fonction de la déformation.

For the other two engagements the process is a bit different. Indeed, because contact surface is farther from the tooth root, the main crack is not the propagation of the first opening crack but of a second one. This is being illustrated through Fig.VI.27.



The first opened crack is the one shown by the black arrow on **Fig.VI.27** (a) and corresponds to the one at the root. Even though contact surface is farther from the root, a crack still opens there. However, the lethal crack is not its prolongation but constitutes a distinct crack. Elements 1 until 4 highlighted in **Fig.VI.27** (a) are on the crack path, the latter is 0.24 mm higher than the first crack. The crack is straight and appears on one element layer. On the side opposite to the contact, elements are being deleted in the CN layer. They are in tensile stress state, due to the upper part of the tooth moving toward the right side. This can be observed as well on the high engagement case **Fig.VI.25** (b). This has been observed in the experiments on the three engagements. Cross section (high engagement) of a tooth showed a crack on the opposite side of the tool (**Fig.III.23**). According to the simulation, it stays only in the CN layer and does not propagate further.

Fig.VI.28 plots the evolution of fracture parameters on the four elements highlighted in **Fig.VI.27** (a) for the medium engagement case. **Fig.VI.29** does the same for the low engagement case; chosen elements are located in the same areas as for the medium and high engagements, enabling comparison.

In all three cases, D increases quickly with tool displacement. This shows damage propagation within the tooth is a fast process. Triaxiality of the first deleted element is high for the three cases and increases up to 0.9 at failure. It is interesting to notice that for the low and medium engagement, stress triaxiality in element 1 is negative (compression) before failure occurs in the CN layer. This failure induces a strong increase of stress triaxiality, which rises up to 0.8 almost instantaneously for the medium engagement configuration. This shows how element deletion in the CN layer influences stress state in the core material.

Then for the low and medium engagement cases, the other three elements have a low triaxiality during most of their loading path $[-0.1; 0.2]$ showing it is a shear crack (mode II dominantly). At the end, triaxiality increases because of the opening mode of the final crack propagation. However, element 3 for the medium engagement has another behavior, triaxiality drops at the last stored time step. This shows the element deletion induces abrupt stress state change on the elements nearby. For the Lode parameter, it evolves within $[-0.1; 0.1]$ for the three cases except for element 4 in the low engagement configuration. Indeed, it increases up to 0.24 to drop down to -0.16 just after. This change is due as well to the element deletion.

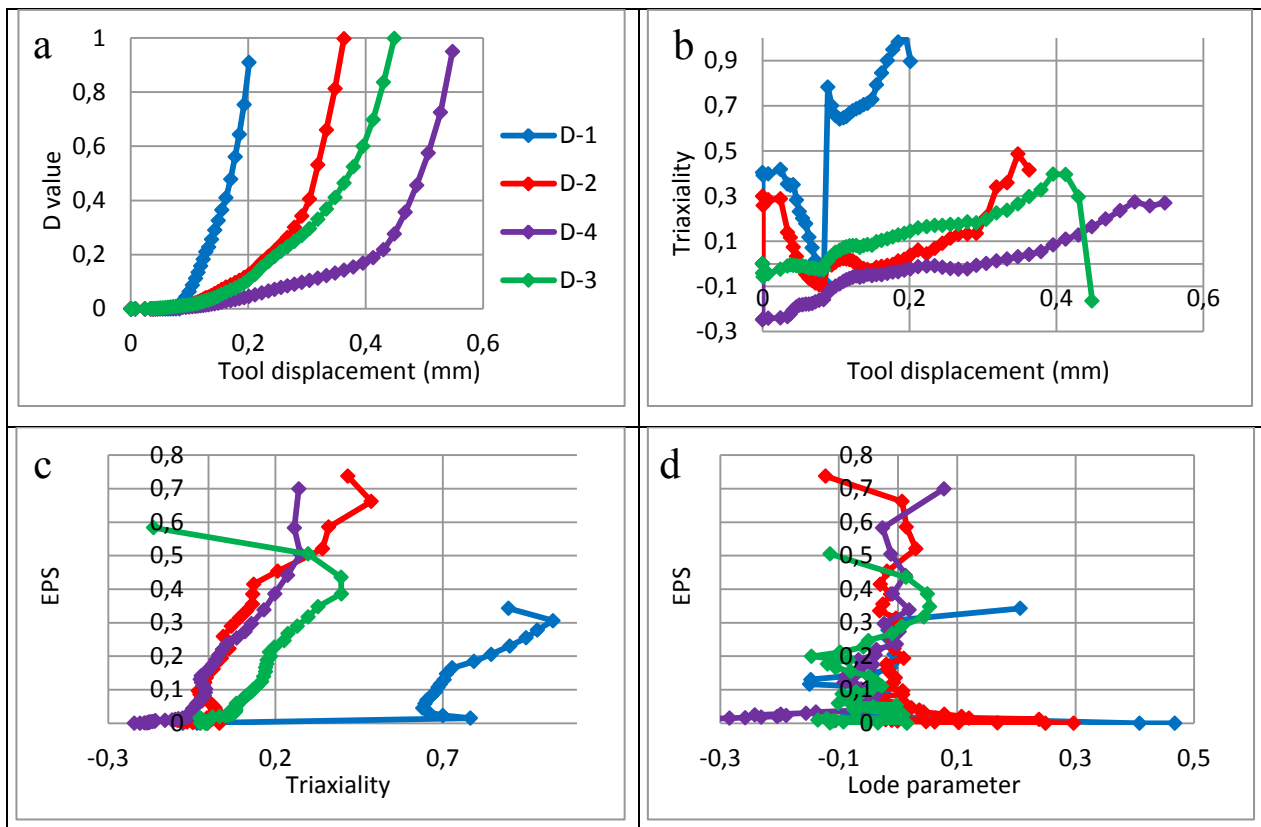


Fig.VI.28: Fracture parameters extracted on 4 elements defined in **Fig.VI.27 (a), medium engagement** case. (a) Evolution of the D parameter; (b) triaxiality; (c) and (d) loading paths, respectively the triaxiality and the Lode parameter vs strain.

// Paramètres de rupture tracés sur 4 éléments définis en **Fig.VI.27 (a), engagement moyen.**

(a) évolution du paramètre d'endommagement D ; (b) triaxialité ;

(c) et (d) trajets de chargement, respectivement triaxialité et paramètre de Lode en fonction de la déformation.

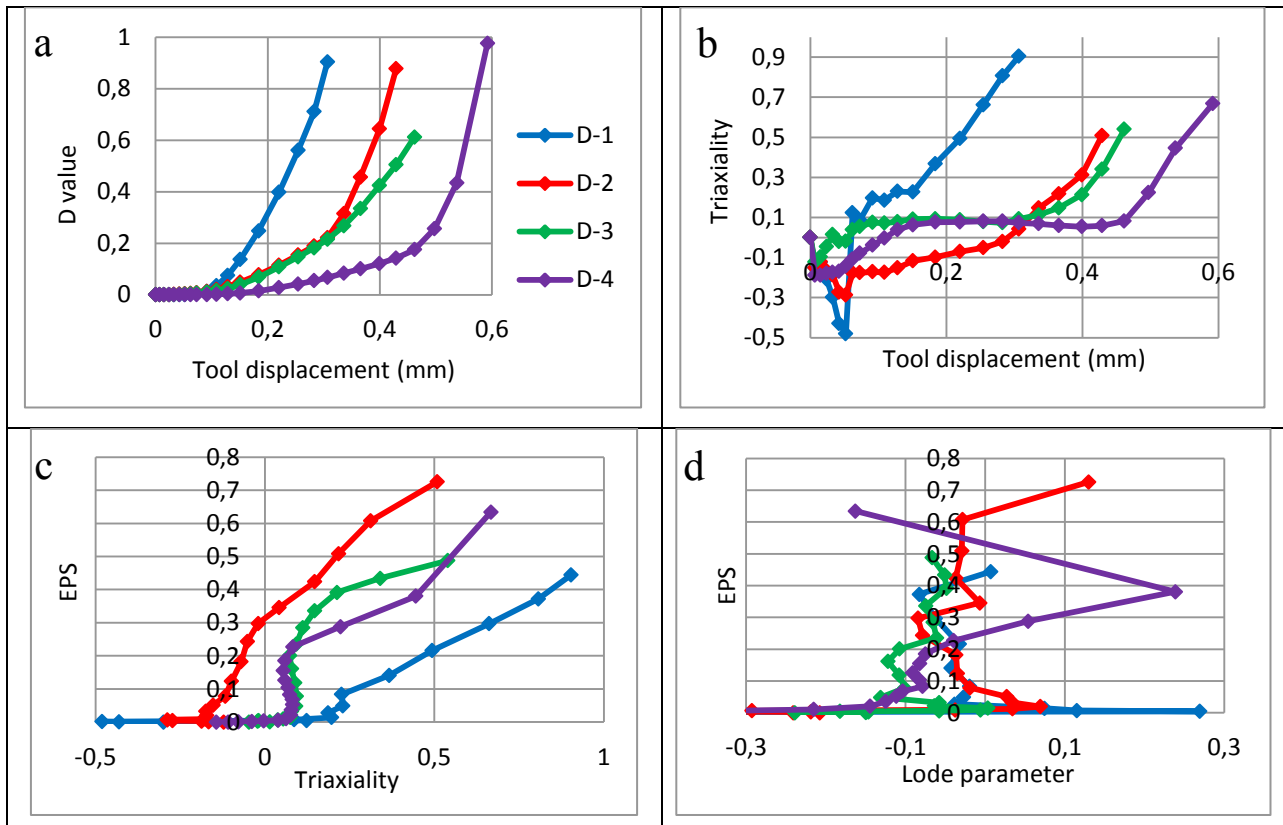


Fig.VI.29: Fracture parameters extracted on 4 elements defined in Fig.VI.27 (a), **low engagement** case.

(a) Evolution of the D parameter; (b) triaxiality;

(c) and (d) loading paths, respectively the triaxiality and the Lode parameter vs strain.

// Paramètres de rupture tracés sur 4 éléments définis en Fig.VI.27 (a), **engagement faible**.

(a) évolution du paramètre d'endommagement D ; (b) triaxialité ;

(c) et (d) trajets de chargement, respectivement triaxialité et paramètre de Lode en fonction de la déformation

VI. 4. 3 Comparison with Faurecia's previous method

Let us recall that the method used by Faurecia before the PhD consisted in declaring the CN layer had failed if $\bar{\epsilon} > 2\%$ versus 5% in a whole section for the core material. **Fig.VI.30** shows the comparison for the three engagements. The vertical line corresponds to the stage at which strain is higher than 2% (resp.) 5% , so failure is being declared. This method underestimates the displacement to failure for the three cases (respectively 30 , 40 and 60% for the low medium and high engagement). However, the max load is higher with the Faurecia method (no element deletion) and closer to the experimental value.

Within the elastic regime, both numerical simulations are in pretty good agreements for the three engagement depths. They both overestimate force in the elastic regime for the medium engagement, and the experimental curve may be questionable for this case.

Globally, failure seems to occur too early with the method developed here. Indeed, the crack starts to propagate within the mesh in the CN layer, which decreases the max load (section is narrower thus lower than the experimental one). Whereas Faurecia's method does not model failure at all, this explains higher load values. In addition, stress concentration induced by the deletion of elements tends to accelerate failure in the core material, which could explain the underestimation of failure displacement for the low engagement.

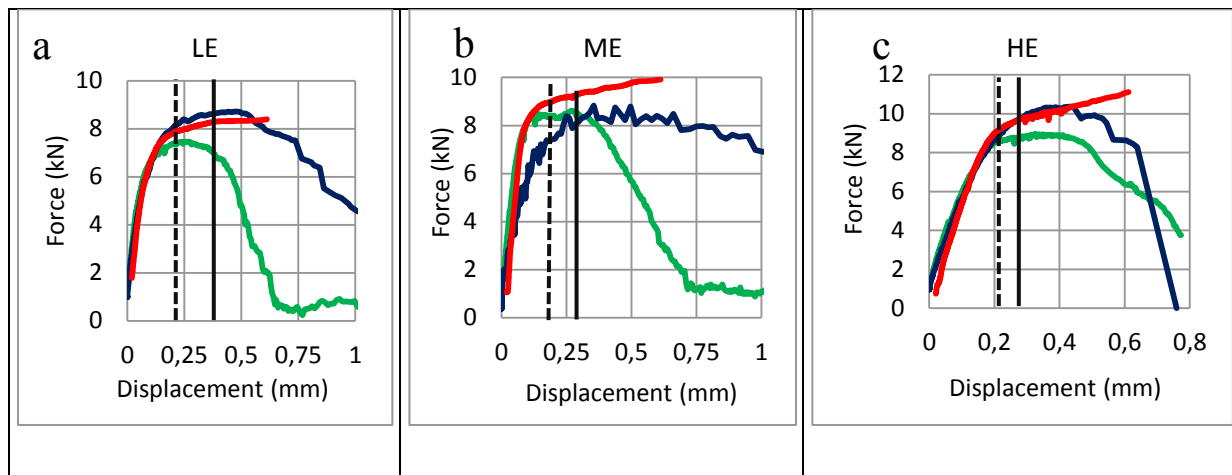


Fig.VI.30: Comparison between the Faurecia method to assess failure and the result of this work, (a) Low Engagement; (b) Medium Engagement; (c) High Engagement.

The vertical lines show where failure is reached according to the Faurecia method (dotted line for the CN layer, full one for the core material).

The blue curve is the experiment, the red curve is the simulation without element deletion, the green one with element deletion.

// Comparaison entre la méthode Faurecia (courbe rouge et ligne verticale noire) pour déterminer la rupture et le résultat du présent travail (courbe verte), la courbe bleue correspond aux mesures expérimentales ;

(a) engagement faible ; (b) engagement moyen ; (c) engagement fort.

Les lignes verticales indiquent que la rupture est atteinte selon la méthode de Faurecia (ligne brisée pour le couche CN, ligne complète pour le matériau de cœur).

VI. 4. 4 Discussion

Many explanations were given in section VI.3.4 for the CMO configuration. In addition, influence of the CN layer critical stress value and influence of mesh size are analyzed here. the use of a simplified failure criterion (Lou & Huh) is discussed as well.

VI. 4. 4. a Impact of variations of the CN behavior

The previous parts showed the correlation between the experimental and the numerical tooth fracture for the FCN. The correlation is globally less accurate than the one with only the core material (CMO). Does this mean that some parts of the model of the CN layer are not efficient? The plastic stress-strain law used is the one defined by [C. Moussa, 2012], the same law used by Faurecia to model the plastic behavior. Since the material does not undergo much plastic strain, the behavior law does not influence the tooth resistance. Indeed the identified critical stress is lower than the plastic yield stress.

A reason could be the fracture criterion. Based on the literature identified in Chapter 2, a fracture criterion based on stress rather than strain is used to model the failure behavior of the CN layer. Chapters 1 and 3 confirm its brittle behavior. Chapter 5 shows also that there is a quite high gap between the critical values assessed with the tensile test and with the four point bending test. Simulations until here were made with the average value since there was no good reason to privilege one test over the other.

Fig.VI.31 illustrates the influence of σ_{ic} on the force-displacement curve. Decreasing this value from 1.93 (Medium Critical Stress, MCS), to 1.7 GPa (Low Critical Stress, LCS), the displacement to fracture increases by 100 %; with this value, the numerical and the experimental displacements to fracture are equal. On the contrary, σ_{ic} does not influence the maximal load (2.1 GPa High Critical

Stress, HCS). This was unexpected since it is consistent to say at first sight that a higher critical stress would increase the peak load sustained by the tooth. This confirms the load is sustained by the core material, not the external layer.

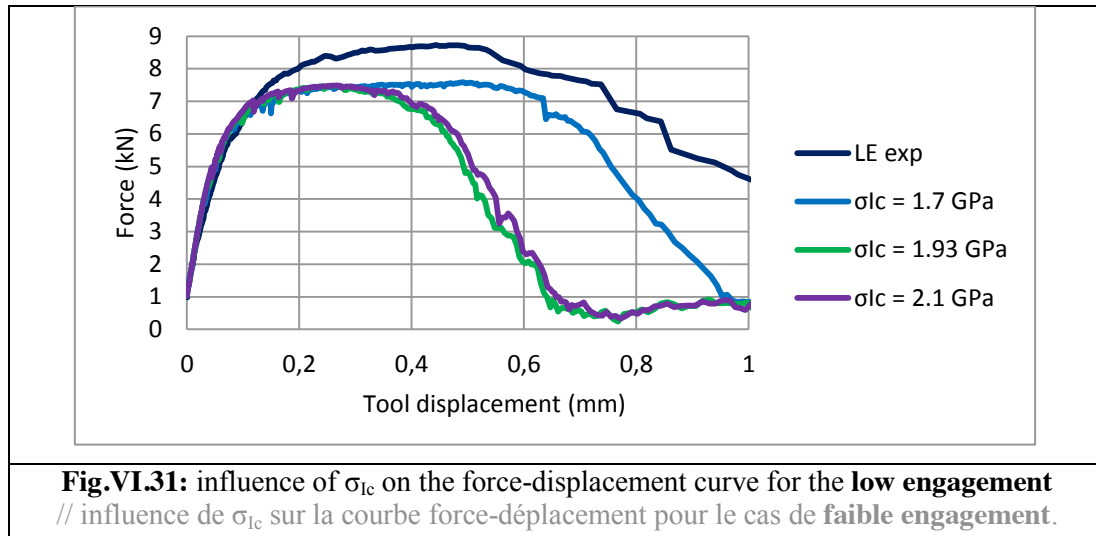


Fig.VI.32 compares the fracture process at three steps for the three critical stresses.

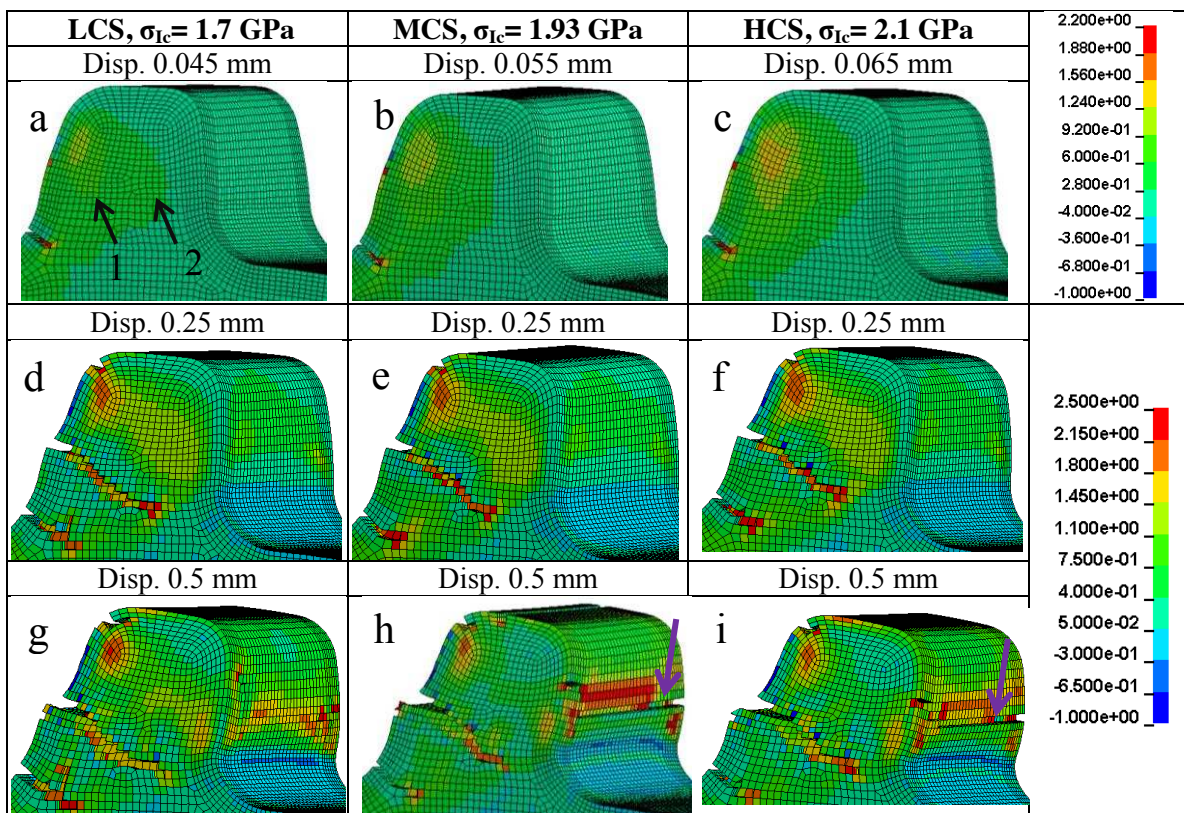


Fig.VI.32: Comparison of the fracture process of the three critical stresses at different displacements for the LE. The color map is for σ_I , scale is on the right.

For (a, b, c) displacements are different and corresponds to crack initiation.

For (d, e, f) displacement is 0.25 mm and for (g, h, i) displacement is 0.5 mm.

// Comparaison de l'état de la rupture pour les 3 contraintes critiques

à différents déplacements pour le LE. L'échelle de σ_I est sur la colonne de droite.

Pour (a, b, c) les déplacements sont différents et correspondent à l'amorçage de fissure.

Pour (d, e, f) le déplacement vaut 0.25 mm et pour (g, h, i) le déplacement vaut 0.5 mm.

The first crack (**Fig.VI.32** (a-b-c)) does not appear at the same displacement for the three cases: the higher the critical stress, the higher the displacement to crack initiation. Difference is only 0.02 mm between the cases. It can also be observed there is no crack on the opposite side of the contact with the tool for the LCS case (cracks are shown by a purple arrow on the two others cases, **Fig.VI.32** (h, i)). This means critical stress state has not been reached in this area.

Explanation is found on **Fig.VI.33**; pressure and σ_I are plotted on elements 1 (**Fig.VI.32** (a-b)) and 2 (**Fig.VI.32** (c-d)) shown in Fig.VI.32a. Those elements are in the CN layer, but at the interface with the core material. Exactly the same elements have been chosen on the three simulations in order to compare the fracture process. Elements 1 reach the critical value sooner than elements 2 because they are located closer to the side in contact with the tool. However, one can see element 1 for LCS (green curve without dots) is deleted at higher displacement than elements 1 for the simulation MCS and HCS. Thus, for LCS case, the interfacial elements can sustain the load longer and delay the propagation of the main shear crack.

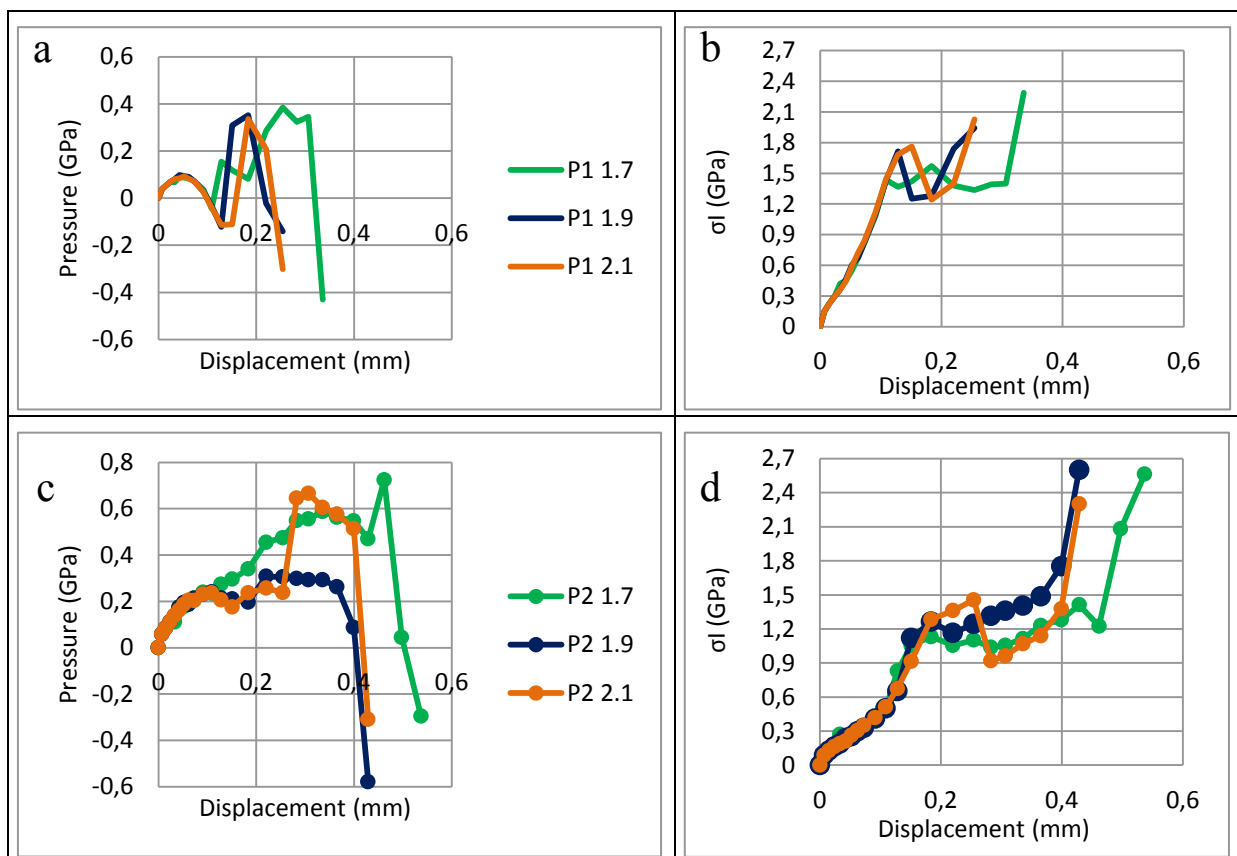


Fig.VI.33: Pressure and σ_I extracted on CN elements at the interface with the core material.

Location on the elements 1 and 2 is given on **Fig.VI.32** (a).

Green color stands for LCS, the blue one for MCS and the orange one for HCS.

Curves without dots are for element 1 and with dots are for element 2.

// Pression et σ_I extraits sur des éléments de la couche CN à l'interface avec le matériau de cœur.

L'emplacement de ces éléments donné sur la **Fig.VI.32** (a).

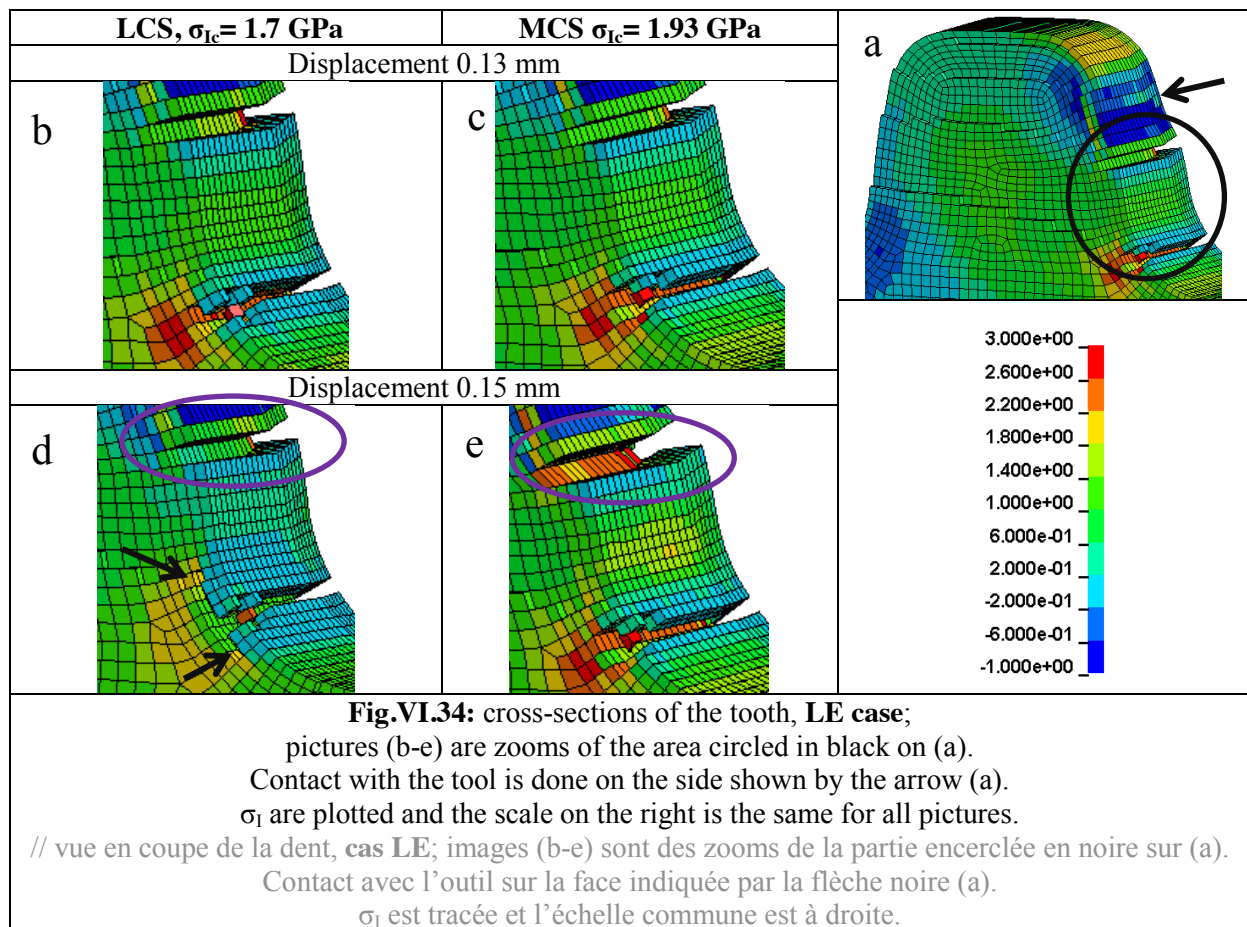
Les courbes vertes sont pour LCS, bleues pour MCS et orange pour HCS. Courbes sans points pour l'élément 1 et avec points pour l'élément 2.

The initial cause of this delay occurs at smaller displacement; it is the deletion of interfacial elements at the tooth root. This is being illustrated through cross-sections in **Fig.VI.34**, where configurations LCS and MCS are compared. The MCS and HCS cases are identical, thus the latter is not illustrated here.

The observed surfaces are located in the middle of the tooth. On **Fig.VI.34** (b-c), most of 2 rows of CN elements have been deleted to create the first crack. More elements have been deleted on (b) than on (c) because of the lower σ_{Ic} value. The key point can be seen on **Fig.VI.34** (d-e): on the former, CN interfacial elements have been deleted (they are located on the elements line between the two arrows on **Fig.VI.34** (d)) but not on the latter. This elements removal enables the upper part of the tooth to bend a bit more, thus stress level is lower in the core material at the location of the upcoming lethal crack (purple circled areas). Indeed, σ_I reaches 3 GPa on the case with no deletion (higher critical stress to failure), whereas it is lower than 2.2 GPa with deletion (lower critical stress to failure). It can be seen as well that core elements are more strained on the MCS case, and elements deletion has already started.

Therefore, higher critical stress (σ_{Ic}) in the CN layer tends to accelerate failure in the core material and consequently decreases displacement to fracture as shown in **Fig.VI.31**. However, based on the results obtained with the tensile tests and the 4PBT, nothing justifies this value of 1.7 GPa rather than any other one. This seems to be a consequence of the fact that the CN layer is modeled with a single material behavior, which tends to increase the properties mismatch between the CN layer and the core material and therefore facilitates failure of CN elements at the interface.

Further studies, should probably account for the progressive hardness decrease (vs. depth) in the CN layer to avoid such non-intuitive results.



VI. 4. 4. b Influence of mesh size

Another important point is the mesh size influence. In every FEM work, convergence with respect to mesh size – as well as time step – should be checked. In this work, after some preliminary tests, a single mesh size has been selected throughout the simulations, with quasi-cubic elements of 0.1 mm side.

Indeed, in chapter 5 the influence of the mesh size on the strain to fracture for tensile tests was studied for two mesh sizes: 0.1 and 0.25 mm. It was shown that EPS at fracture for both meshes was very close for T0 and TN specimens, but high differences were observed (up to 50 %) in the TG1 case, which is the configuration with the highest stress localization. It was thus concluded that decreasing the mesh size from 0.25 mm (initially used by Faurecia) to 0.1 mm was necessary.

In our study, the same mesh size was therefore used in tooth failure modeling and in constitutive parameter identification (butterfly tests, tensile tests).

In the following the influence of the mesh size is studied again on the semi-industrial test. This is interesting from an industrial point of view if Faurecia would like to achieve larger scale simulations (whole recliner, whole seat). **Fig.VI.35** illustrates this influence with force-displacement curves: blue is the experimental curve whereas red and purple are respectively the curves obtained with a 0.1 mm and 0.2 mm mesh size. One can see that the maximum load but most of all the displacement to fracture are deeply modified. **Fig.VI.36** investigates the reasons for these differences with the observation of the maximum principal stress (σ_1) **Fig.VI.36** (a-d) and the triaxiality **Fig.VI.36** (e-h).

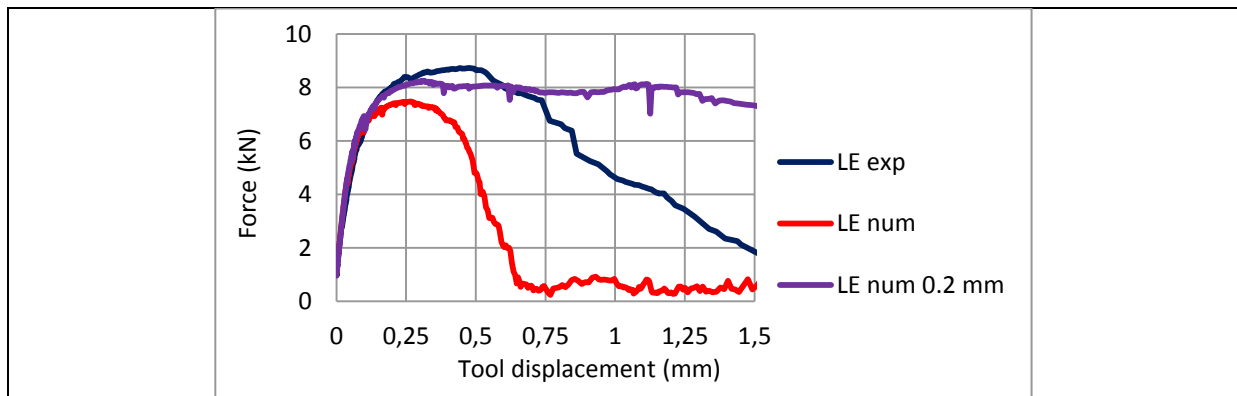


Fig.VI.35: Influence of the mesh size on the force-displacement curve for the **low engagement** case.

// Influence de la taille de maille sur la courbe force-déplacement - **faible engagement**.

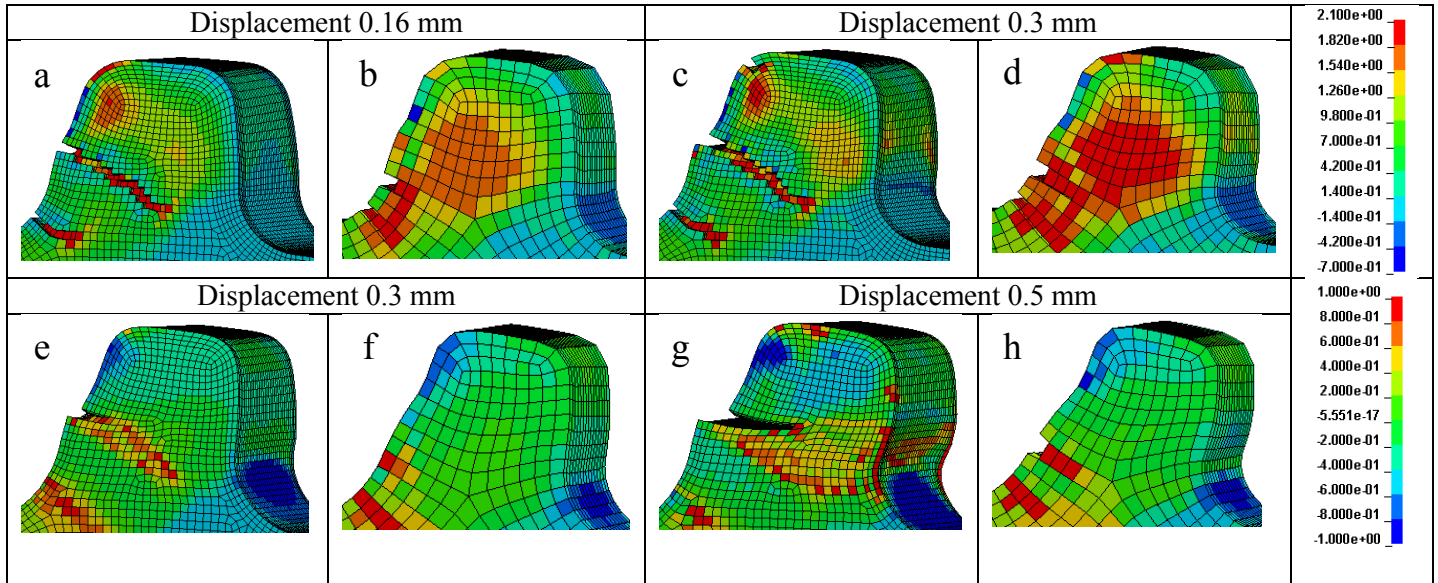


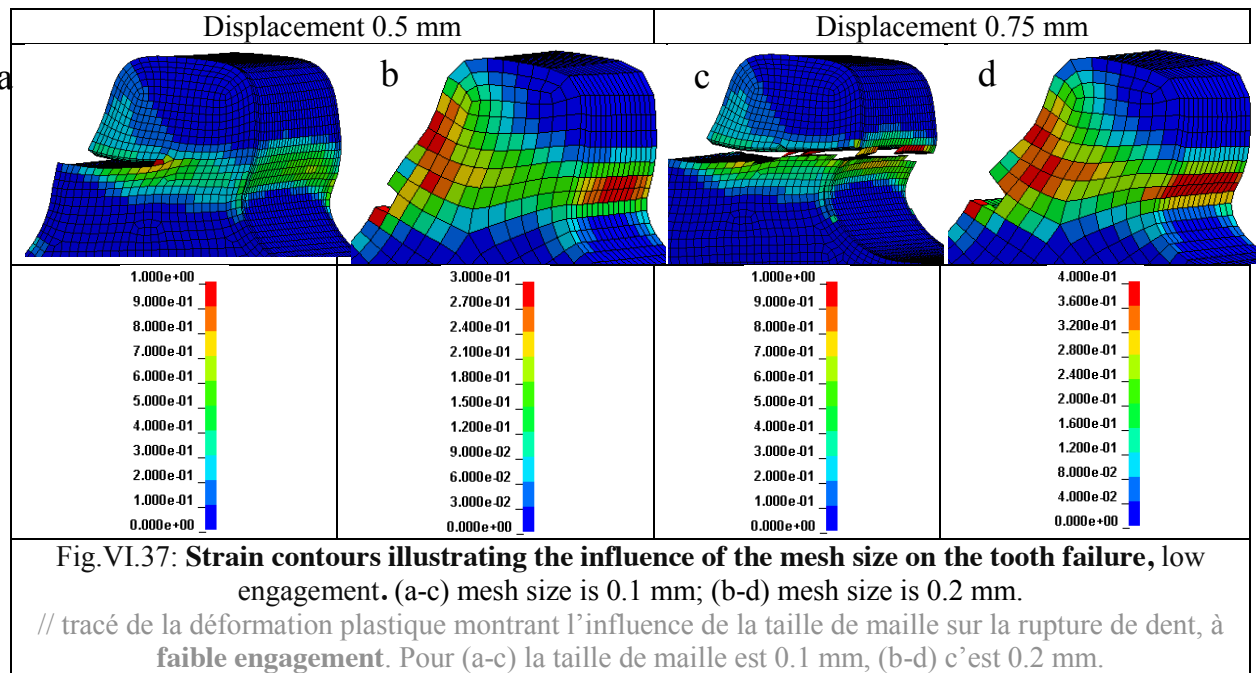
Fig.VI.36: Influence of the mesh size on the tooth fracture – **low engagement** case.

(a, b, c, d) compare σ_I (GPa) at 2 displacements (scale on the right). The CN layer has been peeled off **only on** the 4 following pictures: (e, f, g, h) compare the triaxiality on the core material (scale on the right). (a-c-e-g) mesh size is 0.1 mm; (b-d-f-h) mesh size is 0.2 mm.

// Influence de la taille de maille sur la rupture de dent, **faible engagement**.

(a, b, c, d) comparent σ_I (GPa) à 2 déplacements. La couche CN a été cachée **uniquement** sur les 4 photos: (e, f, g, h) comparent la triaxialité sur le matériau de cœur (échelle située à droite). Pour (a-c-e-g) la taille de maille est 0.1 mm, (b-d-f-h) c'est 0.2 mm.

First, it can be seen that crack paths are not the same. **Fig.VI.36** (a) shows two cracks, the first one at the tooth root and the second one at the edge of the contact surface with the tool. The second one is propagating at right angle to the contact surface with the tool. **Fig.VI.36** (b) (coarser mesh) shows the same first crack at the tooth root, but the second one is farther inside the contact surface with the tool. This influence on the fracture process is particularly clear in **Fig.VI.36** (g – h). **Fig.VI.37** shows the same with the strain; the coarser mesh underestimates propagation considerably. Whereas at 0.5 mm displacement, the highest level of EPS is 100% for the finer mesh (**Fig.VI.37** (a)), it is less than 30% (**Fig.VI.37** (b)) for the coarser mesh. This induces the propagation of the crack in the former, not in the latter. At 0.75 mm displacement, the tooth with the standard mesh size (0.1 mm) reaches complete failure (**Fig.VI.37** (c)) whereas only two rows of the coarser mesh elements have been deleted (**Fig.VI.37** (d)).



The issue of the mesh size in FEM simulation is well known and raises questions. When coupled damage models are used, non-local approaches need to be developed. In our case, there is no coupling between damage and material behavior. The differences observed are presumably due to stress calculation differences between the two meshes. In high stress gradient areas, bigger elements tend to smooth higher values compared to smaller elements. The failure criterion developed here is based on the integration of a stress-based function over the strain path. Underestimating stresses and strain in bigger elements thus induces lower values of damage. In addition, element erosion is activated once all integration points exceed the critical value. Therefore, in bigger elements some integration points may never reach the critical values and consequently prevent from element deletion.

Tooth failure is therefore much influenced by mesh size, partly due to its shear failure mode. Everything is concentrated within a 0.2 mm thick area; stress gradient is very high. The bigger mesh size cannot model accurately this stress distribution; this is why EPS is lower. Using another mesh size to model failure requires re-evaluating the fracture parameters. From an industrial point of view, it is thus recommended to use the same mesh size for models calibration and for the final application. It must be admitted however that modeling such complex failure mechanisms with gradient mechanical properties within the first hundreds of microns require the use of a fine mesh. In addition, due to the element-erosion technique, it must be noted that changing element size also influences the loss of volume (and presumably the stress field at crack tip) at each element deletion.

VI. 4. 4. c Simplified ductile fracture criterion – Lou & Huh criterion

In this section, the influence of the failure criterion used to predict ductile failure of the core material is studied. In Chapter 5, different criteria from the literature were analyzed. It was shown that Bai & Wierzbicki and Lou & Huh criteria were not adapted to predict failure on all ten mechanical testing specimens. This is why an original criterion was developed. It is however interesting to see the influence of the failure criterion and to quantify the differences on the final application.

Fig.VI.38 (a) illustrates this point for the low engagement configuration. Simulation with the simplified form of our exponential criterion (no Lode parameter taken into account) is added as well as with the Lou & Huh criterion (parameters identified in V.2.2 were used). The curves of the

exponential criteria with (red curve) and without (green curve) the Lode parameter are almost superimposable. For such an application, restricting experiments to tests giving Lode parameter close to 0 may be a way to reduce the calibration experimental campaign.

There is however a big difference with the Lou & Huh criterion, with which displacement to fracture corresponds to the experimental one. **Fig.VI.38** (b) compares the two fracture surfaces for $\bar{\theta} = 0$. For a triaxiality within [0.1; 0.5] the Lou and Huh criterion has a higher critical strain, the element is being deleted later. It explains the increase of displacement to fracture. Indeed, it was shown that a large part of the loading paths in the core material is done within this range. On the simulations with the FCN material, the use of the Lou and Huh criterion which overestimates the strain to fracture combined with the earlier failure of the CN elements makes a convincing result. However, the use of this Lou and Huh criterion to predict the failure of the CMO teeth would have overestimated the displacement to fracture by a larger amount.

Unfortunately, there is just the butterfly $+5^\circ$ in this range of triaxiality ($\eta = 0.25$ and $\bar{\theta} = 0.29$). The exponential criterion predicts accurately its fracture (error of 3 % on the final D value), whereas the Lou & Huh criterion was found less accurate for this test (error of -35% on the final D value). Other tests in this triaxiality range should be performed to improve the value of the parameters. The higher ductility allowed by the Lou & Huh criterion within the [0.1; 0.5] triaxiality range could be a way to mask the failure of the CN material happening too soon. The combination of the two errors gives the good displacement to fracture.

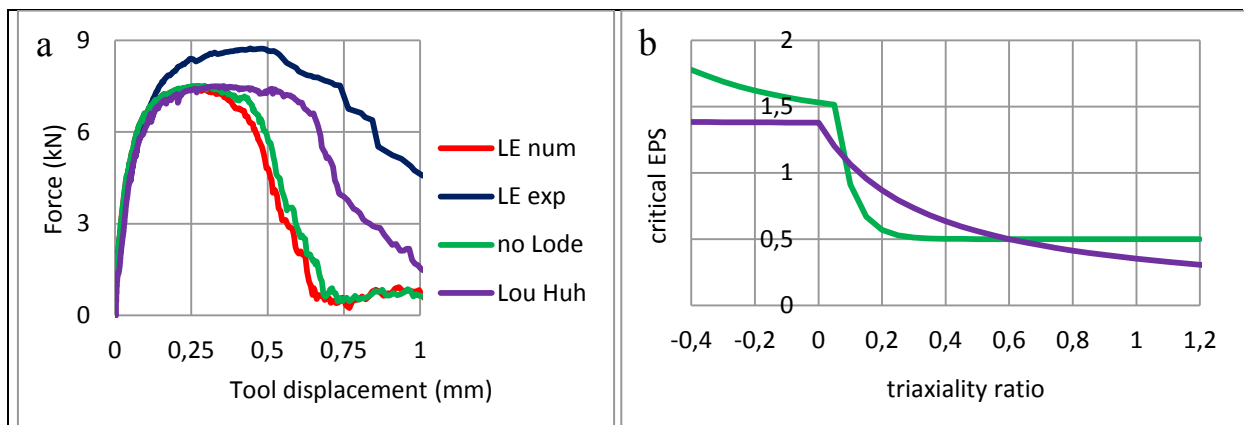


Fig.VI.38: (a) Influence of the core material fracture criterion on the tooth failure – **low engagement**.

Simulations are done with the simplified exponential criterion (green curve) and the Lou & Huh criterion (purple curve);

(b) critical strain to failure vs triaxiality η for $\bar{\theta} = 0$, the blue curve is the exponential criterion, the red one is the Lou & Huh criterion.

// (a) influence du critère de rupture du matériau de coeur sur la résistance de la dent, **faible engagement**.

Les simulations sont faites avec le critère exponentiel (courbe verte), et le critère de Lou & Huh (courbe violette) ;

(b) déformation critique tracée en fonction de la triaxialité η pour $\bar{\theta} = 0$, la courbe bleue correspond au critère exponentiel, la rouge à celui de Lou et Huh.

This raises another general question: can the materials fracture behavior be fitted by a single criterion and therefore a single mathematical formula? Even though there are parameters to be identified, they may not allow enough freedom to be used on all kind of materials. Solution could be to generate a surface fitting all the tests without using any analytical failure criterion. This approach has been done by [Basaran et al., 2010].

VI. 5 Conclusion

The semi-industrial tooth failure test is used to apply all the numerical models presented in previous chapters: the fracture criterion for the CN layer, the behavior law for the core material and its fracture criterion. A first step of the study was to apply those to the tooth with only the core material. Results are accurate; the difference on the max load between the experiment and the simulation does not exceed 8 %, which is convincing for such complicated system. However, the displacements to fracture are overestimated.

For the correlation with the complete CN material, discrepancy is higher and the simulations tend to underestimate the loads and the displacement to fracture. Furthermore, the experimental load increase between the CMO and the FCN teeth is not being modeled. However, a detailed study of the fracture process was provided and gave a better understanding of the fracture process thanks to local analysis of elements belonging to the crack path. Based on this study, it can be concluded that CN layer does not significantly participate to the global strength of the tooth but only improves the contact resistance to fatigue with higher surface hardness. In the meantime, the core material is sustaining the load and is the key part for the global tooth strength. Maximum loads sustained and displacements to fracture are due to the core material.

The comparison between the experimental and numerical tooth fracture shows some discrepancies, especially for the complete CN material, which can be explained through the following reasons:

- It was decided to model the CNed pinion with two materials: the CN layer and the core material, making an interface with brittle fracture on one side and ductile fracture on the other. The progressive decrease of hardness in the CN layer and transition zone is therefore not taken into account, which creates a significant mismatch in terms of material properties between the CN layer and the core material. As shown previously when microstructure and fracture surfaces were studied, there is no real interface but rather a transition layer in which the two kinds of failure modes are coexisting. It is important to model this area where mechanical properties are evolving. An intermediate proposition would be to create a third layer with intermediate plastic and fracture properties deduced from the core material.
- It was seen the CN elements were failing too soon and this induces two issues.
 - these elements being deleted, there is less material sustaining the load, and the maximum load is therefore underestimated.
 - the creation of areas with a high level of stress concentration deeper and thus triaxiality in the core material. This induces faster failure in the core material. A major perspective for future work is to find a way to delay the failure of the CN layer and especially its propagation deeper than 100 μm . One way would be the use of a third material to model the CN material; this third layer would be the intermediate layer. This third layer would decrease, by less than 0.1 mm, the thickness of the CN layer and the one of the core material. This would increase the section capable of undergoing the load, and would thus result in an increase of the maximum load and the displacement to fracture. It will furthermore better account for the gradient properties.
- For the core material, failure prediction is very accurate for tensile and butterfly tests, whereas it is overestimated for the CMO semi-industrial test and underestimated for the FCN

configuration. The delay in failure prediction for CMO configurations may come from the choice made regarding failure displacement of butterfly specimens. Due to the high scatter for these tests, it was decided to use the higher displacement to fracture because we assumed that lower values would probably come from machining-induced defects. Regarding FCN configurations, early failure may be a consequence of overestimated and fast failure of the CN elements.

- The element deletion technique used to propagate failure through the mesh is also questionable for such a complex failure process. In addition to a loss of volume, the deletion of an element modifies significantly the stress field. This creates a stress state which does not exist in the experiment where there is no material deletion but crack opening only. Numerically, new free surfaces are being created. Damage calculation based on this stress state must therefore be used carefully. In the future, it may be interesting to address such a failure process using cohesive zone elements.
- Accounting for the residual stresses in the simulation should delay the failure in the CN layer and the transition one since they are quite compressive inside.
- Numerical simulation of the friction / contact could explain part of the difference between the experiments and the simulations. Indeed, on the experiments, the CN treatment with a harder surface should decrease the friction coefficients compared to the CMO material. It is however difficult to say if a lower friction coefficient would tend to decrease or increase the load. For the numerical simulations, a unique friction coefficient of 0.17 is being used. A sensitivity analysis should be conducted in the future to study the influence of this parameter. Measurement of the resulting horizontal load would also be a good way of estimating this friction coefficient.

Despite these differences, the present methodology and the associated analyses are improving the way carbonitrided teeth failure is modeled at Faurecia. The discrepancies between numerical simulations and experimental observations were discussed regarding the different hypotheses used for the finite element model. The semi-industrial test also needs to be improved and simplified in order to get a better control and reproducibility of experimental CN teeth failure.

Chapter VII : Conclusion

This work aimed at studying and modeling the fracture behavior of carbonitrided steel parts. This project was achieved in collaboration with the car subsystem manufacturer Faurecia. The low carbon steel studied is used in seat recliners, a mechanism fixed to the seat and which keeps the backrest in position. Recliners have a safety role: in case of rear crash, passengers are thrown against the backrest. This creates an effort, rigorously a torque, which must be sustained by the recliner. The latter is composed of several parts, including two gears made out of carbonitrided steel: they are the parts sustaining the torque.

This work started with the study of recliners tested until complete failure. It showed material with heterogeneous fracture surfaces: intergranular on an external layer, indicating brittle failure and then surfaces with dimples, revealing ductile damage and fracture. This observation could be only qualitative since it was impossible to know the precise loading history of broken teeth. Therefore, there were needs to design a dedicated bench able of testing only one tooth at a time, where displacements and load could be controlled and recorded. This test bench should also allow observing progressive failure mechanism of the loaded tooth until fracture and for different engagement depths.

A literature review showed how brittle and ductile fractures should be modeled. The former is being modeled based on stress-based criteria and the latter on strain-based criteria – or rather, most of the time, an integral of a well-chosen stress function along the strain path. Indeed, since a brittle material does not undergo plastic strain, or a very little amount, it is more relevant to assume that a critical stress is the triggering event. It was decided to account for the first principal stress (brittle material fails in tensile mode) and for pressure in the prediction. This combination enabled a more complete description of the stress state in the material and rendered the fracture criterion more flexible. For the ductile core material, a fracture criterion in which the stress function integrated over the strain path depends on stress triaxiality ratio and Lode parameter was chosen.

Considering the industrial framework of this project, coupled damage models were not considered. These models present numerical issues requiring the use of non-local approaches and also require longer parameters identification procedures. In addition, uncoupled ductile fracture criteria such as the ones chosen here showed very good results for proportional loading conditions and seemed well-suited for this particular application. The other restriction coming from the industrial context was the numerical tool used to propagate failure within the mesh. LS Dyna is the software selected for the study for its good performance in structural dynamics. The only 3D failure modeling technique available in LS-DYNA is the element deletion technique. This is a numerically robust technique, but it is known to introduce severe mesh sensitivity and must therefore be used carefully. On the other hand, other techniques such as cohesive zone models (CZM), discrete crack propagation with remeshing or X-FEM are more accurate in terms of failure modeling but are not available in LS-Dyna for 3D solid elements to model failure with unknown crack paths.

The test bench designed during this work enabled to test a tooth until complete fracture; displacement field and load were recorded. It allowed in situ observations: fracture process can be observed as a function of the tool displacement and the load. In the very first 0.15 mm of displacement, a crack is opening at the tooth root. It stays within the CN layer and is stopped when approaching the core material, where toughness is higher. Then, as the load increases, another crack propagates in a direction parallel to the tool movement, going through the whole tooth and cutting it. This crack opens just below the contact surface with the tool. On some cases, a crack on the opposite side of the one in contact with the tool can be seen. Likely, it corresponds to the split between the two parts of the tooth, this crack does not propagate toward the tool. The bench is stiff by design, but considering the small displacements involved in tooth fracture, we suspected that spurious displacements could have

significant impact on results accuracy. Therefore, real displacements were assessed with 3D Digital Image Correlation. This showed there is an unwanted displacement of the tool away from the tooth, decreasing the engagement depth during the test and making the comparison between tests more difficult. Measurements with the micrometric screws have to be checked with DIC. This point should be improved in future experiments. The part on which the tool is fixed should be more massive to better handle the load and deform less. The engagement measurement could be improved also. However this test bench was successfully integrated to a tensile test machine and enabled to better understand the tooth fracture behavior. It is one of the main successes of this PhD project.

Next part was the measurement of the plastic behavior and fracture properties of the materials. Tests with proportional loadings were chosen to characterize quantitatively the fracture behavior of the CN material within a wide range of stress state. Butterfly specimens enabled to test the core material at low triaxiality, close to shear, the dominant tooth fracture mode as shown on the test bench. Grooved and notched tension tests completed the characterization at high triaxiality.

Tests were first carried out on heat-treated but non-carbonitrided material – assumed equivalent to the core material based on hardness tests. The tension tests showed excellent repeatability in terms of force-displacement curves as well as displacement to fracture. Regarding butterfly specimens, force-displacement curves showed good repeatability until failure but the displacement to fracture exhibited more scattering. The machining of these specimens is known as a tricky point. A similar sample preparation issue was met in the bending and tensile specimens used to assess the fracture properties of the CN layer. They were clipped from carbonitrided sheets in such a way that the specimens were slightly bent and twisted. When fixing the specimens into the jaws, they were first unbent before elongation started. Similarly, bending test specimens had an initial curvature, which makes the real bending strain difficult to control. Furthermore, the initial stress state in these materials was not accounted for in the simulations. As seen in Chapter 5, it may have a significant influence since it is a brittle material. As a consequence, fracture stresses identified with the bending specimen were found different from the ones identified with the tensile test, even though stress states were very similar (pure tension) according to the loading paths comparison. Nothing allows saying whether the parameters identified by the bending test are closer to reality than the ones assessed with the tensile test. As possible solutions, new sets of tests could be carried out with better machining (such as wire cutting) of specimens. In addition, a thorough analysis of initial residual stresses after carbonitriding should be conducted.

Fracture properties of the core material have been identified thanks to ten tests, 4 butterfly tests (3 for quasi-shear and 1 for tensile) and 6 tensile tests, together with their systematic numerical simulation. All the loading paths have been extracted using FEM simulation on the elements having the highest level of damage at the experimental displacement to fracture. This needs a two-step method, judged more reliable than extracting the loading path on the element with the highest level of plastic strain at the same displacement, which is the most common way of doing such identification. Indeed, failure will not systematically start where strain is highest.

Surprisingly, none of the criteria from the literature review did match the failure strains on the whole stress state range. Indeed, our material showed an uncommon Lode parameter dependency. It is very low for $\bar{\theta} = [0; 0.7]$ and then exponential. This is why a new criterion was defined. This criterion divides the stress triaxiality axis into three ranges. For each range, the triaxiality is accounted for through an exponential decreasing function. This criterion predicted very accurately the failure strain for all 10 tests.

As for the carbonitrided layer, a dual stress fracture criterion was used, including a critical first principal stress condition and a second condition including a critical hydrostatic pressure. As mentioned above, two tests, bending and tension, were used to identify these two parameters. Multiple cracks occurred in the brittle CN layer and the state of stress at first crack initiation was extracted from numerical simulations. The two tests gave rather different values, which may be attributed either to the imperfections of the clipped specimens, or to unknown residual stresses. An interesting but unexplained observation is that in spite of very similar stress states, cracks were stopped in the transition layer in bending even until large strain, whereas tension specimen broke quickly after CN cracks formed. Crack propagation in the core material forms an angle with the crack in the CN layer as seen in the literature. An additional analysis of cracks arrest in the transition zone and the influence of the microstructure and residuals stresses on brittle (CN layer) to ductile (core material) fracture transition should be interesting for future work.

The tooth failure modeling exploits all the mechanical properties obtained from previous calibration procedures: the fracture criterion for the CN layer, the behavior law for the core material and its fracture criterion.

The first step consisted in comparing with experiments on the tooth with only the core material. Results are accurate in terms of maximum load. The difference between the experiment and the simulation does not exceed 8 %, which is convincing for such complicated system. A systematic overestimation of the failure displacement was noted however. The scattering obtained with butterfly specimens, for which we chose to use the highest experimental displacement to fracture values, may be an explanation. More reliable shear test configurations should be studied in the future. It must be mentioned also that fracture is not always easy to detect experimentally as the load often decreases slowly after the peak, either smoothly or by steps. This can be attributed either to continued sliding and friction between the tool and the stump of the broken tooth, or to sometimes slow, sometimes jerky propagation of the killer crack.

In the comparison with the complete CN material, discrepancy is higher as the simulations tend to underestimate the loads as well as the fracture displacements. This disagreement can be explained by the following reasons:

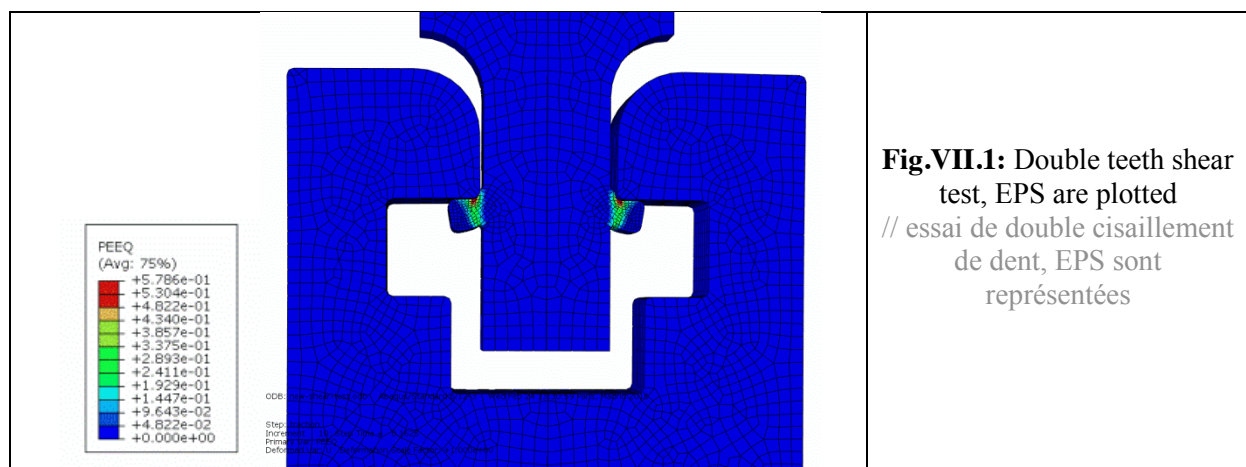
- One can wonder about the accuracy of the tooth failure test bench. There are spurious displacements of the tooth and the tool. Even though these displacements are quite small (lower than 1 mm), they cannot be neglected regarding the value of the displacement to fracture. Solution was found to use optical correction to assess the real displacement, but increasing the test bench stiffness should be envisaged. Furthermore, the mobile part of the bench was in translation thanks to a guide rail with bearings. After numerous tests, translation was not as smooth as at the beginning of its use, which can induce friction and disturb the measured force. However, this additional resistance was quite low (likely a few Newton) compared to the force sustained by the tooth
- Another point to be improved is the model of the CNed steel described here as a two-part material: the CN layer and the core material, building a sharp interface with brittle fracture on one side and ductile damage on the other side. In reality, there is no real interface but rather a transition area in which the two modes are coexisting. It can be important to model this area where parameters are evolving and where we have seen on occasion that brittle cracks could be stopped. An intermediate proposition would be to create a third layer with plastic and fracture properties assessed from the core material. With the hardness profile, the gradient of plastic yield can be quickly calculated to obtain a behavior law. The identification of the

failure criterion is trickier. Firstly, since the material in this area is rather ductile, failure criterion based on the EPS should be used. As for the yield stress, the hardness profile could be used as well. The CN layer is brittle and therefore undergoes a very little amount of plastic strain that could be approximated to 0. The core material withstands 100% plastic strain in tension. The hardness gradient could be used to guess the EPS to failure variations.

- Alternatively, a material state range equivalent to the transition layer could be obtained by performing the CN treatment with lower C content in the oven and slower quench. The parameters of the quench can be assessed with a simulation of the cooling gradient in the studied material. It is more difficult to quantify the Carbon content, even though it is directly linked to the hardness of the martensite grains. This analysis should be carried out with a microstructural study in parallel. It is indeed mandatory to establish a rigorous link between the mechanical properties and the microstructure.

This study could be done in a purely numerical way as well. A sensitivity study on the material and fracture criterion parameters on this intermediate layer can be done. It could be based on the complete CNed components studied in this project with for instance tensile tests.

- Two other points related to the material knowledge are the residual stresses and the behavior of the CN layer in shear stress state. The literature overview showed residual stresses are supposed to be strongly compressive in the CN layer (-800 MPa) and slightly tensile in the core material (+20MPa). It is mandatory to perform this measurement on the steel to have a real idea of such stresses. Indeed, they play an important role in cracks initiation and propagation so their measurement matters. Furthermore, it may help quantifying the suspected difference of the core material obtained in the complete CN material or with only the CMO. For the second point, the CN layer is submitted to shear stress state on the tooth and it should be a good idea to perform a test where everything is controlled according to this stress state. Debonding between the CN layer and the core material could therefore be quantified and would bring more accuracy to the tooth failure prediction. For instance, a symmetrized test which would submit two teeth at the same time to shear stress as on **Fig.VII.1**. The teeth geometry would be different from the ones on the pinions, but the test aims to study the CN layer debonding from the core material. This test would be set up on a tensile test bench and would allow easily camera recording. The robust and easy design would remove the issue of spurious displacements encountered with the semi-industrial test bench.



- The parameters of the CN layer fracture criterion are imprecise as shown by the unexpected difference between bending and tensile tests. This may be due to specimens with unknown initial stress state and imperfect geometry. It is mandatory to perform once again those two tests with improved specimen preparation, all the more as simulations with different critical stresses showed high sensitivity. Lower σ_{lc} increased considerably the displacement to fracture to the point where it did fit the experimental one; whether this is the result of error compensation or a fundamental result needs to be confirmed. A stochastically approach, such as the Weibull model, to model the failure of the CN layer could be study to check if it brings more efficient prediction
- The last topic is the numerical tools used in this work. Because it is an industrial project, we could not use the state of the art tools or extremely fine meshes because they are too time consuming. (1) There is no coupling between damage growth and the material behavior law; coupling plastic behavior with damage might better represent the damaged material behavior and in particular the softening phase leading to final fracture. Such coupling would however come with numerical issues related to damage localization. (2) The numerical technique for failure propagation through the elements could be improved as well. The kill-element technique is certainly robust, but has several drawbacks regarding the accuracy of the failure process: in addition to a numerical loss of volume which depends on elements size, the deletion of complete elements changes significantly stress distribution at crack tips and thus influences a lot damage calculation and subsequent fracture. Using a finer mesh with CZM or discrete crack propagation with automatic remeshing would undoubtedly improve the stress state assessment at cracks tip, compared to stress states obtained after element deletion with 0.1mm size elements. Using the CZM technic will enable to account for the fracture energy (G_f) and should for instance delay the crack propagation in the CN layer and in the transition area.

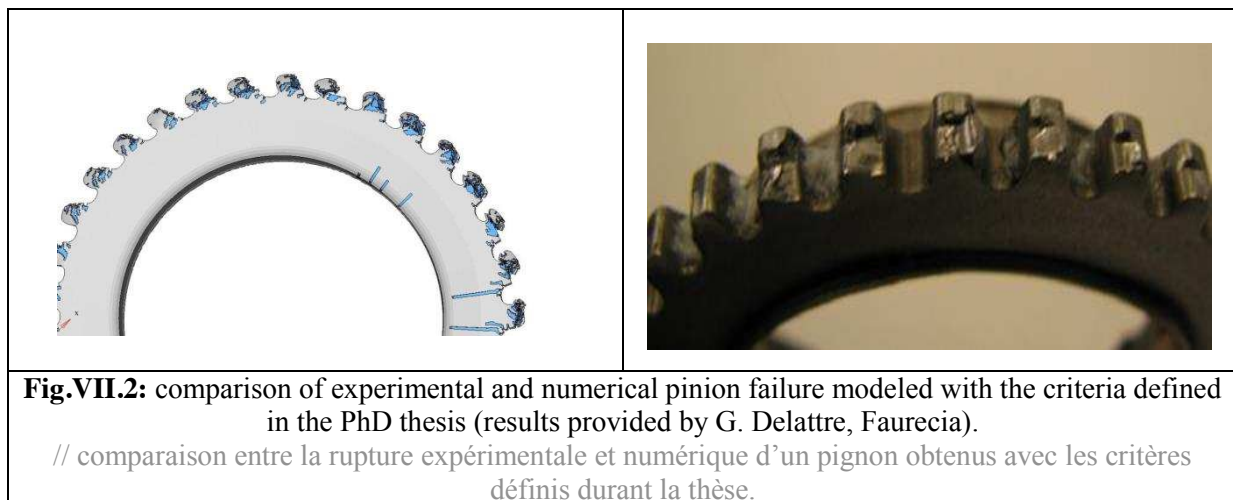
The tooth failure comparison with or without CN layer shows the latter increase a bit the tooth strength. Unfortunately, this was not predicted with the model. This can be justified by the reasons written above and more especially by the simplified two-part model considered to account for the CN material. Indeed, the elements of the CN layer were deleted quite early in the simulation decreasing the material volume capable of sustaining the load. Adding a third material in the simulation to account for the transition area should improve this particular point. For instance, the CN layer thickness could be decreased by 60 μm to have a transition layer thickness of 60 μm inducing a higher volume of ductile material. Using a real crack propagation technique instead of the kill-element technique would improve these results as well.

To sum up, should this work be started from scratch now, on the one hand, the “semi-industrial test” would be designed more rigid and simple for a less ambiguous interpretation; lower engagement depths would be studied as some of the teeth of the recliner display “scalping” of the CN layer on the top – shear in the transition layer or between the transition and the CN layer. On the other hand, experimental efforts would be spent on the **characterization of the transition layer**, mostly in terms of toughness as hardness gives us a clear idea of the plastic properties gradient.

Turning to the numerical work, modeling the transition layer once characterized and adding the residual stress pattern, approximate as it may be, would definitely **improve the physics of the model**. The **crack propagation modeling** would be the other major point. Certainly CZM, discrete crack propagation or XFEM are much more powerful methods, and indeed the former is being developed in LS Dyna now. But software proposing these methods could have been used, such as Abaqus, not as substitutes, but as complements to check conclusions. It was also a matter of time.

The additional work detailed above can now be carried out to improve the modeling of carbonitrided pinion teeth failure. It is made necessary by the extreme complexity of modeling failure of such a graded material with a relatively simple finite element approach. However, the work which has been done represents a real step forward in the understanding of carbonitrided steel components failure thanks to:

- A thorough image analysis of failed recliners explaining the failure mechanisms occurring in several consecutive teeth;
- The design of a completely new controlled test bench offering the possibility of observing in situ carbonitrided tooth failure during loading for different loading conditions;
- The definition of a new ductile failure criterion adapted to 20MnB5 steel grade;
- An extensive experimental campaign for ductile failure criteria calibration together with a reduced set of experiments for simplified industrial calibration procedure;
- An objective analysis of LS-Dyna capabilities (strengths and weaknesses) in terms of modeling failure of carbonitrided steel recliners with the kill-element technique.
- The modeling of multiple teeth failure, which should be useful to Faurecia design department since there was no failure modeled before. Operator was declaring failure as a function of the equivalent plastic strain level on a whole section. On a complete recliner with 33 teeth, load can be sustained even though failure is reached on one tooth. This study can be done with the failure criteria assessed during this project (see **Fig.VII.2**).



Bibliography

- Achouri, M., Germain, G., Dal Santo, P., Saidane, D., (2013). Experimental characterization and numerical modeling of micromechanical damage under different stress states. *Materials & Design*, 50, 207–222.
- Argon, A. S., Im, J., Safoglu, R. (1975). Cavity Formation from Inclusions in Ductile Fracture, *Metallurgical Transactions A*, 6A, 825-837.
- Bahr, H., Balke, H., Fett, T., Hofinger, I., Kirchhoff, G., Munz, D., Neubrand, A., Semenov, A.S., Weiss, H.-J., Yang, Y.Y. (2003). Cracks in functionally graded materials. *Materials Science and Engineering, A*, 362(1-2), 2–16.
- Bai, Y., Wierzbicki, T. (2008). A new model of metal plasticity and fracture with pressure and Lode dependence. *International Journal of Plasticity*, 24(6), 1071–1096.
- Bai, Y., Wierzbicki, T. (2010). Application of extended Mohr–Coulomb criterion to ductile fracture. *International Journal of Fracture*, 161(1), 1–20.
- Bao, Y., Wierzbicki, T. (2004). On fracture locus in the equivalent strain and stress triaxiality space. *International Journal of Mechanical Sciences*, 46(1), 81–98.
- Bao, Y., Wierzbicki, T. (2005). On the cut-off value of negative triaxiality for fracture. *Engineering Fracture Mechanics*, 72(7), 1049–1069.
- Barralis, J., Castex, L., Maeder, G. (1999). Précontraintes et traitements superficiels. *Techniques de l'Ingénieur, Traité Matériaux métalliques*, M1180, 1–50.
- Barsoum, I., Faleskog, J. (2007). Rupture mechanisms in combined tension and shear—Experiments. *International Journal of Solids and Structures*, 44(6), 1768–1786.
- Basaran, M., Wölckerling, S. D., Feucht, M., Neukamm, F., Weichert, D. (2010). An Extension of the GISSMO Damage Model Based on Lode Angle Dependence. In *LS-DYNA Anwenderforum*
- Beremin, F. M. (1983). A Local Criterion for Cleavage Fracture of a Nuclear Pressure Vessel Steel, *Metallurgical Transactions*, 14 A, 2277–2287.
- Besson, J., Berdin, C., Bugat, S., Desmorat, R., Feyel, F., Forest, S., Lorentz, E., Maire, E., Pardoën, T., Pineau, A., Tanguy, B. (2004). *Local Approach to Fracture*, Presses des Mines, edited by J. Besson.
- Bouchard, P.-O., Bay, F., Chastel, Y. (2003). Numerical modelling of crack propagation: automatic remeshing and comparison of different criteria. *Computer Methods in Applied Mechanics and Engineering*, 192(35-36), 3887–3908.
- Bouchard, P.-O., Bourgeon, L., Fayolle, S., Mocellin, K. (2010). An enhanced Lemaitre model formulation for materials processing damage computation. *International Journal of Material Forming*, 4(3), 299–315.
- Bousquet, A., Marie, S., Bompard, P. (2012). Propagation and arrest of cleavage cracks in a nuclear pressure vessel steel. *Computational Materials Science*, 64, 17–21.

- Bridgman, P.W. (1952). *Studies in large plastic flow and fracture*, Harvard University press, Cambridge, Massachusetts.
- Brown, S.B., Kim, K.H., Anand, L. (1989). An internal variable constitutive model for hot working of metals. *International Journal of Plasticity*, 5, 95–130.
- Brünig, M., Brenner, D., Gerke, S. (2015). Stress state dependence of ductile damage and fracture behavior: Experiments and numerical simulations. *Engineering Fracture Mechanics*, 141, 152–169.
- Cao. (2013). *Modeling ductile damage for complex loading paths*, PhD thesis, Mines ParisTech.
- Cao. (2014). Numerical simulation of 3D ductile cracks formation using recent improved Lode-dependent plasticity and damage models combined with remeshing. *International Journal of Solids and Structures*, 51(13), 2370–2381.
- Cao, T. S., Bouchard, P.-O., (2016). Modélisation de l' endommagement ductile en mise en forme des métaux, *Les techniques de l'ingénieur*, M3033, 1-33.
- Cao, T.-S., Gachet, J.M., Montmitonnet, P., Bouchard, P.-O. (2014). A Lode-dependent enhanced Lemaitre model for ductile fracture prediction at low stress triaxiality. *Engineering Fracture Mechanics*, 124-125, 80–96.
- Cao, T.-S., Gaillac, A., Montmitonnet, P., Bouchard, P.-O. (2013). Identification methodology and comparison of phenomenological ductile damage models via hybrid numerical–experimental analysis of fracture experiments conducted on a zirconium alloy. *International Journal of Solids and Structures*, 50(24), 3984–3999.
- Chaboche, J.L. (1984). Anisotropic creep damage in the framework of continuum damage mechanics, *Nuclear Engineering and Design*, 79, 309–319.
- Denitru, M.J. (2007). Comportement mécanique et endommagement d' un materiau carbonitruré, *Master thesis, Université d'Orléans*.
- El khaoulani, R., Bouchard, P.O. (2012). An anisotropic mesh adaptation strategy for damage and failure in ductile materials. *Finite Elements in Analysis and Design*, 59, 1–10.
- Feld-Payet, S., Chiaruttini, V., Feyel, F. (2013). A crack insertion strategy based on a gradient type criterion and local remeshing, *Proceedings of the Third International conference on computational modeling of Fracture and failure of materials and structure*
- Firrao, D., Ugues, D. (2005). Fracture of nitrided and nitrocarburized blunt notch three-point bending die steel specimens. *Materials Science and Engineering: A*, 409(1-2), 309–316.
- Gachet, J. M. (2013). *Intégration de la phase de mise en forme dans le dimensionnement de flasques de sièges automobile*, PhD thesis, Mines Paristech.
- Galerie, A., Baillet, F., Michel, H., Belmonte, T. (2002). *Traitements de surfaces en phase vapeur, Mécanique et Ingénierie des Matériaux*, Hermes Sciences Publications, Lavoisier.
- Ghiglione, D., Leroux, C., Tournier, C. (1994). Cémentation. Carbonituration. *Techniques de l'Ingénieur*, M1226.

- Ghosh, A.K.. (1976). A Criterion for Ductile Fracture in Sheets Under Biaxial Loading, *Metallurgical Transaction*, 7A, 523-533.
- Griffith, A. A. (1921). The phenomena of rupture and flow in solids. *Philosophical Transactions of the Royal Society of London*, 221, 163–198.
- Gruben, G., Hopperstad, O.S., Borvik, T. (2012). Evaluation of uncoupled ductile fracture criteria for the dual-phase steel Docol 600DL. *International Journal of Mechanical Sciences*, 62(1), 133–146.
- Gurson, A.L. (1977). Continuum Theory of Ductile Rupture by void nucleation and growth: Part I- yield criteria and flow rules for porous ductile media, *Journal of Engineering Materials and Technology*, 99(1), 2-15..
- Hahn G.T., Averbach, B.L., Owen, W.S., Cohen, M. (1959). Initiation of cleavage microcracks in polycrystalline iron and steel. *The MIT press*, 91–116.
- Hencky. (1924). Zur theorie plastischer deformationen und der hierdurch im material hervorgerufenen Nebenspannungen. In *Proceedings of the first international congress on Applied Mechanics*, 204-218.
- Henry, J., Vincent, L., Averty, X., Marini, B., Jung, P. (2006). Bending tests on T91 samples implanted with 0.25at.% helium: Experiments and mechanical analysis. *Journal of Nuclear Materials*, 356(1-3), 78–87.
- Hollomon, J.H. (1945). Tensile deformation. *American Institute of Mining and Metallurgical Engineers*, 162, 268–290.
- Holm, T. (2006). *Linde Gas: Carburizing and Carbonitriding Preface, Furnace Atmospheres 1, Linde Gas Division, Germany*.
- Johnson, G.R., Cook, W.H. (1985). Fracture characteristics of three metals subjected to various strains , strain rates , temperatures and pressures. *Engineering Fracture Mechanics*, 21(1), 31–48.
- Kanchanomai, C., Limtrakarn, W. (2008). Effect of Residual Stress on Fatigue Failure of Carbonitrided Low-Carbon Steel. *Journal of Materials Engineering and Performance*, 17(6), 879–887.
- Krauss, G. (2001). Deformation and Fracture in Martensitic Carbon Steels Tempered at Low Temperatures, *Metallurgical and Materials Transactions*, 32(B), 205-221.
- Lemaitre, J. (1986). Local approach of fracture, *Engineering Fracture Mechanics*, 25(5b), 523-537.
- Lemaitre, J., Desmorat, R., (2005). *Engineering damage mechanics: Ductile, Creep, Fatigue and Brittle failures*, Springer, Berlin. ISBN 978-3-540-21503-5.
- Leroux, C. (2012). Cémentation par le carbone et carbonituration - Procédés, *Techniques de l'Ingénieur*, 33(M1225), 1–27.
- Lou, Y., Huh, H., Lim, S., Pack, K. (2012). New ductile fracture criterion for prediction of fracture forming limit diagrams of sheet metals. *International Journal of Solids and Structures*, 49(25), 3605–3615.

- Malaplate, J., Vincent, L., Averty, X., Henry, J., Marini, B. (2008). Characterization of He embrittlement of a 9Cr–1Mo steel using local approach of brittle fracture. *Engineering Fracture Mechanics*, 75(11), 3570–3580.
- McClintock, F.A. (1968). A criterion for ductile fracture by the growth of holes. *ASME Journal of Applied Mechanics*, 35, 363–371.
- Mediavilla, J., Peerlings, R. H. J., Geers, M. G. D. (2006). Discrete crack modelling of ductile fracture driven by non-local softening plasticity. *International Journal for Numerical Methods in Engineering*, 66(4), 661–688.
- Mises, R.V. (1913). Mechanics of solid bodies in the plastically-deformable state. *Mathematics Physics*, 4, 582–592.
- Moes, N., Dolbow, J., Belytschko, T. (1999). A finite element method for crack growth without remeshing. *International Journal for Numerical Methods in Engineering*, 46, 131–150.
- Moinereau, D., Dahl, A., Masson, R., Gilles, P., Chapuliot, S., Yuritzinn, T. (2006). The effect of warm prestress in RPV assessment: some experimental results and their interpretation by local approach to fracture, Local approach to fracture, *conference proceedings 9th european mechanics of materials conference*, (pp. 51–56).
- Moussa, C. (2012). *Caractérisation mécanique par indentation instrumentée d ' aciers carbonitrurés : aspects numériques et expérimentaux*, PhD thesis, Université de Rennes.
- Moussa, C., Bartier, O., Mauvoisin, G., Pilvin, P., Delattre, G. (2011). Characterization of homogenous and plastically graded materials with spherical indentation and inverse analysis. *Journal of Materials Research Society*, 27(01), 20–27.
- Murry, G. (2012). Transformations dans les aciers. *Techniques de l'Ingénieur*, 33(m1115).
- Nahshon, K., Hutchinson, J. W. (2008). Modification of the Gurson Model for shear failure. *European Journal of Mechanics - A/Solids*, 27(1), 1–17.
- Nakoneczny, A. (2006). Fatigue fracture of nitrided and carbonitrided layers, *Journal of theoretical and applied mechanics*, 44(3) 713–730.
- Needleman, A., Tvergaard, V. (1984). An analysis of ductile rupture in notched bars. *Journal of the Mechanics and Physics of Solids*, 32(6), 461–490.
- Papasidero, J., Doquet, V., Mohr, D. (2013). Determination of the Effect of Stress State on the Onset of Ductile Fracture Through Tension-Torsion Experiments. *Experimental Mechanics*, 54(2), 137–151.
- Papasidero, J. (2014). *Étude expérimentale et numérique de la rupture ductile sous chargement multiaxial*, PhD thesis, Ecole Polytechnique Paris.
- Papasidero, J., Doquet, V., Lepeer, S. (2014). Multiscale investigation of ductile fracture mechanisms and strain localization under shear loading in 2024-T351 aluminum alloy and 36NiCrMo16 steel. *Materials Science and Engineering*, 610(A), 203–219.
- Picqué, M. B. (2004). *Experimental study and numerical simulation of iron oxide scales mechanical behavior in hot rolling*, PhD thesis, Mines ParisTech.

- Rice, J. R., Tracey, D. M. (1969). On the ductile enlargement stress of voids in triaxial stress fields, *Journal of the Mechanics and Physics of Solids*, 17, 201–217.
- Ritchie, R. O., Knott, Rice, J. R. (1973). On the relationship between critical tensile stress and fracture toughness in mild steel, *Journal of the Mechanics and Physics of Solids*, 21, 395–410.
- Roth. (2015). *Experimental and Numerical Investigation of Ductile Fracture Initiation at Low , Intermediate and High Strain Rates*, PhD thesis, Ecole Polytechnique.
- Roux, E. (2011). *Assemblage mécanique : stratégies d'optimisation des procédés et d'identification des comportements mécaniques des matériaux*, PhD thesis, Mines ParisTech.
- Shouler, D. R., Allwood, J. M. (2010). Design and use of a novel sample design for formability testing in pure shear. *Journal of Materials Processing Technology*, 210, 1304–1313.
- Siegele, D., Friedmann, V., Hohe, J. (2006). Investigation on damage evolution and cleavage based on combined experimental and numerical methods, Local approach to fracture, *conference proceedings 9th european mechanics of materials conference*, 27-32.
- Swift, H.W. (1952). Plastic instability under plane stress. *Journal of the Mechanics and Physics of Solids*, 1, 1–18.
- Tohgo, K., Hadano, A. (2006). Characterization of Fracture Process in Ceramic-Metal Functionally Graded Material under Three-Point-Bending, *JSME International Journal*, 49(3), 321–330.
- Tsuchiyama, T., Fujii, Y., Terazawa, Y., Nakashima, K., Ando, T., Takaki, S. (2008). Factors Inducing Intergranular Fracture in Nickel-free High Nitrogen Austenitic Stainless Steel Produced by Solution, *ISIJ International*, 48(6), 861–867.
- Tvergaard, V. (1981). Influence of voids on shear band instabilities under plane strain conditions, *International Journal of Fracture*, 17(4), 389–407.
- Tvergaard, V., Needleman, A. (1984). Analysis of the cup-cone fracture in a round tensile bar. *Acta Metallurgica*, 32(1), 157–169.
- Voce, E. (1955). A practical strain hardening function. *Metallurgica*, 51, 219–226.
- Wang, K., Greve, L., Wierzbicki, T. (2015). FE simulation of edge fracture considering pre-damage from blanking process. *International Journal of Solids and Structures*, 71, 206–218.
- Wang, K., Wierzbicki, T. (2015). Experimental and numerical study on the plane-strain blanking process on an AHSS sheet. *International Journal of Fracture*, 194(1), 19–36.
- Wang, Z., Nakamura, T. (2004). Simulations of crack propagation in elastic–plastic graded materials. *Mechanics of Materials*, 36(7), 601–622.
- Weck, A., Wilkinson, D. S. (2008). Experimental investigation of void coalescence in metallic sheets containing laser drilled holes. *Acta Materialia*, 56, 1774–1784.
- Xue, L. (2007). *Ductile Fracture Modeling - Theory , Experimental Investigation and Numerical Verification*, PhD thesis, Massachusetts Institute of Technology.

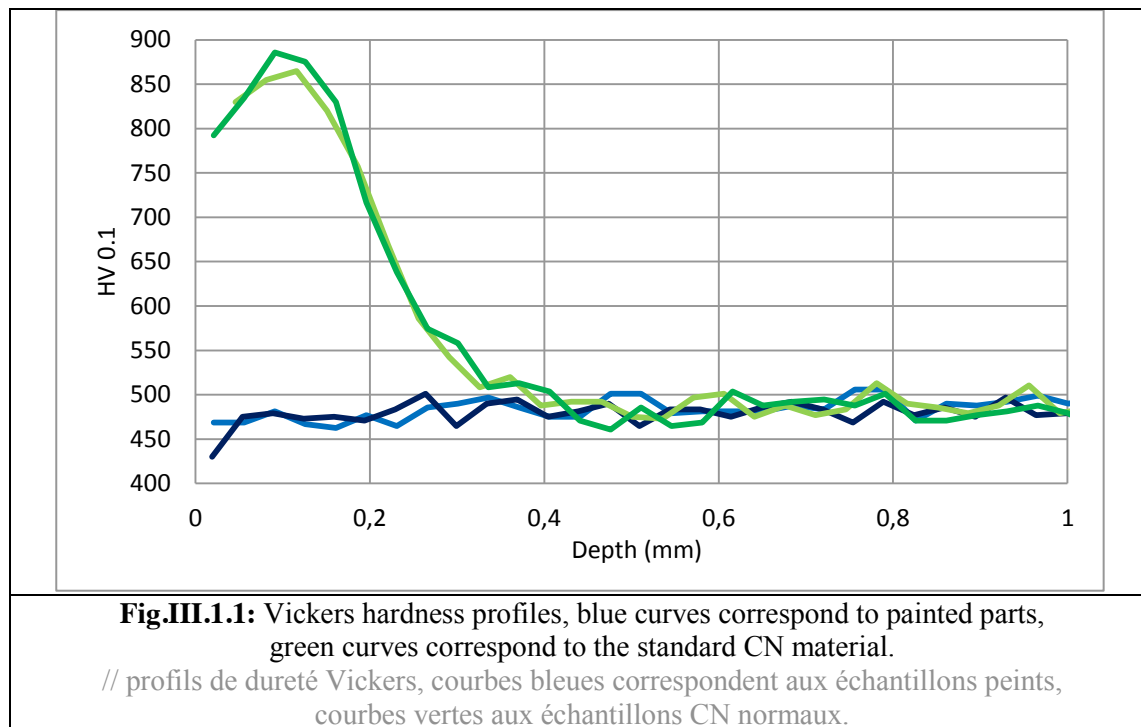
- Yahia, M. (1995). *Contribution à l'étude de l'influence de l'azote dans les traitement thermochimiques de surface des aciers en phase austénitique*, PhD thesis. INPL.
- Yin, Q., Soyarslan, C. Isik, K., Tekkaya, A.E.. (2015). A grooved in-plane torsion test for the investigation of shear fracture in sheet materials. *International Journal of Solids and Structures*, 66, 121–132.
- Zhang, Z.J., Paulino, G. H. (2005). Cohesive zone modeling of dynamic failure in homogeneous and functionally graded materials. *International Journal of Plasticity*, 21(6), 1195–1254.

Appendix.III.1: obtaining CMO with CarboStop paint

Obtaining bulk material with only the core material is a key point for this work. Below are presented three solutions with advantages and drawbacks:

- 1- Grinding the CN layer can be possible on the tensile tests but not on teeth. Testing teeth with only the core material is mandatory to better understand the fracture process.
- 2- Parts can be treated in another oven than the one used by Faurecia for the CN treatment. However, this method could bring variability on the temperature fields submitted to the parts and could therefore lead to different core material obtained in the two treatment lines. This is why this idea was abandoned.
- 3- The third possibility is to apply a specific paint, which prevents the diffusion of carbon and nitrogen in the material. Thus, the part will be submitted to only a thermal treatment even though the atmosphere is rich in carbon and nitrogen atoms. So, all the specimens will be treated at the same time and with the same thermal loading history, which should result in a microstructure as close as possible to the treated core material.

To check the core material obtained in the two ways are the same, hardness profiles are performed. **Fig.III.1.1** plots the hardness variation for four specimens: two classical carbonitrided specimens and two with the paint applied on them. One notices deeper than 0.4 mm, the hardnesses are identical and equal to 475 HV average.



So deeper than 0.4 mm, materials are identical. Toward the surface, the hardness is increasing for the CN material and is rather constant for the painted specimens. Consequently, it is fair to assume that

the specimens obtained with anti-carbonitriding paint are made of the core material only. Further studies involving microstructure analyses could be carried out in the future to confirm this assumption.

Appendix IV.1: Butterfly measurements and experimental force displacement curves

This annex shows the measurements of the butterfly specimen and the raw force-displacement curves.

butterfly ID	2	3	6	7	5	8	10
Loading conditions	-10	-10	-10	-10	Shear	Shear	Shear
shoulder thickness (mm)	3.016	3.029	3.03	2.97	2.98	3.02	3.02
relative error, % ((thickness-3)/3)	0.5	1.0	1.0	-1.0	-0.7	0.7	0.7
gage thickness (mm)	1.15	1.15	1.15	1.17	1.16	1.14	1.14
relative error, % ((gage-1.15)/1.15)	0	0	0	1.7	0.9	-0.9	-0.9

Table.IV.1. 1: butterfly specimen measurements, specimens tested in shear and compression and pure shear
 // dimensions des éprouvettes butterfly, échantillons testés en cisaillement et compression et cisaillement pur

butterfly ID	13	14	18	22	9	16	19	21
Loading conditions	5	5	5	5	Tensile	Tensile	Tensile	Tensile
shoulder thickness (mm)	3.025	3.018	3	3.026	3.02	3.023	3	3.026
relative error, % ((thickness-3)/3)	0.8	0.6	0.0	0.9	0.7	0.8	0.0	0.9
gage thickness (mm)	1.17	1.16	1.16	1.16	1.14	1.15	1.15	1.16
relative error, % ((gage-1.15)/1.15)	1.7	0.9	0.9	0.9	-0.9	0.0	0.0	0.9

Table.IV.1.2: butterfly specimen measurements, specimen tested in shear and tension and pure tension
 // dimensions des éprouvettes butterfly, échantillons testés en cisaillement et traction et traction pure

Table.IV.1. 1 and Table.IV.1.2 show the measurement of the butterfly specimen and the calculated relative error. **Fig.IV.1.1** (a) and (b) show the methodology applied to measure the specimen: (a) shows the shoulder thickness measurement, (b) shows the gage thickness measurement. One must keep in mind the last measurement is quite tricky since it is not a flat surface but a double curvature one. Anyway, repeatability was done while measuring and was accurate. One can see the machining is quite good though, with relative errors mostly lower than 1%. It is however difficult to account for the eventual surface roughness discussed in Chapter 4 with this tool. An optical roughness measurement device would have been required. This work was done at MIT and the equipment was not available in the same lab.

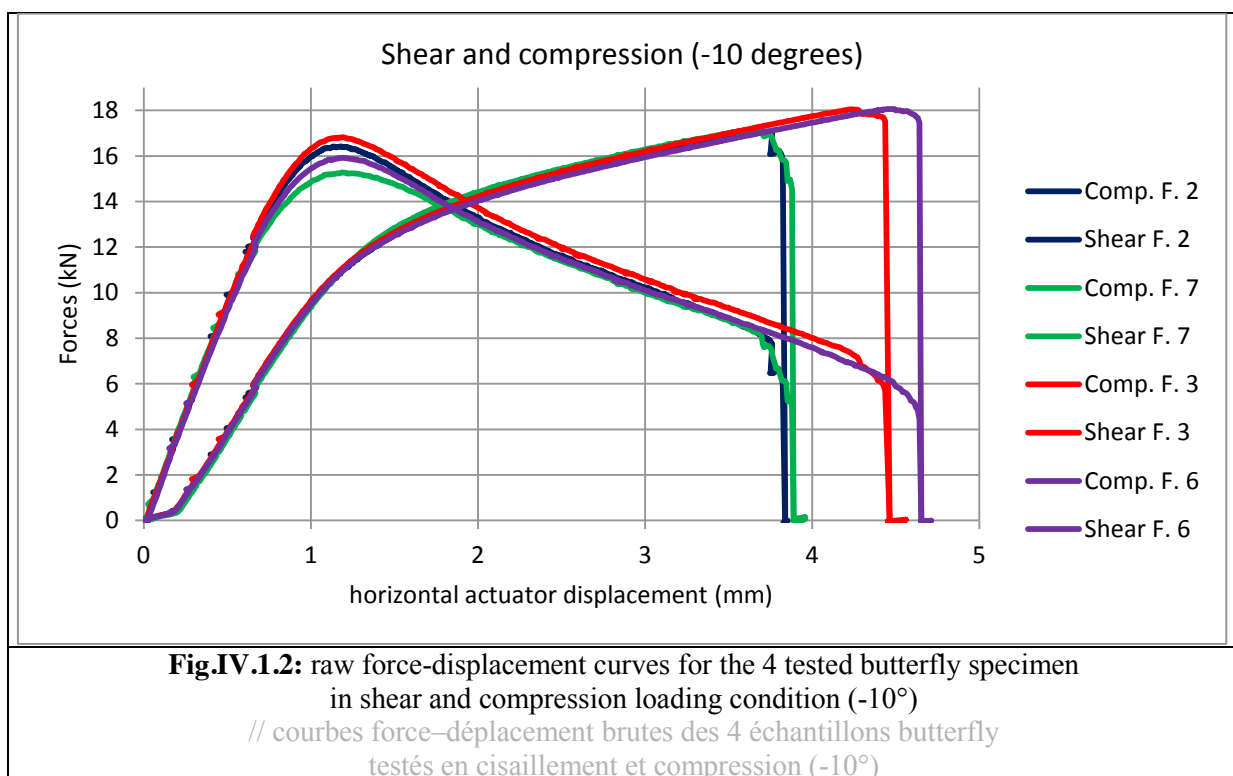
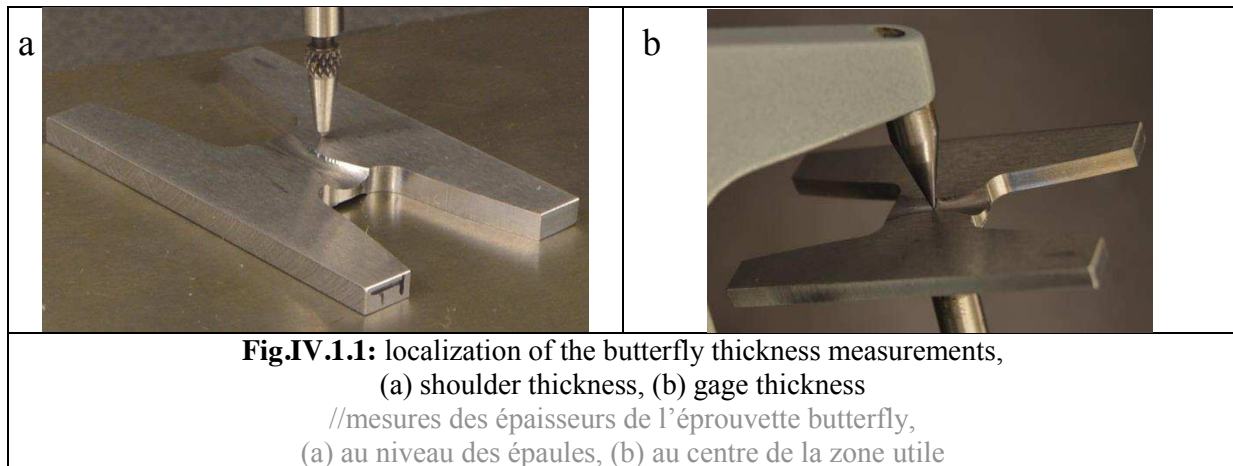
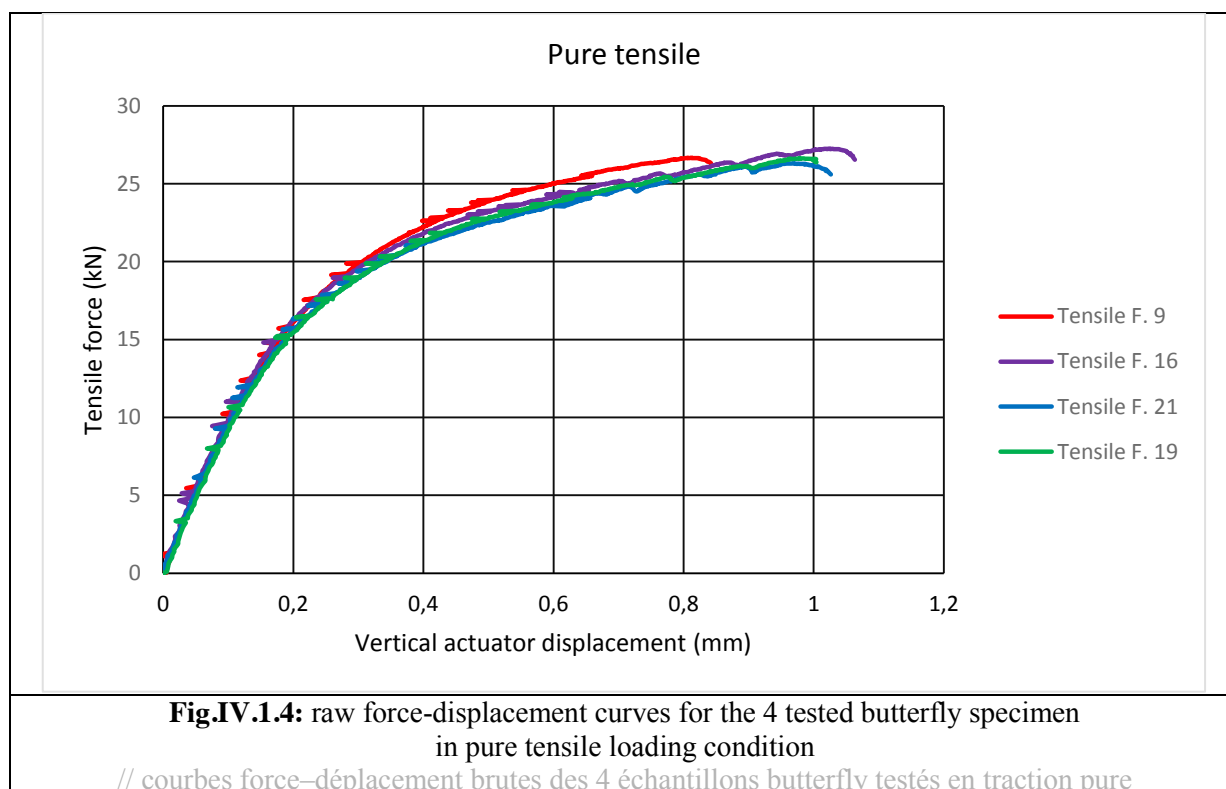
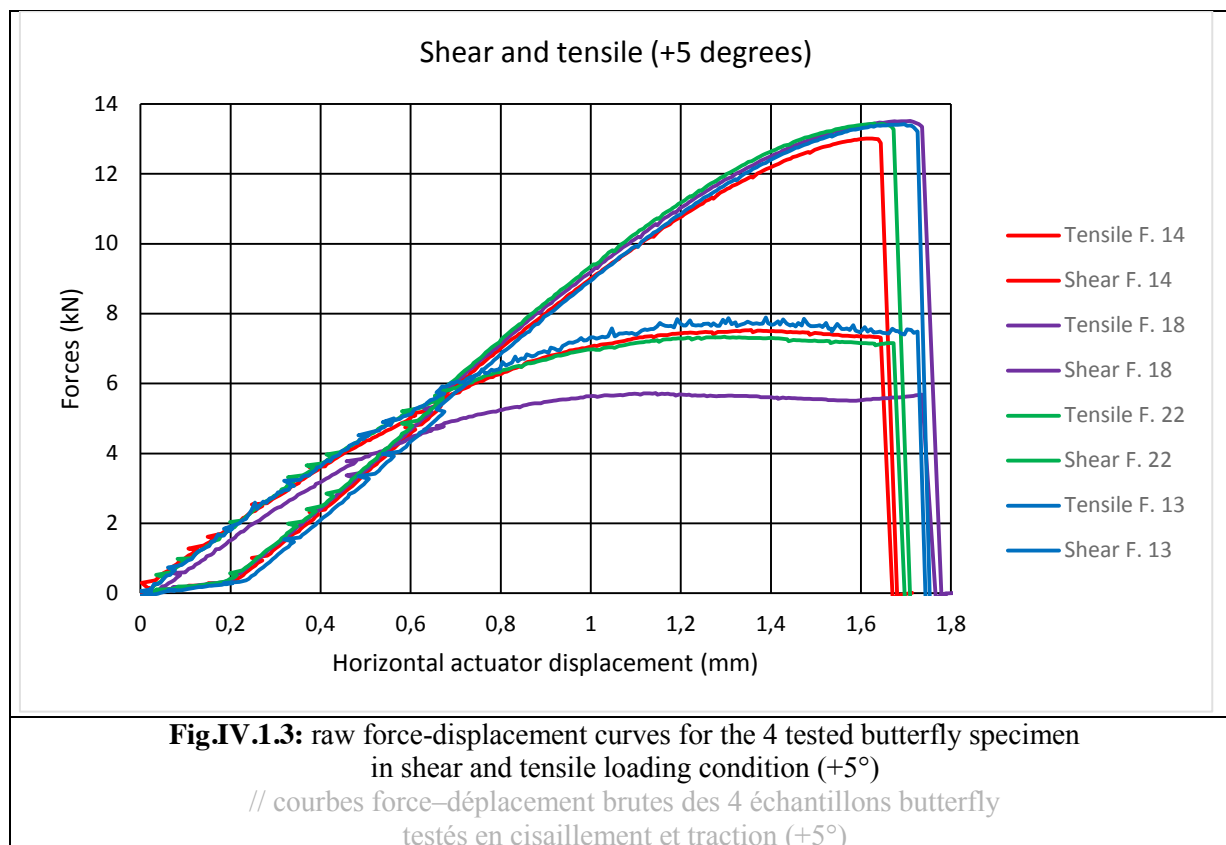


Fig.IV.1.2 shows the experimental force versus raw displacement curves. The fitting in the elastic and plastic parts is quite good, except the peak on the compressive forces at 1.2 mm displacement (scattering of about 10% max). There are two behaviors in terms of displacement to fracture: two specimens fail at 3.7 mm displacement, the two others at 4.4 mm. It is supposed the early failure of the two specimens is due to machining defects inducing possible roughness issue. This is the loading conditions with the highest experimental discrepancy.

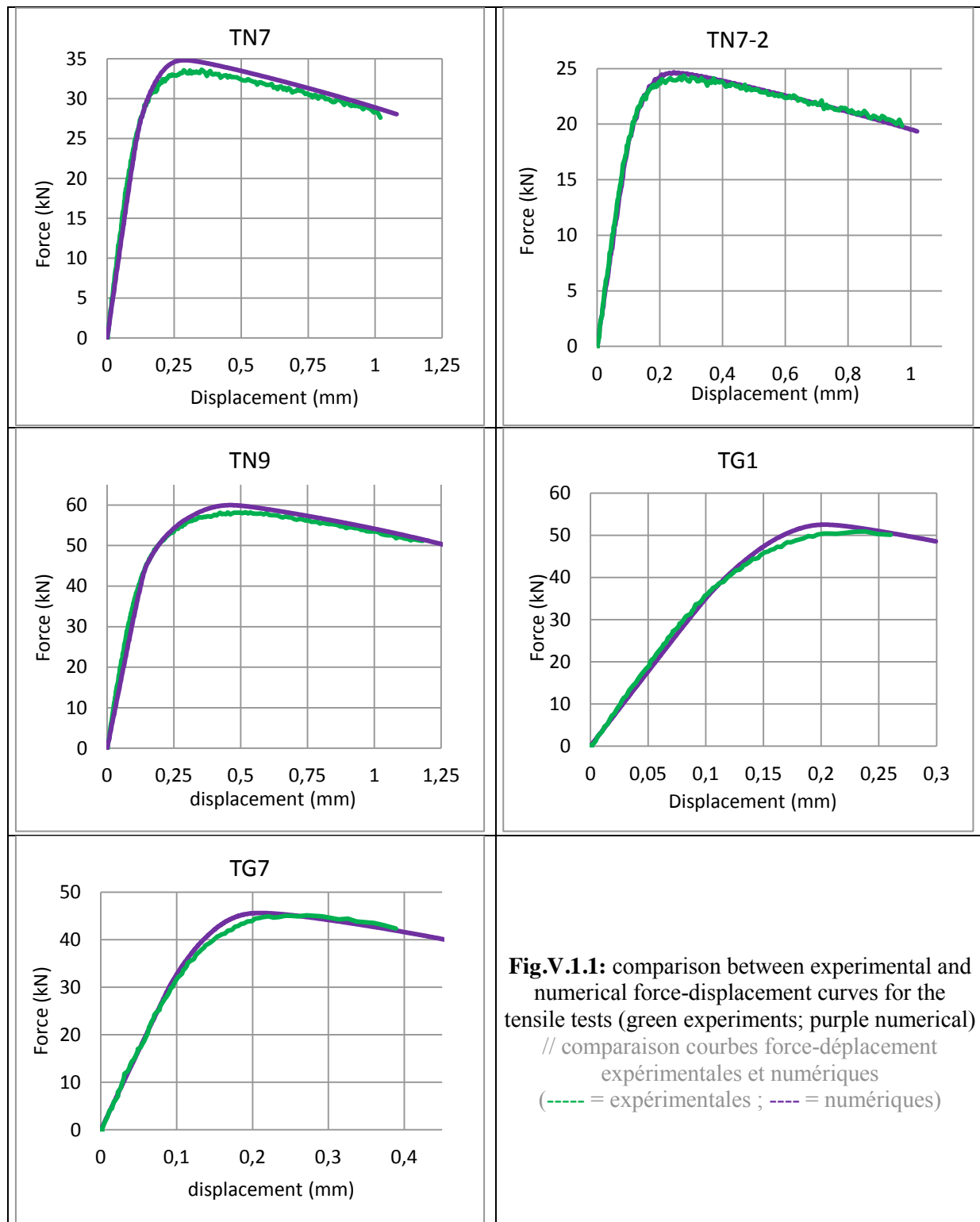
Fig.IV.1.3 plots the force – displacement curves for the shear with tensile loading condition. Except for specimen N°18, the repeatability is accurate for such specimens with bi-axial loading conditions.

Fig.IV.1.4 plots the force – displacement curves for the pure tensile specimen. The repeatability is good in the elastic and plastic part of the curves. If specimen N°9 is removed, the scatter of the displacement to fracture is quite low, 6%.



Appendix V.1: comparaison experimental numerical forces displacements curves

This Annex shows the comparison between the experimental and the numerical curves obtained with the identified modified Voce law (see **Table.V.1** and **Fig.V.2**).



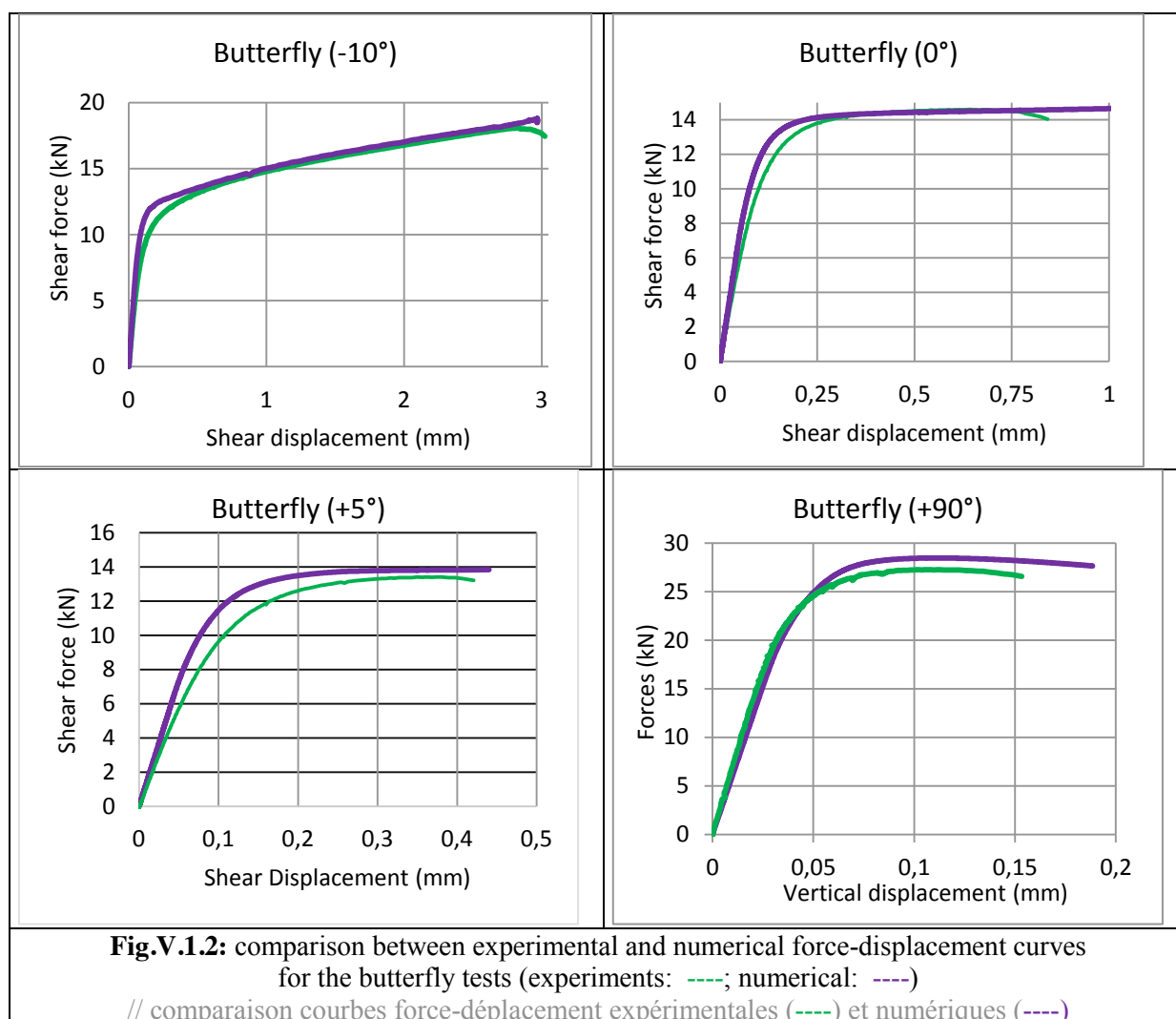


Fig.V.1.1 and **Fig.V.1.2** plot the comparison of the experimental and numerical curves for the tensile and butterfly tests. The fitting can be considered accurate despite a little overestimation of the stress hardening at low plastic strain. Indeed, the numerical curves are always slightly higher than the experimental ones. However the material behavior is well fitted at high level of plastic strain. Indeed, for the butterfly pure shear and shear with compression, the fitting is perfect. Thus, identified parameters are validated.

Résumé

Ce travail vise à améliorer la compréhension et la modélisation de la rupture des matériaux métalliques à gradient de propriétés. L'application se fait sur des pignons en acier 20MnB5 carbonitrurés insérés dans un "recliner", mécanisme de sécurité des sièges automobiles. La carbonituration confère à ces pièces une dureté très élevée en surface tout en conservant une ductilité significative à cœur. L'analyse de la rupture de mécanismes de sièges en test industriel a confirmé le double comportement à rupture du matériau : fragile sur une couche externe, ductile à l'intérieur. Un banc d'essai, spécialement conçu pour ce projet, soumet une dent à un effort latéral jusqu'à rupture complète. Des observations in situ sont effectuées et la courbe force-déplacement est enregistrée, montrant la diversité de comportement en fonction de la profondeur d'engagement des dents et de la présence ou non de la couche carbonitrurée. Des essais faisant varier l'état de contraintes sont utilisés pour mesurer les propriétés plastiques et calibrer les critères de rupture de la couche carbonitrurée comme de l'acier de base. La plasticité de von Mises avec une loi d'écrouissage simple rend très bien compte de tous ces essais mécaniques. Devant l'incapacité des critères de rupture ductile de la littérature de représenter les phénomènes observés, un critère plus adapté est proposé en conclusion de cette campagne expérimentale. La simulation de la rupture dans LS-Dyna est réalisée avec une technique d'érosion d'éléments dont les limitations sont discutées. La comparaison avec la rupture de dent expérimentale permet d'évaluer les critères numériques identifiés et d'analyser les limites actuelles de la simulation, en particulier la nécessité de prendre en compte plus finement à l'avenir le gradient de propriétés mécaniques ainsi que les contraintes résiduelles de compression de la couche carbonitrurée.

Mots Clés

carbonituration, rupture ductile – fragile, matériau à gradient, critères de rupture, taux de triaxialité des contraintes, paramètre de Lode

Abstract

This work aims at a better understanding and modeling of the failure of gradient metallic materials. It is applied to carbonitrided pinions made out of 20MnB5 steel, inserted in a "recliner", a safety mechanism of automotive seats. Carbonitriding induces high surface hardness while preserving significant core ductility.

The experimental analysis of the fracture behavior of seat recliners in an industrial test confirmed the dual failure behavior of the component: brittle external layer, ductile core material. A test bench has been specifically designed for the project: one tooth is submitted to a lateral force until complete failure. In situ observations are performed and the load-displacement curve recorded, showing a variety of behaviors as a function of the teeth engagement depth and of the presence or not of the carbonitrided layer. Experimental tests with various stress states were conducted to measure plastic properties as well as to calibrate fracture criteria, for the carbonitrided layer and for the core steel. Von Mises plasticity and a simple strain hardening curve fit very well all these experiments. As fracture criteria from the literature were unable to predict failure correctly for all the mechanical tests, an adapted criterion has therefore been proposed as an outcome of this extensive mechanical testing campaign. Fracture simulation in LS Dyna has been performed using the element erosion technique, the limitations of which are discussed. Comparison with the experimental tooth fracture measurements allows evaluation of the proposed failure criteria, and enables to stress out and discuss the present limits of the simulation, concluding that it will be necessary in future work to account more finely for the mechanical property gradient together with the compressive residual stresses in the carbonitrided layer.

Keywords

carbonitriding, ductile - brittle failure, graded material, failure criteria, stress triaxiality ratio, Lode parameter